Development of a Lymphatic Organotypic Microfluidic Model to Study the Influence of the Tumor Microenvironment in Lymphatic Vessel Function

By

Karina M. Lugo-Cintrón

A dissertation submitted in partial fulfillment of the

requirements for the degree of

Doctor of Philosophy

(Biomedical Engineering)

at the

UNIVERSITY OF WISCONSIN – MADISON

2020

Date of final oral examination: 12/05/2019

The dissertation is approved by the following members of the Final Oral Committee:

David J. Beebe, Professor, Pathology and Laboratory Medicine

Paul Harari, Professor, Human Oncology

Manish Patankar, Obstetrics and Gynecology

Suzanne Ponik, Senior Scientist, Cell and Regenerative Biology

Linda A. Schuler, Professor, Comparative Bioscience

Acknowledgements

I want to start by thanking the Summer Undergraduate Research Experience (SURE) program for providing me the opportunity to work for a summer with Dr. Tony Jimenéz in Dr. David Beebe's laboratory. This summer experience opened the doors of my graduate degree and, the Graduate Engineering Research Scholars (GERS) program provided part of the financial support needed for my degree. For this reason, I am very grateful for these two programs. I feel very fortunate to have had the opportunity to join Dr. David Beebe's lab, where I have learned, faced challenges and growth as a scientist and person. Dave, thank you for all your advice and for always believing in me. Thanks for discussing directions that my projects could take while giving me the freedom to decide what I wanted to pursue. I am not going to lie; having this freedom was very challenging in my early grad school years. However, now I genuinely appreciate it and feel privileged to have had that freedom.

I would also like to thank the members of my thesis committee for providing support and insightful discussions, Professors Paul Harari, Manish Patankar, Suzanne Ponik, and Linda A. Schuler. In particular, I want to thank Suzanne for many encouraging discussions that have helped me shape my doctoral research. I was very fortunate to have had the opportunity to work with different post-docs in the lab. Max Gong, José Ayuso, and María Virumbrales thank you for all the scientific and life-related conversations; I consider you my mentors and friends. I am especially thankful to María; I don't have words that can explain how much you have helped me and how much I have learned from you. Thank you for your feedback, insight, trust, and patience. I want to thank current and past members of the MMB lab for their support, Mouhita, Patrick M., Sheena, Bridget, Pete, Alice, Molly, Jake, and Megan.

To my family and friends, thank you for ALWAYS supporting and believing in me. Thank you to my parents, Ramonita Cintrón and Manuel Lugo, for supporting my college career unconditionally and never stop pushing me, so much of what I have achieved I owe to you. You have taught me to work hard, to care for others, and to believe in myself, and you have no idea how much this kind of mindset has helped me during my graduate career. To my parents and sisters, Wanda, Glenda, Yessenia, and Angelica, I would not have been here without any of you. Your support has been crucial in allowing me to build my career and will never go unappreciated.

Finally, I would like to give a huge thank you to Rafael Medero for his support, understanding, and confidence in me. Your support has helped me scientifically and emotionally throughout my entire Ph.D. journey. I would also like to thank you for introducing me to biking, which changed our lifestyle during grad school, allowing us to truly enjoy Madison. Finally, thank you for making the last several years a time of happiness and growth.

Abstract

Metastasis is the leading cause of death in cancer patients and, once cancer cells spread from the primary tumor, treatment becomes challenging. A key step during cancer metastasis is cancer cell intravasation (i.e., entry of cancer cells into the blood or lymphatic vasculature) that results in tumor cell dissemination to distant organs. Certain cancers (e.g., breast and head and neck), preferentially spread out of the primary tumor using the lymphatic vasculature, a process that is regulated by the interactions between cancer cells, the lymphatic vasculature and the surrounding tumor microenvironment (TME). Despite the identification of mechanisms that cancer cells use to intravasate into lymphatic vessels, lymphatic metastasis remains a problem. In this regard, recent studies have highlighted the critical role the TME plays in lymphatic metastasis and, recently emerged as a potential new target to inhibit tumor growth and metastasis. Therefore, there is a need to better understand how components of the TME influence lymphatic vessels to identify new therapeutic targets that prevent metastasis. To study lymphatics, traditional cell culture approaches (e.g., petri dishes) have been used, however, these approaches lack the complexity of the biological structures. Hence, to understand the influence of different TME components in lymphatics, a microfluidic *in vitro* model that can recapitulate the physiological conditions found *in vivo* would be a beneficial tool to advance cancer research. Thereby, ***this Ph.D. thesis presents the development of an organotypic lymphatic vessel model to study the influence of different tumor microenvironment components in lymphatic vessel remodeling.*** The following thesis is divided into 5 chapters and an appendix. From which each part can be independently read but all of them should be considered within the overall picture.

In chapter 1, an introduction about lymphatic metastasis, the tumor microenvironment and current models to study the lymphatics are described. In chapter 2, the *lymphatic* in vitro *model developed* was characterized based on lymphatic vessel hallmarks. Then, in chapter 3, the lymphatic model was used *to investigate the influence of ECM density in lymphatic vessels in the context of breast cancer*. In chapter 4, the lymphatic model was used in for translational research *to investigate the influence of patient-derived head and neck cancer-associated fibroblasts in lymphangiogenesis.* Finally, the main conclusions of this Ph.D. thesis and future directions are described in chapter 5.

Table of Contents

List of Figures

List of Tables

List of Abbreviations

2D	Two-dimensional
3D	Three-dimensional
CAFs	Cancer-associated fibroblasts
ECM	Extracellular matrix
EGF	Epidermal growth factor
HGF	Hepatocyte growth factor
HMF	Human mammary fibroblasts
LECs	Lymphatic endothelial cells
MMPs	Matrix-metalloproteinases
TME	Tumor microenvironment
VEGF	Vascular endothelial growth factor

Chapter 1: Introduction

1.1 Cancer Metastasis

Cancer is the main public health problem worldwide. As for the United States, cancer is the second leading cause of death with many cases diagnosed every year. For 2019, there were an approximate 1,762,450 new cancer cases diagnosed, which is equivalent to more than 4,800 new cases each day[1]. Clinically, cancer metastasis accounts for 90% of cancer-related deaths[2]. Metastasis is a multistep process by which cancer cells invade the surrounding stroma, intravasate the blood or lymphatic vessels, and travel in the circulation to a secondary site in the body where cancer cells can initiate malignant growth and form secondary tumors[3,4] (Figure 1.1). As mentioned before, once cancer spreads to a secondary site, treatment becomes challenging due to the biological heterogeneity of metastases, reducing the survival rate of patients[5]. The heterogeneity of metastasis refers to the fact that the growth and survival of metastases will depend on the interactions between tumor cells and the surrounding microenvironment, making cancer progression challenging to be effectively targeted. The ineffectiveness of treatments is reflected in the five-year survival rates of patients. For example, patients presenting distant cancer metastasis, the five-year survival rates are very low with 27% for breast cancer (compared to 99% for the localized cancer) and 39% for oral cavity & pharynx cancers (compared to 84% for the localized cancer)[1].The statistics described above demonstrate the ineffectiveness to efficiently treat patients with metastatic disease. Therefore, a better understanding of the initial stages of the metastatic cascade could help to identify potential treatments that prevent cancer spread, improving patient's survival rates. In the primary tumor, cancer cells interact with components of the surrounding TME that determine tumor outcome. In the next section, the main aspects of the TME are described.

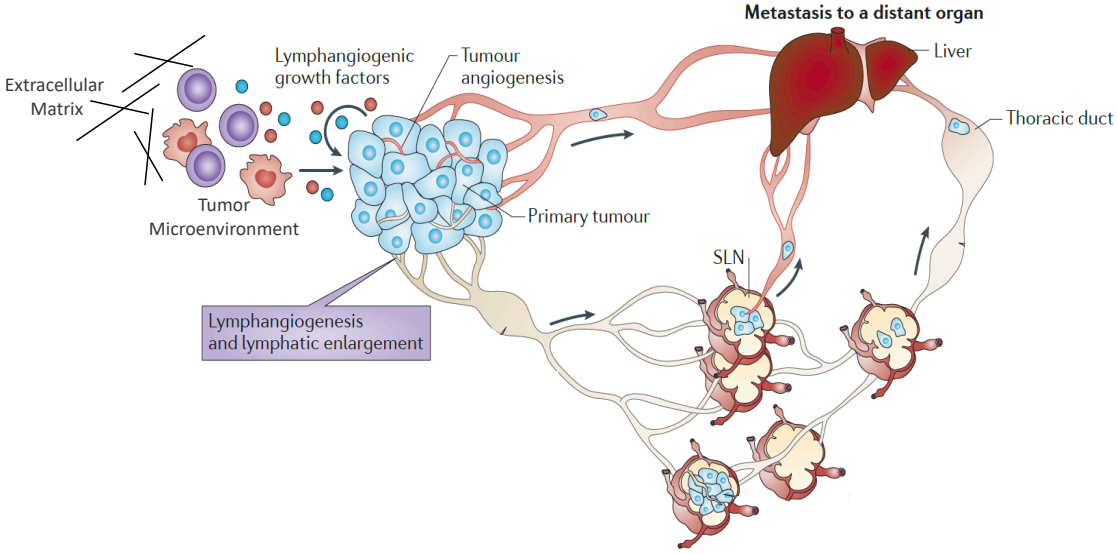

Figure 1.1: Cancer Metastasis. Lymphatic and blood vessels are conducts for tumor spread, metastasis to a distant site. Remodeling of lymphatic vessels in cancer contributes to metastasis. Lymphangiogenic growth factors derived from tumor cells and components of the tumor microenvironment, promote tumor lymphangiogenesis in and around the primary tumor, these processes are thought to facilitate metastasis. Adapted from [6].

1.2 The Tumor Microenvironment (TME)

As previously mentioned, cancers are more complex than just cancer cells that proliferate uncontrollably. Cancers are surrounded and often supported by the tumor microenvironment (TME) [7]. Consequently, the outlook on cancer has changed dramatically and the tumor is no longer viewed as a single component, but rather as a complex TME in which the tumor exists. The TME comprises malignant and non-transformed cells surrounding the tumor, including fibroblasts, immune cells, vasculature (blood and lymphatic), the extracellular matrix (ECM) as well as soluble factors (e.g., cytokines, growth factors and exosomes), which represents the surrounding stroma [7–10]. Cancer cells can modify the adjacent stroma to form a tolerant and supportive microenvironment that leads to tumor progression, known as the "reactive tumor stroma" [11].

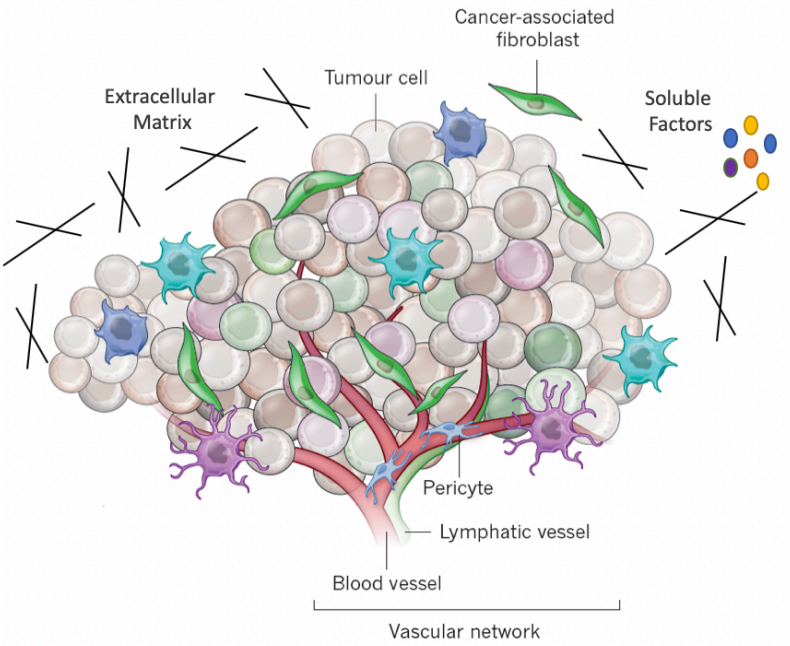

Figure 1.2: The Tumor Microenvironment (TME). Comprised of a cellular and non-cellular component (ECM). Some of stromal components are labeled (e.g., cancer-associated fibroblasts, blood and lymphatic vessels) Adapted from [12].

Through production of growth factors, cytokines and proteases cancer cells modify the surrounding TME. These factors lead to the disruption of normal tissue homeostasis and act in a paracrine way to induce changes in the TME such as angiogenesis, inflammation and the activation of the stromal cells (e.g., fibroblasts) that can then lead to the secretion of additional growth factors and proteases favorable for tumor progression [13]. Activation of fibroblasts in the stroma promote tumor progression through the secretion of growth factors and pro-migratory ECM components, which leads to the increase of ECM stiffness, as well as through the upregulation of matrix metalloproteinases that degrade and remodel the ECM which in turn affects cancer cells (Figure 1.3) [14].

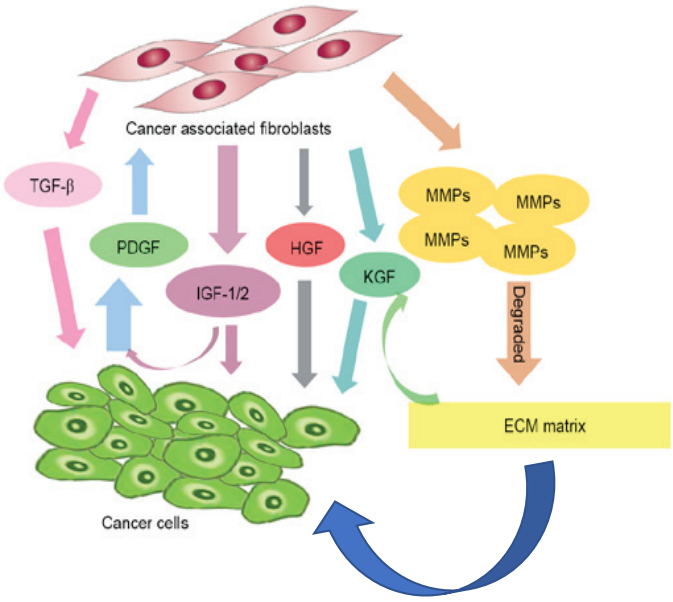

Figure 1.3: Cancer and cancer-associated fibroblasts feedback loop. Cancer cells induce fibroblast activation that leads to cytokine release, in turn, cancer associated fibroblast promote tumor growth, and metastasis. Adapted from [14].

In addition, activated fibroblasts secrete pro-angiogenic factors (e.g., VEGF-C) [15], which are sensed by the surrounding vessels and as a consequence new vessels start to grow towards the tumor in order to increase the blood supply[16,17]. As a result of the formation of new blood vessels there is a boost in tumor growth that, in turn, facilitate the spreading of tumor cells through the blood or lymphatic vasculature (i.e. metastasis) [18]. To sum up, the stromal signals from the TME interact with each other as well as with cancer cells, defining tumor outcome. Thus, as it has been already established, the TME is an important regulator of tumor development, progression and metastasis, which also plays a critical role in response to treatment [19–21]. After revealing the important influence of TME on tumor development, it is not surprising that many recent therapies aim to use stromal cells as therapeutic target. For this reason, newly developed in vitro models should incorporate components of the TME to better understand the TME and to perform drug-testing in more relevant microenvironments. ***Among the many components of the TME,***

activated fibroblasts, the ECM (density and composition) and the lymphatic vasculature are of interest in this dissertation as these components have been reported key players that regulate cancer progression and metastasis [22–24]. In this section, these components of the TME are described, distinguishing between cellular and non-cellular components of the TME.

1.2.1 Cancer-associated Fibroblasts (CAFs)

Activated fibroblasts, better known as cancer-associated fibroblasts (CAFs), are the predominant cell type within the tumor stroma [9,25]. As mentioned before, CAFs are fibroblasts that were altered by cancer cells to maintain a favorable microenvironment for tumor cell growth and proliferation [13]. It has been demonstrated that CAFs present in the TME promote tumor growth, progression and chemoresistance via the secretion of a variety of autocrine and paracrine cytokines and other tumor-promoting factors critical for tumor cell proliferation, angiogenesis, invasion and inflammation [26,27]. Some of the factors include growth factors such as epidermal growth factor (EGF), hepatocyte growth factor (HGF), vascular endothelial growth factor (VEGF). And, cytokines and chemokines such as interleukins (ILs) IL-6 and IL-17A, C-C motif chemokine ligands (CCLs) CCL5 and CCL7 and C-X-C motif chemokine ligands[25,28–31]. In addition, CAFs are also producers of matrix-metalloproteinases (MMPs), which are important in modulating the remodeling of the TME through the degradation of ECM and the release of soluble factors present in the ECM [32–34]. These changes in the ECM, in turn, promote an invasive phenotype of cancer cells. Therefore, the ECM is as important as the CAFs in promoting cancer progression. For this reason, the ECM will be described in the next section.

1.2.2 Extracellular Matrix (ECM)

The extracellular matrix (ECM) is the non-cellular component that supports all tissues and organs by providing surrounding cells with physical and biochemical support that is required for tissue morphogenesis, differentiation and homeostasis[35]. It is mainly composed of proteins, polysaccharides and water, which are crucial for cell function. Each tissue has an ECM with a unique composition and architecture and its dynamic structure is constantly being remodeled by the cells in the ECM[36].

In cancer, it is well recognized that the ECM becomes deregulated and disorganized, which in turn, promotes malignant cell transformation and cancer progression [37,38]. Upon deregulation, the protein composition of the ECM is altered, where higher levels of collagen, fibronectin and tenascin have been found[39], altering cell adhesion and proliferation. As an example of ECM deregulation, the increase in collagen density is one of the major changes in certain tumors such as breast cancer, that leads to tumor progression [40].On the other hand, mounting evidence suggests that the increase in secretion of ECM proteins results in elevated stiffness of the tumor compared to the normal tissue, which supports cancer progression [41,42]. Another example of ECM deregulation is due to the altered function of MMPs, which in addition to degrading the matrix, results in the release of factors that are anchored to the ECM which induce tumor growth, invasion and metastasis[43].

Altogether, the mounting evidence demonstrates that the tumor-associated ECM alters cancer progression by promoting cancer cell migration[44], proliferation[45], and altering cellular metabolism[46]. Given the importance of the ECM and its influence on cells, *in vitro* models should carefully consider the integration of the most representative ECM to obtain relevant results.

After discussing the importance of the ECM in tumor progression and its integration in *in vitro* models, the importance of vessels within the TME is discussed.

1.2.3 Blood and Lymphatic Vessels

In tissues, the main function of the blood and the lymphatic vasculature is to deliver oxygen and nutrients, remove waste and CO_2, and regulate interstitial pressure[47]. Within the TME, cancer cells drive blood vessel growth (i.e., angiogenesis) to obtain oxygen and nutrients to support tumor progression[48]. The resulting blood vessels are variable and abnormal, ranging in size and morphology which often leads to a leakier phenotype [49]. On the other hand, cancer cells induce lymphatic vessel growth (i.e., lymphangiogenesis) to facilitate fluid drainage and metastasis[50,51]. Altogether, blood and lymphatic vessels are critical components of the TME that can lead to metastasis. Therefore, in the following section the role of vessels in cancer metastasis is described.

1.3 The Role of Vessels in Cancer Metastasis

As previously described, in order to metastasize, cancer cells dissociate from the primary tumor and intravasate blood or lymphatic vessels[6]. Historically, it is well documented that cancer cells intravasate into blood vessels to reach distant organs as evidence of circulating cancer cells were found in the blood. Thus, it was assumed that cancer cells used only blood vessels to spread out of the primary tumors. Although now is well known that lymphatic vessel intravasation is another way that cancer cells can enter the circulation, it is not as well understood as compared to blood vessels. One reason for the lack of understanding of lymphatic vessel involvement in metastasis is

because until recently, it was not possible to discern which type of vessel (i.e. blood or lymphatic) cancer cells were using to spread out from the primary tumor.

Recently, the emergence of specific lymphatic markers such as LYVE-1[52], PROX-1[53] and podoplanin[54] have made it possible to distinguish between lymphatic and blood vessel invasion by cancer cells. And, interestingly, the use of these markers has provided strong clinical evidence demonstrating the preferential spread of carcinomas to the regional lymph nodes prior to distant metastasis, which is used as a critical prognostic indicator[55–57]. In fact, having a positive lymph node status has been correlated with a worse clinical prognosis (reduced patient survival), in certain cancers, including breast and head and neck cancer patients[58–60]. Although either route of dissemination (i.e. blood or lymphatic vessels) can lead to venous dissemination as lymphatics drain into blood (Figure 1.4), compared to blood vessels, lymphatic vessels are potentially more advantageous routes given their leakier endothelium and natural fluid draining function[61]. ***Despite the clinical implications of lymphatic metastasis, the mechanisms leading to tumor spread via lymphatic vessels and the contribution of lymphatic vessels on cancer progression are poorly understood.*** Altogether, there is a need to better understand the lymphatics in the context of cancer metastasis. Thus, *in vitro* models should include this essential component of the TME. For this reason, in the next section, the structure of the lymphatic vasculature is described and in the following section lymphangiogenesis and lymphatic vessel remodeling in the context of cancer metastasis is described.

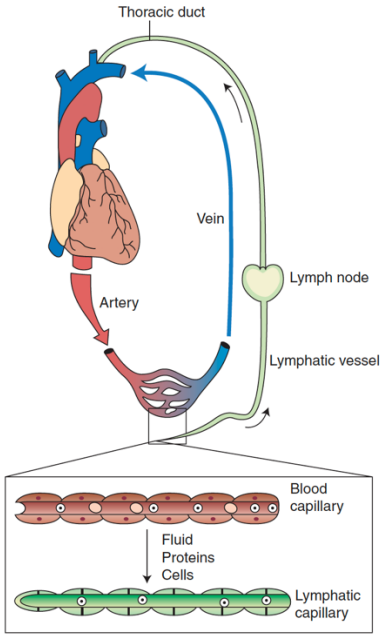

Figure 1.4: Macroscopic view of the blood versus lymphatic system and illustration of the structures of lymphatic capillaries. Figure modified from [62].

1.4 Structure of the Lymphatic Vasculature

The lymphatic system comprises of a network of initial, pre-collecting, collecting lymphatic and lymph nodes (Figure 1.5). Initial lymphatics are small blind-ended (30-80μm diameter) vessels with thin walls that absorb fluid and cells in tissues [63,64]. In contrast to blood vessels, initial and pre-collecting lymphatic vessels have a discontinuous basement membrane and no supporting cells (e.g. smooth muscle cells or pericytes), with occasional valves found in pre-collecting vessels. In the context of cancer metastasis, the lack of basement membrane and supporting cells in lymphatic vessels makes it simpler for cancer cells to intravasate. Going back to the structure of lymphatics, fluid enters the initial lymphatics and it is subsequently transported to thicker collecting lymphatics, which are connected with multiple lymph nodes. Therefore, fluid is eventually returned to the blood circulation through the thoracic or lymphatic ducts that join to the subclavian veins as previously mentioned. Overall, this route serves as the means by which the immune

system continuously samples the periphery of tissues. Where draining the lymph carried by the initial lymphatics into the lymph nodes can elicit the activation of and mobilization of leukocytes, priming the immune responses, and assisting the immune surveillance through the supply of antigen and immune cell-rich lymph. Unfortunately, dysfunction of the lymphatic vessels is implicated in multiple diseases, including lymphedema, inflammation, and cancer[65]. As mentioned before, in the next section, lymphangiogenesis and lymphatic vessel remodeling in the context of cancer metastasis is described.

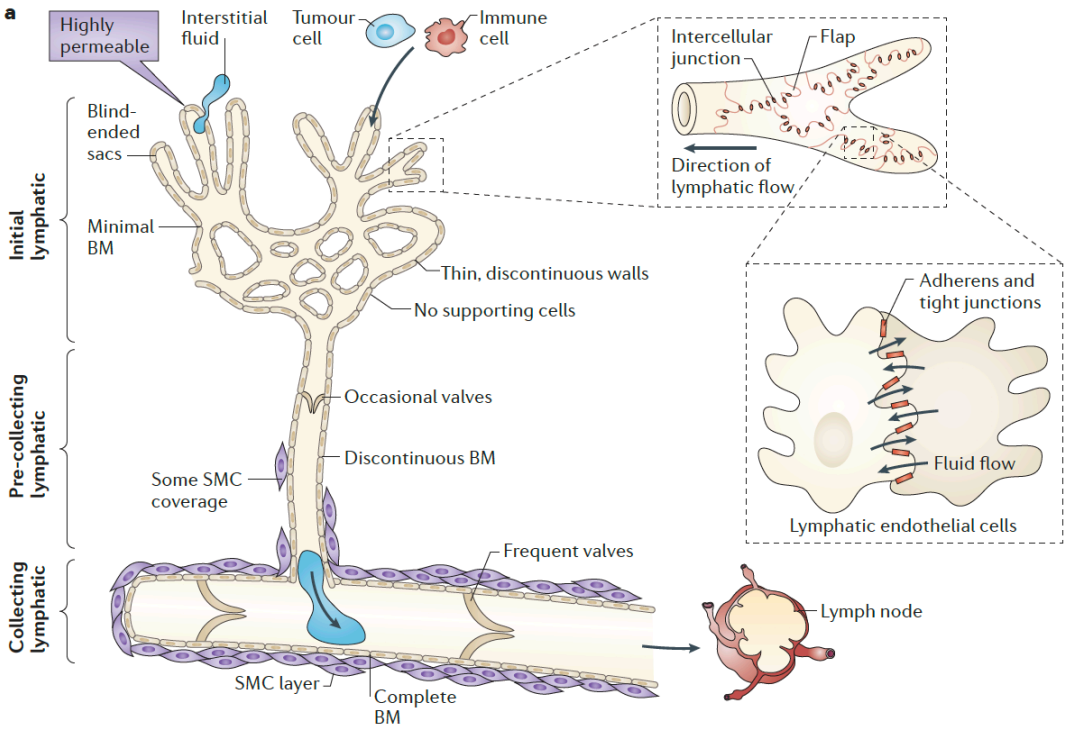

Figure 1.5: Structure of the lymphatic vasculature and of lymphatic endothelial cells from initial lymphatics. Hierarchy of lymphatic vessel subtypes (i.e., initial lymphatic, pre-collecting lymphatic and collecting lymphatic) with the characteristics of the subtypes denoted. Figure modified from [6].

1.5 Lymphangiogenesis and Lymphatic Vessel Remodeling in Cancer Metastasis

In the TME, tumors induce changes in the lymphatic vasculature (e.g., lymphangiogenesis) to increase lymph drainage [51] and to promote metastasis of tumors to draining lymph nodes[66,67].

As mentioned before, lymphangiogenesis is the process in which new lymphatic vessel forms from pre-existing lymphatic vessels. In healthy states, lymphangiogenesis is important for functioning of the immune system, lymphoid organ formation, tissue fluid homeostasis, and absorption of dietary fats[6]. However, dysregulated lymphangiogenesis result in pathological conditions such as lymphedema, abnormal fat metabolism, hypertension, inflammatory diseases and lymph node mediated tumor metastasis[63]. In cancer, blood and lymphatic vessels are formed intratumoral and peritumoral via the angiogenic and lymphangiogenic cues (e.g., VEGF-C and VEGF-D) derived from cancer and stromal cells[68,69]. *Thus, blocking tumor lymphangiogenesis is considered as one anti-metastatic approach*[70,71].

As described before, lymphatic vessels in the TME are considered as a passive route of tumor dissemination. However, recently, a number of studies have reported that lymphatic vessels are conditioned by metastatic breast cancer cells within the pre-metastatic niche to accelerate metastasis through the secretion of CCL5 [72]. *Hence, this study demonstrates that lymphatic vessels are more than a route for cancer dissemination and suggest that lymphatic vessels are an active component of the TME that needs to be better understood.* Another study demonstrated that lymphatic endothelial cells support tumor growth through the secreted factors of the lymphatic endothelial cells (LECs), but not by blood endothelial cells secreted factors[73]. Overall, these studies demonstrate the active role of lymphatics in cancer progression. Interestingly, a recent study using a transwell 3D tri-culture model containing a monolayer of LECs, metastatic cancer cells and normal fibroblasts demonstrated that tumor cell invasion significantly increased in the presence of chemotherapeutic agents when LECs were present. Therefore, this study demonstrates how LECs conferred resistance to chemotherapies, effect that was mitigated by anti-lymphangiogenic therapy [74]. *Taken together, these results demonstrate that lymphatics are an*

active component that regulates cancer progression and suggest that there is an opportunity to target stromal interaction to increase benefits of cancer treatment, and therefore, reduce lymphatic metastasis. In the next section, the influence of TME components in lymphatic metastasis is described.

1.5.1 Influence of TME Components in Lymphatic Metastasis

As established in previous sections, TME components regulate tumor progression and metastasis. Additionally, it was established that lymphatics are the preferential route of metastasis for certain cancers. However, the previous sections focused on cancer-TME interactions and cancer-lymphatics interactions. In this section, the focus is on the clinical evidence that implicate TME components in regulating lymphatic metastasis. As previously described, lymphatic studies have focused on the interactions between cancer cells and LECs [73,75,76]. However, how lymphatic vessels interact with other components of the TME that could promote metastasis is less studied. As an example, TME components such as CAFs have a profound influence in breast and head and neck cancer progression and have been associated to lymphatic metastasis [13,26,77–81]. However, little is known about the interactions between lymphatic vessels and tumor stromal cells (e.g. CAFs) that contribute to cancer progression and lymphatic metastasis. ***Thus, of interest in this thesis is to understand the influence of CAFs on lymphatic vessel remodeling***. As previously described, another component of the TME that can regulate metastasis is the ECM. In the context of breast cancer, a clinical correlation between high ECM density with a positive lymph node status has been found [82].Despite the clinical evidence suggesting that the ECM could be altering the lymphatics, ***it remains to be determined how a tumor-associated ECM affects lymphatic vessels***. ***Altogether, answering these questions is critical for developing potential cancer treatment***

strategies that target lymphatic metastasis and for this, an* in vitro *model that recapitulate these aspects of the TME while including the lymphatic vessel component is essential. In the next section, the approaches for studying lymphatics *in vitro* and *in vivo* are described.

1.6 Lymphatic *in vitro* and *in vivo* Models

To investigate how different components of the TME affect lymphatic vessels and potentially lymphatic metastasis, *in vitro* models that recapitulate the *in vivo* microenvironment would be beneficial. Traditional two-dimensional (2D) *in vitro* methods to study lymphatic biology include monolayer cell culture on plastic dishes or matrix-coated dishes[83]. These methods allow for easy examination of biochemical activity, proliferation, adhesion assays, wound scratch assays and invasion assays. However, the main limitation in the 2D models is the lack of physiological representation (i.e. lack of structure and microenvironmental components). The current state-of-the-art three-dimensional (3D) *in vitro* approach is the lymphatic ring assay, whereby an excised mouse lymphatic thoracic duct is embedded in a 3D collagen matrix[84]. On the other hand, the main *in vivo* approach to study lymphatic vessel-tumor interactions has been xenotransplantation of human tumors into mouse models[85,86]. While the lymphatic ring assay bridges current *in vitro and in vivo* methods, the reliance on excised mice tissue limits its relevance to human physiology and hinders experimental throughput and repeatability. ***Therefore, lymphatic* in vitro *models are currently scarce and fail to recapitulate the TME, which includes vasculature, fibroblasts, as well as the non-cellular composition of the extracellular matrix*** [8,21,87]**.** Although animal models provide relevant *in vivo* microenvironments the experimental control is challenging in these dynamic systems. To bridge this gap, microscale models are often used and are discussed in the next section.

1.7 Rationale for Using Microscale Organotypic *in vitro* Models

Historically, 2D cell culture has being the approach that most biologists use due to the simplicity and efficiency of the experimental approach[88]. 2D cell culture consists on the adherence of cells to a flat surface (e.g., petri dish) to provide mechanical support for the cells, allowing for access to similar amount of nutrient and growth factors present in the media which results in homogenous cell proliferation[89]. However, cells *in vivo* perform bioactivities in response to the stimulation from a complex 3D microenvironment. For this reason, 3D cell cultures have become more commonly used within the last decade since the structure is more physiologically relevant and better represent *in vivo* tissue. Several studies have revealed that cells cultured in 3D behave differently compared to cells cultured in 2D due to the cell-cell and cell-matrix interactions, having a profound effect on cell behavior [90,91]. For example, gene expression is a cellular characteristic found to be modified between 2D and 3D, where the overall gene expression becomes more similar to that observed in tumors[91]. Another example is the mechanisms of cell migration which dramatically change between 2D and 3D environments [92,93]. Although 3D cell culture recapitulates the matrix aspect of the *in vivo* microenvironment, these models often lack the specific tissue geometries found *in vivo*. Nowadays, microfluidic technologies have the ability to engineer specific tissue geometries such as luminal structures, providing an additional level of spatial organization, and recapitulating the *in vivo* structure. The impact of tissue geometry in its function has been previously demonstrated by us and others[94,95]. For example, our lab and others have demonstrated that geometry deeply influences cell function[96] and cytokine secretion by endothelial cells when cultured in an *in vivo*-like structure (i.e. luminal structure) compared to conventional 2D and 3D cultures[94]. Another advantage of microfluidic technologies is that they

consume dramatically less reagents than macroscale or traditional *in vitro* platforms, which greatly decreases the cost of each experiment and allows for the potential use of patient-specific cells[97].

1.8 Thesis Aims

This thesis is aimed to develop a microfluidic organotypic lymphatic vessel model to investigate the role of tumor microenvironmental factors on lymphatic vessel remodeling. As described through the introduction, lymphatic vessel remodeling and lymphangiogenesis are important in the context of cancer metastasis. Unfortunately, lymphatic *in vitro* models are currently scarce and fail to recapitulate the influence of the TME, which includes vasculature, fibroblasts, as well as the non-cellular composition of the extracellular matrix. Taking advantage of microfluidic techniques, the specific aims of this thesis were to (Figure 1.6):

1. **Develop and characterize an *in vitro* organotypic lymphatic vessel model using microfluidic approaches.** The organotypic lymphatic vessel model was developed using a microfluidic device that allows the culture of cells lining a 3D lumen structure surrounded by a 3D matrix.
2. **Assess the influence of ECM density in lymphatic vessel remodeling.** Modification of the 3D matrix composition in the developed organotypic lymphatic vessel model was done to recapitulate the ECM density of the normal breast and breast tumors (i.e., low- and high-collagen density), allowing the study of the influence of ECM in lymphatic vessel remodeling.
3. **Assess the influence of patient-derived head and neck CAFs in lymphangiogenesis.** Patient-derived CAFs from head and neck patients are embedded in the surrounding 3D

matrix of the organotypic lymphatic vessel model to assess the changes in lymphangiogenesis.

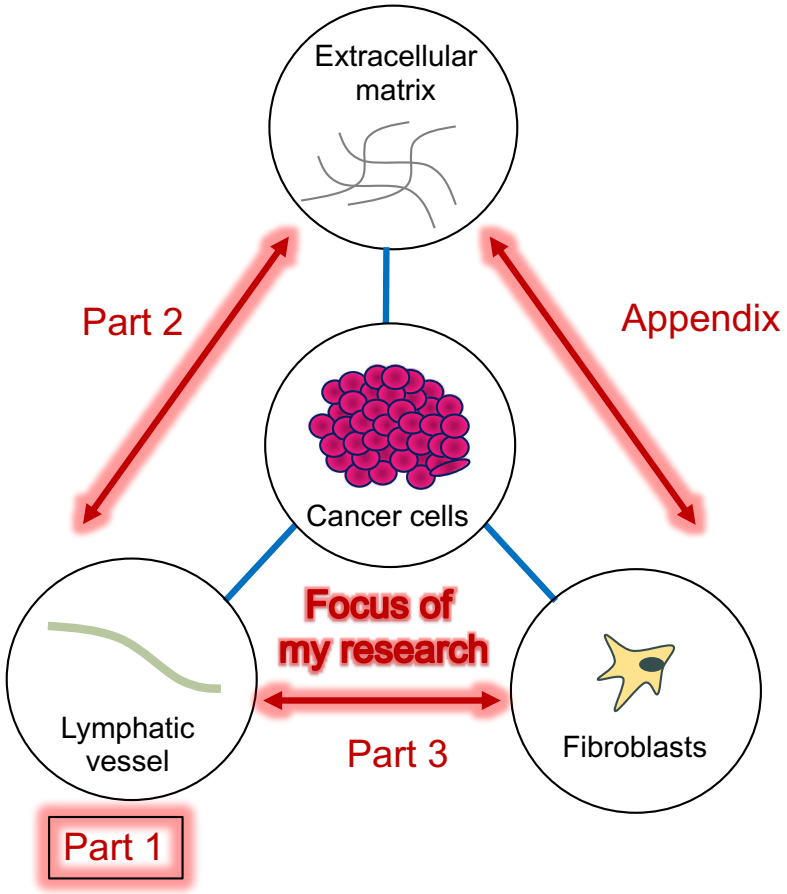

Figure 1.6: Overview of thesis aims.

Chapter 2: Human Organotypic Lymphatic Vessel Model Elucidates Microenvironment-dependent Signaling and Barrier Function[1]

Abstract

The lymphatic system is an active player in the pathogenesis of several human diseases, including lymphedema and cancer. Relevant models are needed to advance our understanding of lymphatic biology in disease progression to improve therapy and patient outcomes. Currently, there are few 3D *in vitro* lymphatic models that can recapitulate the physiological structure, function, and interactions of lymphatic vessels in normal and diseased microenvironments. Here, we developed a 3D microscale lymphatic vessel (μLYMPH) system for generating human lymphatic vessels with physiological tubular structure and function. Consistent with characteristics of lymphatic vessels *in vivo*, the endothelium of cultured vessels was leaky with an average permeability of $1.38 \times 10^{-5} \pm 0.29 \times 10^{-5}$ cm/s as compared to $0.68 \times 10^{-5} \pm 0.13 \times 10^{-5}$ cm/s for blood vessels. This leakiness also resulted in higher uptake of solute by the lymphatic vessels under interstitial flow, demonstrating recapitulation of their natural draining function. The vessels secreted appropriate growth factors and inflammatory mediators. Our system identified the follistatin/activin axis as a novel pathway in lymphatic vessel maintenance and inflammation. Moreover, the μLYMPH system provided a platform for examining crosstalk between lymphatic vessels and tumor microenvironmental components, such as breast cancer-associated fibroblasts (CAFs). In co-culture with CAFs, vessel barrier function was significantly impaired by CAF-secreted IL-6, a possible pro-metastatic mechanism of lymphatic metastasis. Targeted blocking of the IL-6/IL-6R

[1] This chapter has been adapted from the manuscript published in Biomaterials in 2019: "Human organotypic lymphatic vessel model elucidates microenvironment-dependent signaling and barrier function." The manuscript was authored by Max M. Gong*, **Karina M. Lugo-Cintron***, Bridget R. White, Sheena C. Kerr, Paul M. Harari and David J. Beebe. * These authors contributed equally.

signaling pathway with an IL-6 neutralizing antibody fully rescued the vessels, demonstrating the potential of our system for screening therapeutic targets. These results collectively demonstrate the μLYMPH system as a powerful model for advancing lymphatic biology in health and disease.

2.1 Introduction

The lymphatic system is a crucial component of the circulatory and immune systems. It complements blood circulation, modulating interstitial fluid transport, immune cell trafficking, and lipid absorption [98]. Impairment of lymphatic vessels can result in lymphedema, i.e., the swelling of tissue due to interstitial fluid accumulation [98]. The lymph node microenvironment can also facilitate lymphoma progression and dissemination (e.g. non-Hodgkin's lymphoma) [99]. Moreover, lymphangiogenesis is a critical step in the metastasis of cancer cells to secondary organs [100]. Despite their importance in normal health and disease, the lymphatics are often understudied, especially in comparison to blood vasculature. However, there has been renewed effort and substantial progress in advancing lymphatic biology in the last two decades, following recognition of the lymphatic system as a key player in the pathogenesis of human diseases [100]. The discovery of protein markers for isolating lymphatic endothelial cells (LECs) in 1995 [101] and 1999 [53,54,102] has enabled *in vitro* lymphatic cultures and modeling.

Conventional methods for modeling lymphatic vessels comprise LECs cultured as monolayers on plastic surfaces (2D *in vitro*), LECs cultured in or on a matrix (3D *in vitro*), excised vessels from mice cultured in a matrix (3D *ex vivo*), and mouse models (*in vivo*) [103]. The usefulness of these models can be measured on a scale of tractability (i.e. repeatability and control over experimental parameters) versus physiological relevance (i.e. recapitulation of *in vivo* geometry and interactions). *In vitro* LEC cultures enable robust and repeatable experimentation but have limited capability in recapitulating microenvironmental cues (e.g. cell-cell communication, fluid shear stress, and matrix forces). In contrast, animal models provide relevant *in vivo* microenvironments; yet, experimental control is challenging in these dynamic systems. Current organotypic approaches, such as the lymphatic ring assay [84], offer a possible bridge

between *in vitro* and *in vivo* approaches. Nevertheless, their dependence on excised vessels from animal sources reduces repeatability and reproducibility. There is an opportunity, then, to develop organotypic models using human lymphatic tissue that balance tractability and recapitulation of *in vivo* lymphatic structure, function, and microenvironmental interactions in a reliable and repeatable manner.

Microfluidic organotypic models, also known as microphysiological systems or organs-on-chips, show promise to this end. These models enable 3D culture at the physical length scales of cells and tissue. They can recapitulate the form, function, and biophysical and biochemical microenvironments of various organs [104–106]. In the context of vasculature, organotypic vessels have tubular structure, barrier function, and respond to microenvironmental cues (e.g. growth factors) as similar to *in vivo* [107–113]. While endothelial monolayers and cells-in-gels in microchannels can mimic vascular physiology [114–117], capturing the tubular structure of vessels is not trivial and has implications in structure-function relationships. Geometry alone can alter endothelial cell signaling and phenotype [94]. To date, organotypic models of the lymphatic system are scarce. Existing models have examined the effect of cyclic adenosine monophosphate on the permeability of the lymphatic endothelium [118], and the interstitial fluid drainage function of artificial lymphatics (i.e. lumens without LECs) [119]. Further development of microfluidic organotypic lymphatic models would accelerate basic and translational lymphatics research.

Here, we developed a microscale lymphatic vessel (μLYMPH) system for culturing human lymphatic endothelial vessels. The system enables several capabilities for mechanistically studying lymphatic vessel biology, including: (1) basic characterization of vessel phenotype, (2) assessment of vessel cytokine secretion and barrier capacity, (3) assessment of vessel response to exogenous stimuli, (4) simulation of diseased microenvironments via co-culture with disease-

specific stromal cells, and (5) identification of potential therapeutic targets for lymphatic-tumor microenvironmental interactions. Vessels generated in the μLYMPH system had patent tubular structure with diameters in the range of 200-250 μm and expressed classical endothelial junctional proteins (e.g. CD31, vascular endothelial cadherin - VE-cadherin, and zonula occluens-1 - ZO-1) continuously throughout their endothelium, which are characteristics representative of pre-collecting/collecting lymphatic vessels *in vivo* [120,121]. In comparison to blood vessels cultured in the same system, the lymphatic vessels had comparatively leakier endothelia allowing significantly more solute drainage into the vessels. Moreover, vessel physiology was substantially altered when they were stimulated with exogenous lymphangiogenic and inflammatory factors, and co-cultured with fibroblasts. Co-culture with breast CAFs increased vessel permeability through IL-6 signaling, a possible mechanism for promoting lymphatic metastasis. Importantly, barrier function was fully recovered by neutralizing excess IL-6 in the co-culture. Collectively, these results demonstrate the utility of the μLYMPH system for generating functional human lymphatic vessels and enabling the study of lymphatic biology in physiological microenvironments.

2.2 Materials and Methods

2.2.1 μLYMPH system and vessel culture

The μLYMPH system is polydimethylsiloxane (PDMS)-based, consisting of a luminal rod suspended in an extracellular matrix (ECM) gel chamber (Fig. 1a). Devices are fabricated and assembled based on our previously established LumeNEXT approach [112] (Fig. S1). Briefly, the top and bottom layers of the device were fabricated via standard soft lithography using silicon masters containing SU-8 100 photoresist features (Y13273, MicroChem, Newton, MA). The bottom layer contains the ECM gel chamber and a channel for suspending the lumen rod. The top

layer forms the cover for the chamber and contains ports for fluid handling. PDMS with a 1:10 ratio of curing agent to pre-polymer was used for all device layers and lumen rods.

Lumen rods were made using 25-gauge hypodermic needles (inner diameter ~250 μm, 14-840-84, Fisher Scientific, Pittsburgh, PA). Uncured PDMS was pushed through the needles using a syringe, and the needles were heated at 80˚C for 3 hours. Polymerized rods were removed from the needles and cut to fit across the gel chambers of the devices. Following assembly of the device layers, rods were inserted into the channel with a tweezer. Completed devices were then bonded to glass-bottom culture dishes (P50G-1.5-30-F, MatTek Corporation, Ashland, MA) and stored until use.

Devices were UV sterilized for 15 min prior to cell culture. To minimize delamination of collagen in the gel chamber, devices were treated with a 2% polyethyleneimine solution (03880, Sigma-Aldrich, St. Louis, MO) at room temperature for 10 min, followed by treatment with a 0.1% glutaraldehyde solution (G6257, Sigma-Aldrich, St. Louis, MO) at room temperature for 30 min. Devices were then washed five times with sterile deionized water. A solution of rat-tail collagen type I (354249, BD Biosciences, San Jose, CA) was prepared on ice and neutralized using 0.5 M NaOH. The recipes for different collagen densities are provided in Table 2.1. Devices were filled with the prepared collagen solution (6 μL per device), incubated at room temperature for 10 min to initiate polymerization, and then transferred to 37 ºC for 1 hour. For the fibroblast co-cultures, a similar collagen gel solution was prepared containing normal or cancer-associated fibroblasts (250 cells/μL). Devices were filled with the cell-laden collagen solution (6 μL per device) and incubated at 37 ºC for 1 hour.

After gel polymerization, lumen rods were removed using a tweezer to reveal empty lumens molded in the collagen gel matrices. Prior to cell seeding, lumens were incubated with a

fibronectin solution (33 μg/mL, 10 μL per lumen) at room temperature for 30 min to support cell adhesion. HLECs were trypsinized with 0.05% Trypsin-EDTA (25300062, ThermoFisher Scientific, Waltham, MA), suspended in EGM-2 MV medium (~20,000 cells/μL), and seeded into the fibronectin-coated lumens (4 μL per lumen). HLEC-filled lumens were incubated at 37 ºC for an initial cell attachment period of 2 hours, where devices were manually flipped every 25 min to ensure homogeneous cell coverage of the lumen wall. Following this process, lumens were supplemented with 10 μL of medium and cultured overnight at 37 ºC. Cultured vessels were refreshed with medium twice per day post-seeding. During each feeding, vessels were washed three times with medium to remove dead cells and then maintained with 10 μL of medium. All fluid handling procedures were conducted with standard pipettes.

Table 2.1. Recipes for different collagen gel densities at a total volume of 500 μL.

Density (mg/mL)	Collagen gel[a] (μL)	5x PBS (μL)	0.5 M NaOH (μL)	1x PBS (μL)
3	153	31	5.7	311
4	204	41	7.6	248
5	255	51	9.5	185
6	305	61	11.5	122

[a]Stock concentration of 9.82 mg/mL

2.2.2 Vessel culture with and without flow

To assess cell alignment in the lymphatic vessels, vessels were cultured in static and flow conditions, where flow was generated via manual pipetting of media during daily vessel feedings. To achieve static culture, one culture dish of vessels was maintained in 2 mL of media over the entire culture period without daily media exchanges. Vessels cultured in static and flow conditions were fixed after 7 days and stained with phalloidin and DAPI. F-actin images were acquired with the Nikon TI® Eclipse inverted microscope. For each condition, alignment was quantified as the angle of a cell's major axis for at least 20 cells per vessel and presented as histograms with Gaussian curve fits. All images were analyzed using Fiji[122].

2.2.3 Cell culture

Human lymphatic endothelial cells isolated from the lymph node (HLECs, 2500, ScienCell, Carlsbad, CA) and human umbilical vein endothelial cells (HUVECs, C2517A, Lonza, Allandale, NJ) were cultured separately in standard cell culture flasks coated with fibronectin (5µg/cm^2, F1141-5MG, Sigma Aldrich, St. Louis, MO) at a starting cell concentration of 5 x 10^5 as per supplier instructions. Cultures were maintained with Endothelial Basal Medium-2 (EBM-2, CC-3156) supplemented with EGM-2 MV SingleQuot Kit (CC-4147, Lonza, Allandale, NJ). HLECs and HUVECs were cultured to 95% confluency at passages 4 and 5 for all experiments. Normal mammary fibroblasts (provided by Dr. Lisa Arendt's lab at UW-Madison) and breast cancer-associated fibroblasts (provided by Dr. Andreas Friedl's lab at UW-Madison) were cultured separately in standard flasks at a starting cell concentration of 5 x 10^5. Fibroblasts were maintained with Dulbecco's Modified Eagle Medium (11965092, ThermoFisher Scientific, Waltham, MA) supplemented with 10% fetal bovine serum. All cultures were kept in a humidified incubator at 37 ^oC with 5% CO_2.

2.2.4 Flow cytometry

HUVECs and HLECs were cultured in standard flasks as described in the 'Cell culture' section. Cells were lifted with PBS + 5 mM EDTA and resuspended in PBS at 10 x 10^6 cells/mL prior to live/dead staining with Ghost Red 780 (13-0865, Tonbo Biosciences, San Diego, CA) following manufacturer's instructions. 1x 10^6 cells were aliquoted per stain or control sample and 5µl of Fc Block (564219, BD Biosciences, San Jose, CA) was added to the resuspended HUVECs and HLECs. Cells were stained with a cocktail of CD31, LYVE1, and podoplanin antibodies using CD31-PE/Cy7 (303117), LYVE-1-A647 (FAB20892R), and Podoplanin-PE (337003),

respectively. All antibodies were purchased from BioLegend. Cells were then fixed and permeabilized prior to intracellular staining of PROX1 using the FOXP3 staining kit (A25866A, ThermoFisher Scientific, Waltham, MA) as per manufacturer's instructions and PROX-1-A488 (NBP1-30045AF488, Novus Biologicals, Centennial, CO). FMO controls were performed for each of the antibodies. Live/dead controls used a mixture of heat killed and live cells stained with ghost red only, for each cell type. Compensation controls used Ultracomp ebeads labelled with the same amount of antibody as the cells (01-2222-41, ThermoFisher Scientific, Waltham, MA). Marker expression was quantified using the Attune^{TM} NxT flow cytometer (ThermoFisher Scientific). Analysis was completed with the FlowJo software (BD Biosciences), gating on size, singlets and live cells.

2.2.5 Live/dead assays

The viability of cultured vessels was quantified using calcein AM (C3100MP, ThermoFisher Scientific, Waltham, MA) and ethidium homodimer-1 (E1169, ThermoFisher Scientific, Waltham, MA). A staining solution was prepared using 1 mL of EBM-2 medium containing 2.5 µL of calcein AM for live cells and 2 µL of ethidium homodimer-1 for dead cells. Prior to staining, cultured vessels were washed three times with EBM-2. Vessels were then incubated with staining solution (10 µL per vessel) at 37 ºC for 30 min and imaged immediately afterwards.

2.2.6 Cytokine quantification

Cytokines secreted into the media for vessel mono- and co-cultures were analyzed using a human growth factor panel (HAGP1MAG-12K, EMD Millipore, Billerica, MA). Media was collected from six individual vessels (10 ul per vessel) over two days (culture days 3 and 4) and pooled to generate sufficient volume for four technical replicates per experimental condition. The panel was prepared following manufacturer instructions and measured using the MAPGPIX system

(Luminex Corp., Austin, TX). Cytokine concentrations were quantified with the Luminex xPONENT software.

2.2.7 Quantitative reverse transcription PCR (qRT-PCR)

Transcription levels of endothelial junctional proteins, CD31, VE-cadherin, and ZO-1, were measured qRT-PCR using TaqMan probes (ThermoFisher Scientific). mRNA isolation was performed using Dynabeads mRNA direct purification kit (61011, ThermoFisher Scientific, Waltham, MA) and reverse transcription was conducted with the RNA to cDNA kit (4387406, ThermoFisher Scientific, Waltham, MA). The ΔΔCT method was used to assess relative gene expression, where expression of cell junctional protein genes PECAM1 (Hs01065279_m1), CDH5 (Hs00901465_m1), and TJP1 (Hs01551861_m1) were normalized to the housekeeping gene GAPDH (Hs01922876_m1).

2.2.8 Dextran diffusion assays

Solute transport from out of the vessels (i.e. permeability) and into the vessels (i.e. drainage) was measured by dextran diffusion. Texas Red dextran (10 kDa, D1828, and 70kDa, D1830, ThermoFisher Scientific, Waltham, MA) solutions were prepared to working concentrations of 1 μM. For the permeability assays, 3 μL of dextran solution was added to each vessel such that fluid was flush with the lip of the ports to minimize flow from a pressure head. Solute transport was measured over 15 minutes per vessel. Permeability coefficients were calculated using equation 1 [123]:

$$P = (1/I_o)[(I_f - I_o)/(t_f - t_o)](D / 4), \qquad \text{Eq. 1}$$

where I_o is the total initial intensity outside the vessel, I_f is the total intensity outside the vessel at 15 minutes, t_o is the initial time point, t_f is the final time point of 15 minutes, and D is vessel diameter. For the drainage assays, 3 μL of dextran solution was added to one gel chamber port to

create a pressure head for interstitial flow toward the vessel. Solute transport was measured over 30 minutes per vessel. Drainage coefficients were calculated using a modified version of equation 1, equation 2:

$$P = (I_{fvessel} / I_{ovessel})[1/(t_f - t_o)](D / 4), \quad \text{Eq. 2}$$

where $I_{ovessel}$ is the total initial intensity inside the vessel, $I_{fvessel}$ is the total intensity inside the vessel at 30 minutes, t_o is the initial time point, t_f is the final time point of 30 minutes, and D is vessel diameter. Dextran diffusion was imaged with the Nikon TI® Eclipse inverted microscope. All images were analyzed using Fiji.

2.2.9 Blocking and neutralization

MAZ51 (676492, EMD Millipore, Billerica, MA) was used to inhibit VEGF-C/VEGFR-3 signaling. Anti-IL-6R antibody (ab47215, Abcam, Cambridge, UK) and anti-IL-6 antibody (501109, BioLegend, San Diego) were used to inhibit IL-6/IL-6R signaling. Mouse IgG1 (400102, BioLegend, San Diego, CA) and rat IgG1 (400413, BioLegend, San Diego) antibodies were used as isotype controls for the IL-6/IL-6R inhibition experiments. To inhibit VEGFR-3, cultured vessels were primed for 1 hour with media containing MAZ51 (either 1 μM or 5 μM). Subsequently, MAZ51 was added to media containing VEGF-C (50 ng/mL) used to stimulate vessels over culture days 3 and 4. Vessels were washed with fresh media without VEGF-C or MAZ51 on day 5 and used for dextran diffusion analysis. To block vessels stimulated with IL-6 and in co-culture with CAFs, vessels were treated with anti-IL-6R antibody (either 5 μg/mL or 25 μg/mL) overnight from day 2 to day 3. Blocked vessels were then treated with media containing IL-6 (50 ng/mL) or left to co-culture with CAFs over days 3 and 4, and used on day 5 for dextran diffusion analysis. To neutralize IL-6 for the CAF co-cultures, vessels were treated with fresh

medium containing 25 μg/mL of anti-IL-6 antibody from day 2 to day 4 and used on day 5 for dextran diffusion analysis.

2.2.10 Immunofluorescent staining and imaging

All vessels prepared for immunofluorescent staining were cultured at least 3 days post-seeding to ensure confluency. Washing buffer (0.1% PBS-Tween 80) and blocking buffer (3% BSA in 0.1% PBS-Tween 80) were made in advance and stored at 4 ºC until use. Each vessel was 1) incubated with 5 μL of 4% paraformaldehyde at room temperature for 15 min for fixation, 2) incubated with 5 μL of 0.2% Triton X-100 at room temperature for 30 min for permeabilization, 3) incubated with 10 μL of blocking buffer at 4 ºC overnight. All vessels were washed three times with sterile PBS in between each step.

For antibody-based staining of lymphatic-specific markers and cell junctional proteins, primary antibodies were diluted to desired concentrations with staining buffer (blocking buffer plus 1% PBS-Tween 80 at 10:1 v/v) (Table 2.2). Vessels were washed three times with washing buffer and incubated with primary antibodies at 4 ºC overnight. To remove excess primary antibodies from the collagen gel matrix, vessels were washed multiple times for one day (10 min per wash). Secondary antibodies were prepared at desired concentrations using the staining buffer supplemented with 10% goat serum to reduce aspecific binding (Table 2.2). Vessels were incubated with the prepared antibodies at room temperature for 1 hour. Stained vessels were washed over two days and stored in sterile PBS until imaging. Alexa Fluor 488 phalloidin (A12379, ThermoFisher Scientific, Waltham, MA) and DAPI (D3571, ThermoFisher Scientific, Waltham, MA) were used to stain actin cytoskeleton and nuclei, respectively.

Table 2.2. Primary and secondary antibodies used for immunofluorescent staining.

Primary antibody	Company code	Stock conc. (mg/mL)	Working conc. (µg/mL)	Dilution
LYVE1	MAB20892 (R&D Systems)	0.5	10	1:50
CD31	ab9498 (Abcam)	N/A	-	1:50
VE-cadherin	MAB9381 (R&D Systems)	0.5	10	1:50
ZO-1	61-7300 (ThermoFisher)	0.25	10	1:25

Primary antibody	Host species	Secondary antibody[a]	Working conc. (µg/mL)	Dilution
LYVE1	mouse	Alexa Fluor 647 anti-mouse	10	1:200
CD31	mouse	Alexa Fluor 647 anti-mouse	10	1:200
VE-cadherin[b]	mouse	Alexa Fluor 647 anti-mouse	10	1:200
ZO-1[b]	rabbit	Alexa Fluor 488 anti-rabbit	10	1:200

[a]Stock concentration of 2 mg/mL. Goat source.
[b]VE-cadherin and ZO-1 were co-stained

Fluorescent images were acquired using a Nikon TI® Eclipse inverted microscope (Melville, New York) and processed using the National Institutes of Health ImageJ software. Confocal images were acquired using a Leica SP8 3X STED Super-resolution microscope (Wetzlar, Germany) in the UW-Madison Optical Imaging Core.

2.2.11 Statistical analysis

GraphPad Prism 7 (GraphPad Software, La Jolla, CA) was used for statistical analysis. Significance tests were performed using multiple unpaired, two-tailed Student's t-test with Bonferroni-Dunn multiple comparisons test (Fig. 3c), ordinary one-way ANOVA with Bonferroni's multiple comparisons test (Fig. 1d, 4c, 5e, 6c-e, 7d, and 8c-d), and unpaired, two-tailed Student's t-test (Fig. 4d). Tests were considered significant for $p \leq 0.05$. The number of replicates ranged from $n = 3$ to $n = 6$ for each experimental condition.

2.3 Results

2.3.1 Generation of 3D functional lymphatic endothelial vessels

We report an organotypic lymphatic vessel model, called the µLYMPH system (Fig. 2.1), that enables the culture of human lymphatic endothelial vessels and the study of lymphatic vessel biology in tailored microenvironments, such as the tumor microenvironment. The µLYMPH

system is a two-layer polydimethylsiloxane (PDMS) device fabricated using standard soft lithography, consisting of a removable PDMS lumen rod suspended across a gel chamber (Fig. 2.1a). To generate a lymphatic vessel, collagen type I gel is polymerized around the lumen rod, the rod is removed leaving an empty lumen, and the subsequent lumen is seeded with primary human lymphatic endothelial cells (HLECs) isolated from the lymph node (ScienCell) forming vessels with diameters in the range of 200-250 µm (Fig. 2.1b). We previously demonstrated this approach for forming HUVEC and iPSC-derived endothelial vessels with high reproducibility[112,113].

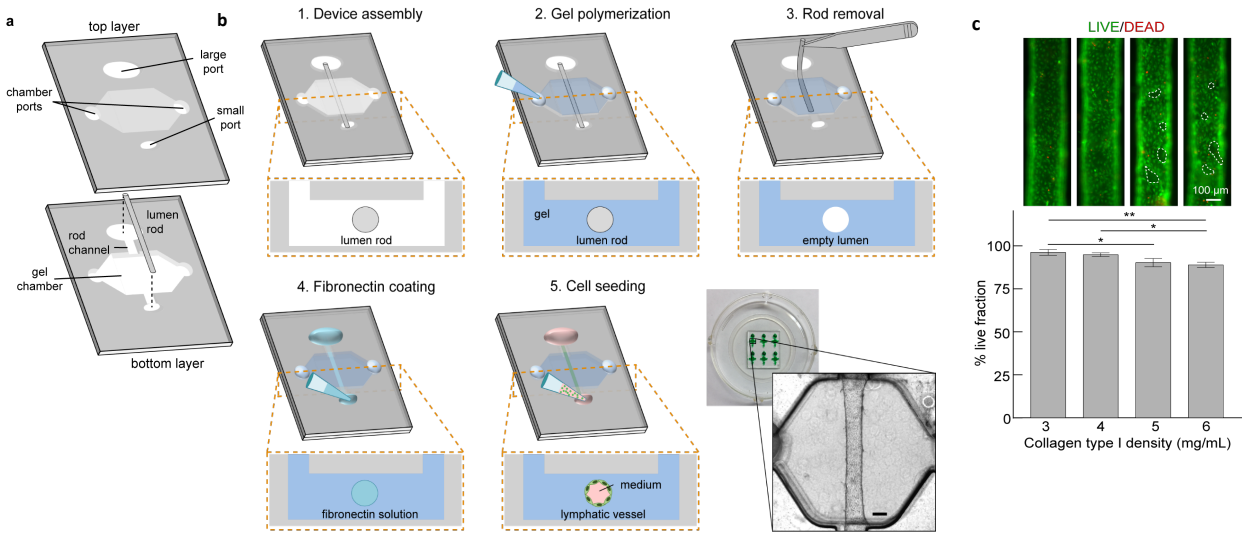

Figure 2.1. **µLYMPH system concept and vessel culture. a** Exploded view of device layers. A bottom layer contains the extracellular matrix gel chamber and a lumen rod suspended across the chamber supported by a channel. A top layer forms the cover for the chamber and contains ports for fluid handling. **b** Schematic of fully assembled device, process and cultured vessel. Representative images of devices and a lymphatic vessel with a diameter of 238 µm, cultured in 3 mg/mL collagen type I gel. **c** Viability images of vessels cultured over 7 days for gel densities ranging from 3 mg/mL to 6 mg/mL. Live cells are green and dead cells are red. The live fraction percentages for all densities are > 85%, with a maximum of 92% for 3 mg/mL. There are regions of cell detachment for 5 mg/mL and 6 mg/mL (dashed outlines). Live fraction percentage values are the average of n = 3 individual vessels with error bars as one standard deviation. *p ≤ 0.05, **p ≤ 0.01.

Lymphatic vessels were viable for at least seven days for collagen densities ranging from 3 mg/mL to 6 mg/mL; however, softer collagen gels (3 mg/mL and 4 mg/mL) produced significantly more viable vessels with a maximum live fraction of 92% for 3 mg/mL (Fig. 2.1c).

At the higher densities of 5 mg/mL and 6mg/mL, there was cell detachment from the endothelium as indicated by the dashed outlines in Fig. 2.1c. Matrix stiffening with increasing collagen density has been shown to alter endothelial cell behavior[124], suggesting that the current lymphatic vessels sense and respond to the changing mechanical composition of the surrounding collagen matrix.

Importantly, the lymphatic vessels are patent tubular structures (Fig. 2.2a), allowing perfusion of growth media through the vessels. Lymphatic phenotype of the vessels was characterized by the immunofluorescent staining of LYVE1 (Fig. 2.2b) and flow cytometry quantification of LYVE1, podoplanin and PROX1 (Fig. 2.2c). These expression profiles are consistent with the literature[125]. Interestingly, the HUVECs used to generate blood vessels also express LYVE1 and PROX1, which has been shown to occur *in vitro*[126,127]. Formation of mature lymphatic endothelia was confirmed by the presence of cell-cell junctional proteins, including CD31, VE-cadherin, and ZO-1 (Fig. 2.2b). To transport media through cultured vessels, we leveraged passive pumping[128], where a bolus of media was transported from the small port to the large port due to the difference in Laplace pressures of fluid droplets at the ports. Vessels were perfused with media in this manner at least 2-3 times per day for maintenance. This manner of perfusion mimics the pulsatile nature of lymph flow through lymphatic vessels[98]. In comparison to vessels maintained in the static condition without daily perfusion, we observed endothelial cell alignment in the direction of fluid flow (angle of 90 degrees) as a result of the repeated media exchanges (Fig. 2.2d and 2.2e), which is representative of lymphatic endothelial cell behavior *in vivo*[129].

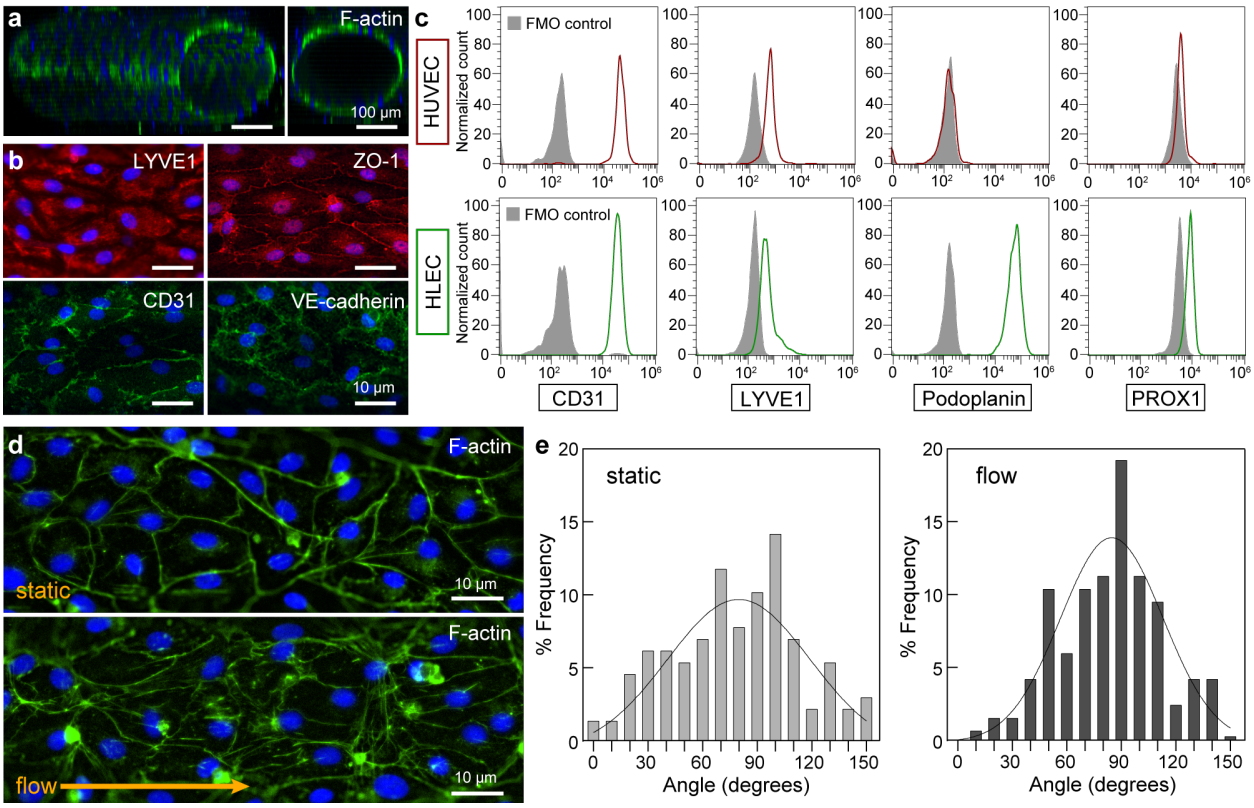

Figure 2.2. Vessel structure and markers. **a** Confocal image of a lymphatic vessel showing patent tubular structure. **b** Immunofluorescent of lymphatic marker - LYVE1, endothelial cell marker - CD31, and endothelial cell junctions - CD31, VE-cadherin, and ZO-1. **c** Flow cytometry quantification of CD31, LYVE1, podoplanin, and PROX1 for both blood (HUVEC) and lymphatic (HLEC) endothelial cells used in the study. HUVECs express CD31, LYVE1, and PROX1, but not podoplanin. HLECs express all four markers. **d** Cells in the endothelium align in the direction of fluid flow from daily medium exchanges as compared to cells maintained in excess medium without flow (static condition). **e** Histograms of cell alignment for static and flow conditions. A higher number of cells in the flow condition align in the direction of flow (angle of 90 degrees). Histogram frequency data was generated by combining values of n = 4 individual vessels for each condition.

2.3.2 Cultured lymphatic vessels are functionally different from blood vessels

The µLYMPH system enables analysis of lymphatic vessel biology, including cytokine secretion and barrier function. These readouts were obtained over a five-day period, which involved culturing the vessels in growth media for two days post-seeding, collecting media for secretion analysis over a subsequent two days, and then assessing vessel permeability at day five with a dextran diffusion assay (Fig. 2.3a). We measured the secretion levels of a panel of growth factors and inflammatory mediators with a multiplex magnetic bead-based immunoassay (i.e. Luminex MAGPIX) (Fig. 2.3b and 2.3c). Both blood and lymphatic vessels produced measurable levels of

all cytokines in the panel. In comparison to blood vessels, lymphatic vessels have a unique secretion profile and generally expressed lower levels of the measured cytokines (Fig. 2.3b). However, there was a particularly striking 18-fold difference in the secretion of follistatin. While blood vessels are known sources of follistatin[130,131], our finding implicates lymphatic vasculature as a major alternative source not previously known. Granulocyte colony stimulating factor (G-CSF) was also produced 2-fold more by the lymphatic vessels. Conversely, the blood vessels expressed significantly higher levels of endoglin (2-fold), hepatocyte growth factor (HGF) (3-fold), placental growth factor (PlGF) (6-fold), vascular endothelial growth factor (VEGF)-C (3-fold), and interleukin (IL)-8 (3-fold).

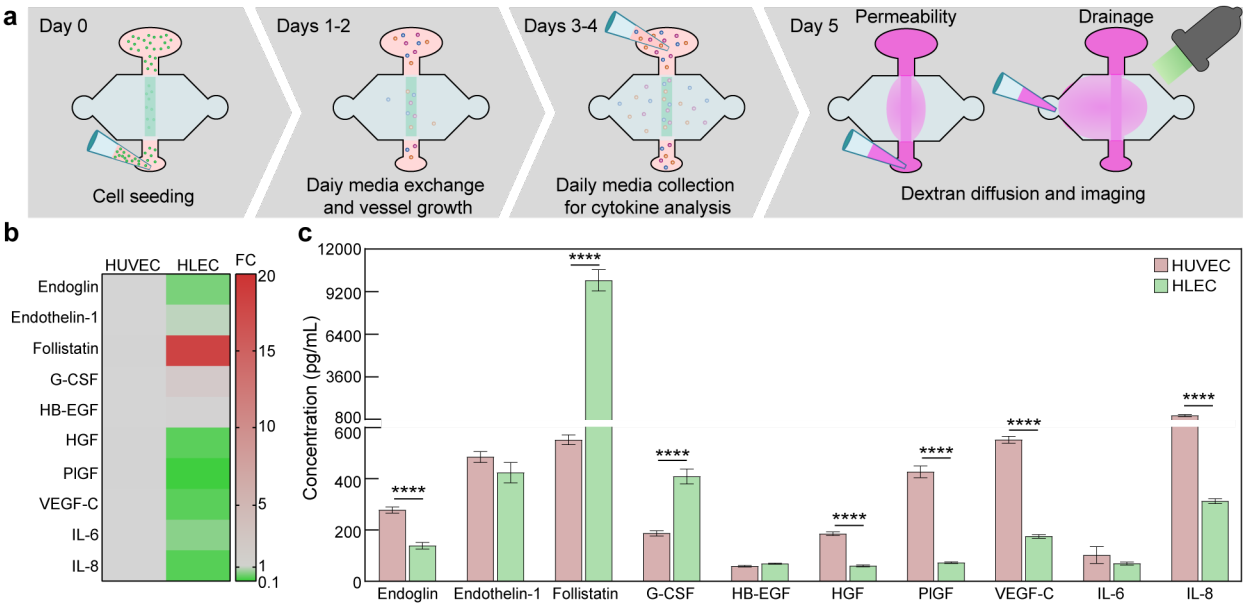

Figure 2.3. **Lymphatic vessel cytokine secretion**. **a** Schematic of experimentation timeline over five days. **b** Direct comparison of the fold change in secretion levels between blood (HUVEC) vessels and lymphatic (HLEC) vessels, with blood vessel levels taken as baseline. Overall, lymphatic vessels have lower secretion levels of the measured growth and inflammatory factors. However, follistatin expression is 18-fold higher for the lymphatic vessels. **c** Concentrations of secreted growth and inflammatory factors. Blood and lymphatic vessels have unique secretion profiles. There are significant differences in the secretion of endoglin, follistatin, G-CSF, HGF, PlGF, VEGF-C, and IL-8. Concentration values are the averages of n = 4 technical replicates of media pooled from 6 individual vessels for each condition.

A hallmark of endothelial vessels is their capacity to regulate the passage of molecules through their endothelium. The permeability of lymphatic vessels cultured in the μLYMPH system was assessed by diffusion assays using 10 kDa and 70 kDa Texas Red dextran. As compared to empty lumens, both blood and lymphatic vessels demonstrated significant barrier function and regulated the passage of the dextran molecules (Fig. 2.4a and 2.4b). Lymphatic vessels, however, were leakier than blood vessels with a 23% decrease in the peak intensity of the diffusion profile over 15 minutes versus a 10% decrease for blood vessels (Fig. 2.4b). We also measured the permeability coefficients of the vessels for both 10 kDa and 70 kDa dextran (Fig. 2.4c). For the 10 kDa molecular weight, the permeability coefficients of the lymphatic and blood vessels were 2.43 $x10^{-5} \pm 0.29 \times 10^{-5}$ cm/s and 1.39 $x10^{-5} \pm 0.43 \times 10^{-5}$ cm/s, respectively. Similarly, for the 70 kDa case, lymphatic vessels were more permeable with a coefficient of $1.38 \times 10^{-5} \pm 0.29 \times 10^{-5}$ cm/s as compared to $0.68 \times 10^{-5} \pm 0.13 \times 10^{-5}$ cm/s for the blood vessels. The barrier capacities of both vessel types were significantly higher for the 70 kDa dextran, indicating tighter regulation of biomolecules in that size range (e.g. serum albumin, ~67 kDa). To further distinguish the physiology of the lymphatic and blood vessels, solute drainage into each vessel type was measured by adding 70 kDa dextran solution to one gel chamber port to generate interstitial flow (Fig. 2.3a-schematic). Drainage into the lymphatic vessels was 1.3-fold higher than for the blood vessels (Fig. 2.4d), which demonstrates that our model can capture the natural drainage function of the lymphatics. Taken together, these results demonstrate the suitability of the μLYMPH system for assessing lymphatic vessel barrier function, which is distinctly different from blood vessels cultured in the same system.

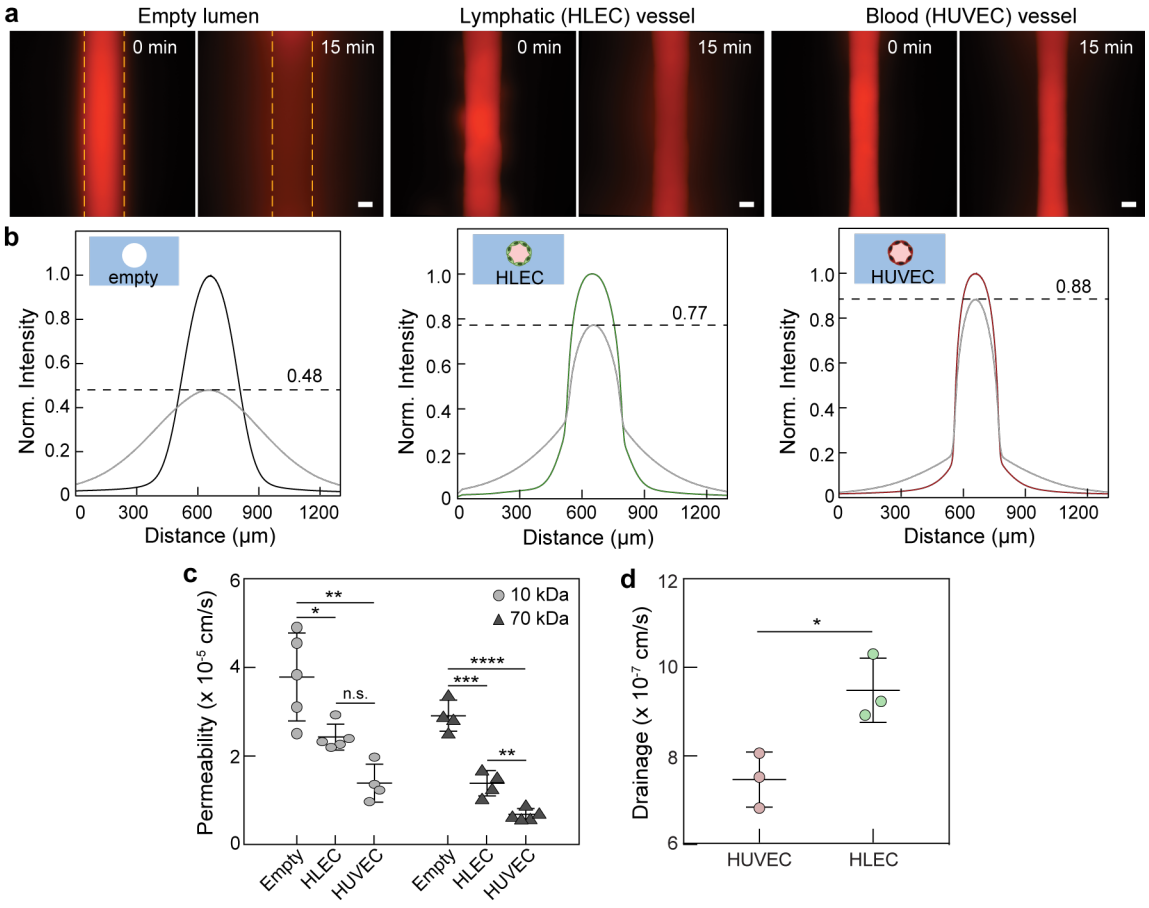

Figure 2.4. Lymphatic vessel barrier function and drainage capacity. a Representative images of 70kDa dextran diffusion in empty, lymphatic, and blood vessels over 15 min. Dashed lines indicate lumen boundaries. **b** Normalized intensity profiles of 70 kDa dextran diffusion, where lymphatic vessels have moderate barrier capacity in comparison to blood vessels. The initial concentration decreases by 12%, 23%, and 52% for blood, lymphatic, and empty vessels, respectively. **c** Quantification of vessel permeability. For both 10 kDa and 70 kDa dextran, lymphatic vessels are ~2-fold leakier than blood vessels. Both endothelial vessels, however, provide barrier function in comparison to empty lumens. **d** Quantification of drainage capacity. Lymphatic vessels uptake significantly more 70 kDa dextran over 30 min. as compared to blood vessels. Permeability values are the averages of at least n = 4 individual vessels. Drainage values are the averages of n = 3 individual vessels. All error bars are one standard deviation. Scale bars are 100 μm. *p ≤ 0.05, **p ≤ 0.01, ***p ≤ 0.001, ****p ≤ 0.0001.

2.3.3 Lymphangiogenic and inflammatory cytokine stimulation alters vessel function

To demonstrate the applicability of the μLYMPH system for examining lymphatic biology beyond basic vessel characterization, we assessed the response of cultured vessels in lymphangiogenic and inflammatory microenvironments simulated by exogenous VEGF-C, VEGF-D, and IL-6 cytokine stimulation. Using a similar workflow as depicted in Fig. 3a, VEGF-C (50 ng/mL), VEGF-D (50

ng/mL), and IL-6 (50 ng/mL) were added to the vessels at two days post-seeding and cultured up to five days. For all conditions, there were notable morphological changes to the endothelium in comparison to untreated vessels, namely, increased actin stress fibers and cell detachment (Fig. 2.5 a-d). Cell alignment, however, remained consistent for all stimulated vessels. In Fig. 2.5e, we limit the results to cytokines with concentration levels greater than 150 pg/mL to better visualize changes in the secretion profile. Stimulation of the vessels with VEGF-C and IL-6 significantly altered the secretion profile, more so than stimulation with VEGF-D (Fig. 2.5e). There was, however, a significant increase in IL-8 concentration by VEGF-D stimulation. Specifically, VEGF-C stimulation triggered significant increases in the secretion of endothelin-1, follistatin, and IL-8. IL-6 stimulation significantly increased the secretion levels of all presented factors (endothelin-1, follistatin, G-CSF, VEGF-C, and IL-8).

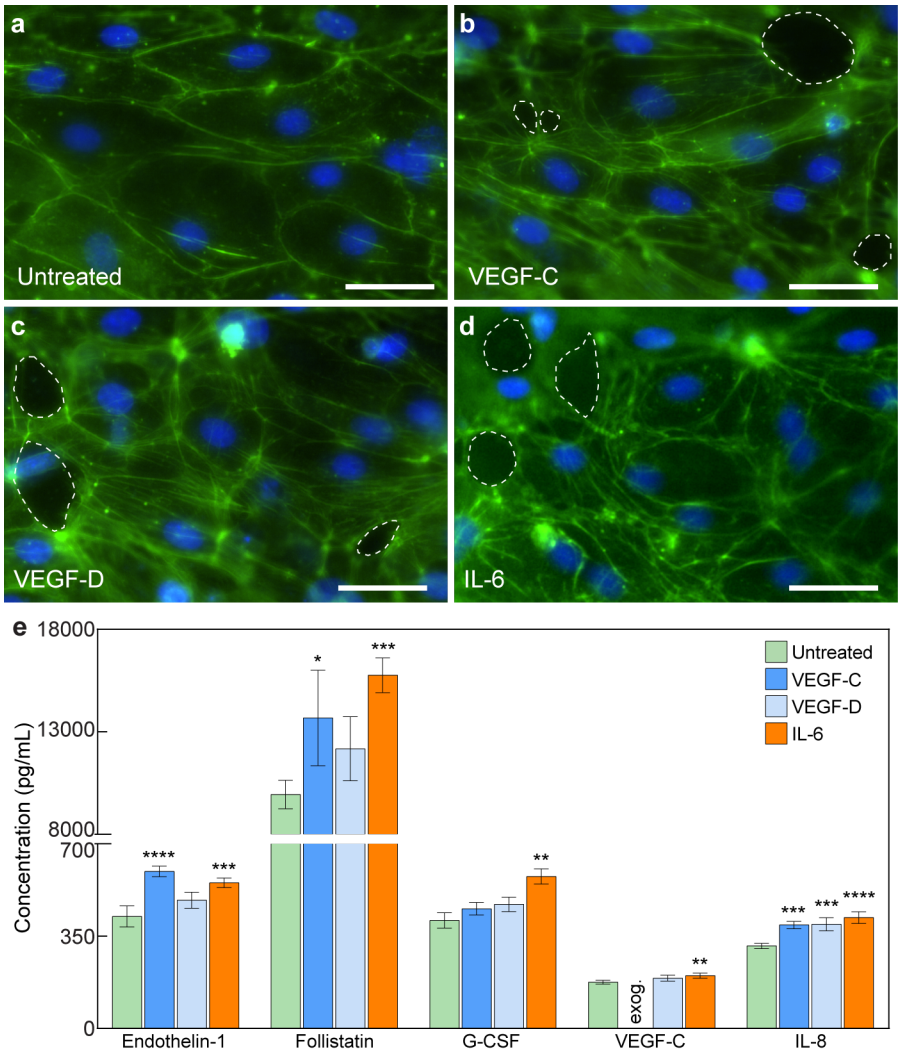

Figure 2.5. Morphological and secretion responses of lymphatic vessels to exogenous lymphangiogenic and inflammatory stimuli. a-d Images of lymphatic endothelia under VEGF-C, VEGF-D, and IL-6 stimulation (F-actin in green and nuclei in blue). In comparison to untreated vessels, LECs in stimulated vessels express increased actin stress fibers. There are also holes the vessel wall (dashed outlines). **e** Cytokine concentrations for untreated and stimulated conditions. VEGF-C and IL-6 induce significant changes in all presented cytokines. Concentration values are the averages of n = 4 technical replicates of media pooled from 6 individual vessels for each condition. All error bars are one standard deviation. Scale bars are 10 μm. *p ≤ 0.05, **p ≤ 0.01, ***p ≤ 0.001, ****p ≤ 0.0001.

Similarly, barrier function was significantly altered when the lymphatic vessels were stimulated with VEGF-C, VEGF-D, and IL-6. Solute (70 kDa dextran) diffusion for all three stimulatory conditions was substantially faster in comparison to untreated vessels, where the peak intensity decreased by 38%, 32%, and 36% for VEGF-C, VEGF-D, and IL-6 stimulated vessels,

respectively, as compared to 23% for untreated vessels over 15 minutes (Fig. 2.6a and 2.6b). Stimulated vessels also responded at the transcriptional level with changes in the mRNA expression of their cell-cell junctional proteins. CD31 transcription was reduced for all stimulatory conditions, whereas VE-cadherin mRNA expression increased for VEGF-C and VEGF-D stimulation, and ZO-1 mRNA expression increased for IL-6 stimulation (Fig. 2.6c). Moreover, we measured significant increases in permeability for the VEGF-C and IL-6 conditions in comparison to untreated vessels. VEGF-C stimulation increased the permeability of the lymphatic vessels by ~2-fold to $2.67 \times 10^{-5} \pm 0.19 \times 10^{-5}$ cm/s from a baseline value of $1.38 \times 10^{-5} \pm 0.29 \times 10^{-5}$ cm/s (Fig. 2.6d). However, this increase was mitigated by supplementing MAZ51 to the VEGF-C media used to stimulate the vessels. MAZ51 inhibits VEGF-C signaling by preventing the autophosphorylation of its receptor, VEGFR3[132]. At a dosage of 1 μM MAZ51, the VEGF-C stimulated vessels were still significantly more permeable than the untreated vessels, however, they were less permeable than vessels treated with VEGF-C alone. At a higher dosage of 5 μM MAZ51, VEGF-C stimulated vessels were fully rescued with no measurable difference in permeability as compared to the untreated vessels. Similar results were observed for the IL-6 stimulated vessels, where their permeability was increased by ~2-fold following IL-6 treatment (Fig. 2.6e). IL-6 induced barrier dysfunction was prevented by treating the lymphatic vessels with anti-IL6R (5 μg/mL and 25 μg/mL), an antibody blocking the binding of IL-6 to its receptor. Collectively, these data demonstrate the utility of the μLYMPH system for simulating different microenvironments by exogenous cytokine stimulation and for targeting molecular pathways that impair barrier function.

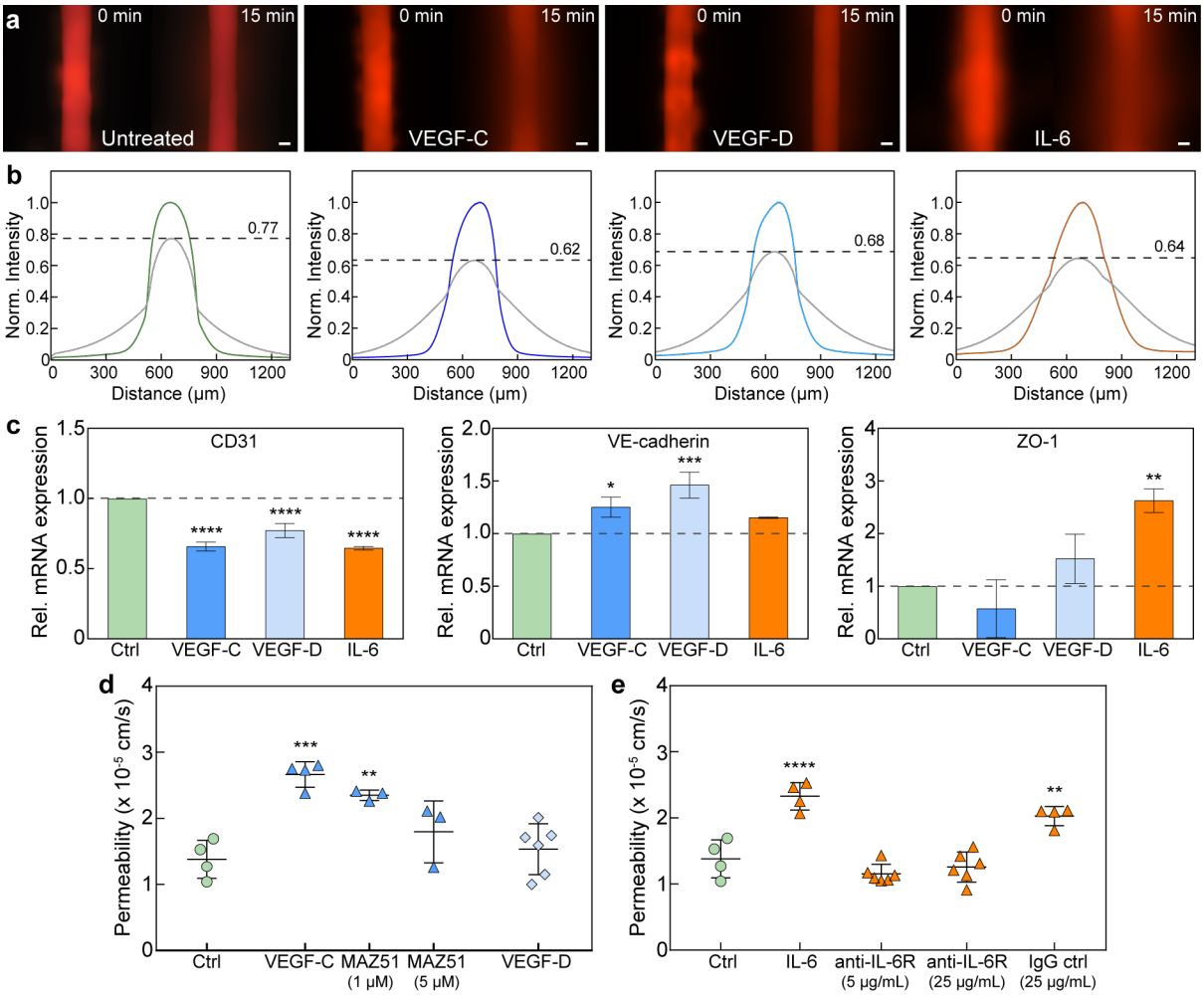

Figure 2.6. Barrier response of lymphatic vessels to exogenous lymphangiogenic and inflammatory stimuli. a Images of 70 kDa dextran diffusion in untreated vessels and vessels stimulated with VEGF-C, VEGF-D, and IL-6. **b** Normalized intensity profiles of dextran diffusion. The initial concentration decreases by 38%, 32%, and 36% for VEGF-C, VEGF-D, and IL-6 stimulation, respectively, as compared to 23% for untreated vessels. **c** Transcriptional expression of intercellular junctions under stimulation. CD31 expression is significantly downregulated for all cases. VE-cadherin expression is upregulated after VEGF-C and VEGF-D treatment, and ZO-1 after IL-6 stimulation. Relative mRNA values are the averages of n = 3 technical replicates with each replicate representing two individual vessels. **d** Vessel permeability significantly increases after VEGF-C treatment. Barrier function can be rescued by inhibiting the phosphorylation of VEGFR3, the receptor for VEGF-C, with MAZ51 (partially at 1 μM and fully at 5 μM). **e** IL-6 stimulation significantly reduces barrier capacity, which can be mitigated via antibody-mediated blocking of the IL-6 receptor on the lymphatic vessels. All permeability values are the averages of at least n = 3 individual vessels. All error bars are one standard deviation. Scale bars are 100 μm. *p ≤ 0.05, **p ≤ 0.01, ***p ≤ 0.001, ****p ≤ 0.0001.

2.3.4 Cancer-associated fibroblasts promote a pro-inflammatory lymphatic microenvironment

We assessed the capacity of the μLYMPH system for examining lymphatic vessel biology in diseased microenvironments, such as the tumor microenvironment (TME), by co-culturing lymphatic vessels with breast cancer-associated fibroblasts (CAFs). CAF-induced responses were compared to co-cultures with normal mammary fibroblasts (NFs). Fibroblast co-cultures were enabled by embedding either CAFs or NFs into the collagen gel prior to forming and seeding the lumen with HLECs (Day 0 in Fig. 2.7a). The co-cultures were maintained and analyzed using the same workflow as the lymphatic vessel monocultures. A dramatic morphological response was observed for vessels co-cultured with CAFs, where HLECs detached in large areas of the endothelium (dashed outlines in Fig. 2.7b). There was no observable cell detachment for the NF co-culture controls. Regarding cytokine secretion, co-culture with CAFs induced larger fold changes in cytokine concentration than with NFs, as compared to vessel monocultures (Fig. 2.7c). Specifically, CAFs upregulated the secretion of pro-tumorigenic growth factors, G-CSF (8-fold) and HGF (15-fold), and pro-inflammatory mediators, IL-6 (20-fold) and IL-8 (15-fold). Interestingly, follistatin secretion, which was at ng/mL levels for the monoculture condition, was reduced to pg/mL levels after co-culture with both CAFs and NFs. Endothelin-1, endoglin, and VEGF-C were also reduced by at least 10-fold for both fibroblast co-culture conditions. PlGF was solely downregulated by NF co-culture.

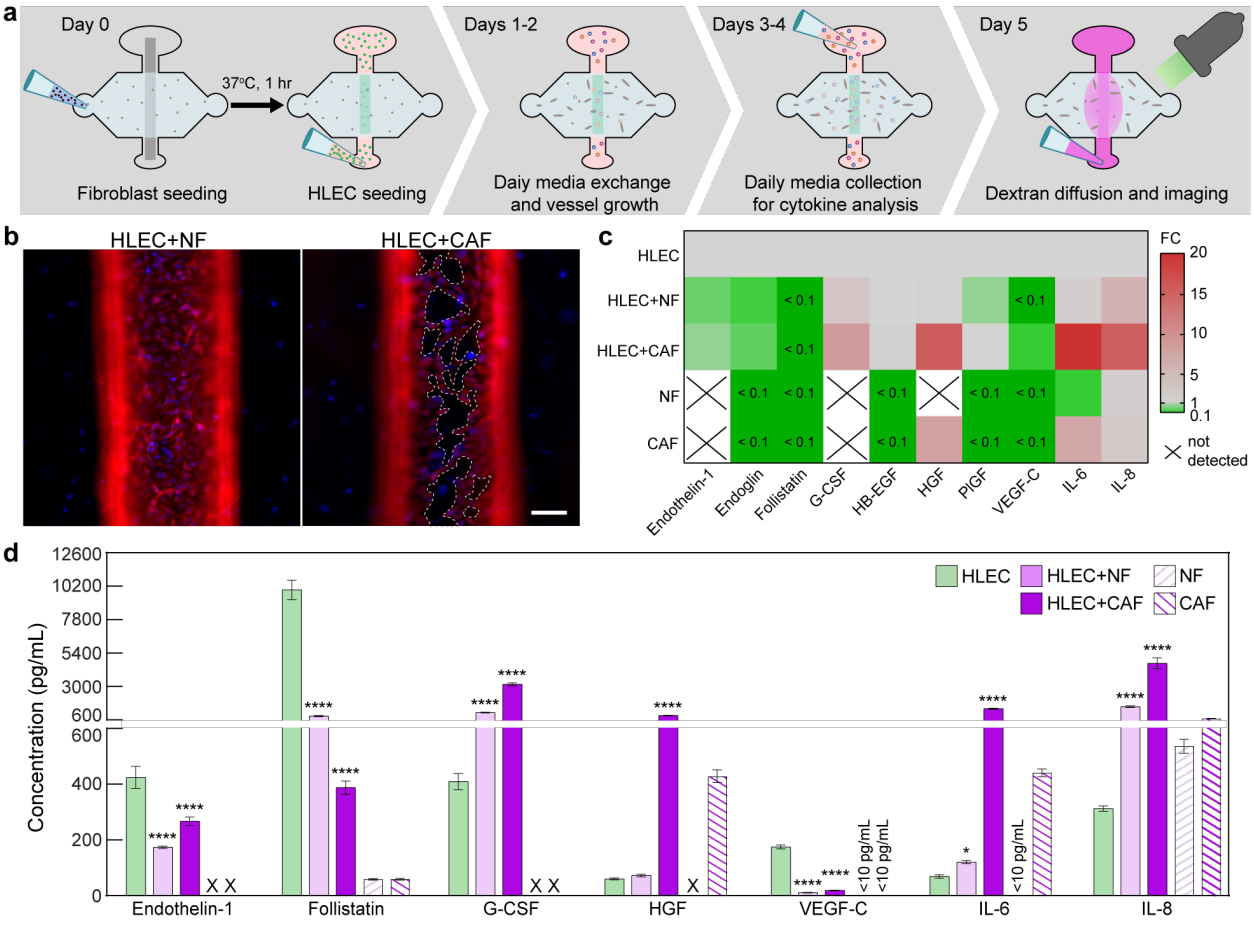

Figure 2.7. Lymphatic vessel co-culture with normal mammary fibroblasts (NFs) and cancer-associated fibroblasts (CAFs). a Schematic of co-culture experimentation timeline over 5 days. **b** Images of vessels co-cultured with NFs and CAFs (vimentin in red and nuclei in blue). The lymphatic endothelium is highly destabilized when CAFs are present, where cells have detached from the extracellular matrix (holes indicated by dashed outlines). **c** Direct comparison of the fold change in secretion levels between fibroblast co-cultures and vessel monoculture, with monoculture levels taken as baseline. CAFs increase the secretion of pro-inflammatory mediators (IL-6 and IL-8) by >15-fold and substantially downregulate the expression of endoglin, follistatin, and VEGF-C. Secretion of G-CSF and HGF is also upregulated by 8-fold and 15-fold, respectively. Secretion levels NF and CAF monocultures are also compared to the HLEC monoculture, where CAFs secrete HGF and IL-6 ~7-fold and 6-fold higher, respectively. **d** Cytokine concentrations for fibroblast co-cultures. CAFs drive vessels toward a pro-inflammatory phenotype significantly more than NFs and amplify the secretion of key growth factors, e.g. HGF, involved in tumor progression. Concentration values are the averages of n = 4 technical replicates of media pooled from 6 individual vessels for each condition. Error bars are one standard deviation. Scale bar is100 μm. *p ≤ 0.05, ***p ≤ 0.001, ****p ≤ 0.0001.

Notably, cytokine concentrations measured in Fig. 2.7d indicate that CAFs and NFs either regulate vessel secretion or contribute to the total concentration by their own secretion (cytokines with concentrations <150 pg/mL are shown in Fig. 2.8). For example, endothelin-1, follistatin, G-CSF, and VEGF-C levels (as well as endoglin, HB-EGF, PlGF levels in Fig. 2.8) were altered in

the fibroblast co-cultures despite negligible secretion of these cytokines by the CAF and NF monocultures, suggesting their associated pathways in the lymphatic vessels are regulated by interactions with the fibroblasts. In the cases of HGF, IL-6, and IL-8, their levels significantly increased in the co-cultures predominantly due to secretion by the CAFs and NFs, as indicated by the accompanying CAF and NF monocultures. Indeed, it is well-known that CAFs are the primary contributors of HGF, IL-6, and IL-8 in the TME[133], demonstrating the capability of our approach to recapitulate pertinent TME stromal interactions.

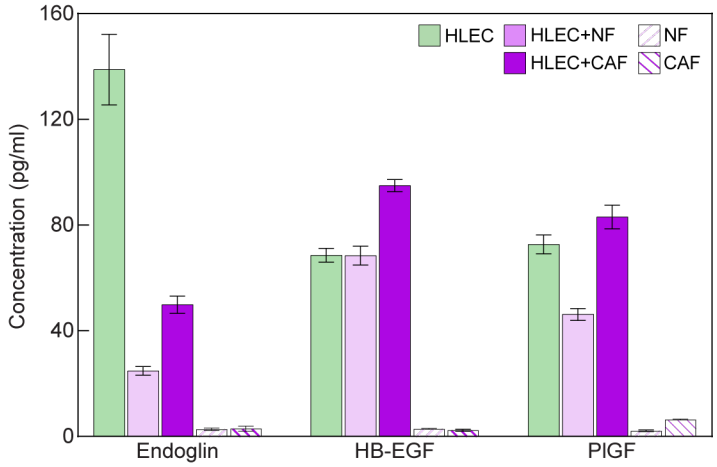

2.8 Growth factors and inflammatory mediators with concentrations lower than 150 pg/mL for vessels co-cultured with normal and cancer-associated fibroblasts.

CAFs also significantly impaired the barrier function of the lymphatic vessels. In agreement with the observed cell detachment in Fig. 2.7b, vessels co-cultured with CAFs were substantially leakier (leakage from areas of cell detachment indicated by arrows in Fig. 2.9a), with a 37% decrease in the peak intensity of the diffusion profile over 15 minutes, as compared to 27% and 23% for the NF co-culture and vessel monoculture conditions, respectively (Fig. 2.9b).

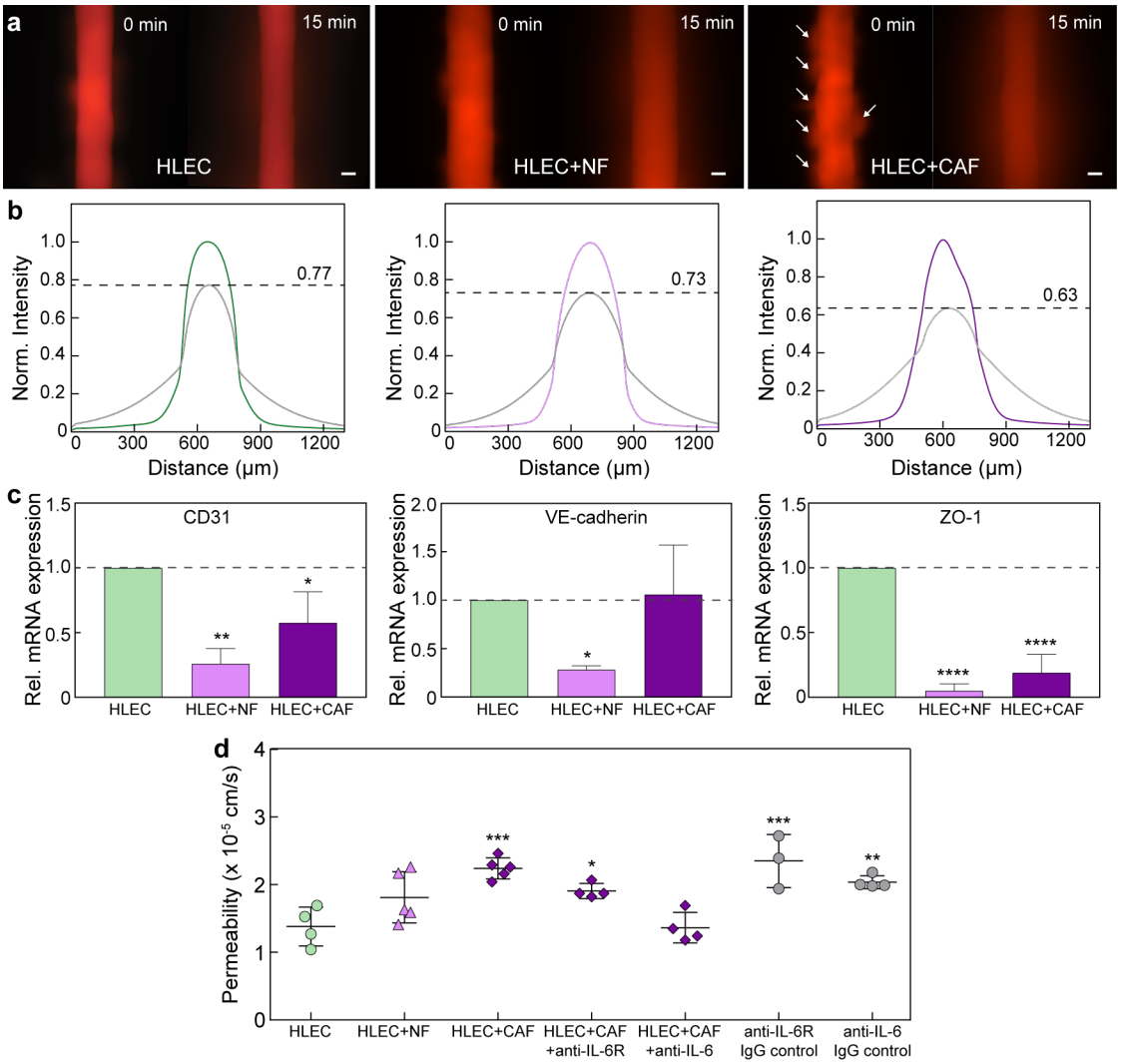

Figure 2.9. Barrier response of lymphatic vessels co-cultured with normal mammary fibroblasts (NFs) and cancer-associated fibroblasts (CAFs). a Images of 70 kDa dextran diffusion for vessels in monoculture and co-culture. There are multiple holes in the endothelium for the CAF co-culture, as indicated by the focal diffusion regions (arrows). **b** Normalized intensity profiles of dextran diffusion. The initial concentration decreases by 27% and 37% when co-cultured with NFs and CAFs, respectively, as compared to 23% for vessels in monoculture. **c** Transcriptional expression of intercellular junctions under co-culture. CD31 and ZO-1 mRNA levels are significantly downregulated for both cases. VE-cadherin expression is downregulated for NFs. Relative mRNA values are the averages of n = 3 technical replicates with each replicate representing two individual vessels. **d** CAFs significantly increase lymphatic vessel permeability. Barrier function can be rescued, in part, by blocking the IL-6 receptor on the lymphatic vessels. Alternatively, vessel permeability was completely normalized when IL-6 was neutralized with an anti-IL-6 antibody. Permeability values are the averages of at least n = 3 individual vessels. All error bars are one standard deviation. Scale bars are 100 μm. *p ≤ 0.05, **p ≤ 0.01, ****p ≤ 0.0001.

However, the impact of CAFs on the transcription of vessel junctional proteins, CD31, VE-cadherin, and ZO-1, was less pronounced in comparison to that of the NFs (Fig. 2.9c). The downregulation in transcriptional activity measured for the NF co-cultures did not correlate to

morphological changes (e.g. cell detachment) or a significant increase in solute diffusion in the vessels. These data suggest that reduction in cell-cell junctional integrity (at the transcription level) may not be the primary mechanism of barrier dysfunction induced by the CAFs. Moreover, vessel permeability significantly increased from $1.38 \times 10^{-5} \pm 0.29 \times 10^{-5}$ cm/s in monoculture to $2.24 \times 10^{-5} \pm 0.16 \times 10^{-5}$ cm/s in co-culture with the CAFs (Fig. 2.9d). There was a moderate, but insignificant, increase in vessel permeability to $1.81 \times 10^{-5} \pm 0.38 \times 10^{-5}$ cm/s induced by the NFs. Importantly, neutralization of excess IL-6 produced in the co-culture with CAFs, using an anti-IL-6 antibody, fully normalized vessel permeability, while blocking IL-6R on the HLECs partially recovered vessel barrier function (Fig. 2.9d). Collectively, these results demonstrate the utility of the μLYMPH system for simulating diseased microenvironments, such as the TME. Notably, our co-culture approach enables direct crosstalk between lymphatic vessels and pertinent tumor stromal cells (e.g. CAFs), providing new insight into biological mechanisms of lymphatic dysfunction.

2.4 Discussion

Organotypic lymphatic models are few in number, especially in comparison to models of blood vasculature. Models that can recapitulate lymphatic vessel structure and function in relevant microenvironments would advance basic and translational lymphatics research. We developed the μLYMPH system that enables the study of lymphatic vessel biology in normal and diseased microenvironments. To the best of our knowledge, only one other study has demonstrated the culture of lymphatic vessels with *in vivo* tubular structure [118], which is critical for recapitulating vessel function *in vitro* [94]. Other microfluidic models have been developed for examining lymphatic vessel permeability and lymphangiogenesis [116,117]; however, they lack *in vivo* tubular structure. Our system offers capabilities comparable to and beyond existing models

including: 1) generation of human lymphatic vessels with physiologically relevant structure and function, 2) characterization of vessel response under cytokine stimulation, 3) co-culture of vessels with stromal components, and 4) assessment of molecular pathways as potential therapeutic targets.

Lymphatic vessels have unique structure-function relationships as compared to their blood vessel counterparts. They are integral components of the blood-lymph loop, specializing in interstitial fluid drainage and recirculation to blood, as well as immunoregulation [98]. The lymphatic vascular tree consists of initial, pre-collecting, and collecting vessels, each having phenotypic differences. For instance, the spatial organization of junctional proteins, such as VE-cadherin, ZO-1, and CD31, differs between the vessel types [120,134]. These proteins form discontinuous button junctions for the initial lymphatic vessels to facilitate fluid drainage and continuous zipper junctions for the pre-collecting and collecting vessels to tightly regulate fluid transport [120,134]. Vessel diameter also changes throughout the lymphatic vascular tree, where diameters range from 10-60 μm for initial vessels [135] and >200 μm for pre-collecting/collecting vessels [121]. Our cultured lymphatic vessels express all three junctional proteins uniformly throughout the endothelium and have diameters in the range of 200-250 μm, suggesting recapitulation of the pre-collecting/collecting phenotype. This is likely the case given the vessels are generated by patterning empty lumens with LECs, rather than grown via lymphvasculogenesis. Nevertheless, the expression of the junctional proteins indicates the vessels have capacity to regulate molecular transport across their endothelia. Indeed, our permeability measurements confirmed moderate barrier function for the lymphatic vessels, situated between little-to-no barrier function for the empty lumens and high barrier function for the blood vessels. This finding is consistent with observations that lymphatic vessels are typically leakier than blood vessels [136].

The permeability of the cultured lymphatic vessels also depended on the size of the diffusing molecule (i.e. 10 kDa versus 70 kDa dextran), demonstrating their capacity to selectively control molecular transport. In comparison to a previous *in vitro* study on assessing lymphatic vessel permeability [118], our baseline permeability is comparable when adjusted for differences in vessel diameters. Our permeability measurements, however, are typically higher than those quantified for collecting vessels in mouse models [137], a discrepancy likely due to species variance. Furthermore, we showed that solute drainage into the lymphatic vessels was representative of *in vivo* behavior when compared to the blood vessels. Collectively, our vessel characterization and permeability results demonstrate the capacity of the μLYMPH system for generating physiological and functional lymphatic vessels *in vitro*.

Lymphatic and blood vessels leverage different molecular pathways for survival and growth, which is evident from their dissimilar cytokine secretion profiles. Previous studies have shown that several angiogenic growth factors, including endoglin, HGF, and VEGF-C measured in our study, can induce lymphangiogenesis [138–141]. Specifically, VEGF-C (and VEGF-D) has been well-characterized as a potent lymphangiogenic factor that activates the VEGFR-3 pathway in LECs [141]. However, our results showed significantly higher VEGF-C secretion by the cultured blood vessels. This finding is consistent with previous work demonstrating higher expression of VEGF-C by blood endothelial cells [142], supporting its role as an angiogenic factor and as a paracrine regulator of lymphatic vessel growth [143,144]. Other than VEGF-C, it is unclear what reciprocal factors are secreted by lymphatic vessels for modulating blood vessel growth. G-CSF, a pro-angiogenic factor [145], is one possible candidate as it was expressed significantly more by the cultured lymphatic vessels. G-CSF also promotes neutrophil differentiation and mobilization to sites of physiological stress via blood circulation [146]. Our

results suggest lymphatic vessels may work synergistically with blood vessels in modulating this process. Similarly, IL-8, a well-known neutrophil chemoattractant [147], was measured in both the cultured lymphatic and blood vessels, further suggesting their combined role in regulating the innate immune response. Moreover, the most striking difference in the cytokine secretion profiles, and perhaps the largest differentiator of lymphatic-blood vessel function, was the expression of follistatin (i.e. 18-fold higher for the lymphatic vessels). Follistatin antagonizes activin A, a member of the transforming growth factor-β superfamily involved in cell proliferation, differentiation, and apoptosis depending on the specific microenvironment [148]. In the context of vasculature, the follistatin/activin axis modulates angiogenesis, lymphangiogenesis, and inflammation [131,149,150]. Follistatin is expressed in the circulation, however, there is speculation on its specific source(s). Previous studies have shown that blood endothelial cells and hepatocytes contribute largely to plasma follistatin [130,131,151]. Consistent with these findings, our results confirmed blood endothelial cells as sources of follistatin. However, its significantly higher secretion by LECs suggests lymphatic vessels as a major contributor to plasma follistatin via recirculation of lymph fluid to blood. The follistatin/activin axis may also play an important role in autocrine regulation of lymphatic vessel maintenance, and in lymphatic vessel crosstalk with other tissues. Collectively, the cytokine secretion results demonstrate the utility of the μLYMPH system for culturing functionally distinct lymphatic vessels and identifying specific molecular pathways important to lymphatic biology.

Lymphatic vessels cultured in the μLYMPH system respond to exogenous lymphangiogenic (VEGF-C, VEGF-D) and inflammatory (IL-6) stimuli. As aforementioned, VEGF-C and VEGF-D are key regulators of lymphangiogenesis via the VEGFR-3 pathway [141]. IL-6 is a classic pro-inflammatory cytokine and has been known to induce lymphatic vessel

dysfunction *in vitro* and *in vivo* [152,153]. Stimulation of lymphatic vessels with all three cytokines resulted in morphological and functional changes, including increased actin stress fibers, holes in the endothelium, altered cytokine secretion, and impaired barrier function. Regarding barrier function, VEGF-C and IL-6 elicited significant increases in vessel permeability, as consistent with similar data for LEC monolayers [152,154]. In the IL-6 study [152], the authors observed a correlation between reduced VE-cadherin protein expression and increased vessel permeability. Our mRNA expression data indicate the opposite, where VE-cadherin mRNA transcription increased following IL-6 stimulation. This discrepancy may be due to differences in approach (i.e. lumens vs monolayers, or gene vs protein expression). Moreover, our mRNA expression and permeability data collectively suggest barrier function may be CD31 mediated, as its transcription was downregulated in all conditions while VE-cadherin and ZO-1 transcription increased or remained near baseline. Furthermore, the increase in vessel permeability is likely compounded by LEC contraction as indicated by the observed increase in actin stress fibers, resulting in localized loss in junctional integrity and holes in the endothelium. Importantly, barrier dysfunction induced by VEGF-C and IL-6 stimulation could be rescued by inhibiting their respective pathways, demonstrating the applicability of the μLYMPH system as a potential therapeutic discovery and screening platform.

In contrast to the established role of blood vasculature in inflammation, the role of lymphatic vasculature remains understudied. Classically, the lymphatic system has been considered a passive player in modulating inflammatory responses, however, emerging data suggests otherwise [155]. Specifically, lymphatic vessels actively remodel (e.g. enlarge) and proliferate to facilitate the clearance of excess interstitial fluid and pro-inflammatory cytokines from the site of inflammation [156,157]. These responses are typically mediated by the increased

expression of lymphangiogenic growth factors, such as VEGF-C [156,157]. Our cultured lymphatic vessels exhibited a similar resolution mechanism by releasing more VEGF-C in response to IL-6 treatment. IL-6 stimulation also increased the expression of neutrophil chemotactic factors, G-CSF and IL-8, suggesting neutrophils play a role in modulating lymphatic vascular inflammation. Interestingly, a previous study demonstrated that neutrophils contribute to inflammation-associated lymphangiogenesis by secreting VEGF-D [158]. Furthermore, inflamed vessels released significantly more follistatin, which is a response that typically follows a rise in activin expression during inflammatory insult to neutralize activin-induced inflammatory effects [150]. A similar follistatin response was observed when vessels were stimulated with VEGF-C. These results indicate lymphatic vessels leverage the follistatin/activin axis as an alternate pathway in regulating inflammatory and lymphangiogenic responses, in addition to the IL-6/IL-6R and VEGF-C/VEGFR-3 pathways. Collectively, our vessel stimulation results demonstrate the utility of the μLYMPH system for examining vessel response in tailored microenvironments.

In the context of cancer, lymphatic vessels, like blood vessels, are conduits for the spread of primary cancer cells to secondary sites in the body. Regional nodal metastasis often precedes distant metastasis, and is a prognostic factor for assessing patient survival [6,159]. The interactions between lymphatic vessels and cancer cells that promote cancer progression typically involve lymphatic release of chemokines that enhance cancer cell invasion (e.g. CCL21/CCR7) and tumor lymphangiogenesis via overexpression of VEGF-C by cancer cells [160,161]. There is less known about the interactions between lymphatic vessels and tumor stromal cells that contribute to pro-malignancy and lymphatic metastasis. We examined the impact of breast cancer CAFs on lymphatic vessel cytokine signaling and barrier function to provide initial insight into lymphatic vessel-tumor stroma interactions. Overall, our fibroblast co-culture results indicate that CAFs

promote a pro-tumorigenic and pro-inflammatory lymphatic microenvironment. Specifically, CAFs alone contributed to the overexpression of HGF, a pro-tumorigenic factor that enhances cancer cell invasion [13]. They also enhanced lymphatic vessel secretion of G-CSF, which promotes breast cancer metastasis by recruiting tumor-associated neutrophils [162]. There is speculation on the sources of G-CSF in the TME, whether it is largely contributed by tumor cells or tumor stromal cells or both. Our results indicate that LECs are potential stromal sources via CAF stimulation, a mechanism not previously known. Moreover, CAFs induced vessel inflammation by releasing significant levels of pro-inflammatory cytokines, IL-6 and IL-8 [13], and reducing vessel secretion of follistatin. Interestingly, follistatin has been implicated as a prognostic factor in breast cancer, where higher levels correlated with reduced invasion and better patient survival [163]. Taken together, breast CAFs may have the capacity to 'recognize' follistatin as an anti-metastatic cytokine and consequently, inhibit its expression. Ultimately, the pro-inflammatory mechanisms induced by the CAFs resulted in significant barrier dysfunction, which has potential implications for lymphatic metastasis. We were able to fully rescue the vessels by neutralizing IL-6 secreted in the CAF co-cultures. Blocking IL-6R on the lymphatic endothelium partially rescued barrier function. This blockade of IL-6 signaling indicates that IL-6 plays a major role in lymphatic vessel dysfunction and may warrant its further investigation as a target to inhibit progression of tumors that commonly rely on lymphatic vessels for spread to regional lymph nodes. Notably, our mRNA expression data showed downregulation of CD31, VE-cadherin, and ZO-1 for both the CAF and NF co-cultures, suggesting that loss of junctional integrity may not be the primary mechanism of CAF-induced barrier dysfunction. Indeed, tumor cells can cause endothelial necroptosis (i.e. inflammatory cell death) as a pro-metastatic mechanism [164], which may extend to CAFs as indicated by the large areas of cell detachment on the endothelium of co-

cultured vessels. Collectively, our co-culture results demonstrate the usefulness of the μLYMPH system for examining lymphatic vessel function in diseased microenvironments, such as the TME.

In conclusion, we developed the μLYMPH system to examine lymphatic vessel biology in normal and diseased microenvironments. Our approach enables the generation of 3D human lymphatic vessels with *in vivo*-like structure-function relationships distinct from blood vessels. The system can be tailored to assess vessel response in different stimulatory conditions. Its capacity for co-culture further extends its modeling capabilities to relevant diseased microenvironments, such as the TME. We identified the follistatin/activin axis as a pathway unique to lymphatic vessels, which has a potential role in modulating lymphatic vascular inflammation and tumor microenvironmental interactions. Importantly, we demonstrated the efficacy of the μLYMPH system as a therapeutic screening platform, being able to mitigate cytokine (VEGF-C and IL-6) and CAF-induced barrier dysfunction by inhibiting relevant molecular pathways. Overall, our system advances the capabilities of existing *in vitro* lymphatic models, offering a powerful alternative to animal models.

2.4 Acknowledgements

We acknowledge a Postdoctoral Fellowship from the Natural Sciences and Engineering Research Council of Canada to M.M.G. and a fellowship from the UW-Madison Graduate Engineering Research Scholars program to K.M.L. Research reported in this publication was supported by NIH (R01EB010039) and the Wisconsin Head & Neck Cancer SPORE (P50DE026787). The content is solely the responsibility of the authors and does not necessarily represent the official views of the National Institutes of Health. Furthermore, we are grateful to Dr. Lisa Arendt's lab for providing the normal human mammary fibroblasts and Dr. Andreas Friedl's lab for the breast cancer-associated fibroblasts.

Chapter 3: Matrix Density Drives Lymphatic Vessel Activation in a 3D Organotypic Model of the Breast Tumor Microenvironment[2]

Abstract

Lymphatic vessels (LVs) have been suggested as a preferential conduit for metastatic progression in breast cancer, where a correlation between the occurrence of lymph node metastasis and an increased extracellular matrix (ECM) density has been reported. However, the effect of ECM density on LV function is largely unknown. To better understand these effects, we used a microfluidic device to recreate tubular LVs in a collagen type I matrix. The density of the matrix was tailored to mimic normal breast tissue using a low-density collagen (LD-3 mg/mL) and cancerous breast tissue using a high-density collagen (HD-6 mg/mL). We investigated the effect of ECM density on LV morphology, growth, cytokine secretion, and barrier function. LVs cultured in HD matrices showed morphological changes as compared to LVs cultured in a LD matrix. Specifically, LVs cultured in HD matrices had a 3-fold higher secretion of the pro-inflammatory cytokine, IL-6, and a leakier phenotype, suggesting LVs acquired characteristics of tumor-associated vessels. Interestingly, LV leakiness was mitigated by blocking the IL-6 receptor on the lymphatic ECs, maintaining endothelium permeability at similar levels of LV cultured in a LD matrix. To recreate a more in vivo microenvironment, we incorporated metastatic breast cancer cells (MDA-MB-231) into the LD and HD matrices. For HD matrices, co-culture with MDA-MB-231 cells exacerbated vessel leakiness and secretion of IL-6. In summary, our data suggest that (1) ECM density is an important microenvironmental cue that affects LV function in the breast tumor

[2] This chapter has been adapted from the prepared manuscript: "Matrix Density Drives Lymphatic Vessel Activation in a 3D Organotypic Model of the Breast Tumor Microenvironment." The manuscript was authored by Karina M. Lugo-Cintrón, José M. Ayuso, Bridget R. White, Paul M. Harari, Suzanne Ponik, David J. Beebe, Max M. Gong and María Virumbrales-Muñoz.

microenvironment (TME), (2) dense matrices condition LVs towards an activated phenotype and (3) blockade of IL-6 signaling may be a potential therapeutic target to mitigate LV dysfunction. Overall, modeling LVs and their interactions with the TME can help identify novel therapeutic targets and, in turn, advance therapeutic discovery.

3.1 Introduction

The tumor microenvironment (TME) is the niche where tumors develop, and comprises many cellular components such as cancer cells, immune cells, fibroblasts, blood and lymphatic vessels, as well as non-cellular components such as the extracellular matrix (ECM)[7]. The ECM consists of a complex meshwork of fibrillar collagens, glycoproteins, and proteoglycans that shape the biochemical and biophysical properties of tissues[35,36,165], regulating cell behavior in normal physiology[166]. In the TME, ECM remodeling contributes to tumor development and progression by altering cell behavior and, importantly, the presence of tumor-associated ECM architecture is a predictive biomarker of patient outcome [39,167–169]. Another aspect of the tumor-associated ECM is the increase in deposition of type I collagen by fibroblasts. The increase in collagen deposition forms a dense fibrous tissue surrounding the tumor, which has been implicated in promoting cancer progression and metastasis in numerous solid tumors[170–173], including breast cancer[40].

ECM remodeling is critical for regulating tumor escape (i.e. metastasis), the leading cause of mortality in cancer patients[174]. For example, it has been demonstrated that increased ECM density enhances cancer progression by promoting cancer cell migration[44], proliferation[45], and altering cellular metabolism[46]. Additionally, cancer cells can interact with other components of the TME, such as blood and lymphatic vasculature, that are also exposed to and could be modified by the remodeled matrix. The vasculature is of interest as it is an essential component that facilitates metastasis, providing a route for cancer cells to intravasate and disseminate to distant organs. Numerous studies have investigated how ECM density influences the physiology of vasculature in the TME and how these changes might contribute to metastasis. In this context, dense ECM has been found to reduce capillary morphogenesis[175,176] and angiogenesis[177],

but also increases the duration of endothelial cell-cell adhesion, cell proliferation, and sprout width[178]. To date, much less is known about the effect of ECM density on conditioning lymphatic vessel morphology and function.

Lymphatic endothelial cells (LECs) have unique structural and functional characteristics compared to endothelial cells from blood vessels[179]. LECs are morphologically different as they lack basement membrane, making them leakier than blood vessels and providing a more advantageous route for cancer metastasis[180,181]. However, it is not known whether a dense ECM alters lymphatic vessel (LV) phenotype. Understanding the influence of a dense ECM on LVs is critical in breast cancer, since increased collagen I deposition has been correlated with increased lymph node metastasis[82] and evidence indicates that breast cancer metastasis preferentially occurs through LVs as compared to blood vessels[182,183] .Therefore, elucidation of the effects of ECM density on lymphatic vasculature is critical to advancing our understanding of breast cancer metastasis. Unfortunately, traditional *in vitro* and animal models of lymphatic vessels present challenges in recapitulating 3D vessel structure and physiology or have low tractability [83]. We have previously reported the development of microfluidic organotypic *in vitro* models for (1) generating endothelial vessels[97,113,184] and (2) demonstrating the importance of tissue structure on tissue behavior[94].

Microfluidic organotypic *in vitro* models are becoming more widely used due to their potential for recapitulating *in vivo* tissue structure and function[94,104,105]. We and others have previously demonstrated the capability of microfluidic devices to recreate luminal geometries in collagen hydrogel[94,185,186], and we recently reported a LV model in these luminal geometries[184]. In the current work, we have used the microfluidic LV model to investigate the effects of ECM density (i.e., low- vs high-collagen density) on LV physiology. We found that LVs cultured in a

dense collagen I matrix exhibited a leakier, more proliferative phenotype and a pro-inflammatory secretion profile, suggesting that dense ECM conditions the LVs toward an activated endothelial phenotype. The inflammatory cytokine, IL-6, was identified as a potential mediator of LV barrier dysfunction given its significantly higher secretion in the dense collagen matrix. Therapeutic targeting of the IL-6/IL-6R pathway, using an anti-IL-6R antibody, decreased LV leakiness. Moreover, LVs were co-cultured with MDA-MB-231 tumor cells in both LD and HD matrices, where vessel dysfunction was heightened in the HD case. Collectively, our findings demonstrate for the first time that ECM density is an important signaling factor that affects LV physiology within the breast TME.

3.2 Materials and Methods

3.2.1 Cell culture

Human lymphatic endothelial cells (HLECs, ScienCell, 2500) were cultured in standard cell culture flasks coated with fibronectin (5 μg/cm^2, Sigma Aldrich, F1141-5MG) at a starting cell concentration of $5 \cdot 10^5$. Cultures were maintained with endothelial basal medium-2 (Lonza, CC-3156) supplemented with EGM-2 MV SingleQuot Kit (Lonza, CC-4147). HLECs were cultured to 90-95% confluency at passages 3 to 5 for all experiments. We used human mammary adenocarcinoma cells, MDA-MB-231, transfected to stably expressing green fluorescent protein (GFP), a kind gift from Dr. Suzanne Ponik (University of Wisconsin, Madison). MDA-MB-231s were routinely cultured in high glucose DMEM (Gibco, 11965092) supplemented with 10% fetal bovine serum (FBS, VWR, 97068-085) and 1% penicillin/streptomycin (ThermoFisher, 15140-122). For all experiments, a one to one mixture of lymphatic endothelial cell and MDA-MB-231 cell media was used (i.e. EGM-2 MV to 10% FBS,1% P/S high glucose DMEM), called

experimental media through the text. All cultures were kept in a humidified incubator at 37°C with 5% CO_2.

3.2.2 Device Fabrication

Fabrication of the organotypic lumen structure was performed as previously described [185]. The microdevice consists of two PDMS layers, which define the microchamber; and a suspended PDMS rod, which is removed after polymerization of a hydrogel in the main chamber to create a tubular lumen structure. In order to fabricate the top and bottom layers of the microdevice, a traditional soft lithography technique was used, in which the layers were spun using SU-8 (MicroChem, Y13273) to create the silicon master molds. Polydimethylsiloxane (PDMS, Dow Corning, Sylgard 184) was mixed at a 10:1 base to curing agent ratio and poured over the SU-8 silicon master molds. Using the same PDMS mixture, PDMS rods were fabricated by filling up a 25 gauge (Fisher Scientific, 14-840-84) hypodermic needle with PDMS. PDMS components were then baked at 80°C for 4 h. After baking, the PDMS rods were extracted from the needles, yielding PDMS rods of 280 μm in diameter. The two layers were aligned, ethanol bonded together and the PDMS rods were placed into the microdevice chamber. Finally, the microdevice was oxygen plasma bonded to a glass-bottom MatTek dish (MatTek Corporation, P50G-1.5-30-F), following a general protocol. The microdevices were sterilized using UV irradiation for 15-20 min for further use.

3.2.3 Organotypic Culture Preparation

3.2.3.1 Device preparation

To achieve maximum hydrogel adhesion to the PDMS chamber, a two-step coating of 2% poly(ethyleneimine) (PEI, Sigma-Aldrich, 03880) diluted in deionized DI water for 10 minutes

was loaded into the side ports. The PEI solution was aspirated and 0.4% glutaraldehyde (GA, Sigma-Aldrich, G6257) diluted in deionized DI water was loaded into the side ports and incubated at room temperature for 30 minutes. During the GA incubation, the collagen solution was prepared on ice (refer to section 3.2). After the 30-minute of GA incubation, the microdevices were washed three times with sterile DI water to remove any GA excess. At this point, devices are ready to be loaded with the collagen solution. To minimize evaporation, sacrificial phosphate buffered saline (PBS) was added around the side of the MatTek dish.

3.2.3.2 Extracellular matrix preparation and loading into the device

High-density rat-tail collagen type 1 (Corning, 354249, referred as collagen through the text) was diluted with 5X PBS and neutralized with 0.5 M NaOH (Fisher Scientific, S318) achieving a final concentration of 1X PBS, and a pH of 7.4. To achieve a final concentration of 3 mg/mL (low collagen density-LD) or 6 mg/mL (high collagen density-HD) dilutions with fibrinogen (Sigma-Aldrich, F8630), fibronectin (Sigma-Aldrich, F1141) and media were performed. For experiments with cancer cells in the matrix, MDA-MB-231s, a final concentration of 250 cells/μL was added to the respective collagen solution (recipes for different collagen gel densities and cultures conditions can be found in Table 3.1). Right after the washes with sterile DI water, 6 μl of collagen solution was loaded through the side ports and polymerized at room temperature for 10 min. Finally, a small droplet of media (5 μL) was placed on top of the side ports to prevent evaporation, and devices were transferred to 37^{o}C for 1 hour to allow collagen to fully polymerize.

Table 3.1. Recipes for different collagen gel densities and cultures conditions

	Lymphatic Vessels monocultures		Lymphatic Vessels co-cultures	
Final collagen I density (mg/mL)	3	6	3	6
Collagen gel[a] (µL)	80	80	80	80
5x PBS (µL)	20	20	20	20
0.5 M NaOH (µL)	3	3	3	3
	Dilutions to get to the final collagen I density:			
1 mg/mL Fibrinogen[b] (µL)	14.4	7.2	14.4	7.2
30 µg/mL Fibronectin[c]	8.6	4.3	8.6	4.3
250 cells/µL Cell suspension[d]	---	---	23.9	12
Experimental media	172.6	36.4	148.7	24.4
Total volume	298.6 µL	150.9 µL	298.6 µL	150.9 µL

[a]Stock concentration of 10.76 mg/mL
[b]Stock concentration of 20 mg/mL
[c]Stock concentration of 1 mg/mL
[d]Initial concentration 3,000 cells/µL

3.2.3.3 Lymphatic endothelial cell seeding in lumens

After incubation, a small drop of media (5 µL) was added to the input port under sterile conditions. To remove the PDMS rod, the rod was pulled through the output port using a sterilized tweezers, leaving a hollow lumen filled up with media within the collagen matrix. All fluid handling procedures were conducted with standard pipettes, uniquely enabled by passive pumping[128]. Lymphatic endothelial cells (HLECs) were trypsinized with 0.05% Trypsin-EDTA (ThermoFisher Scientific, 25300062), counted, resuspended in experimental media at 20,000 cells/µL and seeded into the lumens (4 µL per lumen). HLEC-filled lumens were incubated at 37^{o}C for 2 h to allow for cell attachment, flipping devices every 25 min to ensure homogeneous cell coverage of the lumen wall. After 2 hours, lumens were supplemented with 10 µL of experimental media and cultured overnight at 37^{o}C. Cultured vessel media was refreshed twice a day by flowing experimental media three times through the lumen to remove dead cells.

3.2.4 Immunofluorescence staining and imaging

During immunofluorescence staining, cells were washed with PBS for 30 minutes between each step. Unless specified otherwise, steps took place at room temperature. Washing buffer (0.1% PBS-Tween 80 (Sigma-Aldrich, P1754) and blocking buffer (3% Bovine Serum Albumin (BSA, Sigma-Aldrich, A9056) in 0.1% PBS-Tween 80) were made in advance and stored at 4^{o} C until use. Cells were fixed with 4% paraformaldehyde (PFA) (EMScience, 15700) for 15 min, then incubated with 0.2% Triton® X-100 (MP Biomedicals, 807426) for 30 min for permeabilization. Finally, vessels were incubated with 10 µL of blocking buffer at 4^{o}C overnight.

Primary antibodies were diluted to desired concentrations with staining buffer (blocking buffer with 1% PBS-Tween 80 at 10:1 v/v). Vessels were incubated with primary antibodies at 4^{o}C overnight (Table 3.2). Then, vessels were incubated with the secondary antibodies diluted using staining buffer supplemented with 10% goat serum to reduce unspecific binding for 2 hours. Stained vessels were washed over two days with the washing buffer and stored in sterile PBS until imaging. Texas Red-X Phalloidin (ThermoFisher Scientific, T7471) and DAPI (ThermoFisher Scientific, D3571) were used to stain actin cytoskeleton and nuclei, respectively. Fluorescent images were acquired at 10X using a Nikon TI® Eclipse inverted microscope (Melville, New York) and processed using the National Institutes of Health ImageJ software. Confocal images were acquired using a Leica SP8 3X STED Super-resolution microscope (Wetzlar, Germany) in the UW-Madison Optical Imaging Core.

Table 3.2. Primary and secondary antibodies used for immunofluorescent staining.

Primary antibody	Reference code	Stock conc. (mg/mL)	Working conc. (µg/mL)	Dilution
CD31	ab9498 (Abcam)	N/A	-	1:50
PROX-1	PA5-11899 (Thermo Fisher Scientific)	0.5 mg/mL	N/A	1:25
Primary antibody	**Host species**	**Secondary antibody[a]**	**Working conc. (µg/mL)**	**Dilution**
CD31	mouse	Alexa Fluor 647 anti-mouse	10	1:200
PROX-1	rabbit	Alexa Fluor 488 anti-rabbit	10	1:200

[a]Stock concentration of 2 mg/mL. Goat source.

3.2.5 Matrix visualization by SHG imaging

SHG images were taken on a custom-built inverted multiphoton microscope (Bruker Fluorescence Microscopy, Middleton, WI), as described previously [187]. Briefly, the system consists of a titanium:sapphire laser (Spectra Physics, Insight DS-Dual), an inverted microscope (Nikon, Eclipse Ti), and a 40x water immersion (1.15NA, Nikon) objective. SHG images were taken using an excitation wavelength of 890 nm, an emission bandpass filter of 440/80 nm, and a GaAsP photomultiplier tube (H7422P-40, Hamamatsu).

3.2.6 Collagen fiber quantification

SHG images of low- and high-density collagen matrices were analyzed using CT-FIRE V1.3 Beta2, an open source image processing program developed by the Laboratory for Optical and Computational Instrumentation (https://loci.wisc.edu/software/ctfirev1.3, University of Wisconsin-Madison). As per instructions in the CT-FIRE manual, the count and width of collagen fibers were measured for three separate field of views per device (i.e. top, middle, and bottom

planes of the device). The average fiber parameter per device was calculated as the average value of the three planes.

3.2.7 Fluorescent image quantification

For all images, we conducted a rolling ball background subtraction and a region of interests (ROIs) was drawn over the lumens in one Z-plane. The ROI dimension and background subtraction was kept constant throughout a dataset. To quantify actin stress fibers, we measured the percentage of F-actin covered area within the ROI. To count total Ki67 positive nuclei, we counted all maxima within the ROI defined by a set threshold. To evaluate the percentage of Ki67 positive cells, the number of Ki67 positive nuclei was divided by the total number of nuclei for each lumen. To quantify vessel-tumor interactions throughout the whole vessel, a projection of every five Z-planes from each Z-stack image was performed. In each X-projection, cancer cells in contact or within the lymphatic vessel were quantified.

3.2.8 Dextran diffusion assay

The permeability of the lymphatic vessels was measured by dextran diffusion assays using Texas Red dextran (70kDa, ThermoFisher Scientific, D1830) prepared in PBS to 1 μM. For each replicate, 3 μL of dextran solution was added to the vessel such that fluid was flush with the lip of the ports to minimize flow from a pressure head. Diffusion was measured over 15 minutes per vessel. Permeability coefficients were calculated using equation 1[123]:

$$P = (1/I_o)[(I_f - I_o)/(t_f - t_o)](D / 4), \qquad \text{Eq. 1}$$

where I_o is the total initial intensity outside the vessel, I_f is the total intensity outside the vessel at 15 minutes, t_o is the initial time point, t_f is the final time point of 15 minutes, and D is vessel

diameter. All vessels were imaged with the Nikon TI® Eclipse inverted microscope (Melville, New York), and maintained at 37 ^{o}C and 5% CO_2 by a stage-top incubator (Okolab,Italy).

3.2.9 Targeted blocking and exogenous IL-6 treatment

Anti-IL-6R antibody (Abcam, ab47215) was used to inhibit IL-6/IL-6R signaling. Mouse IgG1 antibody (BioLegend, 400102) was used as an isotype control for the IL-6/IL-6R inhibition experiments. To block vessels cultured in the high-density matrix, vessels were treated with anti-IL-6R antibody (25 μg/mL) from day 2 to day 5 and used for dextran diffusion analysis on day 5. To stimulate vessels cultured in the low-density matrix, IL-6 solutions were prepared to either 5 ng/mL or 30 ng/mL in EGM-2 MV media. Vessels were supplemented with the IL-6 solutions on day 2 and refreshed daily until day 5 for dextran diffusion analysis.

3.2.10 Cytokine secretion assay

Multiplexed protein secretion analysis was performed on HLEC cultured vessels, HLEC vessels co-cultured with MDA-MB-231s and MDA-MB-231s monocultures for both types of matrix densities. The analysis was performed using the Magnetic Bead-Based Multiplex ELISA system MAGPIX (Luminex Corporation) with the Milliplex human cytokine panel bead kit (R&D Systems, LXSAHM-10) as described elsewhere[113]. Collected media (20 μL per lumen) was combined to increase the sample volume in each cultured condition. Briefly, media collection was performed on days 3 and 4 from six cultured vessels pooled per cultured condition, yielding 240 μL in total. Sample preparation and detection was performed following the manufacturer's protocol. Data were collected with xPonent software (Luminex), and soluble factor concentrations

in media were calculated using mean fluorescence intensities (MFI) by creating a standard curve for each analyte using a five-parameter logistic (5-PL) curve fit.

3.2.11 Statistical analysis

All the experiments were repeated at least three times as independent biological repeats. All results are presented as the mean ± one standard deviation of the mean. Data were analyzed using GraphPad Prism 7 (GraphPad Software, La Jolla, CA) and statistical significance was set at $p < 0.05$. One-to-one comparisons were performed with an unpaired Student t-test with Welch's correction (if SD were not the same) after the normal distribution was proved via Shapiro-Wilk test. If the normality test was not passed, a non-parametric test was performed (Mann-Whitney test) (Fig. 2,3, 4 and 5). Multiple comparisons by One-way ANOVA were corrected using the Dunnett test and multiple comparisons by 2-way ANOVA were corrected with a Sidak's test (Fig. 5C).

3.3 Results

3.3.1 3D organotypic lymphatic vessel model generation

To investigate how ECM density affects LV function, we adapted a recently published and validated *in vitro* model that recreates a physiological lymphatic microenvironment, such as lumen structure and matrix composition[188], as illustrated in Fig. 3.1 A and Fig 3.1 B. LVs were generated within a 3 mg/mL collagen hydrogel by lining the lumen structure with primary human lymphatic endothelial cells (HLECs) (Fig. 3.1 C). After 5 days, LVs developed a confluent endothelial monolayer visualized via CD31 staining (Fig. 3.1 D) with evidence of evident tubular structure in cross-section (Fig. 3.1 E), demonstrating generation of a 3D tubular lymphatic vessel

(Fig. 3.1 F). To characterize LV phenotype, the expression of prospero homeobox protein 1 (PROX-1), a protein that co-localizes with the nucleus of lymphatic endothelial cells[189], was assessed and confirmed by immunofluorescent staining (Fig. 3.1 G). We previously demonstrated that HLECs also express lymphatic endothelial hyaluronan receptor 1 and podoplanin[184], which are markers specific to lymphatic ECs.

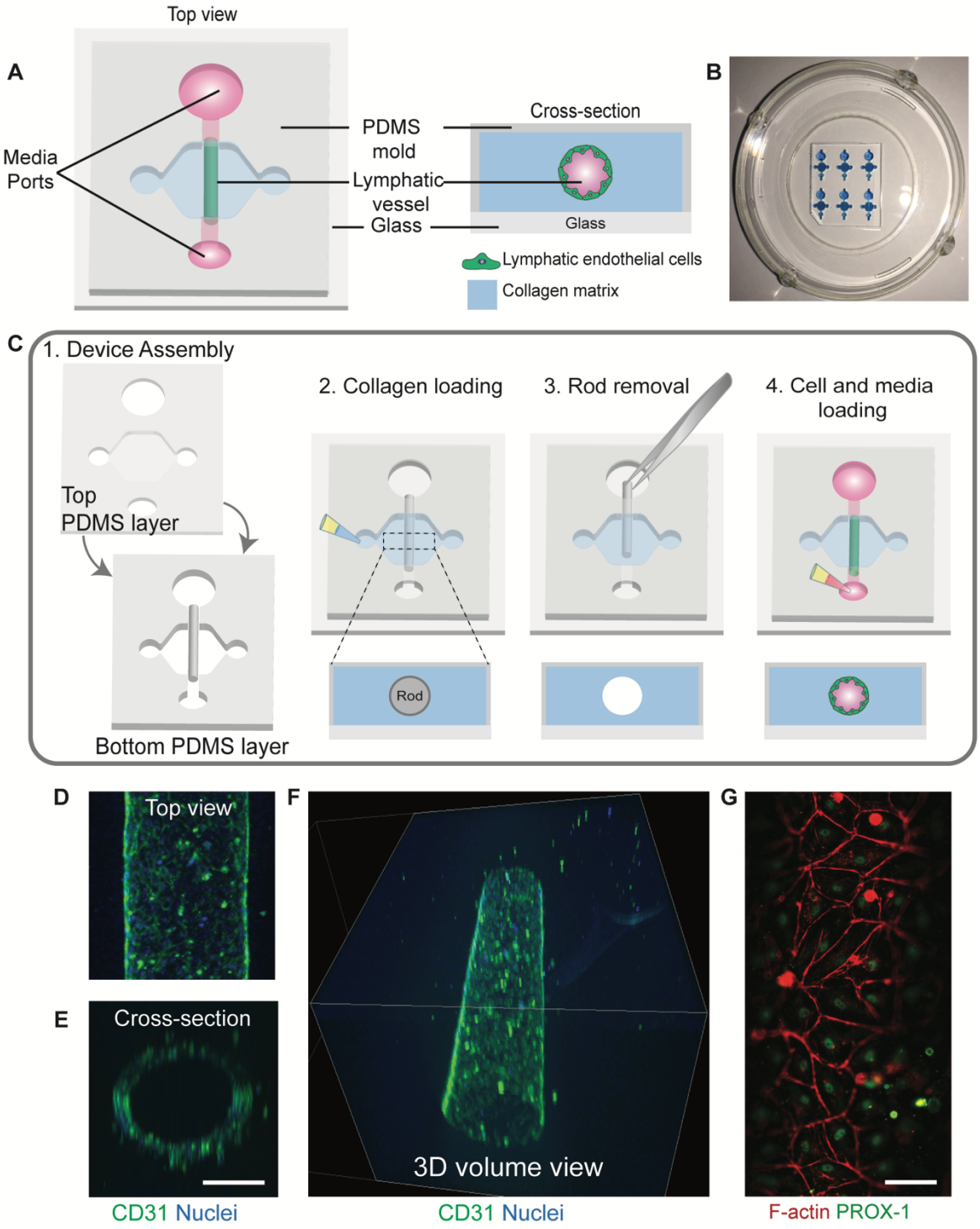

Figure 3.1. **Organotypic lymphatic vessel model. A)** Top view of assembled microdevice (left) with cross-sectional view of the device showing the lymphatic endothelial cells lining the lumen structure within a collagen matrix (right). **B)** Representative image of microdevice array. Microdevices were filled with a blue dye for visualization purposes. **C)** Microdevice design and fabrication scheme. 1)The device consists of two PDMS layers bonded together with a suspended PDMS rod. The PDMS layers defined the microchamber, while the rod allows for the generation of the lumen structure. The top layer of the microdevice contains ports for fluid handling and a cover for the microchamber. For device operation, after plasma bonding to a glass-bottom dish: 2) the microchamber is filled with a hydrogel

solution and left to polymerize, 3) lumen rod is removed exposing an empty lumen within the hydrogel, 4) cells are seeded into the lumen with media and cultured at 37°C. **D)** Top view of a lymphatic vessel stained with a classical endothelial cell junction marker, cluster of differentiation 31 (CD31), and nuclei**. E)** Orthogonal view of the vessel. Scale bar= 140 μm **F)** Confocal image of the lymphatic vessel showing 3D tubular structure. **G)** Top view of cultured vessels stained with a lymphatic-specific marker, prospero homeobox protein 1 (PROX-1), and F-actin. Scale bar = 70 μm.

3.3.2 Formation and characterization of low-density and high-density collagen matrices

Using the LV model, we sought to investigate how LVs are affected by ECM density. To do so, we used a low-density (LD) and a high-density (HD) collagen I matrix. The selected collagen concentration of 3 mg/mL (LD) is representative of healthy normal tissue such as the mammary gland, whereas the 6 mg/mL (HD) collagen gel mimics the tissue stiffening occurring in solid tumors [44,190,191]. Thus, we first aimed to elucidate the differences in matrix architecture in the LD and HD matrices using Second Harmonic Generation (SHG) to visualize and analyze collagen fibers (Fig. 3.2 A). CT-FIRE was used to compare the average fiber count and average fiber width in the LD and HD matrices[192]. The average fiber count was 3638±172.2 for LD and 3759±161.4 for HD, revealing that the number of collagen fibers per field of view is similar for both matrices (Fig. 3.2 B). However, the average fiber width was significantly different for HD at 0.4583± 0.008 μm as compared to 0.411± 0.009 μm for LD (Fig. 3.2 C). Overall, we found that changes in ECM collagen density alters matrix architecture resulting in higher fiber width.

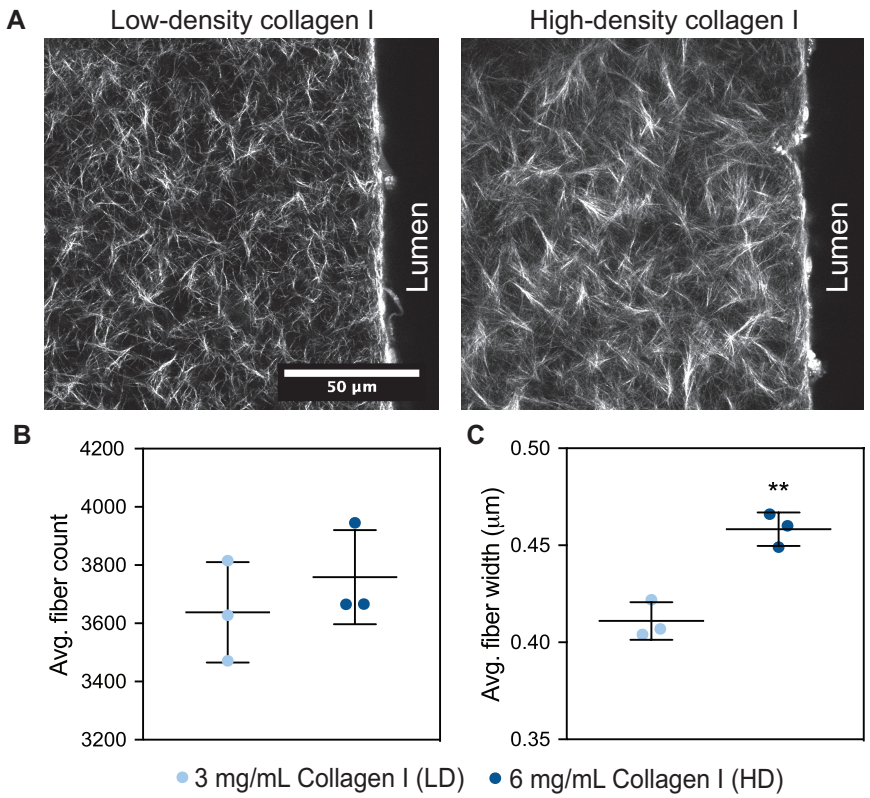

Figure 3.2. Extracellular matrix characterization of a low-density (LD) and high-density (HD) collagen hydrogel. **A)** Second Harmonic Generation images of the collagen type I fibers for the low-density (LD) and high-density (HD) matrices in the microdevice, next to the lumen structure. **B)** Average fiber count for LD and HD matrices. **C)** Average fiber width for LD and HD matrices. Fiber quantification was performed in one optical plane. Bars represent average ± SD of n=3 independent replicates. **$p \leq 0.01$

3.3.3 Influence of low-density and high-density collagen matrices on lymphatic vessel phenotype

To determine the effect of LD and HD collagen on LV phenotype, we seeded HLEC lumens within LD and HD collagen matrices (Fig. 3.3 A), and assessed their phenotype at days 1, 3 and 5. Bright-field images of LVs cultured after one day revealed that HLECs attached to the lumen wall equally in both matrices (Fig. 3.3 B), which was also confirmed via nuclei count (Fig. 3.3 C-top left), revealing no significant differences in the number of cells attached to the lumen on day one as shown by the average nuclei count per area on day 1 (Fig. 3.3 D). However, the average nuclei count significantly decreased in the HD matrix as compared to the LD matrix for day3 and day 5

(Fig. 3.3 D). In addition, LVs were stained for F-actin at day 5. Interestingly, there were noticeable morphological changes to the lymphatic endothelium in the HD matrix, such as cell detachment, as compared to the lymphatic endothelium in the LD matrix (Fig. 3.3 C- bottom right). As previously described by us and others, cell detachment was quantified by measuring the cell coverage area of the lumen, in addition to the average nuclei count per area[193,194]. Cell coverage area significantly decreased in HD matrices as compared to LD matrices (Fig 3.3 E). These observations are consistent with previous reports that point to the capacities of the ECM to modulate capillary network formation and structural integrity of endothelial vessels[195].

In addition, previous studies have demonstrated that endothelial cell proliferation increases in stiffer matrices as compared to more compliant matrices[196]. Therefore, we hypothesized that LVs cultured in HD matrices would be more proliferative than LVs cultured in LD matrices. To evaluate cell proliferation, LVs were stained for the cell proliferation marker Ki67 at days 1, 3 and 5. The percentage of Ki67 positive over total nuclei (DAPI) was quantified using ImageJ[197] and found to be similar at day 1, revealing no differences in LEC proliferation (Fig. 3.3 F). However, the proliferation rate significantly increased in the HD matrix as compared to the LD matrix for day3 and day 5 (Fig. 3.3 F).

Similarly, previous studies have suggested that increases in matrix stiffness, which are associated with increases in matrix density, alters EC-EC adhesion and EC-ECM adhesion by increasing cell contractility and actin stress fiber formation [198,199]. Interestingly, in our model, we observed more actin stress fibers in HD matrices (Fig. 3.3 G). The percentage of actin stress fibers was quantified as 18.9% ± 2.7% for LD matrices and 30% ± 6.6% for HD matrices, indicating a significant increase in actin stress fiber formation per vessel area in the HD matrices.

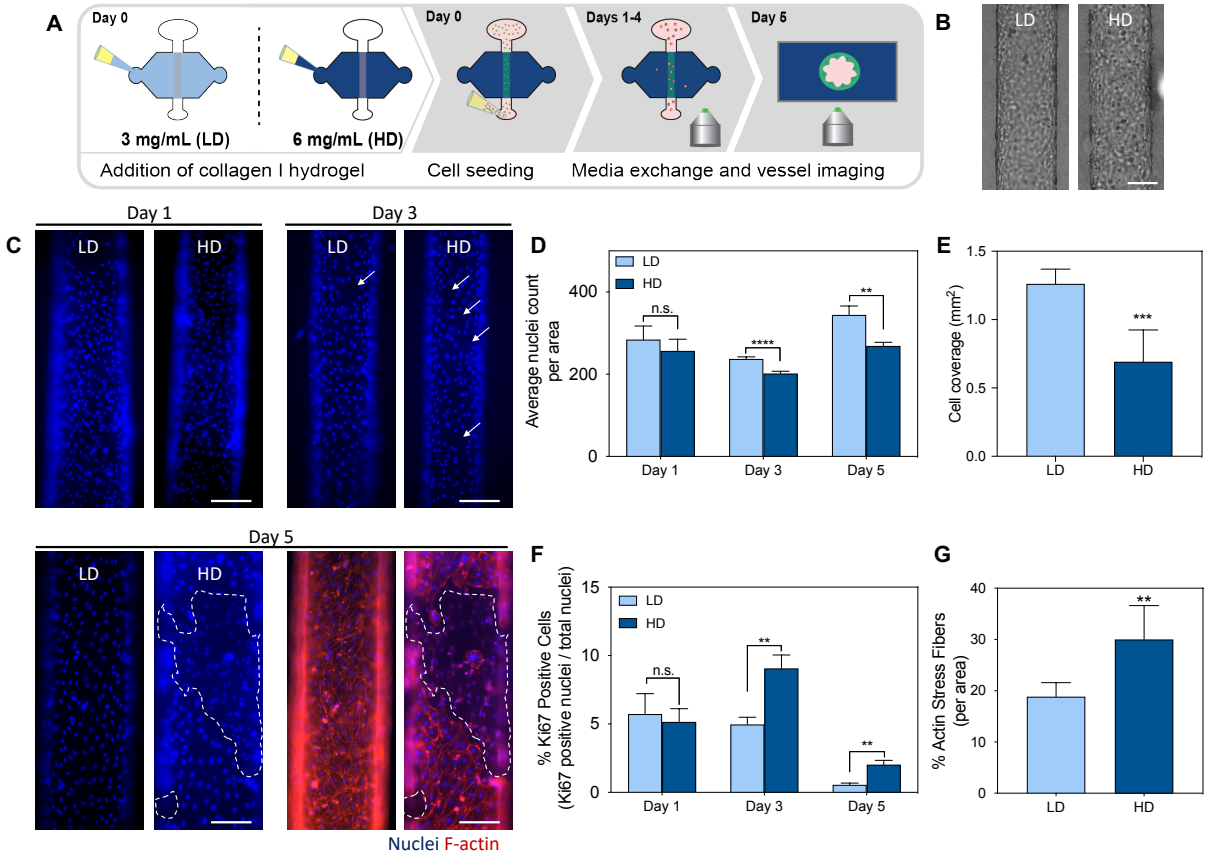

Figure 3.3. **Influence of ECM density in lymphatic vessels morphology, cell coverage, growth and f-actin stress fibers. A)** Schematic of the culture conditions and experiment timeline. **B)** Brightfield images of a lymphatic vessel cultured in LD and HD collagen matrices on day 1. Scale bar = 200 µm **C)** Images of lymphatic endothelial cells nuclei cultured in LD and HD matrices at day 1(top left), day 3 (top right) and day 5 (bottom left) with F-actin in red and nuclei in blue (bottom right). Dashed outline indicates endothelial cell detachment. **D)** Nuclei count of cells conforming the lymphatic vessels per area at day 1, 3 and 5. **E)** Lymphatic endothelial cell coverage area for each lumen cultured in LD and HD collagen matrices at day 5. **F)** % Ki67 positive cells (proliferation) per lumen area in lymphatic vessels cultured in LD and HD matrices at day 1, 3 and 5. **G)** % F-actin stress fibers per lumen area for vessels cultured in LD and HD collagen matrices at day 5. Bars represent average ± SEM, n at least 4 individual vessels. Scale bars = 140 µm. *p ≤ 0.05, **p ≤ 0.01, ***p ≤ 0.001, ****p ≤ 0.0001.

3.3.4 Dense collagen matrix promotes pro-inflammatory cytokine secretion and disrupts barrier function in LVs

After studying the morphological changes of LVs cultured in LD and HD matrices, we focused on studying the secretory profiles of cultured lumens within the different matrices (as shown in Fig. 3.4 A) using a pre-made bead-based ELISA panel (Luminex MAGPIX), from which all factors were within detectable ranges. LVs cultured in HD matrices showed an increase in most of the

chemokines and pro-inflammatory cytokines (Fig. 3.4 B) such as IL-1β (1.4-fold) and IL-8 (1.7-fold), as compared to vessels cultured in LD matrices. The chemokine CXCL12 was not detectable in LD matrices but it was detectable in HD matrices, showing an increase in secretion in HD matrices. In addition, the specific inflammatory cytokines that significantly increased in HD matrices were TNF-α (2-fold), IL-1α (1.8-fold), CCL19 (2.1-fold), CCL21(1.6-fold), CX3CL1 (1.6-fold) and the most strongly upregulated cytokine was IL-6, which increased 3-fold in HD matrices. IL-6 is of interest given that accumulating evidence establishes IL-6 as a key player of the tumor microenvironment which critically regulates endothelial cell dysfunction and tumor progression[200–202].

To further evaluate the change in IL-6 concentration observed in LD and HD matrices, we sought to investigate if there is a relationship between ECM density and IL-6 secretion. For this, we cultured the LVs in two additional matrix densities, covering a range of collagen concentrations between the LD and HD matrices (i.e. 4 mg/mL and 5 mg/mL matrix). Interestingly, we observed an increase of IL-6 secretion in an ECM density-dependent manner (Fig. 3.4 C). Specifically, similar levels of IL-6 were observed in the LD (3 mg/mL) and 4 mg/mL matrices, whereas there was a significant increase in IL-6 secretion in the 5 mg/mL and HD (6mg/mL) matrices as compared to a LD matrix. These results confirm that IL-6 secretion increases in an ECM dependent manner. In the literature, IL-6 is known to be released from endothelial cells in inflammatory states, which can then alter endothelial permeability via autocrine and paracrine interactions[203,204]. Therefore, we hypothesized that LV culture in HD matrices have an increase in vessel permeability as a result of the increase in IL-6 secretion.

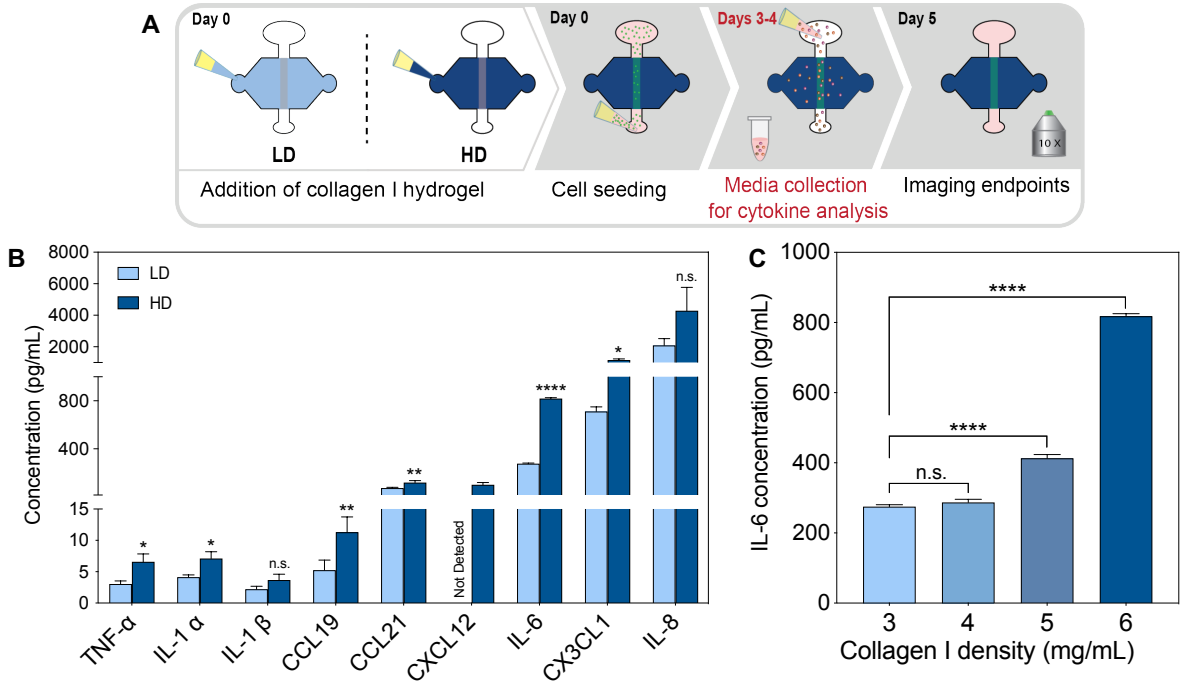

Figure 3.4. Effect of ECM density in lymphatic vessel cytokine secretion. A) Schematic of the culture conditions and experimental timeline. **B)** Pro-inflammatory cytokine and chemokine concentrations for vessels cultured in LD and HD collagen matrix. **C)** IL-6 cytokine concentration in a range of collagen I density matrices (3, 4, 5 and 6 mg/mL). (n =4, pooled samples over 2 days from at least 6 lumens). *p ≤ 0.05, **p ≤ 0.01, ****p ≤ 0.0001.

To test our hypothesis, we assessed the barrier function of cultured vessels in LD and HD matrices by diffusion assays using 70 kDa-Texas Red dextran (as shown by the schematic in Figure 3.5 A), which represents the regulation of diffusion for biomolecules in the size range of serum albumin, ~67 kDa. Specifically, the solution of dextran was perfused through the lumen and tracked using time-lapse fluorescent microscopy for 15 minutes. In the HD matrix, localized leakage was observed at time 0. Representative image of the LD matrix (left image) and HD matrix (right image) after 15 min of dextran perfusion shows more dextran outside of the vessel wall for the HD matrix (Fig. 3.5 B). As shown by the representative curve in the normalized dextran intensity graph, LVs cultured in HD collagen matrices have higher intensity values outside of the vessel wall through the matrix as compared to the LD collagen matrices (Fig. 3.5 C). These results indicate that LVs cultured in HD matrices are leakier than those cultured in LD matrices. We also

calculated the permeability coefficient of the vessels which revealed that in HD density matrices LVs were 1.4-fold leakier than LVs cultured in LD matrices (Fig. 3.5 D). However, the increase in permeability in HD vessels was significantly reduced to the level of LD vessels, by treatment with an IL-6 receptor blocking antibody, IL-6R, (25 μg/mL) (Fig. 3.5 E). In addition, blocking with an IL-6R antibody significantly reduced vessel permeability compared to the control (IgG blocking), while the permeability values for the control and HD matrix were not significantly different. To confirm that IL-6 was responsible for the decrease in barrier function, we added exogenous IL-6 (5 ng/mL and 30 ng/mL) to the vessels cultured in the LD matrix. The addition of exogenous IL-6 led to a significant increase in permeability at 30 ng/mL, increasing permeability to a level equivalent to vessels cultured in HD matrices, $1.5 \cdot 10^{-5} \pm 0.3 \cdot 10^{-5}$ cm/s (Fig. 3.5 F) and leading to a significant increase in vessel permeability as compared to the LD condition. However, treatment with 5 ng/mL of IL-6 did not result in increased vessel permeability, $0.7 \cdot 10^{-5} \pm 0.1 \cdot 10^{-5}$cm/s (Fig. 3.5 F). Overall, our results show that HD matrices promote an activated vessel phenotype in LVs by inducing the secretion of pro-inflammatory cytokines such as IL-6. Overall, IL-6 drives the decrease in LV barrier function in response to HD conditions. Additionally, our results demonstrate the potential of therapeutic treatment using anti-IL-6R to rescue LV barrier function. Taken together, the increase in secretion of pro-inflammatory cytokines and concurrent increase in vessel leakiness in dense matrices suggests that LVs are conditioned by the increased ECM density, which promotes the activation of endothelial cells and the development of a leaky vessel phenotype.

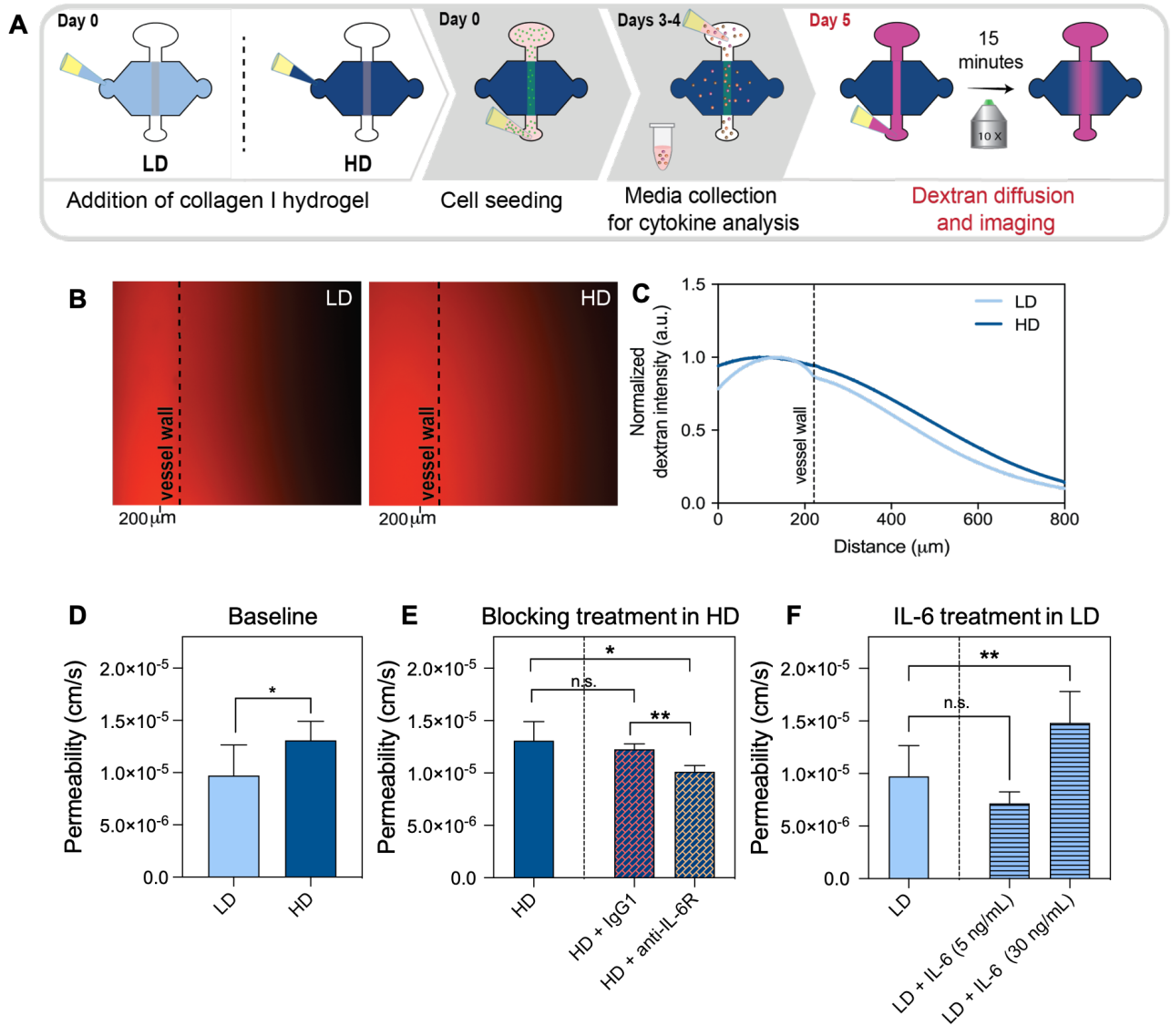

Figure 3.5. Effect of ECM density in lymphatic vessel barrier function. A) Schematic of the culture conditions and experimental timeline. **B)** Representative image of diffusion assay in vessels cultured in LD and HD matrices at t=15 min. Dashed lines indicate lymphatic vessel wall **C)** Normalized dextran intensity profile for vessels cultured in LD and HD matrices. **D-F)** Quantification of solute permeation for vessels cultured in LD and HD matrices. **D)** Vessel permeability in LD and HD matrices (baseline levels). **E)** Vessel permeability in HD matrices treated with IgG1 (control) or anti-IL-6R (blocking treatment) **F)** Vessel permeability in LD matrices treated with IL-6 (5 mg/mL and 30 ng/mL). Bars represent average ± SD, n at least 3 individual vessels. *$p \leq 0.05$, ***$p \leq 0.001$, ****$p \leq 0.0001$.

3.3.5 Lymphatic vessel co-culture with cancer cells in dense matrix enhances vessel dysfunction

Next, we investigated the interactions of breast cancer cells and LVs in the LD and HD matrices. Specifically, triple negative MDA-MB-231cancer cells expressing GFP were embedded in the LD or HD matrix on day zero and co-cultured with LVs for five days, referred to as 231-lymphatic co-cultures (schematic in Figure 3.6 A). After five days of culture, phenotype assessment of co-cultured vessels in LD and HD collagen matrices was performed by staining the vessels for CD31, F-actin, and nuclei to identify all cells whereas cancer cells were identified by GFP. In HD matrix conditions, there was an increase in endothelial cell detachment compared to LVs cultured in LD matrices, similar to our LV monocultures (Fig. 3.6 B). Our previous permeability data (Fig. 3.5 D-F) suggested that LV barrier dysfunction is caused by IL-6. Therefore, to evaluate the levels of IL-6 in co-culture conditions, conditioned media from the 231-lymphatic co-cultures and monocultures in LD and HD was collected on days 3 and 4 for the conditions shown in the schematic and legend (Fig. 3.6 C). Then, the concentration of IL-6 was determined by MAGPIX analysis (Figure 3.6 D). In the LD matrix, IL-6 concentration significantly increased in the LV monoculture as compared to the 231-lymphatic co-culture. However, in the HD matrix, similar concentrations of IL-6 were found in LV monoculture as compared to 231-lymphatic co-cultures. Interestingly, IL-6 concentration was significantly higher in 231-lymphatic co-cultures in HD matrices as compared to the LV monocultures and 231-lymphatic co-cultures in LD matrices.

Then, we sought to compare vessel permeability in 231-lymphatic co-cultures with LV monocultures. Therefore, we analyzed changes in LV barrier function by measuring the permeability coefficient as described previously. The permeability coefficient of the 231-lymphatic co-cultures in LD was $0.7 \cdot 10^{-5} \pm 0.2 \cdot 10^{-5}$ cm/s and $1.3 \cdot 10^{-5} \pm 0.2 \cdot 10^{-5}$ cm/s for HD,

revealing that in HD matrices LVs were 1.9-fold leakier (Fig. 3.6 E). Interestingly, the permeability values in the co-cultures are lower for both matrices as compared to the permeability values for the LVs monocultures (Fig. 3.5 D). Based on the results described in the previous figure, we hypothesized that IL-6 is responsible for decreasing LVs barrier capacity in the 231-lymphatic co-cultures within dense matrices. To test this hypothesis, co-cultures in dense matrices were treated with anti-IL-6R (25 μg/mL) antibody that was previously described for the LV monocultures. Compared to the 231-lymphatic co-cultured in HD matrices, the increase in vessel permeability was significantly reduced to $1.0 \cdot 10^{-5} \pm 0.09 \cdot 10^{-5}$ cm/s by supplementing the anti-IL6R to the media (Fig. 3.6 E) while the control (IgG blocking) did not change ($1.2 \cdot 10^{-5} \pm 0.08 \cdot 10^{-5}$ cm/s). Overall, these results indicate that IL-6 signaling through IL-6R was likely a primary mediator of LV barrier function.

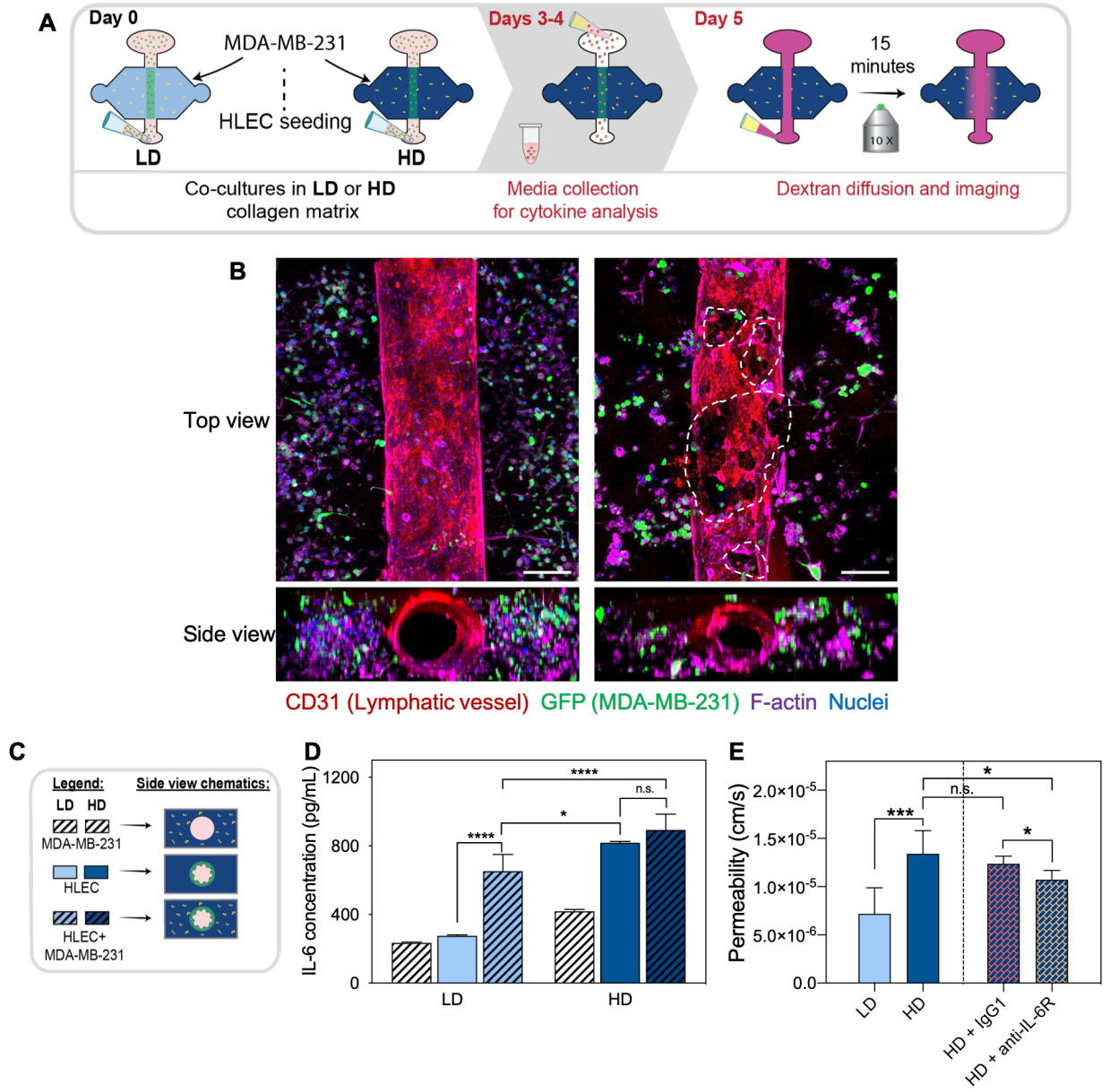

Figure 3.6. Lymphatic vessel co-culture with metastatic breast cancer cells (MDA-MB-231) in LD and HD matrices. A) Schematic of the experimental conditions and timeline. **B)** Top-view and cross-section view of immunofluorescent images of lymphatic vessels co-cultured with metastatic breast cancer cells in LD (left) and HD (right) matrices (F-actin in purple, CD31 in red, MDA-MB-231-GFP in green and nuclei in blue. Dashed outlines indicate endothelial cell detachment in the vessel wall. **C)** Legend and cross-section view schematic of conditions. **D)** Co-cultures IL-6 protein secretion levels in LD and HD matrices. **E)** Quantification of solute permeation for lymphatic lumens in LD and HD matrices and for lymphatic lumens in LD and HD matrices treated with anti-IgG1 (control) and anti-IL-6R (blocking treatment). Bars represent average ± SD, n at least 3 individual vessels. (n =4, pooled samples over 2 days from at least 6 lumens). Scale bar = 140 μm. *p ≤ 0.05, ***p ≤ 0.001, ****p ≤ 0.0001.

3.4 Discussion

Despite the crucial connection between ECM density and lymphatic metastasis in breast cancer, little is known about how ECM density affects LV function. Elucidating the mechanisms by which a dense ECM mediates lymphatic metastasis can help identify new therapeutic targets and, in turn, improve patient outcome. To this end, we applied a LV model recently developed and characterized by our lab[184]. This microfluidic model is capable of reproducing LV hallmarks, such as the expression of lymphatic specific markers, characteristic cytokine profiles, leakier barrier function than blood vessels, and increased drainage capacity[205]. These characteristics make our model representative of in vivo LVs with the additional capability to model different microenvironment conditions[184].

We adapted the LV model to study the effect of the density of the ECM in conditions resembling normal and cancerous breast tissue. To this end, we included cancer cells in the model to study the effects of high/low matrix density on LV and cancer cell crosstalk. To the authors' knowledge, this is the first LV model that incorporates the lumen structure, matrix proteins, and cancer cells into a single system. Our LV model offers unique capabilities for studying the influence of ECM density in LV morphology, barrier function, cytokine secretion and tumor crosstalk. In the literature, a range of 1 mg/mL to 6 mg/mL collagen matrices have been used and correlated to tumor cell behavior *in vitro* (i.e. low density produced a normal phenotype, whereas high density correlated with a tumor-like phenotype)[45,191,206]. In this work, we chose to study the effect of ECM density on LV function by using two collagen densities: low density (3 mg/mL, abbreviated LD) and high density (6 mg/mL, abbreviated HD). We found that a higher collagen density produces significantly thicker collagen fibers, which is observed in breast cancerous tissues and contributes to enhanced mechanical rigidity, leading to tumor progression[41,207]. Therefore,

the selected matrices recapitulate the microenvironment found *in vivo*. With these matrices we sought to investigate the effects of collagen density in LV morphology, changes in actin stress fibers and cell proliferation. After one day lymphatic cells had similar nuclei counts and proliferation levels on both matrices. However, after 3 days of culture, we observed a significant decrease in nuclei count in the HD matrices and a significant increase in cell proliferation, suggesting that dense matrices can condition vessel behavior. Although the similar trend was observed on day 5, compared to day 3, there was an overall increase in nuclei count in both matrices but a decrease in cell proliferation. These results suggest the vessel is stabilizing at day 5, hence, the decrease in cell proliferation. In addition, we observe a significant decrease in cell coverage area and a significant increase in F-actin stress fibers at day 5, revealing that LVs respond to dense collagen matrices by going through vascular damage which results in poor endothelial integrity. Therefore, our results are consistent with the vascular damage observed *in vivo*. Specifically, the increase in cell proliferation that is observed in our model in the HD matrices is described by one of the repair mechanisms of vascular damage where adjacent mature endothelial cells can replicate locally and replace the lost and damaged cells[208]. This local repair mechanism is usually sufficient to maintain vascular integrity in healthy conditions. However, in disease states, loss of endothelial integrity develops as observed in our HD matrices. Although we did not explore this mechanism in more detail, it is important to note that *in vivo* there is another repair mechanism that relies in circulating endothelial progenitor cells for the maintenance and repair of the endothelium[209,210]. Consequently, the phenotype that we observe *in vitro* could potentially be mitigated by the addition of endothelial progenitor cells.

Another characteristic of vascular damage described in the literature is the activation and dysfunction of endothelial cells. The activation of endothelial cells represents the switch from a quiescent phenotype toward one that involves a response from the endothelium, resulting in the expression of chemokines, cytokines and adhesion molecules. Then, the activation of endothelial cells progress to endothelial cell detachment, leading to loss of endothelial integrity[208,211,212]. Therefore, to examine the activation of LV, we assessed the secretion of inflammatory cytokines and chemokines of cultured lumens within the different matrices by measuring the secreted factors in the culture media. Interestingly, we found a significant increase in most of the cytokines and chemokines analyzed. We also identified a significant increase in IL-6 secretion in LVs cultured in HD matrices as compared to LD matrices and we found that IL-6 secretion increases in a density dependent manner as we observed the increase in the 5mg/mL and 6 mg/mL (HD) matrices but not the 3mg/mL (LD) or 4 mg/mL matrices. Hence, these results indicate IL-6 increases in response of the increase in ECM density and demonstrate that LV respond to changes in the surrounding ECM density, suggesting that in dense ECM conditions endothelial cells are being activated.

Previous studies have shown that the increase in pro-inflammatory cytokine secretion results in endothelial barrier dysfunction[152,213,214]. In particular, endothelial cells have been shown to secrete IL-6 in inflammatory states (e.g. vascular damage), thereby altering vessel permeability[203,204]. For this reason, we next examined the permeability and barrier function of the LV in LD and HD matrices through diffusion assays using 70 kDa-Texas Red dextran. We determined that LV cultured in HD matrices were significantly more permeable than LV cultured in LD matrices, which has implications in the context of cancer metastasis. Based on the literature and our results, we hypothesized that the increase in permeability was a result of the increase in

IL-6 secretion which in turn led to an increase in cell actin stress fibers and cell detachment, resulting in gaps in the LV.

Previous studies have shown that the secretion of IL-6, a major pro-inflammatory cytokine, has been implicated in the regulation of LV barrier function *in vitro*[152,215] and in promoting breast cancer[78,216–219]. In our model, blocking the IL-6 receptor mitigated vessel leakiness in HD, whereas leakiness was induced in LV cultured in LD matrices after treatment with IL-6. Thus, these results confirm that IL-6 is responsible for increasing LV permeability. Interestingly, treatment with 5 ng/mL of IL-6 did not induce leakiness in the LV cultured in LD matrices. This could indicate that a constant and localized source of IL-6 might be necessary to induce vessel permeability in an autocrine manner. The mitigation of HD-induced LV leakiness may have implications in breast cancer metastasis by reducing the potential of intravasation events through the stabilization of the endothelium. In addition to IL-6, the overexpression of chemokines that serve as chemotactic signals for cancer cells (e.g. CX3CL1, CXCL12) have previously been found to be secreted by lymphatic vessels, having an important contribution to cancer metastasis[220–224]. In our system we observed that an increased ECM density results in an increase in cytokine secretions, which in turn disrupted the endothelial barrier.

As for cancer cells, breast cancer cells have been shown to play a role in the conditioning of the lymphatic vasculature[74,225]. For example, a study reported that LECs support tumor growth in breast cancer[73], demonstrating important interplay between lymphatic cells and breast cancer cells. To our knowledge, no study has investigated the effect of matrix density in a microenvironment that incorporates both LVs and cancer cells, despite the known correlation between dense matrices and lymph node metastasis in breast cancer[82]. Therefore, we leveraged

our model to investigate the effect of the ECM density in breast cancer cell crosstalk with LVs, where we also found a significant increase in IL-6 secretion in HD matrices. Although IL-6 secretion increased in both matrices, we observed disruption of the LV in dense matrices only, which illustrates the importance of the matrix and cellular composition in organotypic models of cancer. Despite the apparent presence of gaps in the LVs co-cultured with breast cancer cells in dense matrices, we observed lower permeability coefficient levels as compared to monocultures. This discrepancy could be due to matrix remodeling exerted by the breast cancer cells. For example, the density of the matrix increases due to cell proliferation and reorganization of the collagen fibers by the cells, which may limit the diffusion of the dextran molecule through the matrix[226]. Another explanation for this discrepancy could be due to the crosstalk between the LVs and cancer cells. It is also important to note that the increase in IL-6 secretion in the co-culture within a LD matrix did not result in a permeability increase. Interestingly, the increase in IL-6 in LD matrix co-cultures did not reach the levels of LV monocultures cultured in HD matrices, suggesting that there might be a threshold of IL-6 that produces LV barrier destabilization.

There is ample literature demonstrating that IL-6 also has a role in in breast cancer cell migration[117,183], growth and metastasis[75]. Specifically, a study demonstrated that breast cancer cells secrete IL-6 and educate LECs in pre-metastatic organs, facilitating breast cancer metastasis[72] and revealing the significance of IL-6 as a therapeutic target in cancer therapy. Therefore, the 231-lymphatic co-culture model allowed us to test the effect of IL-6 receptor blocking, a potential therapeutic target, to mitigate LVs leakiness in the HD matrix. Although the increase in permeability was significantly reduced by supplementing the anti-IL-6R to the media, the effect was lower than in the LV monocultures and the permeability levels did not return to baseline levels. These results suggest that there may be other factors besides cancer cells and IL-6

that contribute to the permeability of the vessels, which is an important factor that allows metastasis. Altogether, our findings demonstrate the usefulness of our model to dissect the contribution of different microenvironment components (e.g. ECM density, cancer cells) on LV biology.

Our microfluidic *in vitro* model allowed us to mimic important aspects of the breast tumor microenvironment by including only a few key players in the tumor microenvironment. Future experiments utilizing this model could incorporate stromal cells such as fibroblasts, which are known to influence tumor behavior and LV function. The small number of cells required in our model allows us the potential to use primary patient cells to test translational relevance of our system. In the future, it would be interesting to decouple the effects of matrix density and stiffness on LVs. Taken together, these results demonstrated the capability of our model to investigate the effects of ECM density on LV physiology and tumor-lymphatic crosstalk, which can contribute to the understanding of breast cancer metastasis in the context of ECM mechanics and demonstrates the potential of the model for therapeutic assessment.

In this paper, we elucidated how a dense ECM matrix conditions the lymphatic vasculature toward an activated phenotype through the increase in secretion of chemokines and pro-inflammatory cytokines such as IL-6. Furthermore, we demonstrated how IL-6 secretion exacerbated vessel leakiness in LV monoculture and co-culture with breast cancer cells, both of which were mitigated by blocking the IL-6R. Therefore, our results provide a possible therapeutic target to inhibit breast cancer metastasis by modulating the lymphatic vasculature.

3.5 Acknowledgements

We acknowledge a fellowship from the UW-Madison Graduate Engineering Research Scholars program to KML. We also thank the NIH (R01EB010039 BRG) and the Wisconsin Head & Neck SPORE (P50 DE026787) for funding support. The authors would like to acknowledge the help of Sheena Kerr reviewing the manuscript.

Chapter 4: Primary Head and Neck Cancer Associated Fibroblasts Promote Lymphangiogenesis in a Lymphatic Organotypic Model[3]

Abstract

Head and neck cancer cell metastasis to lymph nodes via lymphatic vessels is a major determining factor of patient outcome. In this type of cancer, a high intratumoral lymphatic density and tumor lymphangiogenesis has been correlated with lymphatic metastasis. Hence, understanding the lymphatic-promoting factors that lead to the presence of a positive lymph node (e.g., lymphangiogenesis), would be beneficial to improve patient outcomes. Within the primary microenvironment, cancer-associated fibroblasts can modulate lymphangiogenesis and its presence has been correlated with lymphatic metastasis. Therefore, a better understanding of how CAFs can modulate lymphangiogenesis, and in turn lymphatic metastasis is needed. To better understand the effect of CAFs in lymphangiogenesis, we used a lymphatic organotypic model to investigate lymphatic vessel conditioning (i.e., lymphangiogenesis) by patient-derived CAFs. Using CAFs from three different patients, different models were developed, in which CAFs were embedded within a 3D matrix surrounding the tubular lymphatic vessel and co-cultured for five days. We demonstrated that our model allows the conditioning of the lymphatic vessels by CAFs, as we observe that the presence of CAFs induced vessel sprouting, altered vessel permeability and angiogenic gene expression profiles. Overall, tumor-induced lymphangiogenesis is a critical component in head and neck tumor metastasis and having a better understanding of the pathways leading to lymphangiogenesis for each patient could potentially provide a therapeutic target.

[3] This chapter has been adapted from the manuscript in preparation: "Primary head and neck cancer associated fibroblasts promote lymphangiogenesis in a lymphatic organotypic model." The manuscript is authored by Karina M. Lugo-Cintrón, María Virumbrales-Muñoz, José M. Ayuso, Mouhita Humayun, Max M. Gong, Suzanne Ponik, Paul M. Harari and David J. Beebe.

4.1 Introduction

Head and neck squamous cell carcinoma (HNSCC) accounts for 90% of the head and neck cancers (HNC), which can be detected at different anatomical sites (e.g., oral cavity and larynx)[227]. In the United States, there will be an estimated 50,000 new cases this year, with a mortality rate of ~20% [1]. Similar to other cancers, distant metastases are a primary cause of death for HNSCC patients, where the spread of HNC cells to lymph nodes via lymphatic vessels is a major determining factor of patient outcome. Specifically, the presence of cancer cells in a lymph node (i.e., a positive lymph node status) is indicative of distant metastasis and has been associated with poor patient prognosis and low survival rates[228,229]. Additionally, a high intra-tumoral lymphatic density and tumor lymphangiogenesis in the primary tumor has been correlated with lymphatic metastasis[50,230]. Therefore, understanding the lymphangiogenic-promoting factors that lead to the presence of a positive lymph node (e.g., lymphangiogenesis), would be beneficial to improve patient outcomes.

Lymphangiogenesis is a multi-step mechanism, requiring the proliferation, migration and sprouting of lymphatic endothelial cells to generate a new lymphatic vessel[231]. Several *in vitro* and animal studies indicate that lymphangiogenesis signaling cascades from the binding of the vascular endothelial growth factor (VEGF) -C/D- to VEGF receptor (VEGFR)-3 [232]. Recent studies have demonstrated the implication of other factors such as cytokines[233], matrix-metalloproteases (MMPs)[234], interstitial flow[235], extracellular matrix (ECM)[234] and changes in cellular metabolism[236,237] in lymphangiogenesis. In addition, during tumor progression, cancer cells produce pro-lymphangiogenic growth factors that lead to tumor-induced lymphangiogenesis and lymphatic vessel remodeling[66]. Cancer cells can also promote lymphangiogenesis by activating fibroblasts (cancer-associated fibroblasts) to secrete pro-

angiogenic factors, such as hepatocyte growth factor (HGF) that leads to lymphangiogenesis [238,239].

In HNC, cancer-associated fibroblasts (CAFs) are the most abundant stromal component within the tumor microenvironment (TME) [9]. Several *in vitro*, *in vivo* and pre-clinical studies have demonstrated that CAFs enhance cancer cell proliferation, invasion, progression, stemness and metastasis, indicating that CAFs are a major contributor in HNSCC metastasis[80,81,240,241]. And, in the context of cancer metastasis, the presence of CAFs is correlated with lymphatic metastasis[242,243]. Therefore, to improve HNSCC patient outcomes, a better understanding of how CAFs modulate lymphangiogenesis, and in turn lymphatic metastasis is needed. To unravel these mechanisms and determine potential pharmacological targets, a model that allows the investigation of tumor-induced lymphangiogenesis within a relevant TME would provide more in-depth insight into current knowledge, therefore, advancing translational HNSCC research.

The spectrum of current lymphatic models ranges from 2D/3D *in vitro* cultures to *in vivo* animal and human subjects[83]. Conventional *in vitro* cultures offer simplicity and the greatest experimental control of parameters and readouts, but do not incorporate physiological components. On the other hand, the dynamic nature of animal and human subjects diminishes experimental tractability. Microscale organotypic models bridge the gap between these conventional approaches, these models are *in vitro* models that recapitulate *in vivo* 3D geometries and interactions, allowing precise interrogation of microenvironmental conditions. Recently, the use of microscale organotypic models has been used to include patient-specific cells, demonstrating a viable approach for examining patient-specific gene expression alterations and to examine response to anti-angiogenic therapies[97]. Therefore, the use microscale organotypic models

would be beneficial to improve the precision medicine approach that takes in consideration how patient-specific CAFs induce changes in lymphangiogenesis and angiogenic gene expression.

In this chapter, we developed a lymphatic organotypic co-culture model to investigate lymphatic vessel conditioning by HNSCC patient-derived CAFs. For this, patient-derived CAFs were successfully isolated from three different HNSCC patients where the CAFs phenotype was verified by gene expression analysis. Then, patient-derived CAFs were embedded within a 3D matrix and a tubular lymphatic vessel model was co-cultured with CAFs for five days. We demonstrated that in our model, lymphatic vessels are conditioned by CAFs as evidenced by increased angiogenic sprouting and permeability. Gene expression analysis of lymphatic cells co-cultured with patient-specific CAFs revealed differential dysregulation of angiogenic genes as compared to lymphatic cells in monoculture, with patient-specific profiles unique to each patient. Additionally, we found that some of the dysregulations in angiogenic genes are common across the different patients. Overall, these results demonstrate the utility of our model for elucidating patient-specific mechanisms of tumor-induced lymphangiogenesis and informing relevant therapies.

4.2 Materials and Methods

4.2.1 Head and Neck Cancer Patient Sample Processing

All patient resection samples were provided by the Translational Science Biocore according to University of Wisconsin IRB protocol 2016-0934. Resected samples were maintained in transport media (DMEM basal media with gentamycin, amphotericin, and penicillin streptomycin at 1% v/v each) prior to processing. Processing of a sample for enzymatic digestion was performed as

follows: Samples were cut to pieces of 1-2 mm width using a sterile scalpel and tweezer. Cut pieces were transferred to a 15 mL conical tube containing digestion media (6 mL of transport media with 0.1% collagenase (Thermo-Fisher, 17100017), 0.1% hyaluronidase (Sigma, H3506), and 0.02% DNAse (Roche, 04716728001)). The tube with the digestion mixture was attached to a rotating platform in an incubator and incubated overnight at 37^{o}C. Following overnight digestion, cells were isolated from the digested sample. To that end, enzymatic activity was neutralized by adding 6 mL of primary HNC media (DMEM with 10% FBS, 1% penicillin streptomycin, 1 µg/mL hydrocortisone, 10 µg/mL bovine insulin, and 50 ng/mL EGF). Then, the digested sample was filtered into a new 50 mL conical tube using a 40 µm cap filter. Filtered debris in the cap filter was collected and cultured with primary HNC media in a separate flask and the filtrate was centrifuged at 400 g for 10 min. The cell pellet was washed with 10 mL of PBS and centrifuged at 300 g for 3 min, and the PBS supernatant was removed. Cells were resuspended with primary HNC media for culture in a T25 cm^2 flask. Cultured cells were expanded into a new T75 cm^2 flask (Corning, CLS430641U), depending on confluency after 7-10 days. After cell expansion in the T75 cm^2, fibroblasts were removed by trypsinizing (0.25% trypsin) the culture at room temperature for a few minutes using cold trypsin, where fibroblasts detach faster than epithelial cells as previously described[244]. This step was done multiple times until the fibroblast population was recovered from the flask. The recovered fibroblasts were then cultured and expanded in a T75 cm^2 using fibroblast media (described in the next section).

4.2.2 Cell culture

Human lymphatic endothelial cells (HLECs, ScienCell, 2500) were cultured in standard cell culture flasks (Corning, 430641U) coated for 30 min at room temperature with fibronectin (Sigma Aldrich, F1141-5MG, diluted to 5 µg/cm^2 with distilled 1X PBS,) at a starting cell concentration

of $5 \cdot 10^5$ cells as per supplier instructions . Cultures were maintained with endothelial basal medium-2 (Lonza, CC-3156) supplemented with EGM-2 MV SingleQuot Kit (Lonza, CC-4147), referred as endothelial media through the text. HLECs were cultured to 90-95% confluency at passage 3 for all experiments. Head and neck fibroblasts were routinely cultured in high glucose DMEM (Gibco, 11965092) supplemented with 5% fetal bovine serum (FBS, VWR, 97068-085), 1% penicillin/streptomycin (ThermoFisher, 15140-122), 1% sodium pyruvate (Lonza, 13-115E) and 1 μg/mL hydrocortisone (StemCell, 07925). All cultures were kept in a humidified incubator at 37ºC with 5% CO_2.

4.2.3 Device Fabrication

Fabrication of the PDMS microdevice was performed as previously described[185]. The microdevice consists of two PDMS layers, which define the microchamber; and a suspended PDMS rod, which is removed after polymerization of a hydrogel in the main chamber to create a tubular lumen structure. In order to fabricate the top and bottom layers of the microdevice, a traditional soft lithography technique was used, in which the layers were spun using SU-8 (MicroChem, Y13273) to create the silicon master molds. Polydimethylsiloxane (PDMS, Dow Corning, Sylgard 184) was mixed at a 10:1 base to curing agent ratio and poured over the SU-8 silicon master molds. Using the same PDMS mixture, PDMS rods were fabricated by filling up a 25 gauge (Fisher Scientific, 14-840-84) hypodermic needle with PDMS. PDMS components were then baked at 80°C for 4 h. After baking, the PDMS rods were extracted from the needles, yielding PDMS rods of 280 μm in diameter. The two layers were aligned, ethanol bonded together and the PDMS rods were placed into the microdevice chamber. Finally, the microdevice was oxygen plasma bonded to a glass-bottom MatTek dish (MatTek Corporation, P50G-1.5-30-F), following

a general protocol. The microdevices were sterilized using UV irradiation for 15-20 min for further use.

4.2.4 Organotypic Co-Culture Preparation

4.2.4.1 Device preparation

To achieve maximum hydrogel adhesion to the PDMS chamber, a solution of 2% poly(ethyleneimine) (PEI, Sigma-Aldrich, 03880) diluted in deionized water was loaded into the side ports and incubated for 10 min. Subsequently, PEI was aspirated and a 0.4% glutaraldehyde (GA, Sigma-Aldrich, G6257) solution in deionized water was loaded into the side ports and incubated at room temperature for 30 min. During the GA incubation, the collagen solution was prepared on ice (refer to the next section). After the 30-min of GA incubation, the microdevices were washed three times with sterile deionized water to remove any GA excess.

4.2.4.2 Collagen hydrogel preparation and loading into the device

High-density rat-tail collagen type 1 (Corning, 354249, referred to as collagen through the text) was diluted with 5X PBS and neutralized with 0.5 M NaOH (Fisher Scientific, S318) achieving a final concentration of 1X PBS, and a pH of 7.4. Final concentration of 3 mg/mL collagen type I, was achieved through the addition of fibrinogen (Sigma-Aldrich, F8630), fibronectin (Sigma-Aldrich, F1141) and fibroblast media. For co-culture experiments, fibroblasts were added in the fibroblast media. Fibroblasts were diluted to a final concentration of 250 cells/µL (final volumes are detailed in Table 4.1). Right after the washes with distilled water, 6 µl of the collagen solution was loaded through the side ports and polymerized at room temperature for 10 min. Finally, a droplet of media (5 µL) was placed on top of the side ports to prevent evaporation and sacrificial phosphate buffered saline (PBS) was added around the side of the MatTek dish. Finally, devices were transferred to 37oC for 1 hour to allow collagen to fully polymerize.

Table 4.1. Recipes for different collagen matrices

	Lymphatic Vessels monocultures **(µL)**	Lymphatic Vessels co-cultures **(µL)**
Collagen gel[a] (µL)	80	80
5x PBS (µL)	20	20
0.5 M NaOH (µL)	3	3
1 mg/mL Fibrinogen[b] (µL)	11.7	11.7
100 µg/mL Fibronectin[c]	13.4	13.4
250 cells/µL Cell suspension[d]	---	58.4
Fibroblasts media	108.6	50.2

[a]Stock concentration of 10.76 mg/mL
[b]Stock concentration of 20 mg/mL
[c]Stock concentration of 1 mg/mL
[d]Initial concentration 1,000 cells/µL

4.2.4.3 Lymphatic endothelial cell seeding in lumens

After incubation, a small drop of media (5 µL) was added to the input port under sterile conditions. The rod was removed by pulling through the output port using sterilized tweezers. Following rod removal, the hollow tubular structure remained filled up with media within the collagen matrix. All fluid handling procedures were conducted with standard pipettes, leveraging the passive pumping mechanism uniquely enabled by the microdevice design [128]. Lymphatic endothelial cells (HLECs) were trypsinized with 0.05% Trypsin-EDTA (ThermoFisher Scientific, 25300062), resuspended in endothelial media at 20,000 cells/µL and seeded into the lumens (4 µL per lumen). HLEC-filled lumens were incubated at 37°C for 2 h to allow for cell attachment, flipping devices every 25 min to ensure homogeneous cell coverage of the lumen wall. After 2 h, lumens were supplemented with 10 µL of endothelial media and cultured overnight at 37°C. Cultured vessel media was refreshed twice a day by flowing endothelial media three times through the lumen to remove dead cells.

4.2.5 Immunofluorescence staining and imaging

During immunofluorescence staining, cells were washed with PBS for 30 min between each step using washing buffer (0.1% Tween 80 (Sigma-Aldrich, P1754) in PBS). Unless specified otherwise, steps took place at room temperature. Cells were fixed with 4% paraformaldehyde (PFA) (EMScience, 15700) for 15 min, then incubated with 0.2% Triton® X-100 (MP Biomedicals, 807426) for 30 min for permeabilization. Finally, vessels were incubated with 10 μL of blocking buffer (3% Bovine Serum Albumin (BSA, Sigma-Aldrich, A9056) in 0.1% PBS-Tween 80) at 4ºC overnight.

Primary antibody mouse anti-CD31 (Abcam, ab9498) was diluted (1:50) with staining buffer (blocking buffer supplemented with 1% Tween 80 in PBS at 10:1 v/v), whereas secondary antibodies were diluted using staining buffer supplemented with 10% goat serum to reduce unspecific binding. Vessels were incubated with primary antibodies at 4ºC overnight. Then, vessels were incubated with the secondary antibodies for 2 hours, Alexa Fluor 647 anti-mouse (Abcam, ab150115). Stained vessels were washed over two days with the washing buffer and stored in sterile PBS until imaging. Texas Red-X Phalloidin (ThermoFisher Scientific, T7471) and DAPI (ThermoFisher Scientific, D3571) were used to stain actin cytoskeleton and nuclei, respectively. Fluorescent images were acquired at 10X using a Nikon TI® Eclipse inverted microscope (Melville, New York) and processed using the National Institutes of Health Fiji software [122]. Confocal images were acquired using a Leica SP8 3X STED Super-resolution microscope (Wetzlar, Germany) in the UW-Madison Optical Imaging Core.

4.2.6 Fluorescent image quantification

For all images, background subtraction was performed. To quantify sprout length in each vessel, a projection of every 10 Z-planes from each Z-stack image was performed. In each Z-projection, each sprout was traced from which the length was measured.

4.2.7 Dextran diffusion assay

The permeability of the lymphatic vessels was measured by dextran diffusion assays using Texas Red dextran (70kDa, ThermoFisher Scientific, D1830) prepared in PBS to 1 μM. For each replicate, 3 μL of dextran solution was added to the vessel such that fluid was flush with the lip of the ports to minimize flow from a pressure head. Diffusion was measured over 15 minutes per vessel. Permeability coefficients were calculated using equation 1[123]:

$$P = (1/I_o)[(I_f - I_o)/(t_f - t_o)](D / 4), \qquad \text{Eq. 1}$$

where I_o is the total initial intensity outside the vessel, I_f is the total intensity outside the vessel at 15 minutes, t_o is the initial time point, t_f is the final time point of 15 minutes, and D is vessel diameter. All vessels were imaged using a Nikon TI® Eclipse inverted microscope (Melville, New York), and maintained at 37 ºC and 5% CO_2 by a stage-top incubator (Okolab, Italy).

4.2.8 Verification of CAFs phenotype via qPCR

RNAs were extracted from cells seeded in a confluent 60-mmculture dish. mRNA was isolated in 15 μL 10 mM Tris buffer using Dynabeads mRNA DIRECT Purification Kit (Invitrogen, #61011) per the manufacturer's instructions. Immediately following mRNA isolation, a reverse transcription reaction was run using iScript cDNA Synthesis kit (Bio-Rad, #170-8891). Custom

qPCR primers (Biorad) were used for the genes presented in Table 4.2, where primers are also detailed. Screened and reference (housekeeping) genes are detailed in Table 4.2.

Table 4.2. Primers used for CAFs identification

Primer	Fluorescence
GAPDH	Vic
HPRT	Vic
PO	Vic
Coll I	Fam
Vim	Fam
EPCAM	Fam

GAPDH, HPRT and PO were used for normalization of the data. Finally, qPCR reactions were run using Light cycler 480 probes master mix (Roche 04887301001) in Roche's Lightcycler 480 II (Roche Molecular Systems, Indianapolis, IN). Target gene expression was normalized using the geometric mean of the mentioned reference genes. Relative gene expression fold changes were determined using the $2^{-\Delta\Delta Ct}$ method compared to the reference genes.

4.2.9 RT-qPCR

RT-qPCR was used to analyze the changes in expression of multiple genes related to angiogenesis in lymphatic cells as a result of the co-culture with head and neck primary fibroblasts. Briefly, after 5 days of co-culture in the microfluidic device, the collagen hydrogel was digested using 6 mg/mL collagenase type I solution (Thermo-Fisher, 17100017) to separate the cells from the matrix. Lymphatic cells were positively isolated from the fibroblasts using the Dynabeads® CD31 Endothelial Cell (ThermoFisher Scientific, 11155D). Then, lymphatic cells were lysed, and mRNA was isolated using the Dynabeads™ mRNA DIRECT™ Purification Kit (ThermoFisher Scientific, 61011) as previously described[97]. mRNA was retrotranscribed to cDNA using the RT2 PreAMP cDNA Synthesis Kit (Qiagen, 330451) with the RT2 Nano PreAMP Primer Mix- Angiogenesis pathway (Qiagen, 330241). cDNA was analyzed by RT-qPCR using a Qiagen RT2 profiler custom

panel (Qiagen, PAHS-024ZA) and data was analyzed using the Qiagen online software (http://pcrdataanalysis.sabiosciences.com/pcr/arrayanalysis.php).

4.2.10 GSEA

We used the upregulated genes identified via qPCR with GSEA to perform a gene set enrichment analysis. GO term p-values were acquired and are presented as -log10.

4.2.11 Statistical analysis

All the experiments were repeated in three independent experiments. All results are presented as the mean ± standard deviation of the mean (S.E.M.). Data were analyzed using GraphPad Prism 8 (GraphPad Software) and statistical significance was set at $p < 0.05$. One-to-one comparisons were performed with an unpaired Student t-test with Welch's correction (in case of variance in homogeneity) after the normal distribution was proved via Shapiro-Wilk test. If the normality test was not passed, a non-parametric test was performed (Mann-Whitney test) Comparisons among multiple groups were performed using One-way ANOVA with post-hoc Dunnett test.

4.3 Results

4.3.1 Development of the HNSCC patient-specific CAF-lymphatic co-culture microfluidic model

To investigate the effect of HNSCC patient specific-CAFs on the lymphangiogenic response of HLECs we adapted a recently published and validated *in vitro* model that recreates physiological aspects of the lymphatic vasculature. Aspects such as lymphatic specific markers, leaky lumen structure and differential protein secretion that are characteristics of the lymphatic vasculature as compared to blood vessels[184]. Briefly, the device consists of a chamber that is filled with a solution of unpolymerized collagen type I hydrogel with a PDMS rod suspended in the chamber

that is removed after collagen polymerization (Figure 4.1A-B). Once the rod is removed, the lumen structure is loaded with commercially available primary human endothelial cells (HLECs) and after an hour cells are attached to collagen, resulting in the cell lining in the wall of the lumen. After 5 days of culture, lymphatic vessel has a confluent endothelial monolayer (Figure 4.1B). As we previously demonstrated, the model allows the incorporation of stromal components such as fibroblasts embedded in a collagen matrix.

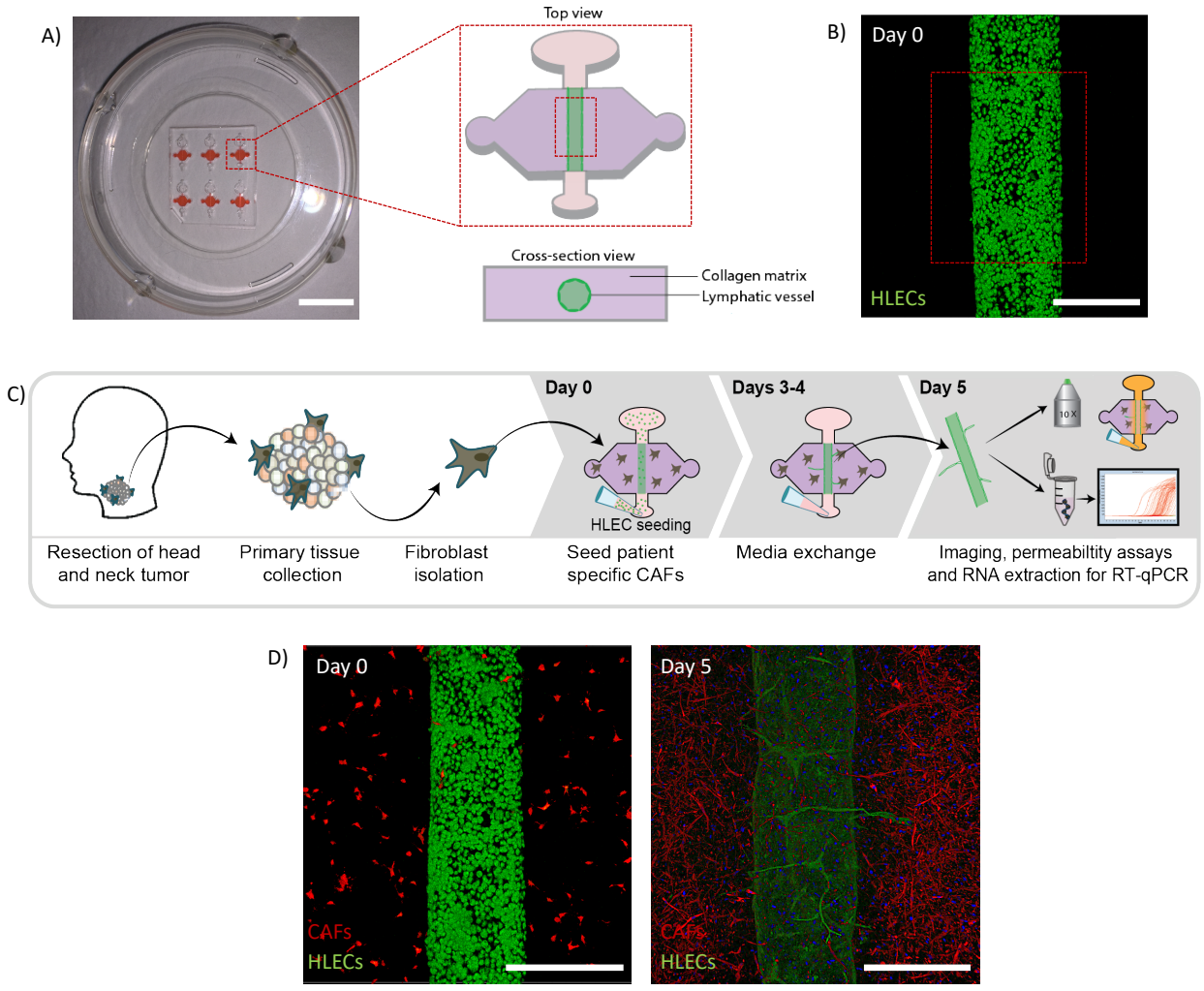

Figure 4.1: Image of the model and schematic of methodology. A) Photography of the microdevice with schematic of the microdevice. Top view and cross-section view of the devices are shown. **B)** Lumen with lymphatic endothelial cells (HLECs) attached at day 0, which generate the lymphatic vessel. **C)** Schematic of the process, from collecting a primary sample to incorporating the isolated cancer-associated fibroblasts in the collagen matrix surrounding the lymphatic vessel. **D)** Lumen with HLECs attached in the lumen (green) surrounded by cancer-associated fibroblasts (red) isolated from patient 1 at day 0 (left) and at day 5(right). Scale bar= 250 µm

To incorporate CAFs in the matrix, biopsy samples were collected. To harvest HNSCC patient-derived CAFs, biopsy samples from three patients with HNSCC were collected from the tumor tissue and normal adjacent tissue (Figure 4.1C), from which tumor grade and lymph node status was different for each patient (Table 4.2). Briefly, samples were mechanically dissociated and enzymatically digested. All cells from the tumor tissue were cultured and expanded in a standard cell culture flask (T75).

Table 4.3. Patients tumor stage and lymph node status

Patient	Primary tumor classification	Lymph node status
1	pT4a	pN2b (positive)
2	pT4a	pN0 (negative)
3	pT2	pN1 (positive)

To isolate CAFs, cell trypsinization at room temperature was performed multiple times due to the lack of specific and unique CAF markers, this led to CAFs detachment and not the epithelial population of the tumor tissue. CAFs were then expanded and frozen at the same passage number to be used for further experiments. To verify the fibroblast and to confirm the population of CAFs, RT-qPCR was performed for a set of genes that are characteristic of CAFs (i.e., collagen Ia, vimentin) in the cultured cells and a negative control (i.e., EpCAM) was used to demonstrate that these cells are not epithelial cells. Results revealed expression of collagen 1a and vimentin in the samples from the three different patients and, no expression of EpCAM was observed (Figure 4.2).

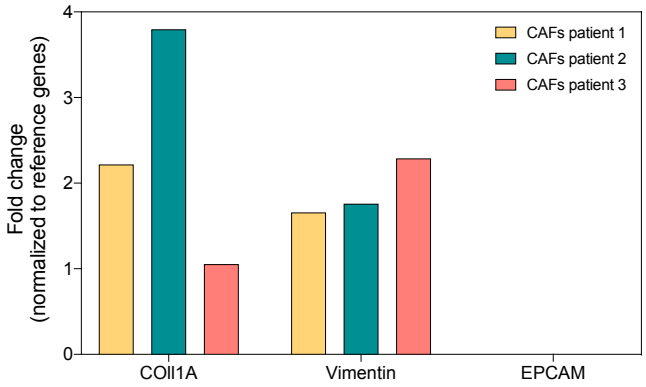

Figure 4.2: Preliminary patient-derived CAFs characterization. N=1.

After positive fibroblast identification, CAFs were embedded within the collagen matrix surrounding the lumen, which was then lined by lymphatic endothelial cells, mimicking what is found *in vivo* (Figure 4.1C). Following an hour of co-culture, the model shows lymphatic endothelial cell attachment into the tubular structure with no matrix invasion and CAFs in the surrounding matrix (Figure 4.1D). After 5 days of co-culture, sprouts can be observed in the lymphatic lumens (Figure 4.1D). Overall, patient-derived CAFs were successfully isolated and cultured in the lymphatic microfluidic model.

4.3.2 Co-culture with HNSCC patient-derived CAFs induce lymphatic vessel sprouting

Lymphatic vessels were co-cultured with HNSCC patient-specific CAFs from three different patients to evaluate CAFs influence in tumor-induced lymphangiogenesis and vessel remodeling, that could in turn lead to HNC metastasis (Figure 4.3A). Qualitatively, endothelial sprouts are selectively stained with CD31 and are shown invading the matrix in the co-cultures (Figure 4.3C-E) more than in monocultures (Figure 4.3B). Thereafter, vessel sprouts were counted, as a readout of lymphangiogenesis. Interestingly, for the lymphatic monoculture, single cell migration is observed, but not vessel sprouting (Figure 4.3 B). Conversely, in the co-cultures, vessel sprouts

are observed (Figure 4.3C-E). Specifically, heterogeneity in angiogenic sprouting induced by CAFs from different patients was observed.

First, we measured the length of sprouts per vessel. In the HLEC monoculture, the average sprout length was 126.4 ± 39.9 μm. In the co-cultures, the average sprout length increased to 233.2 ± 97.8 μm for patient 1, 230.9 ± 90.0 μm for patient 2 and 187.0 ± 53.4 μm for patient 3, revealing a significant increase in sprout length when comparing the co-cultures with the HLEC monoculture (***P<0.0001 via one-way Anova) (Figure 4.3F). When comparing the sprout length between patients, sprouts of patient 1 and patient 2 where significantly longer than patient 3 (**P=0.0018 and **P=0.0075, respectively). Next, we quantified the number of sprouts per vessel to determine if there was a difference in the incidence of vessel sprout between patients. For this, the number of sprouts was quantified, sprouts longer than the average length of HLEC monoculture (126 μm) were considered since we wanted to exclude the potential to quantify single cell migration observed in the monoculture.

In the HLEC monoculture, the average number of sprouts was 4.8 ± 1.2. In the co-cultures, the average number of sprouts was increased to 18.0 ± 2.5 for patient 1, 11.0 ± 1.1 for patient 2 and 10.5 ± 1.1 for patient 3, revealing a significant increase in sprouts when comparing the co-cultures with the HLEC monoculture (***P<0.0003, **P=0.0011, **P=0.0016, respectively) (Figure 4.3G). When comparing the number of sprouts among patients, the number of sprouts of patient 1 was significantly higher than patient 2 and patient 3 (*P=0.0234 and **P=0.0160, respectively). Therefore, we observe heterogeneity in the length of vessel sprouts and the number of sprouts. between the co-cultures with CAFs from different patients.

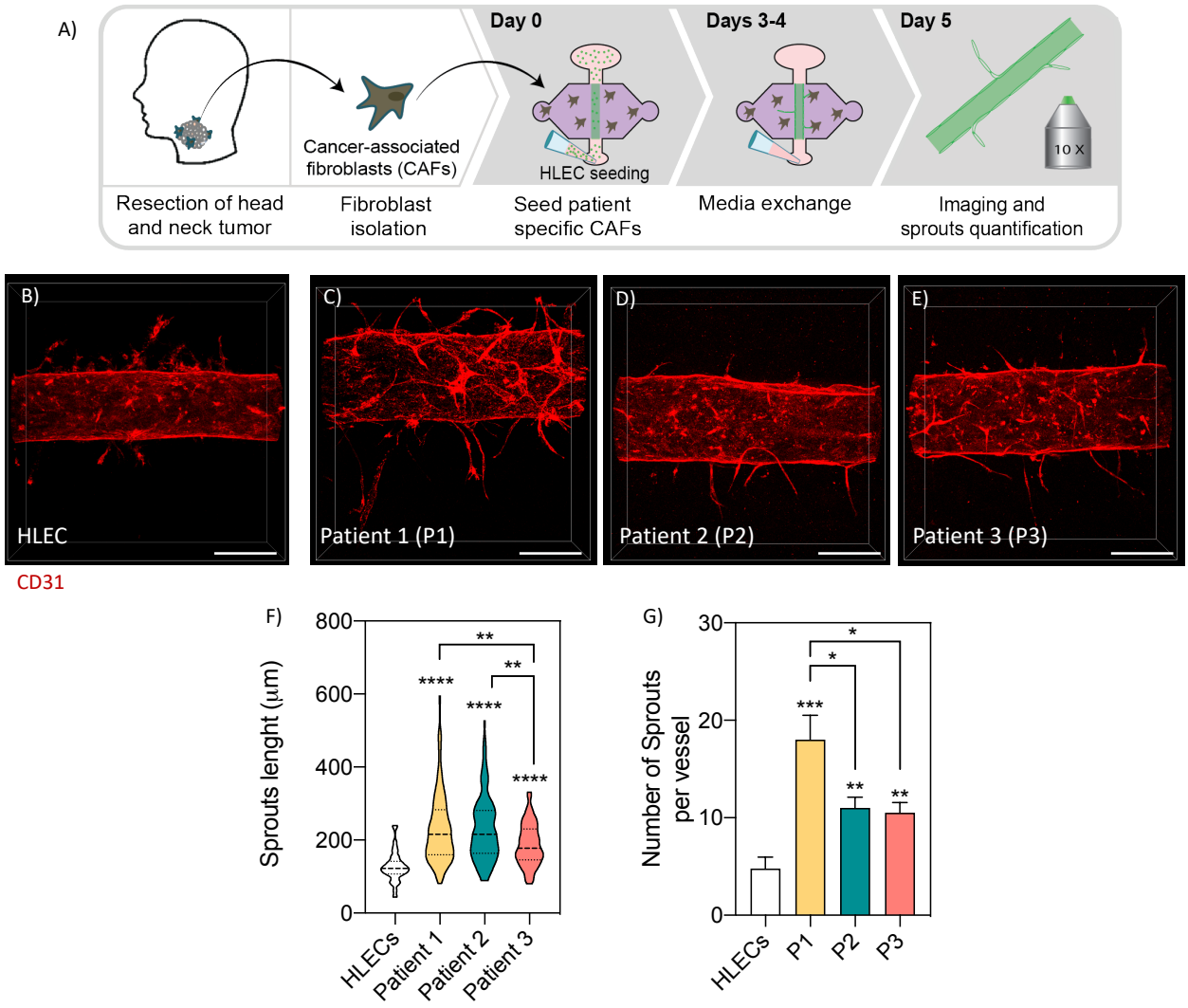

Figure 4.3: Lymphatic vessel sprouting induced by HNSCC patient-derived CAFs. A) Schematic indicating the seeding procedure and imaging. **B-E)** CD31 stained lymphatic **B)** monoculture and co-culture with CAFs from **C)** Patient 1, **D)** Patient 2 and **E)** Patient 3. **F)** Sprouts length. **G)** Number of sprouts per vessel. n= 12 lumens from at least 3 independent experiments. Bars represent average ± S.E.M. Scale bar= 250 µm *p ≤ 0.05, **p ≤ 0.01, ***p ≤ 0.001, ****p ≤ 0.0001.

4.3.3 Co-culture with HNSCC patient-derived CAFs alter lymphatic vessel permeability

Lymphangiogenesis, in addition to vessel sprout formation, is associated with a decreased vessel integrity, which leads to an increased permeability to solutes. In the context of metastasis, the mentioned vessel characteristics have been associated with the potential to facilitate metastasis[245]. For this reason, we assessed the barrier function of cultured vessels by diffusion assays using 70 kDa-Texas Red dextran (Figure 4.4A), which is representative of proteins such as

serum albumin (~67kDa). Briefly, the solution of dextran was perfused through the lumen and tracked using time-lapse fluorescent microscopy for 15 min. Representative image and diffusion profile of the monoculture (Figure 4.4B) at time 0 min and after 15 min of dextran perfusion shows that the dextran was contained to the lumen region at time 0 min in the monoculture and was mostly retained in the lumen after 15 min. For the monoculture example, the diffusion profiles show that ~20% of the dextran diffused into the matrix.

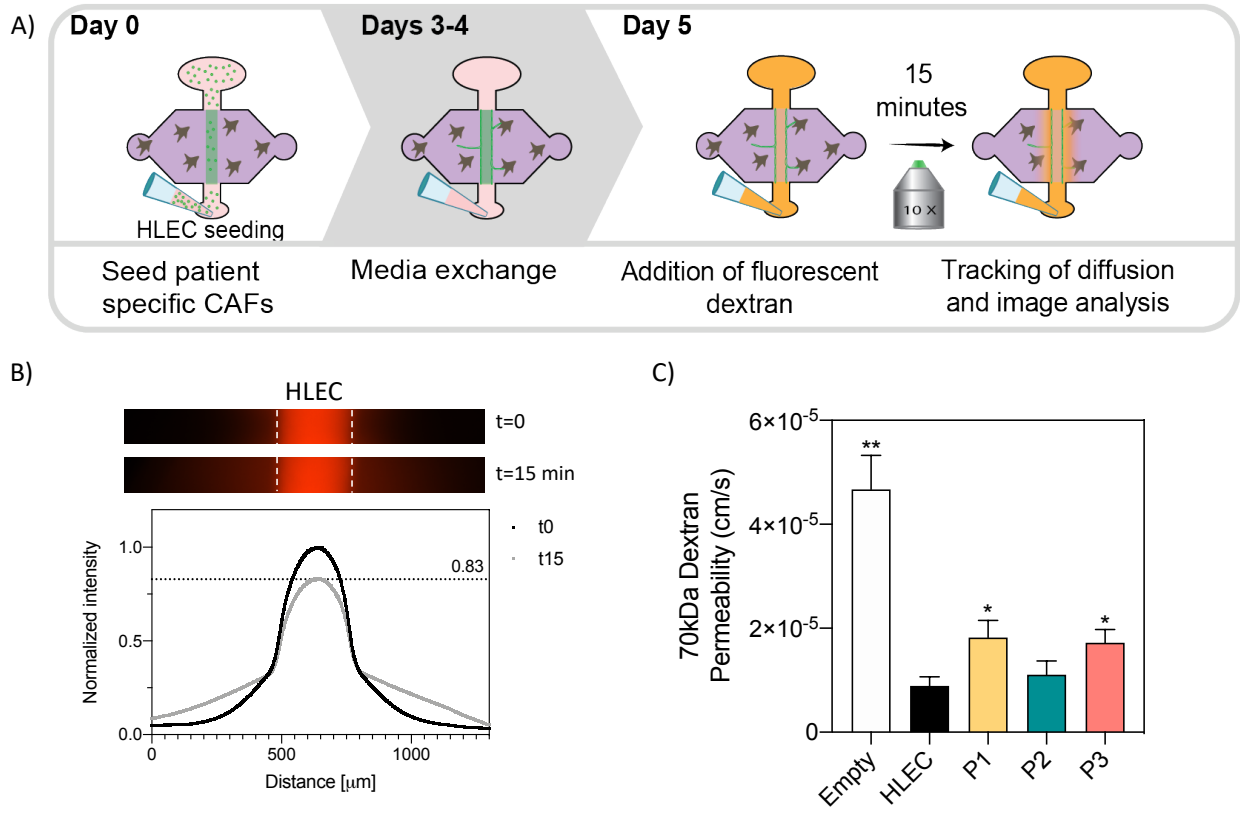

Figure 4.4: Lymphatic vessel permeability in monoculture and co-culture with HNSCC patient-derived CAFs. **A)** Schematic indicating the seeding procedure and dextran diffusion assay for permeability calculation. **B)** Representative images of 70 kDa dextran diffusion in lymphatic monoculture (HLEC). **C)** Permeability values calculated for an empty lumen structure, lymphatic vessel monoculture and co-cultures with CAFs and were compared to the lymphatic vessel monoculture (as calculated via multiple t-tests). n= 12 lumens from at least 3 independent experiments. Bars represent average ± S.E.M. *$p \leq 0.05$, **$p \leq 0.01$.

For a more detailed quantification, we calculated the permeability coefficient for the lymphatic vessel monoculture, co-cultures and an empty lumen (cell-free collagen hydrogel

tubular structure) (Figure 4.4F) according to equation 1. The quantification revealed that lymphatic vessel monoculture has an average permeability of $0.8 \pm 0.2 \cdot 10^{-5}$ cm/s. Compared to lymphatic vessel monoculture, patient 1 and patient 3 have significant higher permeability values, $1.8 \pm 0.3 \cdot 10^{-5}$ cm/s and $1.7 \pm 0.3 \cdot 10^{-5}$ cm/s respectively(*P=0.0237 and *P=0.0159, respectively). Interestingly, the permeability of patient 2 was similar as the lymphatic vessel monoculture, $1.1 \pm 0.3 \cdot 10^{-5}$ cm/s. On the other hand, empty lumens show a significant increase in permeability $4.6 \pm 0.6 \cdot 10^{-5}$ cm/s compared to lymphatic vessel monoculture (**P=0.0080), demonstrating that the lymphatic endothelium model exhibits a barrier function. Taken together, these results demonstrate the ability of HNSCC patient-derived CAFs to alter the permeability of the lymphatic vessels and how the changes are dependent on the patients.

4.3.4 HNSCC patient-derived CAFs induce gene-expression changes in lymphatic vessels

Next, we sought to determine the expression differences among patients leading to a phenotypically different lymphatic vessel sprouting and changes in vessel permeability. For this, lymphatic vessels were cultured for five days and the expression of 84 genes related to angiogenesis was analyzed in the lymphatic vessels specifically (i.e, both seeded in monoculture and in co-culture). The unsupervised expression of the 84 genes is presented (Figure 4.5), revealing that lymphatic vessels have a distinct gene expression profiles compared to lymphatic vessel co-cultures.

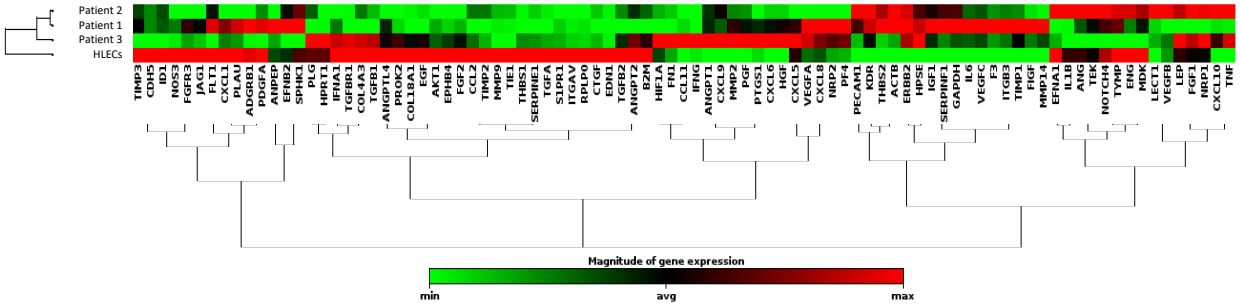

Figure 4.5: Unsupervised clustergram analysis of qPCR from lymphatic vessel co-cultured with different CAFs normalized to correlative lymphatic vessel monocultures. N=3 independent experiments per patient with 4 pooled lumens each

Regarding gene ontology in the clustergrams, we observe how patient 1 and patient 2 group are more closely related, and farther than patient 3 and lymphatic monoculture. Then, we identified the significantly changed genes and presented them in clustergrams for each patient (Figure 4.6A-C). When observing the clustergrams for each patient, a size difference is noticeable where patient 1 has 24 significant genes (Figure 4.6A), patient 2 has 18 significant genes (Figure 4.6B) and patient 3 has 16 genes (Figure 4.6C).

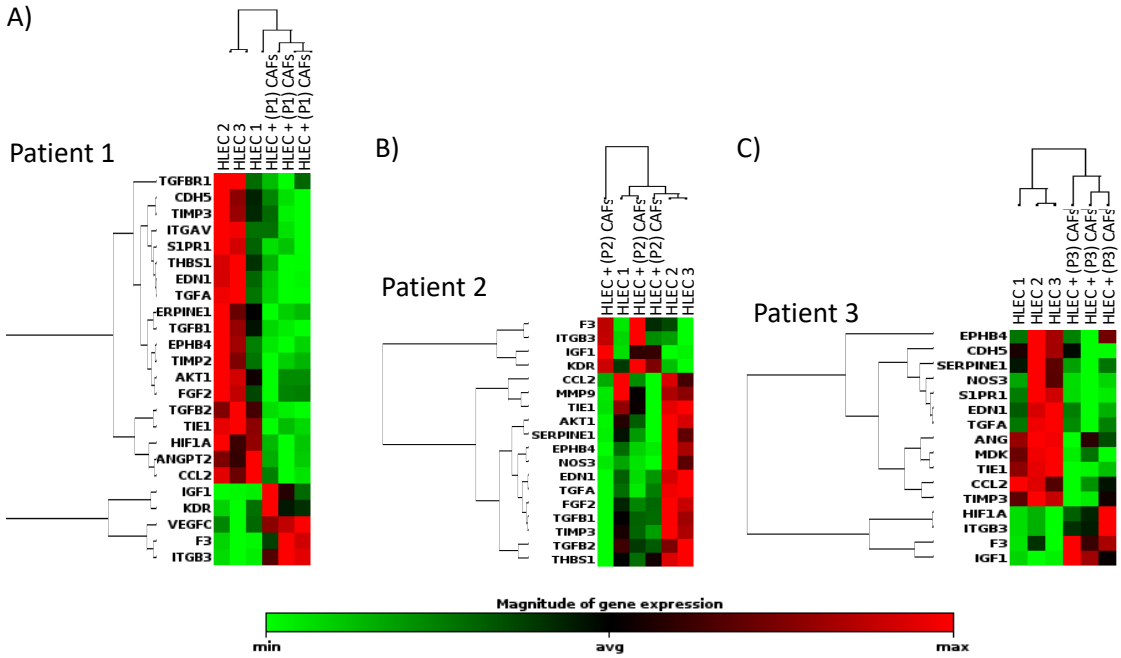

Figure 4.6: Unsupervised clustergrams analysis showing significant changes for each patient. Clustergrams were produced using genes showing significant changes for each patient. **A)** Patient 1. **B)** Patient 2. **C)** Patient 3.

The expression of the significantly dysregulated genes from each patient is presented in a single clustergram summarizing the control and all three patients (Figure 4.7A). This patient-focused clustergram revealed the same results as the complete 84 gene expression clustergram previously presented where lymphatic vessels have a distinct gene expression profiles compared to lymphatic vessel co-cultures. Using the gene expression data, we performed quantitative analysis for each patient in which we plotted the fold change of the significantly dysregulated genes for each patient (Figure 4.7B-D). Although we observed that the composition of the gene expression profiles is different for each patient, we observe some upregulated and downregulated genes in common between patients 1, 2 and 3. For example, the most upregulated angiogenesis driver gene in all patients is IGF1. In addition, we observe an upregulation in different angiogenic genes for each patient. We observed an upregulation for VEGF-C (2.1 ± 0.4-fold change) in patient 1(Figure 4.7B) and an upregulation for KDR (2.0 ± 0.3-fold change) in patient 2 (Figure 4.7C).

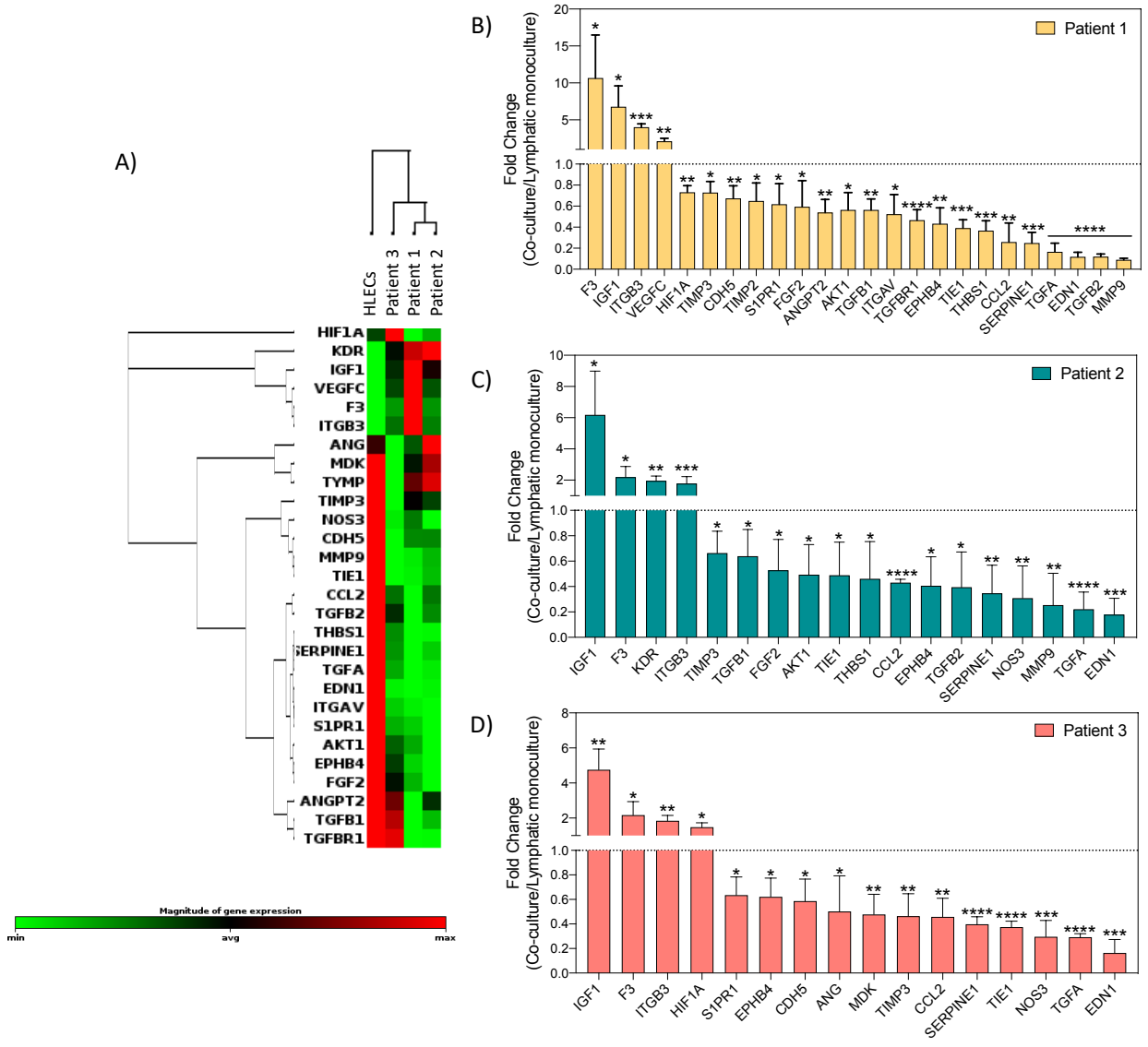

Figure 4.7: Results of qRT-PCR analysis for genes that significantly changed. A) Unsupervised clustergrams were produced using only those genes showing significant changes. N=3 independent experiments per patient with 4 pooled lumens each. B-D) Significant changes in gene expression for each patient were plotted for patients 1, 2, and 3 to reflect the direction of the change. Bars represent average ± S.D. $p \leq 0.05$, $^{**}p \leq 0.01$, $^{***}p \leq 0.001$, $^{****}p \leq 0.0001$.

For a more in-depth analysis of the profiles, we classified shared and private dysregulated genes using a Venn diagram (Figure 4.8A), where the upregulated genes are shown in red. In the Venn diagram we can observe that the conditioning of the CAFs from different patients resulted in having ten shared dysregulated genes. We can also observe that patient 1 and patient 2 share six genes and that patient 1 and patient 3 share only two genes. From the shared genes in all patients,

we identified two upregulated and downregulated genes of interest (Figure 4.8B). For the upregulated genes, insulin like growth factor 1(IGF1) has been found to induce cell migration and has a pro-angiogenic role[246]. In patient 1 and patient 2, IGF had an increase of ~6-fold change as compared to lymphatic vessel monoculture (*P=0.0455 and *P=0.0330, respectively) and, patient 3 had a 4-fold change (**P=0.0053) (Figure 4.8B-left). Another upregulated gene was integrin beta-3 (ITGB3), which is a pro-angiogenic factor[247]. We observed the higher fold change in patient 1 (4-fold) (***P=0.0004) and a similar fold change was observed in patient 2 and patient 3 (~1.8-fold) (*P= 0.038 and **P=0.0091, respectively) (Figure 4.8B-left). As for the downregulated genes, tissue inhibitor of metalloproteinases-3(TIMP3) and plasminogen activator inhibitor-1(SERPINE1) have been shown to have an anti-angiogenic role[248,249]. In patient 1 and patient 2, TIMP3 was similarly downregulated with a 0.72-fold change (*P=0.0112) and 0.66-fold change (*P=0.0280) respectively (Figure 4.8B-right). Interestingly, patient 3, TIMP3 had a 0.46-fold change (**P=0.0071), lower than in patient 1 and patient 2. As for SERPINE1, patient 1 had a 0.25-fold change, patient 2 had a 0.35-fold change and patient 3 had a 0.40-fold change (***P=0.002, **P=0.0070, ****P<0.0001, respectively) (Figure 4.8B-right).

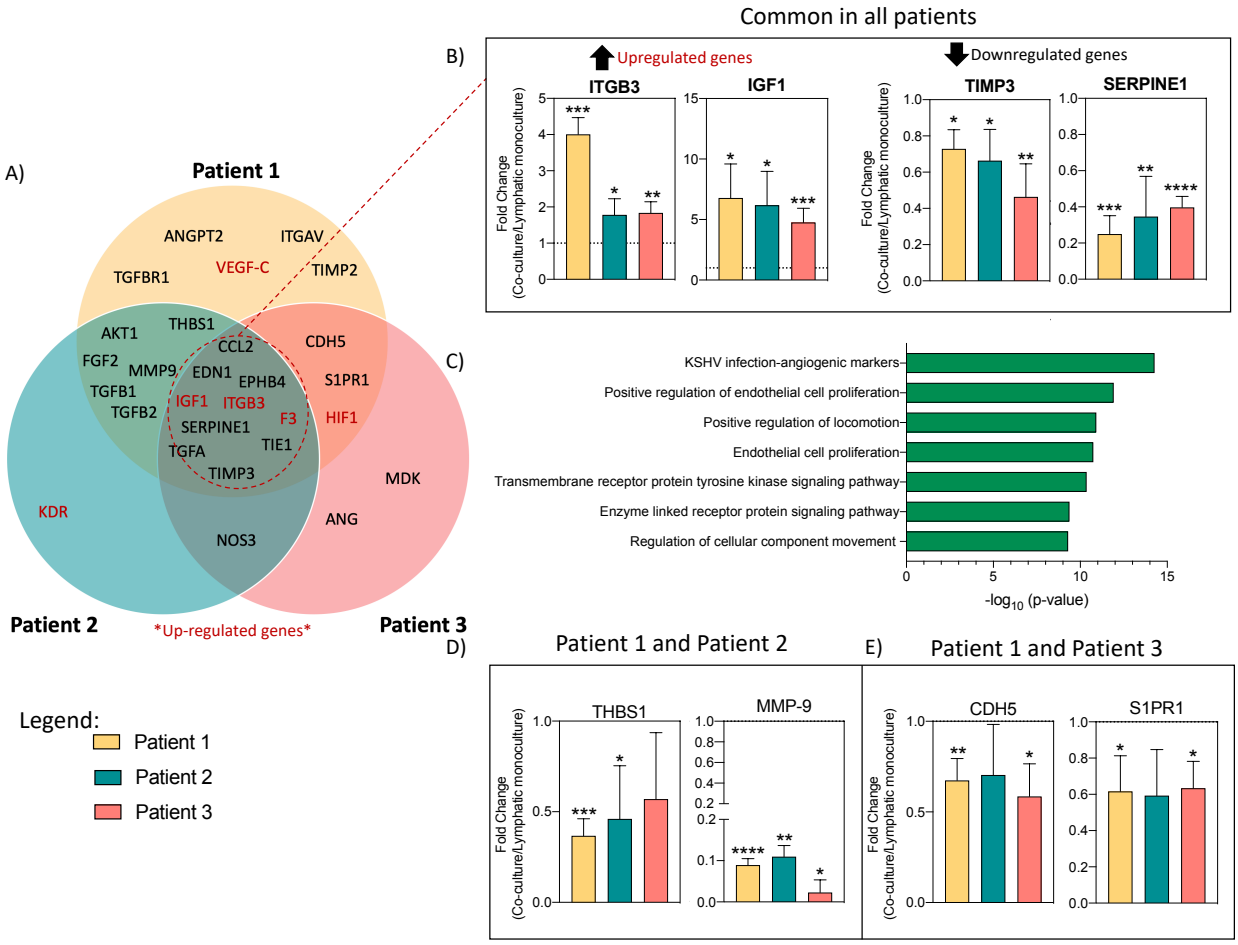

Figure 4.8: Breakdown of gene dysregulation among patients, overlaps and differences. A) Venn-diagram shows that some genes are shared between patients. **B)** Significant changes in gene expression (upregulated and downregulated) in all patients. **C)** Upregulated genes were used to compute expression profiles (GSEA) showed as GO_terms. **D)** Significant downregulated genes of interest in patient 1 and 2. **E)** Significant downregulated genes of interest in patient 1 and 3. Bars represent average ± SD. $p \leq 0.05$, $^{**}p \leq 0.01$, $^{***}p \leq 0.001$, $^{****}p \leq 0.0001$.

Using the upregulated genes from all three different patients we performed a gene ontology (GO) enrichment analysis named GO_terms. The GO_terms provide a defined term representing the gene product properties which covers cellular components, molecular function and biological process (Figure 4.8C). The search revealed GO_terms related to a pro-angiogenic phenotype, such as “KSHVinfection-angiogenic markers”, “Positive regulation of endothelial cell proliferation”, “Positive regulation of locomotion” and “Transmembrane receptor protein tyrosine kinase signaling pathway”. Overall, these results confirm that all HNSCC patient-specific co-culture

models have a pro-angiogenic profile as compared with the mono-culture lymphatic model. Future work will include GO-enrichment profiles for the downregulated gene for each patient to illustrate the inter-patient heterogeneity that is observed in the functional readouts.

Next, we wondered if the dysregulated genes shared by patient 1 and patient 2 explained the changes observed in the functional readouts. For example, we observed an increase in the length of sprouts from patient 1 and patient 2 and we observed that patient 1 had the highest number of sprouts. One of the shared genes between patients 1 and 2 is thrombospondin-1 (THBP1), which is reportedly anti-angiogenic[250]. Interestingly, THBP1 is downregulated in patient 1 and patient 2 (***P=0.003 and *P=0.0335, respectively) (Figure 4.8D). Another gene shared by patient 1 and patient 2 is matrix-metalloprotease-9 (MMP-9), which is reportedly pro-angiogenic[250,251]. We observe a significant downregulation of MMP-9 in all patients, from which the lowest levels where observed in patient 3 (patient 1 ****P<0.0001, patient 2 **P=0.0067 and patient 3 *P=0.0142) (Figure 4.8D). As for genes shared between patient 1 and patient 3, we found that VE-Cadherin (CDH5) is significantly downregulated in patient 1 and patient 3 (**P=0.094 and *P=0.0163, respectively). It is well known that VE-Cadherin is necessary for cell-cell adhesion (Figure 4.8E), and that its downregulation corresponds to one of the first stages of angiogenesis[252,253]. Another common downregulated gene in these patients is the sphingosine-1-phosphate receptor 1 (S1PR1), which is implicated in the regulation of cell-to-cell interactions and has been recognized as an anti-angiogenic[254,255]. Specifically, it is well known that S1PR1 downregulation correlates with a VEGF pathway upregulation. We observe a significant downregulation of S1PR1 in patient 1 and patient 2 (*P=0.0279 and *P=0.0128, respectively) (Figure 4.8E). Although S1PR1 was not significantly downregulated in patient 2, the fold change was similar to patient 2 and patient 3. Taking all the data together, we demonstrated

how patient-specific fibroblasts condition differently lymphatic endothelial cells to promote lymphangiogenesis.

4.4 Discussion

In this chapter, we evaluated the influence of HNSCC patient-derived CAFs from three different patients in lymphatic vessel remodeling (i.e., lymphangiogenesis), that could lead to HNC metastasis. We found that patient-derived CAFs induced a lymphangiogenic response with variable readouts (e.g., sprout length and quantity), consistent with inter-patient heterogeneity. Specifically, we observed that patient 1 and patient 2 had longer sprouts compared to patient 3. On the other hand, we found that vessel permeability increased in patient 1 and patient 3, whereas it was not altered in patient 2, as compared to the lymphatic vessel monoculture. Interestingly, we observed that the changes observed in sprout length go in hand with the patient tumor grade (i.e., patient 1 and patient 3 had higher grade than patient 2) as seen in Table 4.2. As for vessel permeability, the increase in vessel permeability observed in patient 1 and patient 3 correlates with the patient lymph node status, where patient 1 and patient 3 have a positive lymph node status but patient 2 has a negative lymph node status. These results suggest that there is a relationship between tumor grade and vessel sprouting and a relationship between tumor grade and vessel permeability. However, the cohort size is too small to corroborate the relationships.

Recent studies have studied sprouting lymphangiogenesis using microfluidic platforms[117,256]. Yet, to the authors' knowledge this is the first report demonstrating how patient-derived CAFs from HNC patients induce lymphangiogenesis using an organotypic microfluidic model. To explain the changes in the functional readouts and to potentially identify a therapeutic target, gene expression analysis for each patient was performed. Gene expression analysis revealed that lymphatic vessels have a distinct gene expression profiles compared to

lymphatic vessel co-cultures. In the gene expression profiles we observe how patient 1 and patient 2 are ontologically more closely related, and farther than patient 3 and lymphatic monoculture. These results suggest that CAFs derived from patient 1 and patient 2, which had a tumor stage four, share more gene expression similarities with each other than with patient 3. We also observe that the conditioning of the lymphatic vessels by patient-derived CAFs from three different patients share some genes in all patients, but we also observe a distinct expression profile for each patient. Some of the upregulated genes shared by all patients are IGF1 and ITGB3, which are both pro-angiogenic[246,247]. Although these genes are upregulated in all patients, we observe that the level of regulation differs between patients. For example, ITGB3 has a 2-fold change upregulation in patient 1, compared to patient 2 and 3. These results suggest that in patient 1, ITGB3 could be one a key player in the sprouting process. We were interested in the genes shared among patients that could explain the differences in functional readouts. In patients 1 and 2, where we observed the longest sprouts, thrombospondin-1 (THBP1), an angiostatic factor, is significantly downregulated [250]. Therefore, THBP1 downregulation would lead to a more angiogenic phenotype which is consistent with our observations in these patients' specific models. For patients 1 and 3, we observed an increase in vessel permeability. Interestingly, a down-regulation in VE-Cadherin (CDH5) and sphingosine-1-phosphate receptor 1 (S1PR1), which are involved in cell-to-cell adhesions [252–255]. Specifically, CDH5 downregulation corresponds to one of the first stages of angiogenesis and S1PR1 downregulation correlates with a VEGF pathway upregulation. Therefore, the gene expression profiles explain the functional readouts and could be used to target sprouting lymphangiogenesis and changes in vessel permeability.

Altogether, these experiments demonstrate how HNSCC patient-derived CAFs can induce lymphatic vessel remodeling (e.g., lymphangiogenesis and changes in permeability). Specifically, we showed that sprouting length and quantity depends on the patient specific CAFs and is not induced in the same way for every patient. We also found that the permeability of the vessel was increased in co-culture with CAFs in a patient-specific way, where in patient 2 a change in vessel permeability was not observed. Finally, we identified potential genes that could be responsible for the functional changes. Future work will require larger patient cohorts to correlate what we are observing *in vitro* with the patients. Additionally, examination of the cells' crosstalk would help to identify potential targets to reduce lymphangiogenesis. Moving forward, incorporation of cancer cells into the model would provide a better picture of what is happening and provide a better understanding of the changes induced from each patient to the lymphatic vessels, therefore, identifying the best potential therapeutic targets. For example, from the results presented here, therapeutic targets points toward classic anti-angiogenics drugs such as sunitinib, which would target VEGF-VEGFR2 pathway, which is upregulated in a particular way among all patients.

4.5 Acknowledgements

We acknowledge a fellowship from the UW-Madison Graduate Engineering Research Scholars program to KML. We also thank the NIH (R01EB010039 BRG) and the Wisconsin Head & Neck SPORE (P50 DE026787) for funding support.

Chapter 5: Concluding Remarks and Future Directions

This dissertation focusses on the development of an organotypic lymphatic model to investigate the contribution of different tumor microenvironmental components in lymphatic vessel function and remodeling. The introduction (Chapter 1), describes the significance of lymphatic vessels in cancer metastasis and how components of the tumor microenvironment play a role in promoting metastasis. In addition, this chapter describes why lymphatics are understudied (compared to the blood vasculature) and the current models and approaches to study lymphatics. This chapter also explains the need for an *in vitro* model to study important physiological events associated with lymphatic vessels that could lead to metastasis.

In chapter 2, the development and characterization of a new organotypic lymphatic vessel model are presented with potential implications in cancer research. The focus of the chapter is the characterization of the lymphatic vessel markers, permeability, drainage capacity and the secretion of soluble factors compared to blood vessels. In this chapter, it was demonstrated that lymphatic vessel permeability and drainage capacity in the model is higher than in blood vessel models, which is consistent with *in vivo* observations. As a proof-of-concept, lymphatic vessel models were co-cultured with breast fibroblasts (i.e., normal fibroblasts and cancer-associated fibroblasts), examining their crosstalk. In co-culture with cancer-associated fibroblasts, IL-6 was identified as an upregulated secreted factor. Vessel permeability decreased after blocking the IL-6 receptor with an FDA approved drug. Therefore, this chapter demonstrated the application of this model to examine the influence of TME components in lymphatic vessels and the potential to test therapeutic options. In chapter 3, the lymphatic model was used to investigate the influence of ECM density in the context of breast cancer. The ECM around the lymphatic vessel was modified to mimic the density of the normal mammary gland (low-density collagen) and to mimic the

density of a breast tumor (high-density collagen). This chapter revealed that high-density collagen promotes lymphatic vessel dysfunction, as observed by the increase in cell detachment, cytokine secretions and increase in vessel permeability. It was demonstrated that the increase in collagen density promoted an increase in IL-6 secretion, which in turn increased vessel permeability, consistently with the findings of chapter 2. This model was used to recapitulate more accurately the breast TME by embedding metastatic breast cancer cells within both matrices. In the presence of breast cancer cells similar findings as in lymphatic monocultures were found, increased permeability and secretion of IL-6. However, targeting IL-6 receptor was not as effective in the co-culture with cancer cells as in the lymphatic monoculture. Therefore, this chapter demonstrates the importance of including different components of the TME in *in vitro* models, allowing to identify the contribution of each component.

Lastly, in chapter 4, the lymphatic vessel model was used for a more translational approach to investigate the influence of head and neck patient-derived cancer-associated fibroblasts (CAFs) in lymphatic vessel remodeling (e.g., lymphangiogenesis). This chapter demonstrated how cancer-associated fibroblasts induce different amounts of lymphangiogenesis. Importantly, it was observed that conditioning with patient-derived CAFs from three different patients induced the upregulation of common genes that regulate angiogenesis but at different levels. Although CAF conditioning induced the upregulation of common genes, it was observed that the CAFs conditioning induced distinct gene expression profiles for each patient. Altogether, this dissertation highlights the first microfluidic organotypic lymphatic model that enabled the examination of TME-lymphatics interactions, demonstrating that changes in ECM density and fibroblasts composition can induce lymphatic vessel remodeling. This work has also demonstrated the potential of the model to use patient-specific cells (i.e., primary cells isolated from human samples)

to identify the changes induced to the lymphatic vessels. Overall, this thesis established the foundations and demonstrated the applications of the lymphatic organotypic model. Future studies are needed to better determine the influence of other TME components that could facilitate metastasis and, the use of this model could be expanded to a diverse set of research areas.

5.1 Examine the effect of lymphatic-stromal signaling as potential therapeutic targets

In Chapter 2, the lymphatic vessel was co-cultured with breast normal fibroblasts (NF) and cancer-associated fibroblasts (CAFs). Results from this chapter revealed changes in lymphatic vessel barrier function and cytokine secretions (e.g., IL-6). Using this model, it was determined that IL-6 was responsible for the changes in barrier function, demonstrating the potential of the model to assess therapeutic targets. In addition of IL-6, other potential therapeutic targets found in this chapter are found in Table 5.1. As future directions, this model could be used to screen the potential of these therapeutic targets. To increase the relevance of the model, incorporation of breast cancer cells could be performed, as demonstrated by preliminary results (Figure 5.1). Incorporation of cancer cells allows testing of the response using readouts such as cancer cell proliferation, migration and intravasation into the lymphatic vessel. The end goal of this approach is to build similar models using patient-specific components to improve precision medicine.

Table 5.1. Potential tumor-stromal therapeutic targets.

Chemokine/cytokine	Blocking Agents in Clinical Trials
HGF	Anti-HGF
IL-6	Anti-IL6R
IL-8	Anti-IL8R
CXCL12	Anti-CXCR4 (AMD3100)

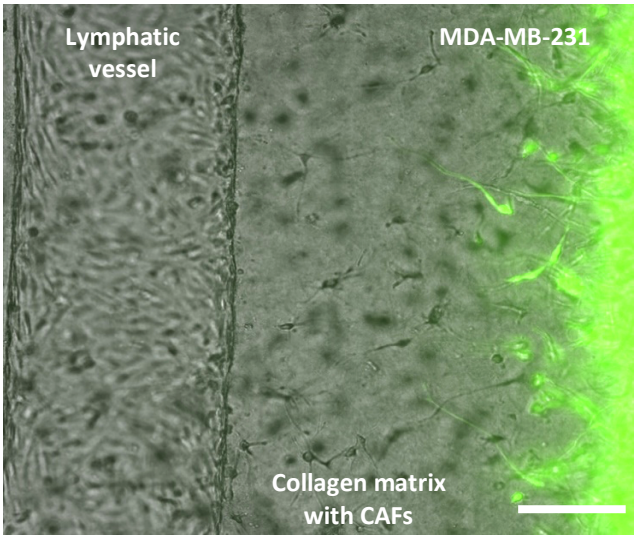

Figure 5.1. Lymphatic organotypic vessel co-cultured with GFP-tagged MDA-MB-231 and CAFs embedded in the 3 mg/ml collagen matrix after 24 hours. Scale bar is 140 μm.

5.2 Determine the influence of additional ECM properties and compositions in lymphatic vessel remodeling

The results showed in Chapter 3 demonstrated that ECM density affects lymphatic vessels. Specifically, it was demonstrated that a high-density collagen induced endothelial cell detachment, increase vessel cytokine secretion and increase vessel permeability. However, by changing the collagen density, other parameters are affected (e.g., matrix stiffness). Thereby, future work should decouple the effects of matrix density and stiffness on lymphatic vessels. Additionally, as described in Appendix B, the composition of the ECM is altered in breast tumor tissue as compared to the normal tissue. Therefore, future work could leverage the optimization performed in both chapters to evaluate the influence of different matrix components in lymphatic vessel remodeling.

5.3 Evaluation of head and neck primary fibroblasts in an expanded patient cohort

In Chapter 4, we showed that lymphatic vessels co-cultured with CAFs from head and neck squamous carcinoma patients induced lymphangiogenesis. Specifically, we demonstrated that lymphatic vessel sprout (i.e., lymphangiogenesis) number and length was different among patients. For example, patient 1 and patient 2 had longer sprouts compared to patient 3, which correlated with the patient grade (e.g., patient 1 and patient 2 were grade 4 and patient 3 was grade 2). On the other hand, we found that vessel permeability increased in patients 1 and 3, and that vessel permeability did not change in patient 2, as compared to the lymphatic vessel monoculture. Interestingly, the changes in vessel permeability correlate with the patient lymph node status, where patients 1 and 3 have a positive lymph node status but patient 2 has a negative lymph node status. Based on these results, it is hypothesized that targeting changes in vessel permeability would be more effective for patients 1 and 3 than targeting lymphangiogenesis. Therefore, the

significance of these preliminary results relies on the potential of finding targets to inhibit lymph node metastasis, which is the dominant factor affecting patient prognosis. While these findings are exciting and promising, future studies are needed to confirm the predictive value of the assay. Therefore, future work should focus on including an increased sample size. In addition, due to patient availability, all patient samples used for the preliminary experiments were human papillomavirus positive (HPV^{+}). Hence, it would be worthwhile to have fibroblasts from patients with an HPV^{-} status, given that this status has poorer clinical prognosis, to compare them with the HPV^{+} patients. While the focus of this thesis has been in the effects of tumor microenvironmental components in lymphatic vessel remodeling, future studies could also consider including other patient-specific cell fractions into the model to expand the current readouts (e.g., intravasation, cancer cell proliferation) and to determine if the current readouts are affected.

Appendix A: Modeling Mammary Ducts in Breast Cancer[4]

Background & Significance

Breast cancer is the most common type of cancer affecting women in the United States, accounting for 15 % of all new cancer cases and 7% of all cancer related deaths[257]. Understanding the factors that contribute to breast cancer initiation and progression are crucial to prevent further development and progression of the disease and to effectively target the disease. For this, *in vitro* models that allow to mimic the *in vivo* microenvironment are essential. Of particular interest in this review is cancer initiation and progression in the mammary ducts (i.e. ductal subtype), which accounts for the vast majority of the breast carcinoma cases (83%)[258].

Function and structure of the mammary gland

The mammary gland is an organ in female mammals composed of a complex structure with networks of ducts and glands designed for lactation (i.e. milk production)[259]. The main components of the mammary gland are lobules and ducts which are formed by an epithelial layer surrounded by myoepithelial cells[260]. Within the breast, the ducts branch out from the nipple and terminate at functional units known as terminal ductal lobular unit, which is comprised of blind-ended tubules called acini that are responsible for milk secretion. The milk is carried from the acini through the tubular ducts to the nipple. These ducts and lobules are surrounded by a fibrous material, known as the extracellular matrix (ECM), and various cell types, comprising

[4] This chapter has been adapted from the manuscript accepted in Chem. Soc. Rev. (2019) "Microfluidic lumen-based systems for advancing human disease modeling." The manuscript was authored by Gong et al. and this section was co-authored section by Megan K. Livingston and **Karina M. Lugo-Cintrón.**

together the tissue known as stroma, which is embedded within the mammary fat pad (i.e. adipose tissue).

Stages of breast cancer: initiation, progression and metastasis

Most breast cancers arise from the cells located in the lobules and terminal ducts, which is how the histological cancer subtypes are divided (i.e. lobular or ductal). In pre-invasive breast cancer, ductal carcinoma in situ (DCIS) accounts for 80% of the cases as compared to lobular carcinoma in situ (LCIS) which accounts for 20% of the cases[261]. As for invasive breast cancer, invasive ductal carcinoma (IDC) accounts for 79% of the cases as compared to invasive lobular carcinoma (ILC) which accounts for 10% of the cases[261]. Hence, a better understanding of the ductal subtype has the potential to improve the outcome of thousands of patients.

The current hypothesis of how ductal breast cancer progress indicates that breast cancer advances in a linear progression from a benign lesion such as (1) ductal hyperplasia to (2) carcinoma in situ, (3) invasive carcinoma and, ultimately, (4) metastasis[262,263] (Figure A.1) Thus, atypical ductal hyperplasia (ADH) is one of the initial steps of breast cancer progression, which is considered to be an early and premalignant epithelial abnormality[264,265]. Followed by ductal carcinoma *in situ* (DCIS), which is a stage of cancer cell proliferation with no evidence of basement membrane penetration (i.e. no invasion into the surrounding matrix)[266]. In this stage, proliferation of cells occurs within lumen of ducts and results in the loss of a hollow lumen and distortion of the duct. Cells within DCIS lesions acquire further genetic abnormalities that promote cell migration and invasion such as loss of E-cadherin.[267] Additionally, DCIS tumor

cells increase secretion of proteinases (i.e. MMPs)[268] that facilitates the degradation of the basement membrane and the entry into the surrounding matrix.

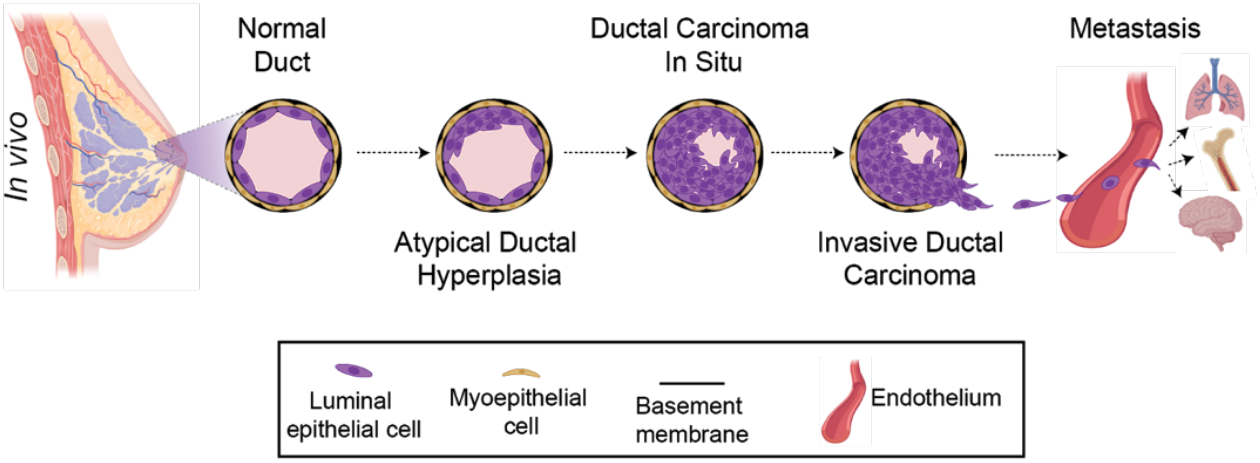

Figure A.1. Hypothetical model of breast cancer progression. Schematic view of a normal duct, atypical ductal hyperplasia, ductal carcinoma in situ, invasive ductal carcinoma and metastasis (i.e. intravasation and extravasation).

As cancer cells invade the surrounding matrix, they interact with biochemical and biophysical components of the tumor microenvironment (i.e., oxygen gradients, stiffness gradients) as well as stromal components such as blood vessels, fibroblasts and immune cells. Once in the matrix, cancer cells can migrate through the tissue toward the vasculature, which may lead to cancer spreading to distant organs (i.e. metastasis). Metastasis is a multistep process by which tumor cells migrate from the primary tumor through the surrounding matrix, intravasate into the vasculature (blood or lymphatic), extravasate and colonize a distant organ. Each of these events is driven by (1) genetic and/or epigenetic alterations within tumor cells and the (2) involvement of stromal cells[269](which has been recently begin to be appreciates). Although we are aware of the steps of the metastatic cascade, metastasis still accounts for 90% of cancer-related deaths[174], demonstrating the lack of complete knowledge of the underlying mechanisms in the cascade. *In vivo* mouse models have been widely used for the study of metastasis[270–272], however, often

these models do not allow researchers to dissect the contribution a specific component responsible for certain event. On the other hand, 2D *in vitro* models have been mainly used for understanding the biology of cancer cells[273], but these models certainly do not represent the components found *in vivo*. Thus, our limited understanding of complex events such as cancer cell intravasation and extravasation is in part because of the lack of physiologically relevant *in vitro* models that allow for the study of such events.

Modeling the Human Mammary Gland in vitro

Our limited understanding of the complex relationships between breast tumors and the surrounding tumor microenvironment has motivated the field to develop *in vitro* models of the human mammary gland spanning from models of a healthy mammary gland to invasive ductal carcinoma (IDC). A recent example, from Carter et. al. in 2017, utilized organoids in a channel of a micro-device to demonstrate that mammary gland cells could be isolated from patients undergoing breast reduction surgery, split into myoepithelial and luminal cell populations and cultured on a 2D plastic dish. The cells on the dish were transfected for fluorescent protein and the ability to initiate overexpression human epidermal growth factor receptor 2 (HER2), then recombined in a 3D matrix. The 3D embedded recombined cells arranged themselves in a layered geometry with myoepithelial cells surrounding a hollowed lumen formed from luminal cells, as seen *in vivo*. The study also showed that DCIS could be achieved when treated with a compound, doxycycline, known to induce progression of breast cancer. When HER2 overexpression was initiated, the researchers showed that DCIS did not respond to drug trastuzumab, but lower HER2 expressing cells were able to clear the DCIS tumor and return to the normal luminal geometry[274]. The 3D nature of these organoids provides insight into the factors involved in tumor progression by

allowing researchers to visually study the cellular arrangements within a relevant breast cancer model. While these embedded 3D models have contributed to understand the relationship between the tumor and the microenvironment, they are not amenable to control the spacio-orientation of several cell types or manipulation of the organoid itself. Herein, we discuss the role of microfluidic technologies in the study of breast cancer progression. We have narrowed the scope to only include microfluidic technologies with relevant luminal geometries, unless otherwise indicated.

In addition to studying tumor cells alone, there is also interest in studying how tumor cells interact with other cells and body systems. For example, breast cancer progression is not limited to the interactions of the tumor and its surrounding microenvironment, breast cancer also undergoes metastasis to distant sites in the body. Unfortunately, metastasis accounts for 90% of total breast cancer related deaths[174]. Where factors that regulate intravasation, extravasation, and ultimately colonization of a secondary site are a studied area that would benefit from modeling the events in micro-devices since they enable spatio-control of materials and multiple cell types in one culture system, making possible to study the interplay of multiple factors while retaining tractability. The following studies do not incorporate a luminal geometry, but do incorporate micro-scale modeling of steps in the metastatic cascade and are worth noting due to their contributions to the field. Intravasation and extravasation are critical steps in the metastasis of breast tumor cells, since it allows cancer cells to move from the primary tumor to a secondary location. Current micro-scale efforts to model intravasation and extravasation have been implemented in micro-devices that allow for 2D mono-layer of cells on the surface of the device itself or on top of an ECM mimicking hydrogel. In 2015, one model of metastasis studied the DCIS to IDC transition, the first step in metastasis, of a DCIS spheroid (DCIS.com) cultured on a mono-layer of normal human mammary cells, on a planar layer of vitrified collagen. A mono-layer of

primary mammary fibroblasts were seeded on the opposite side of the planar collagen. This model accurately accounts for the spatial orientation of the mammary epithelium and stromal components found in the mammary gland, but does not include the appropriate luminal geometry or varieties of ECM proteins. The study showed that DCIS spheroids did not grow in size when exposed to paclitaxel, a commonly used breast cancer drug, but did not explore any other details in the metastasis process[275]. In the same year, a study was published including another relevant cell type in the dissemination of breast cancer cells around the body, lymphatic endothelial cells. The body's lymphatic system is a commonly utilized highway for breast cancer cells in the metastasis process. In this study, researchers used a similar spatial orientation of cell types as in the study above, but instead of designing an all-encompassing micro-device, they modified and fabricated a platform for a transwell insert. Using micro-scale channels in the platform, they were able to induce flow across the bottom of the transwell membrane, which they had seeded with a mono-layer of lymphatic endothelial cells. Additionally, researchers could induce flow through the top of the well which contained a 3D hydrogel matrix embedded with highly migratory breast tumor cells, MDA-MB-231. They were able to track the migration events across the lymphatic membrane to show that luminal flow increased transmigration of the MDA-MB-231 cells by acting on the lymphatic endothelial cells, and the addition of flow through the 3D embedded hydrogel increased the tumor cells' migration even more[276].

Micro-scale studies that focused on metastatic events utilized co-culture of breast cancer tumor cells and endothelial cells from the human vasculature initiated in 2009. An early micro-device modeled tumor adherence to a layer of vascular endothelial cells exposed to different compounds. The device was constructed such that the endothelium was seeded in a mono-layer on a membrane separating it from a network of micro-channels beneath orthogonal to the endothelial

chamber. The device allowed researchers to screen several compounds by exposing the basal side of polarized endothelial cells to the compounds, which increased the device's bio-mimetic relevance. Results indicated that circulating MDA-MB-231 cells adhered most to endothelium exposed to tumor necrosis factor alpha (TNF α)[277]. Another study also looked at the effects of TNFα and co-culture with macrophages on MDA-MB-231 migration across an ECM hydrogel towards a monolayer of vascular endothelial cells oriented vertically in the device. The device allowed researchers to expose the system to compounds with spatial separation of the cell types, biomimetic orientation, and the ability to track tumor cell migration paths through relevant ECM matrix against a gradient[278]. A similar study compared the extravasation of MDA-MB-231 and a normal mammary epithelial cell line, MCF10A, across a monolayer of vascular endothelial cells, hMVEC. Results showed that both breast epithelial cell types were able to migrate but MDA-MB-231 cells extravasated at a much higher percentage[279]. Breast cancer metastasis shows patterns of site specificity, meaning secondary tumors tend to occur in certain organs (i.e. brain, lungs and bone) rather than at random sites. Utilizing a micro-device platform allows researchers the ability to probe specific organ microenvironments and study the response of migratory cancer cells in those environments. The small-scale nature of micro-devices also allows for screening of tumor response many organ types, individual components from the microenvironment of interest, and the ability to screen compounds' effects on the system. Jeon *et. al.* utilized a three channel microdevice to determine the components of the bone microenvironment that encourage site specific metastasis of breast cancer cells. The middle channel of the device contained a hydrogel with protein components found in bone with embedded primary human bone marrow-derived mesenchymal stem cells (MSC), vascular endothelial cells, and C2C12 myoblast cells to mimic muscle in order to model the bone microenvironment. The flanking channels were used to provide cell culture

medium, initiate interstitial flow through the hydrogel, and perfuse MDA-MB-231 cells through the modeled vasculature. By including or not including certain cell types in the hydrogel matrix, the study was able to probe which cell types were important in initiating extravasation of the MDA-MB-231 cancer cells from the modeled vasculature into the surrounding bone microenvironment. The MDA-MB-231 cells adhered to the vasculature and extravasated at a significantly higher rate in the bone microenvironment with all cell types included versus into the hydrogel matrix alone or the hydrogel embedded with C2C12 myoblasts. These results provide great insight into bone specific metastasis because it demonstrates that MSCs are necessary to provide cues for breast cancer cells to recognize and metastasize to bone[280]. Results from the studies discussed above no doubt provide valuable understanding of events included in the progression of breast cancer. The platforms are amenable to chemical screening, allow multiple cell types to communicate with each other, and therefore, are considerably closer to mimicking *in vivo* than traditional 2D on plastic cell culture studies.

However, with advances made in micro-scale culture, we've seen evidence that organ-mimicking geometry is also a necessity when trying to replicate *in vivo* response to changes in the system[94]. Examples include: a self-folding poly(ethylene glycol diacrylate) (PEGDA) free-floating viable mammary duct, a luminal endothelial cell lined vessel through ECM embedded breast tumor cells, an endothelial lumen in porous PDMS surrounding a tumor spheroid, and a collagen derived DCIS model in a luminal geometry have all been created with intention to carry out further biological testing[281–284].

The first study to highlight the biological impact of geometry in mammary duct-mimicking micro-fluidic models is from the Lelievre lab in manuscripts published in 2011 and 2014. The earlier of the two manuscripts explored a method of creating a semicircular geometry in a

hemichannel, in which, the cells were seeded in a monolayer in a curved geometry at the bottom of the channel[285]. The group was able to create the model in both polydimethyl siloxane (PDMS) and acrylic, and showed that addition of laminin 111, a protein found in the breast microenvironment, as a coating of the hemichannel supported correct apical/basal polarity of both S1 (normal) and T4-2 (tumor) cells. The later manuscript used the hemichannel device to screen commonly used anti-tumor drugs and looked at the sensitivity of the cells' responses to the drugs in planar and semi-circular geometries. They found that cells in the hemichannels were significantly less sensitive to bleomycin and doxorubicin when compared to their 2D counterparts[286]. Because lower sensitivity in the hemi-channels may be more indicative of *in vivo* response, traditional 2D screening assays could miss the relevant chemical or drug activity window completely.

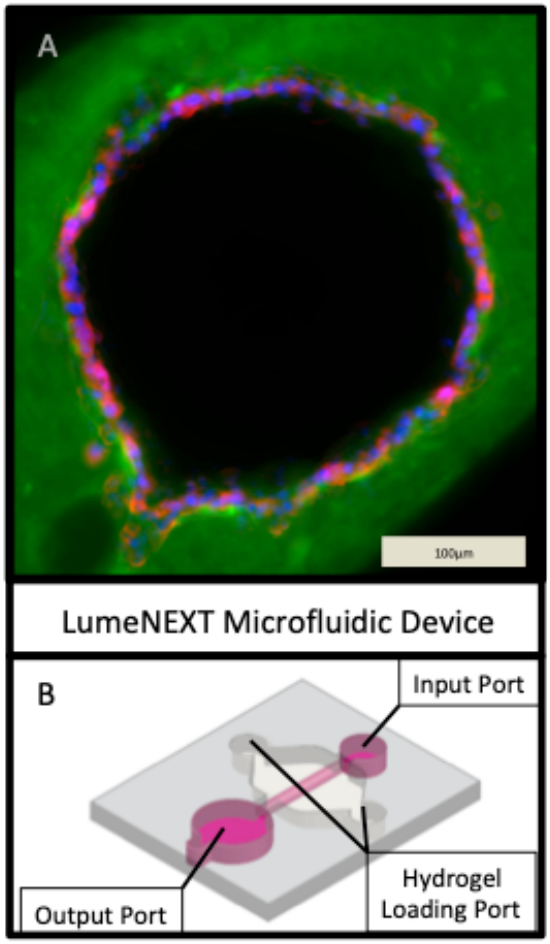

Figure A.2. Use of LumeNEXT to model luminal geometry of the mammary duct. A) Cross-section of MCF12a cells (blue nuclei, red f-actin) lining a col I (green) ductal structure in LumeNEXT model. **B)** Schematic for device operation. Hydrogel is loaded through side ports. A sacrificial rod is removed to create luminal geometry through polymerized hydrogel. Cells are seeded via passive pumping from small to large port (as are subsequent replenishing of media/compound doses). Figure credit: Megan K. Livingston

The ability to include relevant ECM hydrogels surrounding the mammary duct impacts the biological response of the cells, as demonstrated in the cell polarization observed in the hemi-channel model. LumeNEXT is a microfluidic device, developed in the Beebe lab, that allows for repeatable luminal geometry formation through relevant ECM hydrogels and proteins (Fig. A.2)[112]. LumeNEXT has the added benefit of relying on passive pumping for operation, therefore the operator does not need to use fluid pumps. In LumeNEXT, a range of ECMs with biologically relevant hydrogel stiffness and cell types from the mammary duct microenvironment

can be used to fabricate the luminal geometry. When MCF7 cells were cultured with human mammary fibroblasts (HMF) in LumeNEXT embedded within collagen, they polarized with apical/basal orientation. Signaling from HMF cells also decreased MCF7 cell proliferation rates to approximately 3%, matching proliferation rates of the mammary duct epithelium *in vivo*. The chemical, 17β-estradiol (E2) was used as an ER agonist, to model the progression of ER+ breast cancer. Similar to progression *in vivo*, E2 induced hyperplasia of MCF7s into the center of the luminal geometry, the response was significantly enhanced with the addition of HMFs in the surrounding collagen matrix. Co-culture with HMFs also increased the level of ER transactivation in MCF7 cells, decreased apoptosis, and increased overall viability in the LumeNEXT platform[287]. Next, the luminal platform was used to screen effects of body mass index on breast cancer by co-culturing MCF7 cells with commercially available primary adipose derived mesenchymal stem cells (AdMSCs). AdMSCs metabolize androgens to estrogens via aromatase. To characterize this metabolism in the model, MCF7s were exposed to testosterone in mono-culture and co-culture with AdMSCs. In co-culture, the testosterone induced an estrogenic response of the MCF7s, detected through luminescent readout of ER transactivation, indicating that AdMSCs were able to metabolize the testosterone to estrogen in the surrounding col1 matrix. The co-culture was exposed to the compound anastrazole, an aromatase inhibitor, and the ER transactivation was completely diminished, highlighting the ability of the platform to screen for compounds that act on the surrounding microenvironment to impact the progression of breast cancer. After characterizing MCF7 response to testosterone when co-cultured with AdMSC cells, the ductal model was then co-cultured with healthy patient derived AdMSCs (PD-AdMSC) obtained from breast reduction surgery. The study concluded by comparing PD-AdMSC from patients categorized in low and high body mass index (BMI). When exposed to testosterone and

anastrazole. MCF7s co-cultured with PD-AdMSC from higher BMI patients had a significantly lower sensitivity to anastrazole, highlighting the ability of this screening platform to screen compounds for tissue response from individual patients and demonstrates the importance of carefully considering components of the microenvironment[288]. An adaptation of the LumeNEXT platform, to include 3 luminal geometries, was used to study the effect of hypoxia and nutrient starvation of a DCIS model in response to drug compounds. The study demonstrated the ability to set up hypoxia gradient across the DCIS model and determine the hypoxia/normoxia status of individual cells in the tumor via metabolic imaging. Treatment with drugs resulted in the ability to kill tumor cells in hypoxia, but normoxic cells remained viable[187]. Platforms such as these not only promote higher relevance to *in vivo* biology, but also support medium throughput of drug and compound screening. Because the biology more closely matches that *in vivo*, we can begin to rely on these models to help with diagnostics and predictive modeling.

Appendix B: Breast fibroblasts and ECM components modulate breast cancer cell migration through the secretion of MMPs in a 3D microfluidic co-culture model[5]

Abstract

Within the tumor microenvironment, cancer cells partake in crucial crosstalk with stromal cells (e.g., fibroblasts) that will define tumor outcomes. In addition, biophysical and biochemical cues, such as those from the extracellular matrix (ECM), are known to alter cell invasion greatly. However, these interactions are often overlooked in traditional *in vitro* migration models. Therefore, creating reproducible models that incorporate organotypic structure, ECM, and stromal support have the potential to improve migration and invasion assays. Here, we use a microfluidic platform that consists of a luminal structure filled with a mixture of cancer cells and a surrounding 3D collagen matrix that enables the testing of heterogeneous ECMs with different stromal components. Thus, the presented platform mimics an invasive stage of breast cancer surrounded by a complex and relevant TME. Using this model, we demonstrate that cancer cell migration is influenced by the synergistic effect of the matrix and fibroblast composition. Specifically, we show that in the presence of normal breast fibroblasts, a fibronectin-rich matrix induces more cancer cell migration. On the other hand, in the presence of cancer-associated fibroblasts, cancer cell migration increases to levels higher than in co-culture with normal fibroblasts regardless of matrix composition. Analysis of the extracellular matrix revealed an increase in matrix degradation in co-culture with fibroblasts observed by the presence of pores in the matrix. In addition, cancer-stromal crosstalk induced an increase in the secretion of MMPs in co-cultures. Specifically, in the co-

[5] This chapter has been adapted from the manuscript in preparation: "Breast fibroblasts and ECM components modulate breast cancer cell migration through the secretion of MMPs in a 3D microfluidic co-culture model." The manuscript was authored by Karina M. Lugo-Cintrón, Max M. Gong, José M. Ayuso, Lucas Tomko, Suzanne Ponik, David J. Beebe and María Virumbrales-Muñoz

culture with normal fibroblasts, MMP secretion increased in the fibronectin-rich matrix and, in the co-culture with cancer-associated fibroblasts there was an increase regardless of the matrix composition. MMP inhibitor experiments revealed a decrease in migration distance in the collagen matrix but not in the fibronectin-rich matrix in the co-culture with HMFs. These data reveal the importance of using *in vitro* models that incorporate components of the tumor microenvironment that are essential in regulating cancer progression. Overall, this data demonstrates the capability of the model to pinpoint the contribution of different components of the TME.

Introduction

Breast cancer is among the three most common cancers worldwide and the most common malignancy in women[289]. Currently, cancer metastasis accounts for 90% of cancer related deaths[174]. Cancer metastasis is a multistep process by which tumor cells migrate from the primary tumor through the surrounding matrix, intravasate into the vasculature (either blood or lymphatic), extravasate and colonize a distant organ[290]. In order to metastasize, cancer cells must degrade the surrounding ECM to invade and migrate through the stroma. Within the surrounding matrix, cancer cells interact with biochemical and biophysical components of the matrix (e.g., matrix composition) as well as stromal components such fibroblasts, that regulate metastatic outcome[291]. Despite significant advances in the understanding of breast cancer, metastasis remains a poorly understood process and is the main cellular event leading to poor patient survival. Therefore, it is essential to understand the migration of cancer cells within the stroma to develop successful strategies that target metastasis.

The tumor microenvironment (TME) has emerged as a critical player in cancer progression and metastasis[292–294]. The TME has two major components, a cellular and a non-cellular component[7,295]. The cellular component comprises malignant and non-transformed cells including fibroblasts, immune cells, vasculature, and adipocytes[8,87]. Among the many components of the TME, fibroblasts have been reported as the major cellular component that regulates cancer cell progression due to the ability of cancer cells to alter fibroblasts into an activated phenotype[296–299]. In breast cancer, fibroblast have been shown to promote tumor growth, migration and metastasis[300]. Fibroblasts can promote tumor progression by remodeling the extracellular matrix structure and composition. The extracellular matrix (ECM) is the non-cellular component of the TME and it is mostly composed of collagen I, which has been

demonstrated to align next to the boundary of the tumor, thereby facilitating cancer cell migration[37,301]. In addition, recent *in vivo* proteomics data revealed that breast tissue of invasive ductal carcinoma patients have an increase deposition of other components of the ECM (e.g., fibronectin) as compared to normal tissues[39]. Furthermore, areas of collagen alignment surrounding the tumor significantly correlated with increased levels of FN, TNC, TSP2, and Col12. Clinically, the increase in fibronectin expression has been associated with poor clinical outcome, decreased survival rates and therapeutic resistance[302,303]. Although it is evident then that the TME plays a crucial role in tumor progression and metastasis, critical TME components, such as fibroblasts and alterations in ECM composition are not included in traditional *in vitro* assays that investigate cancer cell migration.

Traditional *in vitro* models for studying cell migration include wound healing assays and transwells, and present several limitations[304,305]. For example, studies using wound healing assays are performed in two-dimensional substrates (2D). However, it is well known that the mechanisms of cell migration used in 2D differ from those in 3D environments[92,93]. On the other hand, transwells have been used to study cell migration in 3D environments, but do not recapitulate the structural characteristics of the TME[306]. Another limitation from traditional *in vitro* cell migration assays is the lack of additional cell types from the TME, which are known to have an impact in cancer cell migration [307]. Microfluidics has been recently used to better recapitulate the TME[308–313]. In the context of breast cancer migration, microfluidic models have been developed to co-culture cancer cells with components such as endothelial vessels[278] and immune cells[314]. Several studies have focused on the interaction between cancer cells and fibroblasts in breast cancer migration and progression[187,315,316]. As for the ECM, microfluidic models have investigated the migration of cancer cells in 3D collagen matrices[317] and have

changed parameters of the ECM such as density[191] and composition[318]. However, most studies have focused on studying only one parameter at a time, either the matrix or the stromal composition, therefore limiting our understanding of more complex microenvironments.

In this work, we incorporated specific TME components such as fibroblasts and a fibronectin-rich matrix in a relevant 3D platform to build the complexity of the TME. Specifically, we mimicked an invasive stage of breast cancer surrounded by a complex and relevant TME using a microfluidic platform previously developed in our lab. This platform allows the creation of a lumen structure within a 3D collagen matrix which is easily modified to include different fibroblasts and ECM compositions. Based on *in vivo* proteomics literature, we chose to assess the effects of fibronectin within a collagen matrix, in addition to either human mammary fibroblasts (HMF) or cancer associated fibroblasts (CAF) which were embedded into the matrix. In this setup, we added metastatic breast cancer cells (MDA-MB-231) into the lumen structure to recreate a tumor-like mass invading the surrounding stroma and then we assessed their migration distance and matrix remodeling, as well as the crosstalk with HMF or CAF. Overall, in this paper we used previously reported ECM proteomics data to recapitulate tumor-like conditions *in vitro* to understand how different ECM compositions, matrix and fibroblast composition, impact the migration of breast cancer cells. Finally, we discuss the effects of TME components in potential therapeutic options (i.e., MMP inhibitors). To our knowledge, this is the first report of a microfluidic device being used to screen the effects of TME components on cancer cell migration and TME effects on the efficacy of cell migration inhibitors.

Materials and methods

Cell Culture

Human mammary adenocarcinoma cells MDA-MB-231 were selected for high invasiveness and their ability to metastasize *in vivo*[319]. MDA-MB-231s were transfected to stably expressing green fluorescent protein (GFP), a kind gift from Dr. Suzanne Ponik (University of Wisconsin, Madison). Immortalized human mammary fibroblasts, referred as HMFs, were derived from the stromal vascular fraction of a reduction mammoplasty and were gifted to us from Dr. Lisa Arndt's lab (University of Wisconsin, Madison). Cancer Associated Fibroblasts were gifted from Dr. Andreas Friedl's lab. All cells were routinely cultured in high glucose DMEM (Gibco, 11965092) supplemented with 10% fetal bovine serum (FBS, VWR, 97068-085) and 1% penicillin/streptomycin (ThermoFisher, 15140-122) and were kept in a humidified incubator at 37^{o}C with 5% CO_2. All cells were cultured to 90-95% confluency at passages X to X for all experiments and media was changed every 2-3 days.

Device Fabrication

LumeNEXT fabrication was performed as previously described [185]. Briefly, the microdevice consists of two PDMS layers, which define the microchamber; and a suspended PDMS rod, which is removed after polymerization of a hydrogel in the main chamber to create a tubular lumen structure. In order to fabricate the top and bottom layers of the microdevice, a traditional soft lithography technique was used, in which the layers were spun using SU-8 (MicroChem, Y13273) to create the silicon master molds. Polydimethylsiloxane (PDMS, Dow Corning, Sylgard 184) was mixed at a 10:1 base to curing agent ratio and poured over the SU-8 silicon master molds. Using the same PDMS mixture, PDMS rods were fabricated by filling up a 25 gauge (Fisher Scientific,

14-840-84) hypodermic needle with PDMS. PDMS components were then baked at 80°C for 4 h. After baking, the PDMS rods were extracted from the needles, yielding PDMS rods of 280 μm in diameter. The two layers were aligned, ethanol bonded together and the PDMS rods were placed into the microdevice chamber. Finally, the microdevice was oxygen plasma bonded to a glass-bottom MatTek dish (MatTek Corporation, P50G-1.5-30-F), following a general protocol. The microdevices were sterilized using UV irradiation for 15-20 min for further use.

Organotypic Culture

LumeNEXT device preparation

To achieve maximum hydrogel adhesion to the PDMS chamber, a two-step coating of 2% poly(ethyleneimine) (PEI, Sigma-Aldrich, 03880) diluted in deionized DI water for 10 minutes was loaded into the side ports. The PEI solution was aspirated and 0.4% glutaraldehyde (GA, Sigma-Aldrich, G6257) diluted in deionized DI water was loaded into the side ports and incubated at room temperature for 30 minutes. During the GA incubation, the collagen solution was prepared on ice (refer to section 3.2). After the 30-minute of GA incubation, the microdevices were washed three times with sterile DI water to remove any GA excess. At this point, devices are ready to be loaded with the collagen solution. To minimize evaporation, sacrificial phosphate buffered saline (PBS) was added around the side of the MatTek dish.

Extracellular matrix preparation and loading into the device

High-density rat-tail collagen type 1 (Corning, 354249, referred as collagen through the text) was diluted with 5X PBS and neutralized with 0.5 M NaOH (Fisher Scientific, S318) achieving a final concentration of 1X PBS, and a pH of 7.4. To achieve a final concentration of 2.25 mg/mL dilutions with fibrinogen (Sigma-Aldrich, F8630) and media were performed. For the collagen

solution containing fibronectin, a final concentration of 100 μg μl^{-1} fibronectin (Sigma-Aldrich, F1141) solution was added to the collagen. For experiments with stromal cells in the matrix, HMFs or CAFs, a final concentration of 500 cells μl^{-1} was added to the respective collagen solution. Right after the washes with sterile DI water, 8 μl of collagen solution was loaded through the side ports and polymerized at room temperature for 10 min. Finally, a small droplet of media (5 μL) was placed on top of the side ports to prevent evaporation, and devices were transferred to 37^{o}C for 1 hour to allow collagen to fully polymerize.

Preparation of collagen I solution containing MDA-MB-231 and loading into device

After incubation, a small drop of media (5 μL) was added to the input port under sterile conditions. To remove the PDMS rod, the rod was pulled through the output port using a sterilized tweezers, leaving a hollow lumen filled up with media within the collagen matrix which is ready for cell loading. All fluid handling procedures were conducted with standard pipettes, uniquely enabled by passive pumping[128]. A 1.5mg/ml collagen solution containing MDA-MB-231s was prepared as indicated in section 3.2, with the addition of the MDA-MB-231s at final concentration of 16,666 cells μl^{-1}. Then, to fill up the lumen with the collagen solution containing MDA-MB-231, the media from the lumen was aspirated and 3 μl of collagen solution containing MDA-MB-231 was loaded through the input port and polymerized at room temperature for 10 min. Finally, a droplet of media (10 μL) was placed on top of the side ports to prevent evaporation, and devices were transferred to 37^{o}C for 1 hour to allow collagen to fully polymerize. After incubation, collagen solution left in the output port was aspirated to remove the excess of cancer cells. Then, 20 μL media was added to the output port and devices were transferred to the incubator for overnight incubation. The next morning, media was replenished and was changed every day.

Imaging Acquisition

Cancer cell migration and migration distance quantification

The GFP signal from the MDA-MB-231 was used to track cancer cell migration out of the lumen. For each device, a Z-stack imaging was performed after 48 hours of culture. Bright-field images were acquired at 4X using a Nikon TI® Eclipse inverted microscope (Melville, New York) and processed using the National Institutes of Health ImageJ software. To analyze the migration distance, each Z-stack was projected, and the distance were the MDA-MB-231 is located was measured from the lumen using Image J[197].

Cytokine secretion assay

Multiplexed protein secretion analysis was performed on the cancer-fibroblasts co-cultures, cancer monocultures and fibroblast monocultured in both type of matrix composition. The analysis was performed using the Magnetic Bead-Based Multiplex ELISA system MAGPIX (Luminex Corporation) using a Human MMP Magnetic Panel (3-Plex) (R&D Systems, FCSTM07-03) as described elsewhere[113]. Collected media was combined to increase the sample volume in each cultured condition. Briefly, media collection was performed at 24 and 48 hours of culture from six cultured vessels. Collected media was combined to increase the sample volume of each condition. Sample preparation and detection was performed following the manufacturer's protocol. Data were collected with xPonent software (Luminex), and soluble factor concentrations in media were calculated using mean fluorescence intensities (MFI) by creating a standard curve for each analyte using a five-parameter logistic (5-PL) curve fit.

Matrix visualization by SHG imaging

Collagen hydrogel structure was visualized by second harmonic (SHG) using a custom-built inverted multiphoton microscope (Bruker Fluorescence Microscopy, Middleton, WI), as described previously[187]. The system consists of a titanium:sapphire laser (Spectra Physics, Insight DS-Dual), an inverted microscope (Nikon, Eclipse Ti), and a 40x water immersion (1.15NA, Nikon) objective. Collagen fibers were excited using an 890 nm infrared laser and collecting the emission at 450 nm.

Matrix quantification

SHG images the different collagen matrices were analyzed using image J. Images were uploaded to the program and a threshold was applied, which was maintain constant for all the images. The pore area on each image was measured resulting in a distribution of different pore area sizes.

Cell tracker and immunofluorescence staining

In some experiments cell were fluorescently labeled with Red or Blue cell tracker. Stock solutions of cell tracker red CMTPX (Thermo Fisher, C34552) and blue (Thermo Fisher, C2110) were prepared following supplier instructions. Then, the stock solution was diluted 1/1000 in growth medium and cells were trypsinized and incubated in this medium for 30 min. Finally, cells were washed twice with 1X PBS to remove the excess of cell tracker.

For immunofluorescence staining, cells were washed with PBS for 30 minutes between each step. Unless specified otherwise, steps took place at room temperature. Washing buffer (0.1% PBS-Tween 80 (Sigma-Aldrich, P1754) and blocking buffer (3% Bovine Serum Albumin (BSA, Sigma-Aldrich, A9056) in 0.1% PBS-Tween 80) were made in advance and stored at 4^{o} C until

use. Cells were fixed with 4% paraformaldehyde (PFA) (EMScience, 15700) for 15 min, then incubated with 0.2% Triton® X-100 (MP Biomedicals, 807426) for 30 min for permeabilization. Finally, devices were incubated with 10 µL of blocking buffer at 4ºC overnight. Texas Red-X Phalloidin (ThermoFisher Scientific, T7471) and DAPI (ThermoFisher Scientific, D3571) were used to stain actin cytoskeleton and nuclei, respectively. A fibronectin antibody was used to stain the presence of fibronectin in the collagen gel (Abcam, ab2413). Fluorescent images were acquired at 10X using a Nikon TI® Eclipse inverted microscope (Melville, New York) and processed using the National Institutes of Health ImageJ software.

MMP inhibition

Marimastat was used to inhibit the activity of different MMPs such as (MMP -1, 2, -7, -14). A stock solution was prepared at 10mM concentration following supplier instructions. For the treatment with Marimastat in the different microenvironments, the stock solution was diluted to a final concentration of 30 µM Marimastat. Treatment with 30 µM Marimastat or a vehicle control (DMSO) was performed for 48 hours, following imaging acquisition. Image analysis was performed to determine changes in migration distance, which was quantified as previously described.

Statistical analysis

All the experiments were repeated at least three times as independent biological repeats. All results are presented as the mean ± standard deviation of the mean. Data were analyzed using GraphPad Prism 8 (GraphPad Software, La Jolla, CA) and statistical significance was set at $p < 0.05$. One-to-one comparisons were performed with an unpaired Student t-test with Welch's correction (if SD

were not the same) after the normal distribution was proved via Shapiro-Wilk test. If the normality test was not passed, a non-parametric test was performed (Mann-Whitney test).

Results and Discussion

In vitro 3D microfluidic model incorporating different stromal and matrix compositions

In recent years, the TME has emerged as a highly regulative factor of cancer progression[320]. It is well known that the ECM of the breast TME can promote cancer cell invasion, migration and metastatic potential[321,322]. However, the few *in vitro* models assessing the influence of the TME components on cancer cells have been performed in 2D platforms, which do not accurately mimic the *in vivo* microenvironment. To mimic an invasive stage of breast cancer surrounded by a distinctive fibroblast and a relevant matrix composition (i.e., collagen and fibronectin as observed for highly invasive breast cancers) we used a microfluidic device previously described by us called LumeNEXT (**Fig. B.1 A**). Using this device, the lumen was filled with a solution of collagen containing metastatic breast cancer cells (MDA-MB-231) surrounded by a collagen matrix with fibroblasts (**Fig. B.1 B**), recapitulating the scenario of a tumor mass invading the stroma. The surrounding matrix was then tailored to incorporate normal mammary fibroblasts or cancer associated fibroblasts (referred as HMFs and CAFs throughout the text) (**Fig. B.1 C**), allowing for cancer-stromal crosstalk. In addition, to determine the influence of the matrix composition in cancer cell migration, the protein composition of the matrix was changed by incorporating 100 μg/ml fibronectin that was mixed in the collagen solution before polymerization. The successful incorporation of fibronectin in the collagen was validated by immunofluorescence staining (**Fig. B.1 D**) as seen in red, and the collagen fibers were visualized by second harmonic imaging (SHG). Overall, this model includes allows to investigate the synergistic effect of the fibroblasts and ECM composition in cancer cell migration.

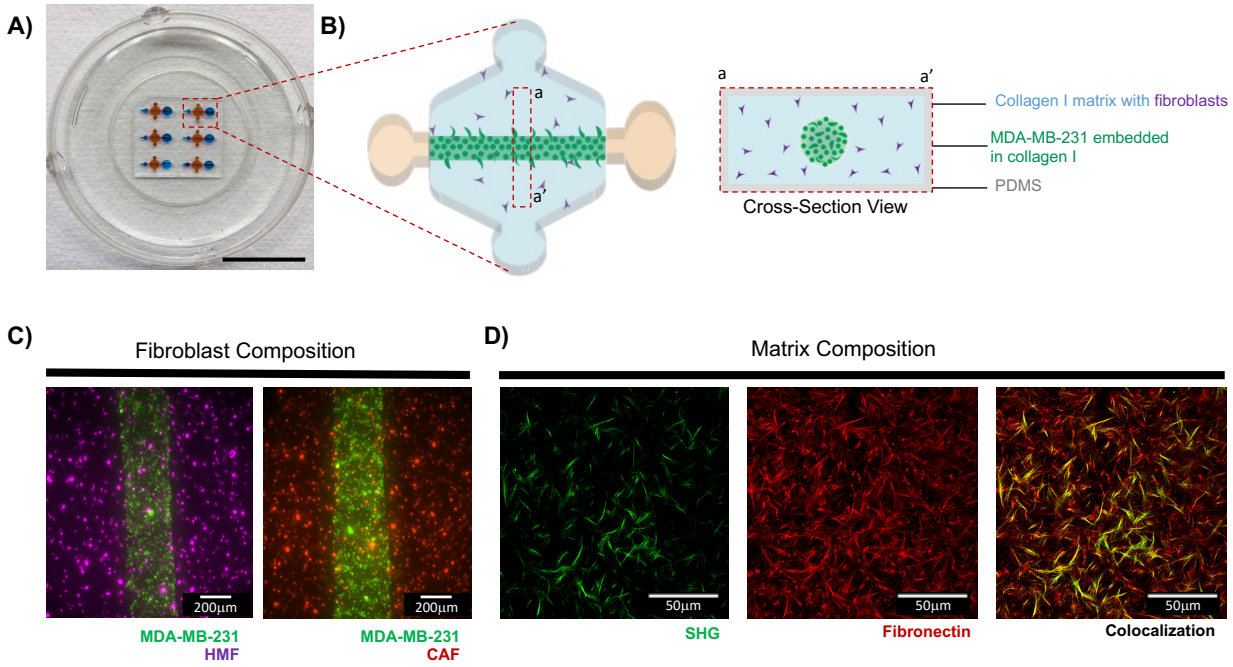

Figure B.1: **3D co-culture model that recapitulate different tumor microenvironments. A)** Photograph of the co-culture model (Scale bar= 10 mm). **B)** Schematic magnification of the device, top view (left) and cross-section view (right). Cross-section schematic shows the basic components of the microenvironment that are included in the model including a 3D collagen I matrix with fibroblasts and cancer cells embedded in collagen I. The matrix and fibroblast composition are tailored to mimic different microenvironments. **C)** Top view image showing MDA-MB-231s (green) co-cultures with normal fibroblasts (purple) or cancer associated-fibroblasts (red) one hour after seeding. Scale bar=250 µm D) Collagen I matrix is supplemented with 100 µg/ml fibronectin to mimic a tumor-like microenvironment. Visualization of the matrix was performed were collagen fibers are shown in green and were visualized by Second Harmonic Generation imaging (left panel). Immunofluorescence staining was performed on gels to detect the presence of fibronectin as shown in red (middle panel). Composite image shows some fibers overlaps (right panel).

Cancer cell migration within different tumor-like microenvironments

To better understand cancer cell migration within different tumor-like microenvironments, we used the 3D microfluidic model that recapitulates different microenvironments. Using this model, we sought to investigate the effect of a fibronectin-rich matrix and the role of fibroblasts on MDA-MB-231 migration. To this end, cancer cells were seeded in the different matrix compositions (i.e., fibronectin-rich collagen or collagen alone) with embedded fibroblasts (i.e., CAFs or HMFs) for 48h (**Fig. B.2 A-C**). Cancer cells were visualized in all four conditions via the GFP-expression of cancer cells from which the number of migrating cancer cells and the migration distance from

the edge of the lumen was quantified using Image J. Qualitatively, an increase in the number of migrating cells is observed in a fibronectin-rich matrix as compared to the collagen only matrix regardless the type of fibroblasts present (**Fig. B.2 B-C**). In the presence of HMFs, the average number of migrating cells was 146 ± 70 cells for the collagen matrix and 319 ± 62 cells for the fibronectin-rich matrix, revealing a significant increase in the number of migrating cells within a fibronectin-rich matrix (**P=0.0019) (**Fig. B.2 D**). In the presence of CAFs, the average number of migrating cells was 224 ± 76 cells for the collagen matrix and 380 ± 61 cells for the fibronectin-rich matrix, revealing a significant increase in the number of migrating cells within a fibronectin-rich matrix (**P=0.0063) (**Fig. B.2 D**). When comparing the influence of HMFs and CAFs in the number of migrating cancer cells, no differences were found, indicating that both type of stromal cells are inducing similar changes in the number of migrating cancer cells. Qualitatively, changes in cell migration distance are observed (**Fig. B.2 B-C**). In the presence of HMFs, the average migration distance was 139.9 ± 20.4 μm for the collagen matrix and 189.6 ± 16.3 μm for the fibronectin-rich matrix, revealing a significant increase in the migration distance through a fibronectin-rich matrix (**P=0.0015) (**Fig. B.2 E**). However, in the presence of CAFs, the average migration distance was 173.2 ± 23.2 μm for the collagen matrix and 192.3 ± 18.7 μm for the fibronectin-rich matrix, revealing no differences in the migration distance within the different matrices (**Fig. B.2 E**). When comparing the influence of HMFs and CAFs in the cancer cells' migration distance, a significant increase was found in the presence of CAFs within a collagen matrix (*P= 0.0365), compared to HMF. However, we observed that the presence of CAFs increased the migration distance of cancer cells regardless of the matrix composition. Interestingly, in the presence of HMFs, a normal component of the TME, the matrix composition induces changes in the fibroblasts that, in turn, enhance the migration of the cancer cells. These results

suggest that within a normal microenvironment (HMFs) and a tumor-promoting component such as the fibronectin-rich matrix, the tumor-promoting factor educate the normal environment to support cancer progression. On the other hand, we did not observe changes in cell migration when including a tumor-promoting component such as the fibronectin-rich matrix in the presence of CAFs. This led us hypothesize that CAFs secrete more fibronectin than HMFs, therefore, the addition of this tumor-promoting component does not make a difference. To determine whether CAFs secrete more fibronectin than HMFs, we assessed the expression of fibronectin via western blots. We used LOX as a loading control for Western blotting because this protein reflected total protein amount in both fibroblasts cultured on the collagen gels. Fibronectin was highly expressed in CAFs as compared with HMFs (**Fig. B.2 F-G**). Therefore, these results could explain the unchanged migration distance in tumor-promoting microenvironment (i.e. in the presence of CAFs) when we changed the matrix composition.

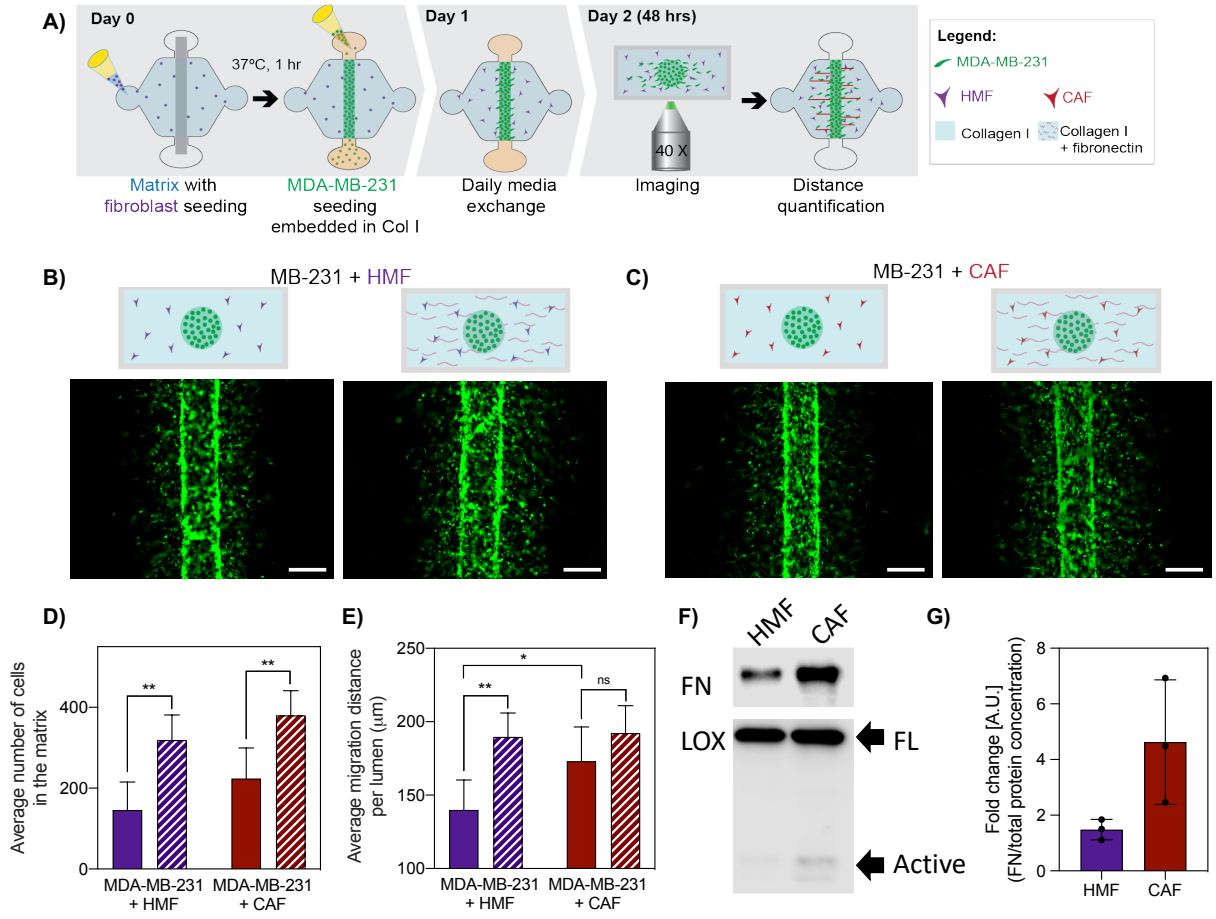

Figure B.2: Influence of ECM protein and fibroblast composition in cancer cell migration. **A)** Experimental schematic of the process consisting in cell seeding, media exchanges and imaging after 48 hours of culture to track cell migration. **B-C**) Fluorescence images of GFP tagged MDA-MB-231s within different matrix compositions in co-culture with HMFs and CAFs. **B**) MDA-MB-231 co-cultures with HMFs in a collagen matrix (left) and a fibronectin-rich matrix (right). **C**) MDA-MB-231 co-cultures with HMFs in a collagen matrix (left) and a fibronectin-rich matrix (right). **D**) Average number of cells in the matrix. **E)** Average migration distance measured from the edge of the lumen after 48 hours of culture. **F)** Representative western blot for many fibronectin **G)** Quantification of western blot as normalized to 0.3% total cell lysate fractions by SYPRO Ruby staining (whole lane fluorescence)**.** Bars represent average ± SD, n at least 4 individual devices. Scale bar = 200 μm. *p ≤ 0.05, **p ≤ 0.01.

Influence of ECM protein and fibroblast composition on MMPs secretion

In breast cancer, tumor progression and metastasis has been found to be driven by matrix metalloproteinases (MMPs) shaping of the TME[323–325]. In this regard, *in vitro* studies have revealed that cancer cells induce stromal fibroblasts to express MMP-9[326], demonstrating the complex tumor-stromal crosstalk that occurs in breast cancer. Additional studies have found that

a subset of the MMPs (e.g. MMP-2 and MMP-9) are upregulated in breast cancers and are associated with poor outcome[43,327]. In addition, other MMPs (e.g., MMP-3), have been found to not only promote matrix degradation, but to act as a signaling molecule that regulates mammary stem cell formation[328]

Therefore, we next focused on studying the secretion of MMPs within the different tumor-promoting microenvironments (**Fig. B.3 A**). To achieve this, we measured the secretion levels of several MMPs implicated in breast cancer progression with a multiplex magnetic bead-based ELISA (i.e. Luminex MAGPIX). All studied factors were within detectable ranges. In general, an increased level of MMPs (i.e., MMP-2, MMP-3 and MMP-9, respectively) was observed in most of the co-cultures (**Fig. B.3 B-D**), compared to the fibroblast monocultures. The MMP secretions were compared to the fibroblast monoculture since the MMP levels of the cancer cell monocultures were lower, which is consistent with previous reports showing that fibroblasts secreting more MMPs than cancer cells (**Fig. B.4**) [329].

In the co-culture with HMFs, a significant increase in MMP-2 (4.3-fold), MMP-3 (2-fold) and MMP-9 (2.3-fold) within a fibronectin-rich matrix was observed (*P=0.0351, P=0.0101 and P=0.0121, respectively). On the other hand, in co-culture with CAFs, a significant increase in MMP-3 was found for the collagen matrix (12-fold) and the fibronectin-rich matrix (14-fold) (**P=0.0013 and ***P=0.0006, respectively) and, a significant increase in MMP-9 (3-fold) within a fibronectin-rich matrix (**P=0.0084) (**Fig. B.3 B-D**).

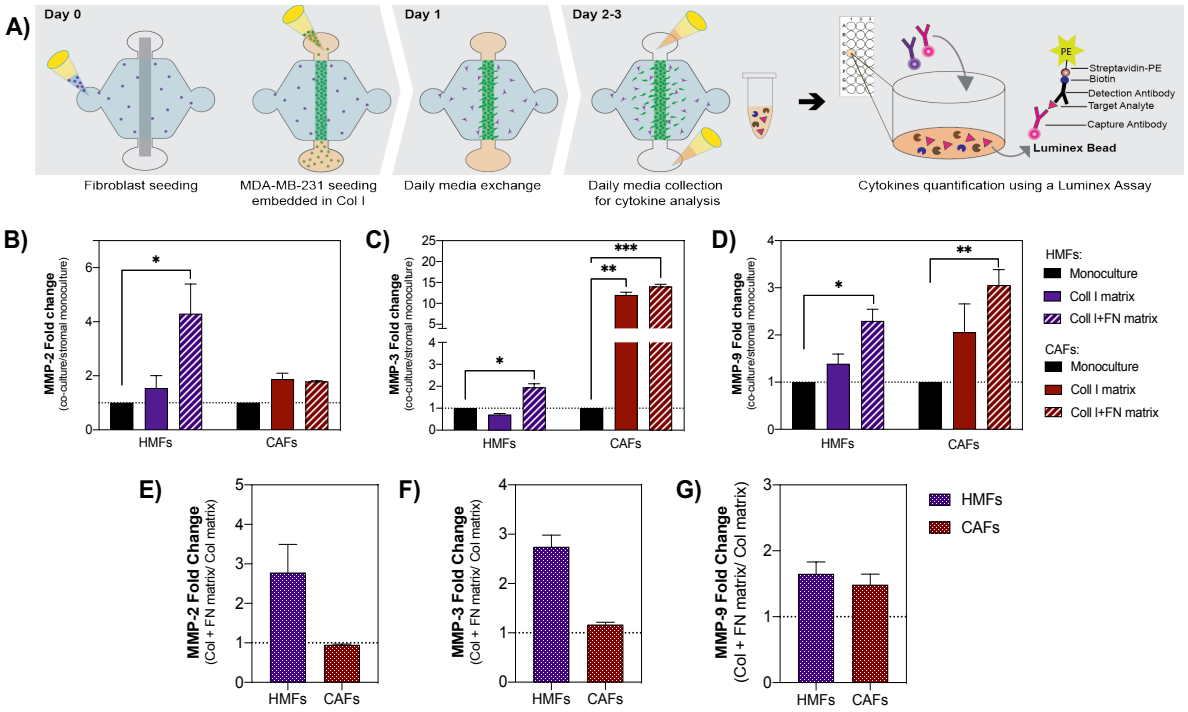

Figure B.3: Influence of ECM protein and fibroblast composition on MMPs secretion. **A)** Schematic of theprocess. MMP concentration for the different microenvironments was determined via a multiplex bead-based ELISA. **B-D)** MMPs fold change in co-culture with HMFs (purple bars) and CAFs (red bars) within a collagen matrix (solid bar) and a fibronectin-rich matrix (striped bar) Fibroblast monoculture showed in solid black). **B)** MMP-2-fold change. **C)** MMP-3-fold change. **D)** MMP-9-fold change. **E-G)** MMPs fold change based on matrix composition for the co-culture with HMFs (purple dotted bars) and CAFs (patterned red). **E)** MMP-2-fold change. **F)** MMP-3-fold change. **G)** MMP-9-fold change. Bars represent average ± SD, n at least 4 individual devices. *p ≤ 0.05, **p ≤ 0.01, *** p < 0.001.

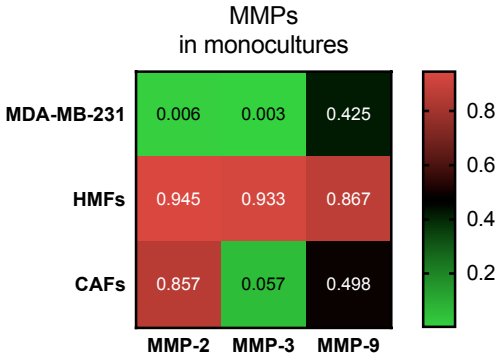

Figure B.4: MMP protein secretion in monocultures. Heat-map demonstrates that MMP-2, -3 and -9 secretion is higher in the HMFs and CAFs monocultures compared to the MDA-MB-231 monoculture. Heat-map represent the average, n at least 4 individual devices

In order to determine if matrix composition modified cell MMP secretions, we calculated the fold change of the fibronectin-rich matrix over the collagen matrix for the different MMPs (**Fig. B.3 E-G**). In the co-culture with HMFs, we found an increase in MMP-2 (2.8-fold), MMP-3 (2.7-fold) in the fibronectin-rich matrix as compared to the collagen matrix. These results demonstrate that the presence of a fibronectin-rich matrix drives the secretion of MMPs by the HMFs. Conversely, in the co-culture with CAFs, no increase in MMPs were found, revealing that the change in matrix composition did not affect the secretion of MMPs. These results support our hypothesis that the fibronectin-rich matrix induced changes in the normal component (HMFs), such as an increase in MMP secretion, that allows cancer cells to migrate further. Overall, these results suggest that the matrix composition stimulates the normal component of the tumor microenvironment to secrete more MMPs, promoting cancer cell migration in normal microenvironments.

Co-culture with fibroblasts induces matrix degradation

It is well recognized that fibroblasts can interact and communicate with the surrounding ECM, resulting in ECM structure remodeling. The remodeling of the ECM is regulated through the secretion of matrix-degrading enzymes (i.e., MMPs), which are known to facilitate cancer invasion through degradation of the ECM. Since we observed an increased secretion of MMPs in the co-cultures, we sought to determine if this increase had an effect on matrix degradation and remodeling. To visualize the collagen fibers, Second Harmonic Generation (SHG) imaging was performed after 48 hours of culture **(Fig. B.5 A)**. Evident matrix degradation is observed in co-cultures with HMFs and CAFs in both matrix compositions, in the form of pores within the matrix **(Figure B.5 B-E)**. Qualitatively, in co-culture with HMFs within a fibronectin-rich matrix, larger pores are observed as compared to the collagen matrix. Conversely, in co-culture with CAFs,

similar pore sizes are observed within both matrix compositions. To quantify the pore size area, image analysis was performed using Image J. In the presence of HMFs, the pore size was 2854 ± 2606 pixels^2 for the collagen matrix and 6929 ± 10611 pixels^2 for the fibronectin-rich matrix, revealing a significant increase in the pore size in the fibronectin-rich matrix (*P=0.05) (**Fig. B.5 F**). In the presence of CAFs, the pore size was 2479± 2901 pixels^2 for the collagen matrix and 2941 ± 2294 pixels^2 for the fibronectin-rich matrix, revealing no differences in pore size within the different matrices (**Fig. B.5 F**). Overall, there is an increase in pore size area in the co-culture with HMFs within a fibronectin-rich matrix, consistent with the increase in MMP-2, -3, and -9 secretion in previous figures. Interestingly, these MMPs can degrade fibronectin and not collagen I, suggesting that the fibronectin matrix is signaling the HMFs to produce MMPs that can degrade the surrounding matrix. As for the degradation of collagen I, these MMPs have the potential to activate other MMPs to degrade collagen I.

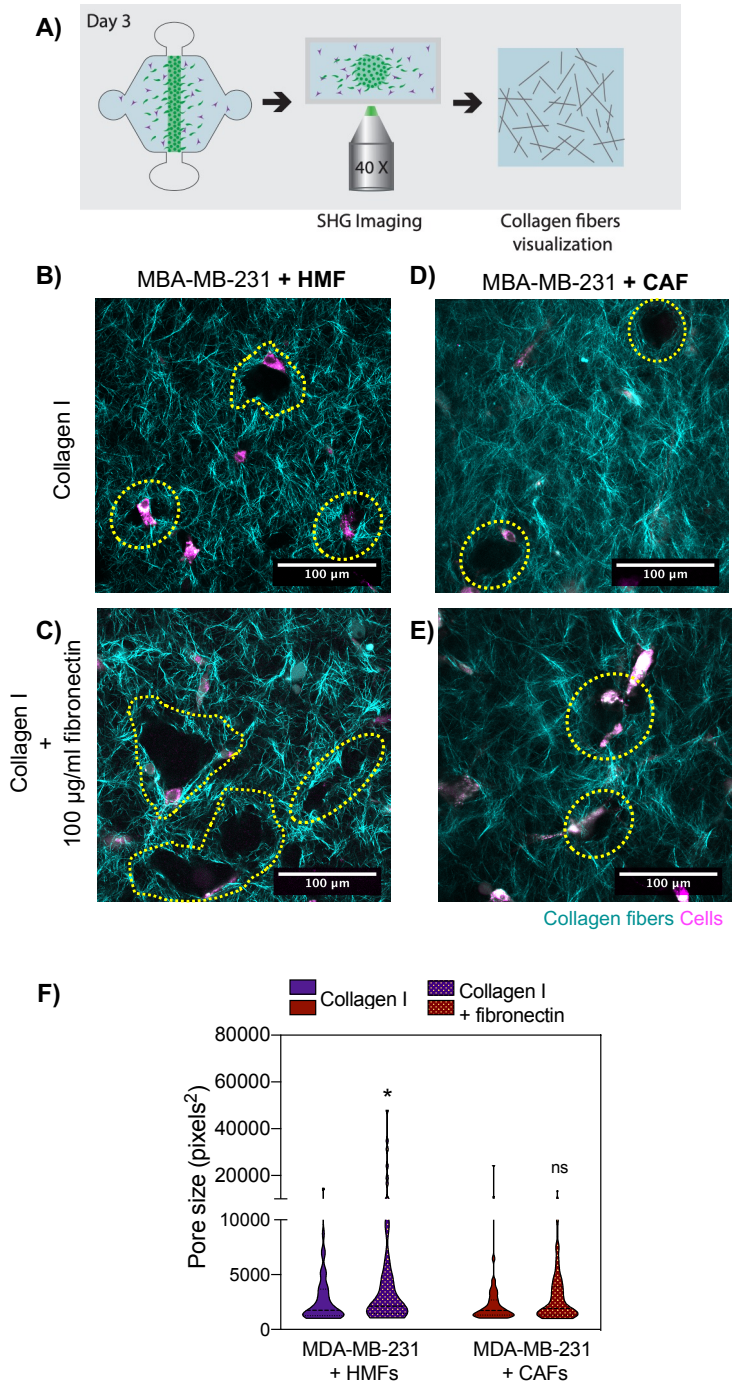

Figure B.5: Matrix visualization via Second Harmonic Generation (SHG) imaging. **A)** Schematic of the process. **B-E)** Collagen fibers are depicted in cyan, whereas cells appear in magenta, were collagen degradation and remodeling are observed in form of pores in the matrix. In co-culture with HMFs, imaging was performed in the **B)** collagen matrix and **C)** fibronectin-rich matrix. In co-culture with CAFs, imaging was performed in the **D)** collagen matrix and **E)** fibronectin-rich matrix. **F)** Quantification of pore size. Violin plot represents the distribution of the data with the average and SD, n at least 4 individual devices. *$p \leq 0.05$.

The pores observed in the matrix are indicative of matrix degradation and are not observed in the MDA-MB-231 monocultures **(Fig. B.6 A-B)**. In the MDA-MB-231 monoculture, the pore size was 1865± 739 pixels ^{2} for the collagen matrix and 2323 ± 1191 pixels ^{2} for the fibronectin-rich matrix, revealing a significant increase in the pore size in the fibronectin-rich matrix (*P=0.0187) **(Fig. B.6 C)**. When comparing MDA-MB-231 monoculture with the co-culture with HMFs, there is a significant increase in pore size in the co-cultures (*P=0.0462), which was not observed in the collagen alone matrix. On the other hand, when comparing MDA-MB-231 monoculture with the co-culture with CAFs, no differences in pore size were found. Interestingly, MDA-MB-231 monoculture and in co-culture with CAFs showed the largest migration distance. Therefore, we hypothesize that migration must occur in a mechanism independent of MMP-2, -3, and -9 in these conditions.

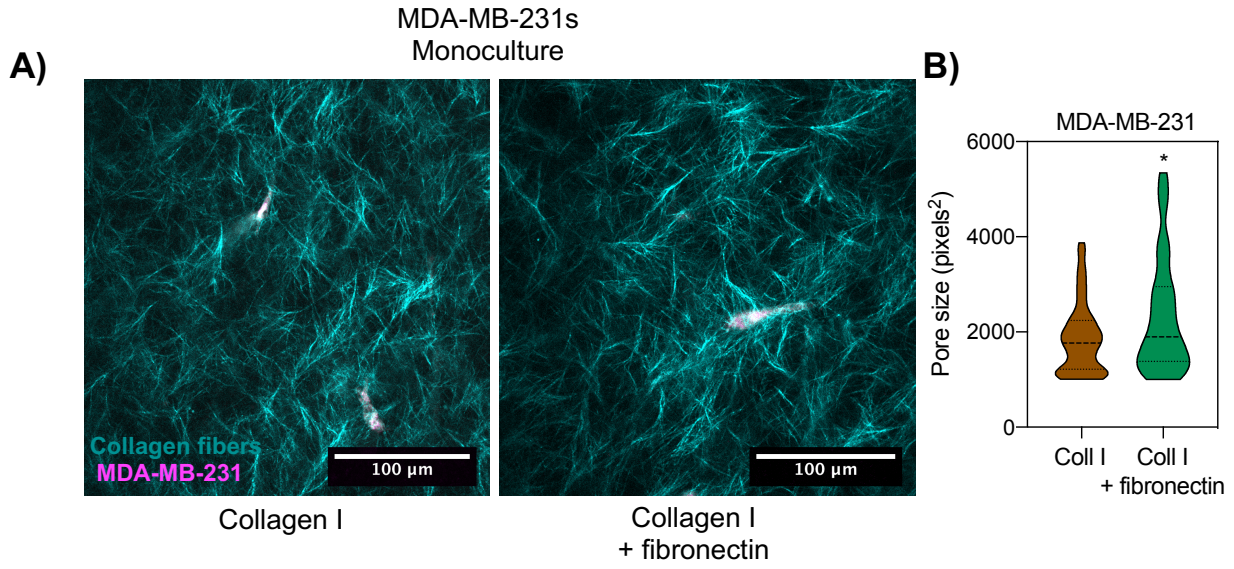

Figure B.6: Matrix visualization via Second Harmonic Generation (SHG) imaging in the MDA-MB-231 monoculture conditions. A) Collagen fibers are depicted in cyan, whereas MDA-MB-231cells appear in magenta. Left: Collagen matrix and Right: fibronectin-rich matrix. **B)** Quantification of pore size. Violin plot represents the distribution of the data with the average and SD, n at least 4 individual devices. *p ≤ 0.05.

Effect of MMP inhibition in breast cancer migration

To investigate if the degradation of the matrix was responsible for changes in MDA-MB-231 migration, an MMP inhibitor cocktail (marimastat) was used. Marimastat inhibits MMP-2, MMP-9, MMP-1 and other MMPs and, it has been reported to inhibit cancer cell migration 3D *in vitro* at a 30 µM concentration[191]. All cultured conditions were treated with 30 µM marimastat or a vehicle control (DMSO) for 48 hours and imaged (**Fig. B.7 A**).

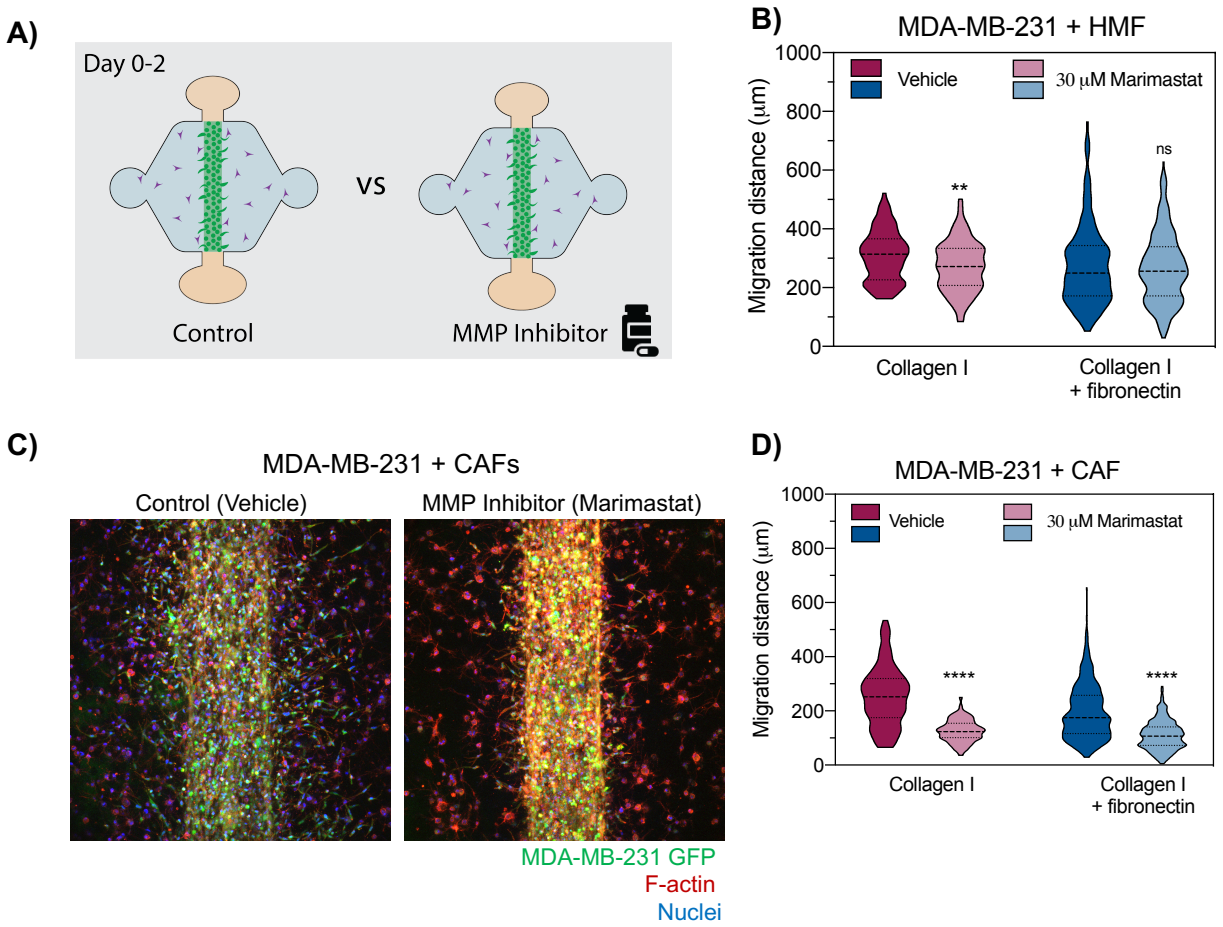

Figure B.7: Effect of MMP inhibition on cancer cell migration. A) Schematics of the general conditions. Co-cultures within the different matrices were treated for 48 hours with 30 µM marimastat (MMP inhibitor) and a DMSO vehicle (control). **B)** Migration distance of MDA-MB-231 in co-cultures with HMFs in the collagen matrix (left) and the fibronectin-rich matrix (right) for the vehicle control and treatment. **C)** Representative image of the co-culture with CAFs for the vehicle control (left image) and treatment with 30 µM marimastat (right image). **D)** Migration distance of MDA-MB-231 in co-cultures with CAFs in the collagen matrix (left) and the fibronectin-rich matrix (right) for the vehicle control and treatment with 30 µM marimastat. Violin plot represents the distribution of the data with the average and SD, n at least 4 individual devices. ** $p < 0.01$ and **** $p < 0.0001$

Then, the migration distance of the cancer cells from the edge of the lumen was quantified. In the presence of HMFs within a collagen matrix, the average migration distance was 308.3 ± 86.1 μm for the vehicle treatment and 272.8 ± 86.0 μm for the marimastat treatment, revealing a significant decrease in migration distance with marimastat treatment (**P=0.0069) (**Fig. B.7 B**). In the presence of HMFs within a fibronectin-rich matrix, the average migration distance was 276.5 ± 135.0 μm for the vehicle treatment and 266.8 ± 117.2 μm for the marimastat treatment, revealing no differences in migration distance with marimastat treatment (**Fig. B.7 B**). In the presence of CAFs within a collagen matrix (**Fig. B.7 C**), the average migration distance was 254.4 ± 109.1 μm for the vehicle treatment and 125.0 ± 40.9 μm for the marimastat treatment, revealing a significant decrease in migration distance with marimastat treatment (****P<0.0001) (**Fig. B.7 D**). In the presence of CAFs within a fibronectin-rich matrix, the average migration distance was 196.1 ± 99.0 μm for the vehicle treatment and 110.3 ± 53.3 μm for the marimastat treatment, revealing a significant decrease in migration distance with marimastat treatment (****P<0.0001) (**Fig. B.7 D**). These results do not match previously described results which demonstrated the efficacy of the inhibitor *in vitro*[191,330]. However, previous studies were performed in cancer cells monocultures and did not considered the contribution of fibroblasts, the major MMP secreting cell. Previous *in vitro* results have led to intensive efforts to develop and translate a broad spectrum MMP inhibitors such marimastat for cancer treatment, which concluded due to disappointing results in multiple clinical trials[331]. Of relevance in breast cancer, a phase III trial of the MMP inhibitor marimastat in metastatic breast cancer found no therapeutic benefit[332]. MMP inhibitor treatments provided no benefit in early stages either, as demonstrated by a phase II trial of marimastat and rebimastat. This study found a high incidence of musculoskeletal toxicity and failure of chronic dose levels to maintain plasma levels within the target range for these

drugs[333,334]. Our results demonstrating that marimastat is not effective in the presence of normal fibroblasts could provide an explanation of differences between the successful MMP inhibitors *in vitro* results and *in vivo* the unsuccessful results in clinical trials. Therefore, this hypothesis led us to investigate the influence of MMPs inhibitors using our model but in MDA-MB-231 monocultures.

In the presence of MDA-MB-231 monocultures within a collagen matrix, the average migration distance was 357.9 ± 108.9 μm for the vehicle treatment and 201.6 ± 67.5 μm for the marimastat treatment, revealing a significant decrease in migration distance with marimastat treatment (****P<0.0001) (**Fig. B.8**). In the presence of MDA-MB-231 monocultures within a fibronectin-rich matrix, the average migration distance was 316.6 ± 134.3 μm for the vehicle treatment and 211.3 ± 99.5 μm for the marimastat treatment, revealing a significant decrease in migration distance with marimastat treatment (****P<0.0001) (**Fig. B.8**).

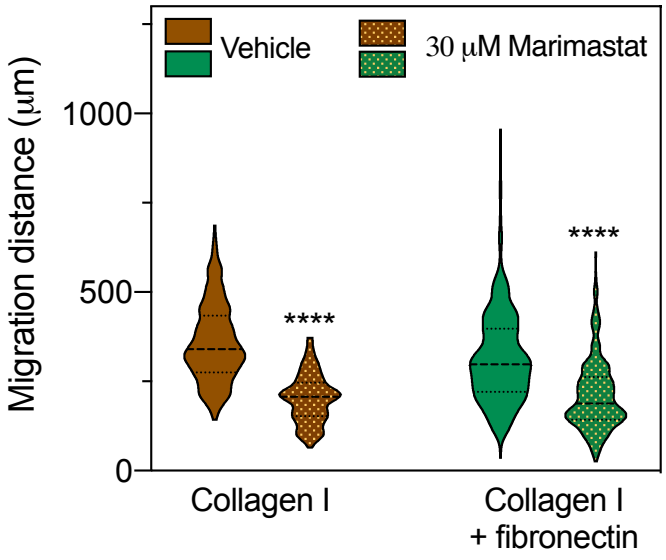

Figure B.8: Effect of MMP inhibition on cancer cell migration in the MDA-MB-231 monoculture conditions. Monocultures within the different matrices were treated for 48 hours with 30 μM marimastat (MMP inhibitor) and a DMSO vehicle (control). Migration distance of MDA-MB-231 in the collagen matrix (left) and the fibronectin-rich matrix (right) for the vehicle control and treatment. Violin plot represents the distribution of the data with the average and SD, n at least 4 individual devices. **** p <0.0001

These results indicate that in monocultures, the MMP inhibitors are highly effective, which are in agreement the literature [191,335]. Our results demonstrate the importance of *in vitro* models that incorporate TME components that are essential in the microenvironment. The best example is the previous *in vitro* studies demonstrating the efficacy of MMP inhibitors[191,335] without incorporating fibroblasts, a highly MMP-secreting cell type. The lack of incorporation of this component could explain limited successes of MMP inhibitors in clinical trials. Due to the poor performance in clinical trials, investment toward MMP inhibitors has fallen short. However, basic researchers support the idea of using more selective inhibitors. For this reason, as future directions, the use of patient-specific cells to build relevant *in vitro* models can be useful to elucidate the specific MMP to be target.

Conclusion

The microfluidic model presented in this paper mimics the *in vivo* invasion of cancer cells within a 3D microenvironment that includes relevant fibroblasts and extracellular matrix composition. We found that a tumor-like matrix such a fibronectin-rich matrix altered the normal mammary fibroblasts over the cancer-associated fibroblasts. Some of the changes observed were an increase in number of migrating cells, longer migration distance, higher secretion of MMPs as well as a resulting increase in matrix remodeling. In co-culture with HMFs, MMP inhibition was effective in the collagen matrix and not in the fibronectin-rich matrix. In addition, MMP inhibition was performed in cancer cells monocultures and was found to be effective regardless of the matrix which is consistent with the literature. In conclusion, without incorporating fibroblasts, a highly MMP-secreting cell type, MMPs inhibitors are highly effective. Therefore, the lack of incorporation of this component in *in vitro* studies could explain the limited successes of MMP

inhibitors in clinical trials. Overall, this data demonstrates the capability of the model to pinpoint the contribution of different components of the TME.

Acknowledgements

We acknowledge a fellowship from the UW-Madison Graduate Engineering Research Scholars program to KML and a Postdoctoral Fellowship from the Natural Sciences and Engineering Research Council of Canada to MMG. We also thank the NIH (R01EB010039 BRG). The authors acknowledge Patrick Ingram for discussions during early steps of the research.

Appendix C: Breast Cancer Cell-Derived Exosomes in Metastatic Progression[6]

Abstract

Breast cancer cell-derived exosomes have recently been found to promote tumor progression and metastasis. However, their effects on the colonization of the secondary tumor site are relatively unexplored. To better understand the effect of breast cancer cell-derived exosomes in lung metastasis, with particular emphasis on extravasation and colonization, we used a 3D organotypic microfluidic model that recreates a secondary lung site within in a collagen type 1 hydrogel. Using this model, we demonstrated the effects of breast cancer cell-derived exosomes in lung vessels and its effects on breast cancer cell extravasation. Preliminary results demonstrate that breast cancer cell-derived exosomes induce angiogenesis in the lung endothelium. In addition, we observed an increase in extravasation events from the lung endothelium when it was conditioned with breast cancer cell-derived exosomes.

[6] This chapter has been adapted from the manuscript in preparation: "Breast Cancer Cell-derived Exosomes Induce Angiogenesis and Facilitate Cancer Cell Extravasation in a 3D Organotypic Lung Microenvironment Model." The manuscript is authored by Karina M. Lugo-Cintrón*, María Virumbrales*, Jiong Chen, Jordan Ciciliano, Brendon Hoover, Regina Murphy, Bong-Hwan Sung, Alissa Weaver, David J. Beebe and Suzanne Ponik. *Contributed to this work equally.

Introduction

Breast cancer metastasis accounts for 90% of cancer-related deaths[174]. Metastasis is a complex and multistep process by which tumor cells migrate from the primary tumor through the surrounding matrix, intravasate into the vasculature (blood or lymphatic), extravasate and colonize a distant organ[336]. This complex process remains a primary challenge in treating cancer, demonstrating the lack of complete knowledge of the underlying mechanisms in the cascade. An increased interest in studying exosomes has recently emerged, since exosomes were found to play a role in cancer cell progression and metastasis.

Exosomes are a type of extracellular vesicle (EV), 30–150 nm in diameter, found to be secreted by most cells[337]. These EVs contain a wide variety of proteins, lipids, and RNAs (e.g., miRNAs) that are specific to their cell origin and can deliver cargo to both nearby and distant cells, having the ability to alter recipient cell bioactivities[337]. Exosomes are found in the supernatant of cultured cells as well as bodily fluids. Therefore, exosomes can act locally and distally, influencing the stroma in the tumor microenvironment (TME) and creating a favorable microenvironment at a distant site. In general, several reports have shown that exosomes play critical roles in modulating cancer cell growth, cancer cell migration[338], angiogenesis[339] and fibroblast differentiation towards an activated cancer-associated phenotype [340,341]. In the context of breast cancer, breast cancer cell-derived exosomes have recently been found to promote tumor progression and metastasis[342,343].

Breast cancer metastasis preferentially occurs to the bone, brain, liver and lung[290]. Recent work on exosome-mediated metastasis has demonstrated that tumor-derived exosomes with specific integrin patterns dictate the site of pre-metastatic niche formation[344]. At the pre-metastatic niche, tumor-derived exosomes educate resident cells and alter the stromal

microenvironment, generating a favorable environment for cancer cells. An example of how tumor-derived exosomes create a favorable pre-metastatic niche formation is demonstrated in breast cancer, where exosomes directly target lung blood vessels to induce vascular leakiness[344]. In addition, another study demonstrated that exosomes modulated resident lung fibroblasts and epithelial cells in breast cancer and melanoma[344,345]. However, the effects of exosomes on the metastatic site and their role in secondary site colonization are relatively unexplored. Hence, the interplay between metastatic breast cancer cells and its influence in the lung microenvironment can be further explored in a more controlled environment.

Although *in vitro* and *in vivo* models have been useful to advance our understanding of cancer, *in vitro* models do not mimic the complexity found *in vivo*. On the other hand, *in vivo* models are expensive, time-consuming and tractability is very challenging. Microfluidic devices are ideally suited to create models that recapitulate components of the microenvironment [94,104,105]. In addition, microfluidic devices allow to easily control the components to be tested and the spatiotemporal organization. In this paper, we used a microfluidic device to mimic the microenvironment of the lung secondary site to study the effects of breast cancer cell exosomes. We found that MDA-MB-231 derived exosomes contain angiogenic factors such as vascular endothelial growth factor (VEGF-C) and urokinase (uPA). In addition, conditioning of the lung microenvironment with exosomes induced an angiogenic-like phenotype in the biomimetic vessels. Furthermore, addition of cancer cells into the lumen and conditioning of the microenvironment demonstrated that exosomes promote breast cancer cell extravasation. Collectively, our findings demonstrate how breast cancer cell derived exosomes condition a lung microenvironment, allowing for the use of this model to further investigate the mechanisms of cancer cell extravasation.

Materials and methods

Cell culture

Human lung microvascular endothelial cells (HLMVECs, 10HU-030, iXCells, San Diego, CA) were cultured in standard cell culture flasks at a starting cell concentration of 5 x 10^5. Cultures were maintained with endothelial basal medium-2 (EBM-2, CC-3156) supplemented with EGM-2 MV SingleQuot Kit (CC-4147, Lonza, Allandale, NJ). HLMVECs were cultured to 90-95% confluency at passages 3 to 6 for all experiments. Human mammary adenocarcinoma cells, MDA-MB-231, transfected to stably expressing green fluorescent protein (GFP) were kind gift from Dr. Suzanne Ponik (University of Wisconsin, Madison). MDA-MB-231s were routinely cultured in high glucose DMEM (4.5 mg/ml, Gibco, Gaithersburg, MD, USA; #11965092) supplemented with 10% fetal bovine serum (FBS, VWR #97068-085) and 1% penicillin/streptomycin (ThermoFisher, Waltham, MA, USA; #15140-122). For all experiments, endothelial media was used. All cultures were kept in a humidified incubator at 37^{o}C with 5% CO_2.

Exosome purification

Exosomes were purified as previously described[346]. Briefly, conditioned media was collected from 80% confluent MDA-MB-231 cells cultured in 12-15 T125cm^2 for 48 h in Opti-MEM. Exosomes were isolated from conditioned media by serial centrifugation at 300 x g for 10 min, 2000 x g for 30 min, 10,000 x g for 30 min, and 100,000 x g for 18 h to respectively sediment live cells, dead cells, debris and large EVs, and small EVs. For further purification of ultra-centrifuged exosomes, a discontinuous iodixanol gradient was prepared by diluting OptiPrep™ (60% (w/v) aqueous iodixanol, 1114542, Axis-Shield PoC) with 0.25 M sucrose/10 mM Tris, pH 7.5 to yield 40%, 20%, 10%, and 5% solutions, which were added from the bottom to the top of polyallomer tube (344060, Beckman Coulter). The ultra-centrifuged-preparation was added on top of the

gradient and the continuous gradient was established through ultracentrifugation at 100,000 x g for 18 h. 12 fractions were collected (1 ml each), each subsequently diluted in PBS, pelleted through ultracentrifugation at 100,000 x g for 3 h, and finally resuspended in PBS. Total protein concentrations were measured with Micro BCA Protein Assay Kit (Thermo Fisher Scientific) as per manufacturer's instructions, using bovine serum albumin as standard. Exosome presence in fractions #6 and 7 was confirmed by Western blotting as described in following sections and used for experiments.

Microdevice fabrication

LumeNEXT fabrication was performed using standard soft lithography techniques, as previously described[185]. The microdevice consists of two PDMS layers, which define the microchamber; and a suspended PDMS rod, which is removed after polymerization of a hydrogel in the main chamber to create a tubular lumen structure. Sylgard 184 silicone elastomer kit (Dow Corning, 1317318) was mixed at a 10:1 base to curing agent ratio and poured over the SU-8 silicon master molds. Using the same mixture, 25 gauge (Fisher Scientific, 14-840-84) hypodermic needles were filled to make PDMS rods. PDMS components were then baked at 80°C for 4 h. After baking, 280 nm-diameter PDMS rods were extracted from the needles. The two layers were aligned and the PDMS rods were cut to ca. 4 mm and placed into the microdevice chamber. Finally, the microdevice was bonded to a glass-bottom dish (MatTek Corporation, P50G-1.5-30-F) using standard oxygen plasma bonding conditions. Finally, the microdevices were UV-sterilized for 15-20 min before use.

Microdevice setup

Devices were treated to achieve maximum hydrogel adhesion to the PDMS chamber. This treatment consisted of a 10 min wash with 2% poly(ethyleneimine) (PEI) (Sigma-Aldrich, 03880) in deionized sterile water (DSW) and a 30 min wash with 0.4% glutaraldehyde (GA) (Sigma-Aldrich, G6257) in DSW. Solutions were loaded into the side ports and aspirated the same way. After the GA incubation, the microdevices were washed thrice with DSW to remove any GA excess. To counteract evaporation, 150 µl of sacrificial phosphate buffered saline (PBS) (Fisher BioReagents, BP3991, diluted 1:10 with DSW) were added around the side of the MatTek dish.

Hydrogel preparation and lumen seeding in microdevices

The chamber was filled with a collagen solution at 4.5 mg/ml and 1 mg/ml of fibrinogen. To prepare this, 101.58 µl of high-density rat-tail collagen type 1 (Corning, 354249; referred to as collagen through the text) was neutralized with 2.81 µl of 0.5 M NaOH (Sigma-Aldrich, S8045), and osmolarity was adjusted by the addition of 10x PBS (20 µl) and DSW. Fibrinogen (Sigma-Aldrich, F8630) was resuspended at 20 mg/ml in DSW and 10 µl were added to the collagen mixture. Provided the pH of the collagen mixture was around 7.4 (verified with Litmus strips, Capitol Scientific, PH1170-7), the mixture was loaded through the side ports and polymerized at RT for 10 min. Finally, a small droplet of media (5 µL) was placed on top of the side ports to prevent evaporation, and devices were transferred to 37ºC for 1 h to allow collagen to fully polymerize. For the co-culture experiments, lung fibroblasts (CCL-210) were routinely trypsinized with 0.05% Trypsin-EDTA (Gibco) and resuspended at 1500 cells/µl in relevant media. 66 µl of the cell suspension were added to the collagen mixture, adjusting the volumes of 10x PBS (13.2 µl) and DSW (6.4 µl) accordingly to achieve relevant osmolarity. A 3 µl droplet of this hydrogel suspension was added onto the larger port of the microdevice to establish the co-cultures.

To seed the lumen models, HLMVECs were routinely trypsinized with 0.05% Trypsin-EDTA and resuspended at a concentration of 20,000 cells/ µl. 3 µl of this cell suspension was added per lumen via passive pumping mechanism. Cells were incubated for 45-60 minutes on either side of the device to ensure confluency on the hydrogel interface. Lumen models were cultured with relevant media for 3 days, refreshing media daily in the lumen and on the droplet located in the larger port. After that, lumens were conditioned each with 15 µl of a 5% solution of exosome suspension in relevant media, or 5% of fraction 2 (protein-free) as a control.

Nanoparticle tracking (NTA)

NTA measurements were performed with a NanoSight LM20 (NanoSight), equipped with a sample chamber with a 640-nm laser and a Viton fluoroelastomer O-ring. The samples were diluted 1:100 with sterile PBS and injected in the sample chamber with sterile syringes (BD Discardit II) until the liquid reached the tip of the nozzle. All measurements were performed at room temperature. The software used for capturing and analyzing the data was the NTA 2.0 Build 127. The samples were measured for 40 s with manual shutter and gain adjustments. Three measurements of the same sample were performed for both a protein-free fraction and the exosome fraction. The error bars displayed on the NTA graphs were obtained by the standard deviation of the different measurements of each sample. The mean size and SD values obtained by the NTA software correspond to the arithmetic values calculated with the sizes of all the particles analyzed by the software.

Western Blot

Equal volumes of the exosome fractions (5 µl) were separated by 4-12% Bis-Tris Plus Gels (Thermo-Fisher, NW04120BOX) and transferred onto PVDF membranes (Thermo-Fisher,

LC2005). The membranes were blocked with 5% bovine serum albumin (Sigma-Aldrich, A9205) in TBST buffer (Thermo-Fisher Scientific, 28358 for TBS and Sigma-Aldrich P1379 for Tween-20) overnight at 4 ºC. Membranes were then incubated in the same buffer containing antibodies specific to CD63 (1:2000; EXOAB-CD63A-1; System Bio Sciences), Alix (1:1000; ab117600; Abcam), Flotillin-1 (1:2000; ab41927; Abcam), HSP70 (1:1000; ab2787; Abcam), TSG-101 (1:1000; ab125011; Abcam), or GM130 (1:2000, ab52649, Abcam). After washing four times with TBST, horseradish peroxidase (HRP)-conjugated goat anti-rabbit IgG secondary antibody (1:10000; 111-035-144; JIR), rabbit anti-mouse (1:10000; 115-035-003; JIR) or donkey anti-goat (1:10000, 705-035-003; JIR) was applied in the same buffer for 1 h at room temperature. Immunoreactive bands were detected with SuperSignal West Femto Maximum Sensitivity Substrate (Thermo-Fisher Scientific, 34096) according to the manufacturer's instructions. Immunoreactive bands were captured using ImageLab image analysis software (BioRad, ver. 6.0.1).

Bead-based ELISA (Luminex-MAGPIX)

Multiplexed protein secretion analysis was performed on MDA-MB-231 derived exosomes. The analysis was performed using the Magnetic Bead-Based Multiplex ELISA system MAGPIX (Luminex Corporation) with a custom made Milliplex angiogenesis panel bead kit (R&D Systems, LXSAHM-24) as described elsewhere[113]. 5 µl of exosomes from a combined fraction 6 and 7, and 5 µl of a control fraction (fraction 1) were analyzed. Sample preparation and detection was performed following the manufacturer’s protocol. Data were collected with xPonent software (Luminex), and soluble factor concentrations in exosomes were calculated using mean fluorescence intensities (MFI) by creating a standard curve for each analyte using a five-parameter logistic (5-PL) curve fit.

Immunofluorescence

Cell-lined lumens were fixed after six days of culture by perfusing 4% paraformaldehyde (Alfa Aesar, 43368) in PBS through the lumen and incubating for 30 min. Lumens were washed three times with 0.1% Tween in PBS for 30 min between every step. Cells were then permeabilized with a 0.2% Triton® X-100 and 0.1 M Glycin solution in PBS for 30 min and blocked with 3% BSA in PBS overnight at 4 °C. Cells were incubated with human anti-CD31 (Abcam, ab9498) at 0.5 µg/ml overnight at 4°C. Cells were then stained with 1:50 Texas Red®-X Phalloidin (5 units), 4 µg/ml AlexaFluor 488 goat anti-mouse (Thermo-Fisher, A32723), and 50 µg/ml DAPI in 1% Tween-20, 3% BSA and 10% Goat Serum (Thermo-Fisher, 16210064) in PBS overnight at 4 °C. Finally, the lumens were washed with 0.1% Tween-20 in PBS to remove excess staining and minimize background.

Cell migration assays

For extravasation experiments, MDA-MB-231s were routinely trypsinized with 0.05% Trypsin-EDTA and resuspended at a concentration of 500 cells/ µl. 3 µl of the cancer cell suspension was added per lumen at day 4. After one hour of cell incubation, lumens were imaged. Then, lumens were conditioned with exosomes as previously described for 48 hours. Lumens were imaged afterwards to quantify the extravasated cancer cells.

Imaging

Confocal imaging was performed on a Nikon Spinning Disc confocal microscope. Microscopy images were analyzed using FIJI® (www.FIJI.com).

Statistics

All results are presented as the mean ± standard deviation. Data were analyzed using GraphPad Prism v8. Statistical significance was set at $p<0.05$. Normal distribution was assessed by the

Shapiro-Wilk test. One-to-one comparisons were performed with a Student's t-test with Welch's correction, after passing the Shapiro-Wilk normality test. Multiple comparisons by ANOVA were corrected using the Tukey test.

Results

For this paper, we first purified exosome fractions from metastatic breast cancer cells (MDA-MB-231) via ultracentrifugation in sucrose gradient, these exosomes where then used for characterization and for microdevice conditioning (**Figure C.1**).

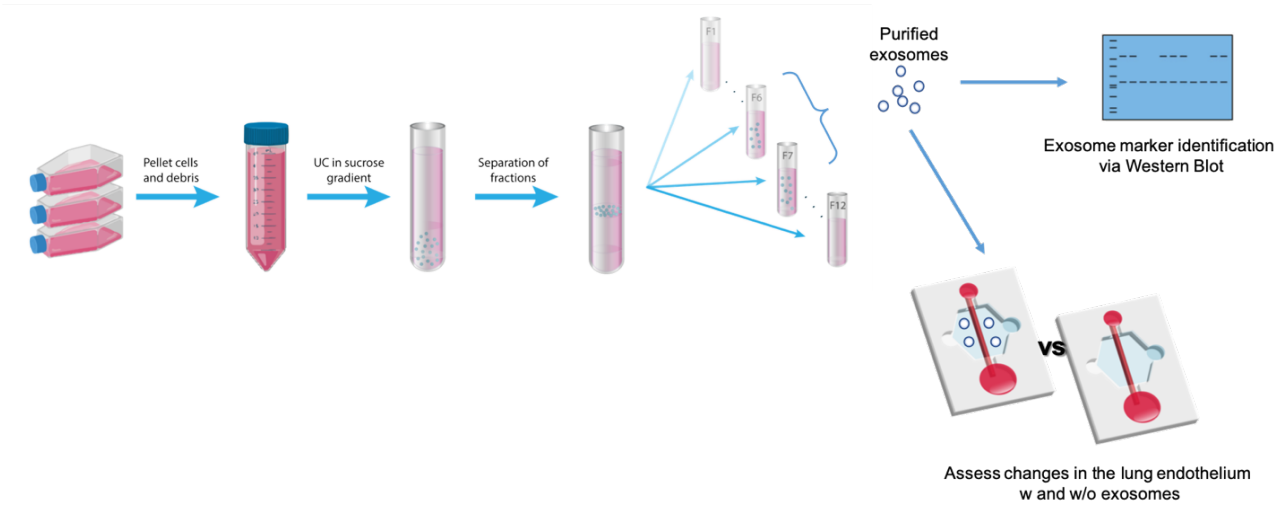

Figure C.1: Exosome isolation workflow. Purified exosomes are (1) characterized via Western Blot and (2) introduced into the microfluidic model to condition the lung endothelial lumen for 48 hours.

After isolation, exosome fractions were quantified via nanoparticle tracking and corroborated via Western Blot (**Figure C.2**). Positive identification of bands consistent with expression of exosome specific markers, CD63, Alix and TSG101 confirmed that the EVs isolated were exosomes (**Figure C.2 A**). In addition, exosomes were the size of the exosomes was analyzed via nanoparticle tracking. The nanoparticle results show a distribution of size for the isolated

exosomes, from 100 nm to 300 nm, in which the highest concentration was observed in 151.1± 2.1 nm with a concentration of $6 \cdot 10^{10}$ particles/mL (**Figure C.2 B**). After verification of our exosome isolate, we were interested in identifying pro-angiogenic soluble factors carried by exosomes. Soluble factors in the exosome fraction were analyzed using a multiplex bead-based ELISA kit. Analysis of soluble factors from exosomes revealed a 2-fold increase of uPA and a 3-fold increase in VEGF-A, two crucial and synergistic drivers of angiogenesis (**Figure C.2 C**).

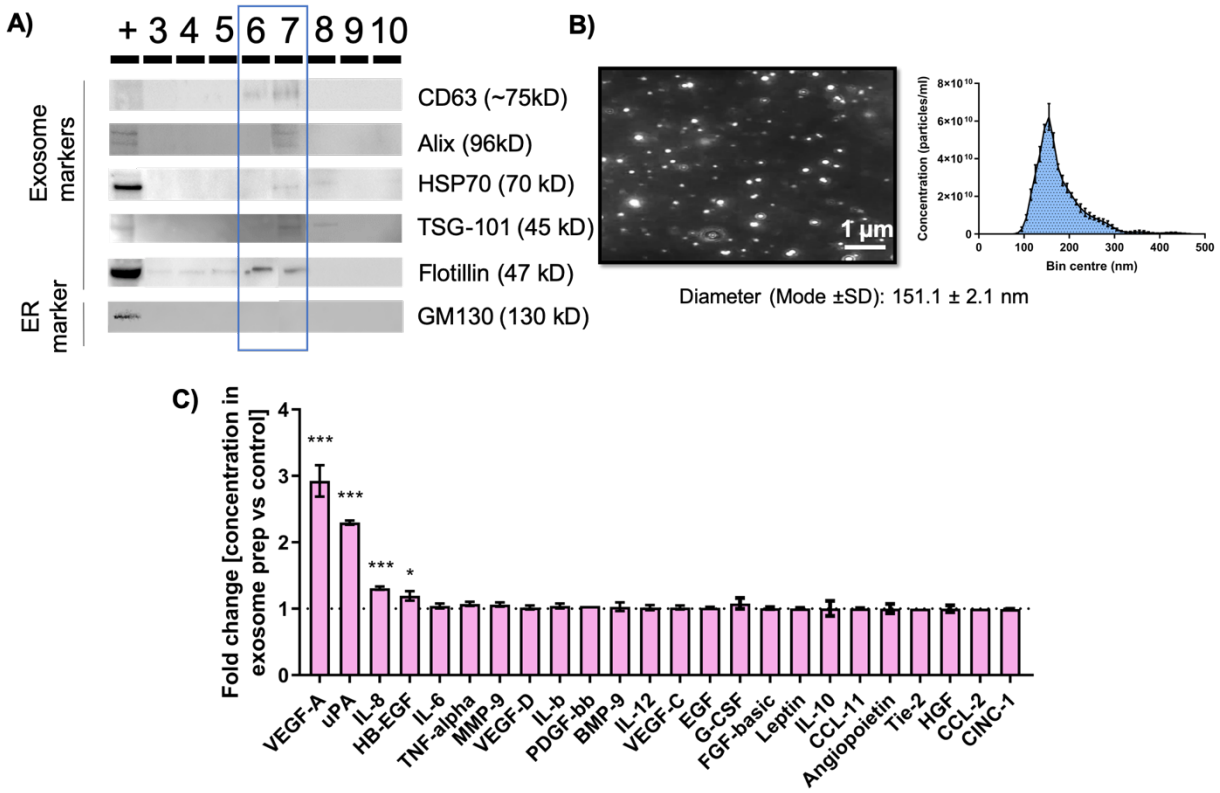

Figure C.2: Exosome characterization via A) western blot, B) nanoparticle tracking and C) bead-based multiplex ELISA.

To generate the 3D organotypic lung microenvironment model, we used a variation of LumeNEXT[185], a PDMS microdevice previously described by our lab. LumeNEXT enables the generation of luminal structures within a collagen hydrogel by polymerizing the collagen around

a PDMS rod. The rod is removed to define a tubular structure that can be lined with human lung microvascular endothelial cells to generate a 3D tubular blood-vessel model (**Figure C.3 A**). A droplet (3 µl) of hydrogel-embedded lung fibroblasts was co-cultured with the model by pipetting in the larger port. This system enabled both cell types to be co-cultured without direct contact between them in the microdevice (**Figure C.3 A-right**). After 4 days of co-culture, lung vessels were conditioned with a 5% dilution of purified exosome in relevant media for 48 hours. We observed that exosome conditioning of our lumen model induced features consistent with angiogenesis, such as weakening of cell-cell junctions, compared to the control (protein-free fraction from exosome isolation (fraction 1)) (**Figure C.3 B**).

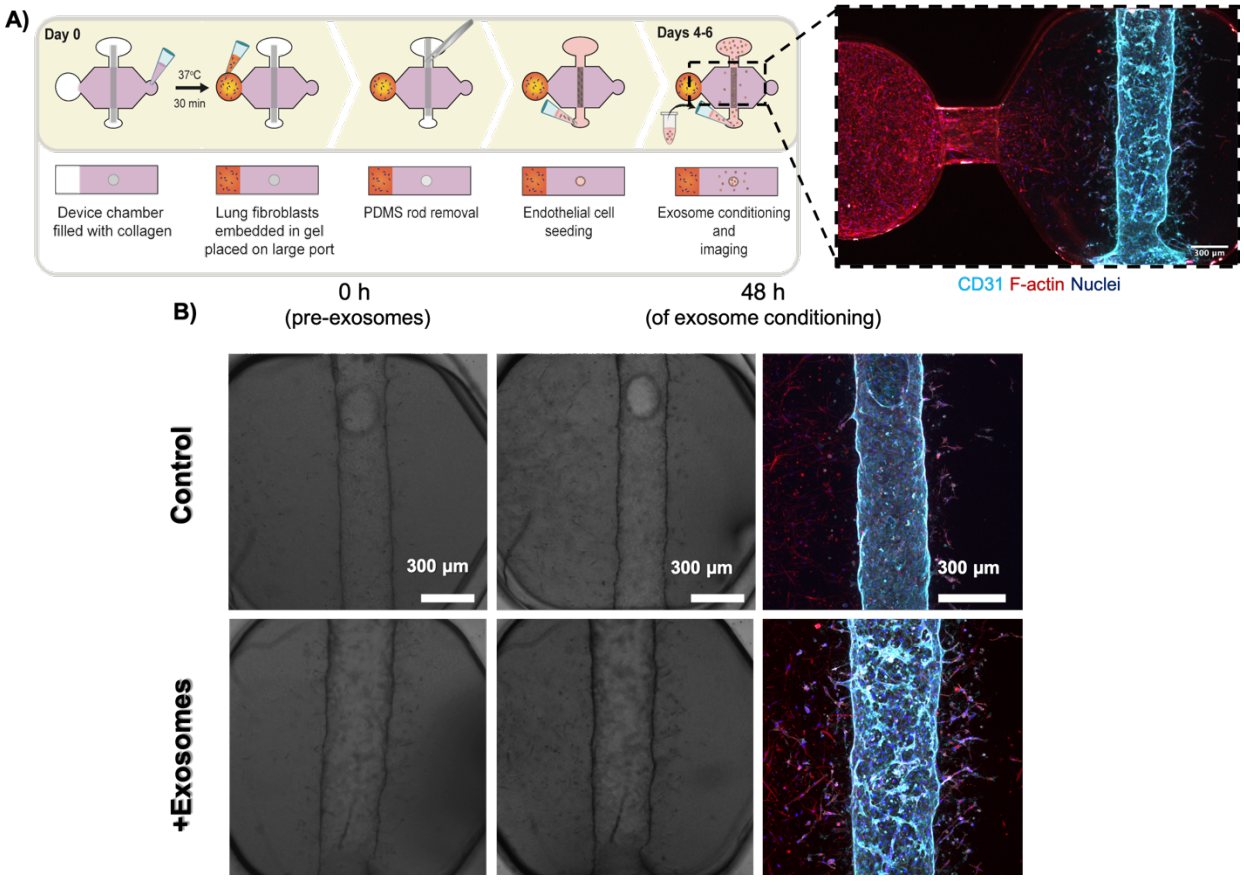

Figure C.3: Conditioning of secondary microenvironment with exosomes. A) Schematic of the microfluidic device and process. Device chamber is filled with collagen and after collagen polymerization, lung fibroblasts embedded in gel are placed on large port. PDMS rod is removed and lung endothelial cells are seeded into the lumen. Exosome conditioning starts on day 4 for 48 hours with imaging afterwards. Right: Confocal image of the device showing the

lung fibroblasts on the left (big port) and lung endothelial lumen in blue. **B)** Brightfield images of the control and exosome conditioning before addition of exosomes and after 48 hrs. Confocal images show endothelial sprouting in the exosome conditioned lumens.

Next, we sought to investigate the influence of exosome conditioning in breast cancer cell extravasation. Therefore, we loaded a solution of metastatic breast cancer cells through the lumen on day 4 (**Figure C.4 A**), vessels were imaged after 1 hour and after 48 hours. Qualitatively, more cancer cell extravasation is observed in the microenvironment that was conditioned with exosomes (**Figure C.4 B**). Indeed, preliminary results demonstrate that exosome conditioning increases breast cancer cell extravasation rates in our model (**Figure C.4 C**). In the control the ratio of extravasated MDA-MB-231 was 0.28 ± 0.03, which significantly increased by the addition of exosomes to 0.37 ± 0.03 (*P=0.0039).

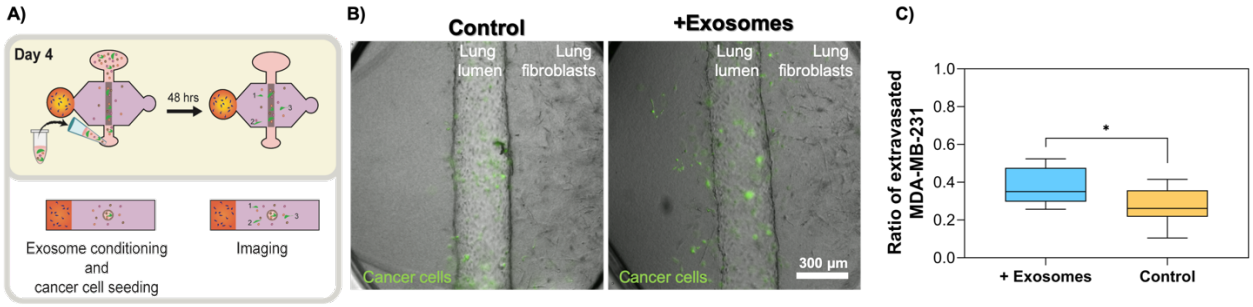

Figure C.4: Conditioning of secondary microenvironment with exosomes and addition of metastatic breast cancer cells (MDA-MB-231) in the device. A) Schematic of the conditioning and cancer cell addition process. **B)** Brightfield images on day 6 of the control and exosome conditioning, MDA-MB-231 are GFP tagged and can be observed in both conditions. **C)** Quantification of extravasation events presented as a ratio (number of extravasated cells with respect the number of cancer cells on day 1). n= 6 lumens from one experiment. Bars represent average ± S.E.M. *p ≤ 0.05.

Discussion and Conclusions:

In this chapter, we developed a microfluidic organotypic model of a lung metastasis site for breast cancer. The 3D organotypic lung model was successfully developed with the presence of lung fibroblasts and both cell types were successfully coculture together, keeping their structure. Characterization of MDA-MB-231-derived exosomes revealed that they contain pro-angiogenic

factors, such as VEGF and uPA. Then, we showed that exosome conditioning can induce a pro-angiogenic phenotype in biomimetic vessels. Finally, preliminary results indicate that exosome conditioning increases breast cancer cell extravasation rates in our model. Current work includes the quantification of vessel permeability, sprout number and length and gene expression analysis of the lumens. In addition, further quantification of factors/cargo in exosomes will be performed in solubilized exosomes. Future work includes the study of the mechanism through which the increased extravasation and invasion occurs in the model. Overall, modeling the lung microenvironment can help unravel the molecular mechanisms underlying breast cancer extravasation, facilitate the identification of new therapeutic targets and, in turn, advance therapeutic discovery.

Acknowledgements

Authors acknowledge Bridget White for help in the initial stages of this project, Dr Brian Burkel and Dr Sheena Kerr for help with western blot experiments and troubleshooting.

References

[1] R.L. Siegel, K.D. Miller, A. Jemal, Cancer statistics, 2019 (US statistics), CA. Cancer J. Clin. 69 (2019) 7–34. doi:10.3322/caac.21551.

[2] Christine L. Chaffer and Robert A. Weinberg, A Perspective on Cancer, (2011) 1559–1565. doi:10.1126/science.1203543.

[3] V. Mahadevan, I.R. Hart, Tumour angiogenesis and metastasis, Eur. J. Cancer Clin. Oncol. 27 (1991) 679–680. doi:10.1016/0277-5379(91)90163-8.

[4] A.M. Alizadeh, S. Shiri, S. Farsinejad, Metastasis review: from bench to bedside, 2014. doi:10.1007/s13277-014-2421-z.

[5] I.J. Fidler, M.L. Kripke, The challenge of targeting metastasis, Cancer Metastasis Rev. 34 (2015) 635–641. doi:10.1007/s10555-015-9586-9.

[6] S.A. Stacker, S.P. Williams, T. Karnezis, R. Shayan, S.B. Fox, M.G. Achen, Lymphangiogenesis and lymphatic vessel remodelling in cancer, Nat. Rev. Cancer. 14 (2014) 159–172. doi:10.1038/nrc3677.

[7] F.R. Balkwill, M. Capasso, T. Hagemann, The tumor microenvironment at a glance, J. Cell Sci. 125 (2012) 5591–5596. doi:10.1242/jcs.116392.

[8] A.E. Place, S. Jin Huh, K. Polyak, The microenvironment in breast cancer progression: biology and implications for treatment, Breast Cancer Res. 13 (2011) 227. doi:10.1186/bcr2912.

[9] J.M. Curry, J. Sprandio, D. Cognetti, A. Luginbuhl, V. Bar-Ad, E. Pribitkin, M. Tuluc, Tumor microenvironment in head and neck squamous cell carcinoma, Semin. Oncol. 41 (2014) 217–234. doi:10.1053/j.seminoncol.2014.03.003.

[10] T.L. Whiteside, Tumor-Derived Exosomes and Their Role in Cancer Progression, 1st ed., Elsevier Inc., 2016. doi:10.1016/bs.acc.2015.12.005.

[11] M.M. Mueller, N.E. Fusenig, Friends or foes - Bipolar effects of the tumour stroma in cancer, Nat. Rev. Cancer. 4 (2004) 839–849. doi:10.1038/nrc1477.

[12] M.R. Junttila, F.J. De Sauvage, Influence of tumour micro-environment heterogeneity on therapeutic response, Nature. 501 (2013) 346–354. doi:10.1038/nature12626.

[13] B. Erdogan, D.J. Webb, Cancer-associated fibroblasts modulate growth factor signaling and extracellular matrix remodeling to regulate tumor metastasis, Biochem. Soc. Trans. 45 (2017) 229–236. doi:10.1042/BST20160387.

[14] L. Tao, G. Huang, H. Song, Y. Chen, L. Chen, Cancer associated fibroblasts: An essential role in the tumor microenvironment (review), Oncol. Lett. 14 (2017) 2611–2620. doi:10.3892/ol.2017.6497.

[15] F.T. Wang, W.E.I. Sun, J.T. Zhang, Y.Z. Fan, Cancer-associated fibroblast regulation of tumor neo-angiogenesis as a therapeutic target in cancer (Review), Oncol. Lett. 17 (2019) 3055–3065. doi:10.3892/ol.2019.9973.

[16] P. Carmeliet, VEGF as a key mediator of angiogenesis in cancer, Oncology. 69 (2005) 4–10. doi:10.1159/000088478.

[17] C.R. Pradeep, E.S. Sunila, G. Kuttan, Expression of vascular endothelial growth factor (VEGF) and VEGF receptors in tumor angiogenesis and malignancies, Integr. Cancer Ther. 4 (2005) 315–321. doi:10.1177/1534735405282557.

[18] R. Paduch, The role of lymphangiogenesis and angiogenesis in tumor metastasis, Cell. Oncol. 39 (2016) 397–410. doi:10.1007/s13402-016-0281-9.

[19] J. Dittmer, B. Leyh, The impact of tumor stroma on drug response in breast cancer,

Semin. Cancer Biol. 31 (2015) 3–15. doi:10.1016/j.semcancer.2014.05.006.
[20] K. Velaei, N. Samadi, B. Barazvan, J. Soleimani Rad, Tumor microenvironment-mediated chemoresistance in breast cancer, Breast. 30 (2016) 92–100. doi:10.1016/j.breast.2016.09.002.
[21] S.D. Soysal, A. Tzankov, S.E. Muenst, Role of the Tumor Microenvironment in Breast Cancer, Pathobiology. 82 (2015) 142–152. doi:10.1159/000430499.
[22] R. Kalluri, M. Zeisberg, Fibroblasts in cancer., Nat. Rev. Cancer. 6 (2006) 392–401. doi:10.1038/nrc1877.
[23] K. Pietras, A. Östman, Hallmarks of cancer: Interactions with the tumor stroma, Exp. Cell Res. 316 (2010) 1324–1331. doi:10.1016/j.yexcr.2010.02.045.
[24] P. Lu, V.M. Weaver, Z. Werb, The extracellular matrix: A dynamic niche in cancer progression, J. Cell Biol. 196 (2012) 395–406. doi:10.1083/jcb.201102147.
[25] M. Augsten, Cancer-Associated Fibroblasts as Another Polarized Cell Type of the Tumor Microenvironment, Front. Oncol. 4 (2014) 1–8. doi:10.3389/fonc.2014.00062.
[26] K. Räsänen, A. Vaheri, Activation of fibroblasts in cancer stroma, Exp. Cell Res. 316 (2010) 2713–2722. doi:10.1016/j.yexcr.2010.04.032.
[27] A. Marusyk, D.P. Tabassum, M. Janiszewska, A.E. Place, A. Trinh, A.I. Rozhok, S. Pyne, J.L. Guerriero, S. Shu, M. Ekram, A. Ishkin, D.P. Cahill, Y. Nikolsky, T.A. Chan, M.F. Rimawi, S. Hilsenbeck, R. Schiff, K.C. Osborne, A. Letai, K. Polyak, Spatial proximity to fibroblasts impacts molecular features and therapeutic sensitivity of breast cancer cells influencing clinical outcomes, Cancer Res. 76 (2016) 6495–6506. doi:10.1158/0008-5472.CAN-16-1457.
[28] C.C. Jia, T.T. Wang, W. Liu, B.S. Fu, X.F. Hua, G.Y. Wang, T.J. Li, X. Li, X.Y. Wu, Y. Tai, J. Zhou, G.H. Chen, Q. Zhang, Cancer-Associated Fibroblasts from Hepatocellular Carcinoma Promote Malignant Cell Proliferation by HGF Secretion, PLoS One. 8 (2013) 1–9. doi:10.1371/journal.pone.0063243.
[29] M. Augsten, E. Sjöberg, O. Frings, S.U. Vorrink, J. Frijhoff, E. Olsson, Å. Borg, A. Östman, Cancer-associated fibroblasts expressing CXCL14 rely upon NOS1-derived nitric oxide signaling for their tumor- Supporting properties, Cancer Res. 74 (2014) 2999–3010. doi:10.1158/0008-5472.CAN-13-2740.
[30] X. Wang, W. Zhang, X. Sun, Y. Lin, W. Chen, Cancer-associated fibroblasts induce epithelial-mesenchymal transition through secreted cytokines in endometrial cancer cells, Oncol. Lett. 15 (2018) 5694–5702. doi:10.3892/ol.2018.8000.
[31] D.W. Jung, Z.M. Che, J. Kim, K. Kim, K.Y. Kim, D. Williams, J. Kim, Tumor-stromal crosstalk in invasion of oral squamous cell carcinoma: A pivotal role of CCL7, Int. J. Cancer. 127 (2010) 332–344. doi:10.1002/ijc.25060.
[32] A. Glentis, P. Oertle, P. Mariani, A. Chikina, F. El Marjou, Y. Attieh, F. Zaccarini, M. Lae, D. Loew, F. Dingli, P. Sirven, M. Schoumacher, B.G. Gurchenkov, M. Plodinec, D.M. Vignjevic, Cancer-associated fibroblasts induce metalloprotease-independent cancer cell invasion of the basement membrane, Nat. Commun. 8 (2017) 1–13. doi:10.1038/s41467-017-00985-8.
[33] L.J.A.C. Hawinkels, M. Paauwe, H.W. Verspaget, E. Wiercinska, J.M. Van Der Zon, K. Van Der Ploeg, P.J. Koelink, J.H.N. Lindeman, W. Mesker, P. Ten Dijke, C.F.M. Sier, Interaction with colon cancer cells hyperactivates TGF-β signaling in cancer-associated fibroblasts, Oncogene. 33 (2014) 97–107. doi:10.1038/onc.2012.536.
[34] C. Gaggioli, S. Hooper, C. Hidalgo-Carcedo, R. Grosse, J.F. Marshall, K. Harrington, E.

Sahai, Fibroblast-led collective invasion of carcinoma cells with differing roles for RhoGTPases in leading and following cells, Nat. Cell Biol. 9 (2007) 1392–1400. doi:10.1038/ncb1658.
[35] A.D. Theocharis, S.S. Skandalis, C. Gialeli, N.K. Karamanos, Extracellular matrix structure, Adv. Drug Deliv. Rev. 97 (2016) 4–27. doi:10.1016/j.addr.2015.11.001.
[36] Frantz Christian, S. Kathleen, V.M. Weaver, The extracellular matrix at a glance, J. Cell Sci. 14 (2010) 4195–4200. doi:10.1242/jcs.023820.
[37] P.P. Provenzano, K.W. Eliceiri, J.M. Campbell, D.R. Inman, J.G. White, P.J. Keely, Collagen reorganization at the tumor-stromal interface facilitates local invasion, BMC Med. 4 (2006) 1–15. doi:10.1186/1741-7015-4-38.
[38] K.R. Levental, H. Yu, L. Kass, J.N. Lakins, M. Egeblad, J.T. Erler, S.F.T. Fong, K. Csiszar, A. Giaccia, W. Weninger, M. Yamauchi, D.L. Gasser, V.M. Weaver, Matrix Crosslinking Forces Tumor Progression by Enhancing Integrin Signaling, Cell. 139 (2009) 891–906. doi:10.1016/j.cell.2009.10.027.
[39] L.A. Tomko, R.C. Hill, A. Barrett, J.M. Szulczewski, M.W. Conklin, K.W. Eliceiri, P.J. Keely, K.C. Hansen, S.M. Ponik, Targeted matrisome analysis identifies thrombospondin-2 and tenascin-C in aligned collagen stroma from invasive breast carcinoma, Sci. Rep. 8 (2018) 1–11. doi:10.1038/s41598-018-31126-w.
[40] P.P. Provenzano, D.R. Inman, K.W. Eliceiri, J.G. Knittel, L. Yan, C.T. Rueden, J.G. White, P.J. Keely, Collagen density promotes mammary tumor initiation and progression, BMC Med. 6 (2008) 11. doi:10.1186/1741-7015-6-11.
[41] I. Acerbi, L. Cassereau, I. Dean, Q. Shi, A. Au, C. Park, Y.Y. Chen, J. Liphardt, E.S. Hwang, V.M. Weaver, Human breast cancer invasion and aggression correlates with ECM stiffening and immune cell infiltration, Integr. Biol. (United Kingdom). 7 (2015) 1120–1134. doi:10.1039/c5ib00040h.
[42] O. Chaudhuri, S.T. Koshy, C. Branco Da Cunha, J.W. Shin, C.S. Verbeke, K.H. Allison, D.J. Mooney, Extracellular matrix stiffness and composition jointly regulate the induction of malignant phenotypes in mammary epithelium, Nat. Mater. 13 (2014) 970–978. doi:10.1038/nmat4009.
[43] E.S. Radisky, D.C. Radisky, Matrix metalloproteinases as breast cancer drivers and therapeutic targets, Front. Biosci. - Landmark. 20 (2015) 1144–1163. doi:10.2741/4364.
[44] D.O. Velez, B. Tsui, T. Goshia, C.L. Chute, A. Han, H. Carter, S.I. Fraley, 3D collagen architecture induces a conserved migratory and transcriptional response linked to vasculogenic mimicry, Nat. Commun. 8 (2017). doi:10.1038/s41467-017-01556-7.
[45] P.P. Provenzano, D.R. Inman, K.W. Eliceiri, J. Patricia, Matrix density-induced mechanoregulation of breast cell pheno, Matrix. 28 (2009) 4326–4343. doi:10.1038/onc.2009.299.Matrix.
[46] B.A. Morris, B. Burkel, S.M. Ponik, J. Fan, J.S. Condeelis, J.A. Aguire-Ghiso, J. Castracane, J.M. Denu, P.J. Keely, Collagen Matrix Density Drives the Metabolic Shift in Breast Cancer Cells, EBioMedicine. 13 (2016) 146–156. doi:10.1016/j.ebiom.2016.10.012.
[47] V.L. Bautch, K.M. Caron, Blood and lymphatic vessel formation, Cold Spring Harb. Perspect. Biol. 7 (2015) 1–14. doi:10.1101/cshperspect.a008268.
[48] J. Folkman, Role of angiogenesis in tumor growth and metastasis., Semin. Oncol. 29 (2002) 15–18. doi:10.1053/sonc.2002.37263.
[49] J.A. Nagy, S.H. Chang, A.M. Dvorak, H.F. Dvorak, Why are tumour blood vessels

abnormal and why is it important to know?, Br. J. Cancer. 100 (2009) 865–869. doi:10.1038/sj.bjc.6604929.
[50] S.J. Mandriota, L. Jussila, M. Jeltsch, A. Compagni, D. Baetens, R. Prevo, S. Banerji, J. Huarte, R. Montesano, D.G. Jackson, L. Orci, K. Alitalo, G. Christofori, M.S. Pepper, Vascular endothelial growth factor-C-mediated lymphangiogenesis promotes tumour metastasis, EMBO J. 20 (2001) 672–682. doi:10.1093/emboj/20.4.672.
[51] J. Hagendoorn, R. Tong, D. Fukumura, Q. Lin, J. Lobo, T.P. Padera, L. Xu, R. Kucherlapati, R.K. Jain, Onset of abnormal blood and lymphatic vessel function and interstitial hypertension in early stages of carcinogenesis, Cancer Res. 66 (2006) 3360–3364. doi:10.1158/0008-5472.CAN-05-2655.
[52] B. S, N. J, W. S, C. S, S. J, T. R, J. M, J. D., LYVE-1, a new homologue of the {CD}44 glycoprotein, J. Cell Biol. 144 (1999) 789–801. doi:10.1083/jcb.144.4.789.
[53] J.T. Wigle, G. Oliver, Prox1 function is required for the development of the murine lymphatic system, Cell. 98 (1999) 769–778. doi:10.1016/S0092-8674(00)81511-1.
[54] S. Breiteneder-geleff, A. Soleiman, H. Kowalski, R. Horvat, G. Amann, E. Kriehuber, K. Diem, W. Weninger, E. Tschachler, K. Alitalo, D. Kerjaschki, Angiosarcomas Express Mixed Endothelial Phenotypes of Blood and Lymphatic Capillaries, 154 (1999) 1–10. papers3://publication/uuid/E73DE9B6-1195-4415-A4F2-8BE66B469C6E.
[55] P.T. Truong, V. Vinh-Hung, G. Cserni, W.A. Woodward, P. Tai, G. Vlastos, The number of positive nodes and the ratio of positive to excised nodes are significant predictors of survival in women with micrometastatic node-positive breast cancer, Eur. J. Cancer. 44 (2008) 1670–1677. doi:10.1016/j.ejca.2008.05.011.
[56] J. Shen, K.K. Hunt, N.Q. Mirza, S. Krishnamurthy, S.E. Singletary, H.M. Kuerer, F. Meric-Bernstam, B. Feig, M.I. Ross, F.G. Ames, G. V. Babiera, Intramammary lymph node metastases are an independent predictor of poor outcome in patients with breast carcinoma, Cancer. 101 (2004) 1330–1337. doi:10.1002/cncr.20515.
[57] V.F.Z. Marinho, K. Metze, F.S.F. Sanches, G.F.S. Rocha, H. Gobbi, Lymph vascular invasion in invasive mammary carcinomas identified by the endothelial lymphatic marker D2-40 is associated with other indicators of poor prognosis, BMC Cancer. 8 (2008) 1–9. doi:10.1186/1471-2407-8-64.
[58] and J.M.D. Sainsbury, J. Richard C., Handbook of Diseases of the Breast, 1998.
[59] P.A. Kyzas, S. Geleff, A. Batistatou, N.J. Agnantis, D. Stefanou, Evidence for lymphangiogenesis and its prognostic implications in head and neck squamous cell carcinoma, J. Pathol. 206 (2005) 170–177. doi:10.1002/path.1776.
[60] N.J.P. Beasley, R. Prevo, S. Banerji, R.D. Leek, J. Moore, P. van Trappen, G. Cox, A.L. Harris, D.G. Jackson, Intratumoral lymphangiogenesis and lymph node metastasis in head and neck cancer, Cancer Res. 62 (2002) 1315–1320.
[61] S. Ran, L. Volk, K. Hall, M.J. Flister, Lymphangiogenesis and lymphatic metastasis in breast cancer, Pathophysiology. 17 (2010) 229–251. doi:10.1016/j.pathophys.2009.11.003.
[62] I. Choi, S. Lee, Y.K. Hong, The new era of the lymphatic system: No longer secondary to the blood vascular system, Cold Spring Harb. Perspect. Med. 2 (2012) 1–23. doi:10.1101/cshperspect.a006445.
[63] T. Tammela, K. Alitalo, Lymphangiogenesis: Molecular Mechanisms and Future Promise, Cell. 140 (2010) 460–476. doi:10.1016/j.cell.2010.01.045.
[64] H. Maby-El Hajjami, T. V. Petrova, Developmental and pathological lymphangiogenesis:

From models to human disease, Histochem. Cell Biol. 130 (2008) 1063–1078. doi:10.1007/s00418-008-0525-5.
[65] K. Alitalo, T. Tammela, T. V. Petrova, Lymphangiogenesis in development and human disease, Nature. 438 (2005) 946–953. doi:10.1038/nature04480.
[66] Y. Cao, Emerging mechanisms of tumour lymphangiogenesis and lymphatic metastasis, Nat. Rev. Cancer. 5 (2005) 735–743. doi:10.1038/nrc1693.
[67] R. Shayan, M.G. Achen, S.A. Stacker, Lymphatic vessels in cancer metastasis: Bridging the gaps, Carcinogenesis. 27 (2006) 1729–1738. doi:10.1093/carcin/bgl031.
[68] R.K. Jain, P. Carmeliet, SnapShot: Tumor angiogenesis., Cell. 149 (2012) 1408-1408.e1. doi:10.1016/j.cell.2012.05.025.
[69] M. Raica, D. Ribatti, Targeting Tumor Lymphangiogenesis: An Update, Curr. Med. Chem. 17 (2010) 698–708. doi:10.2174/092986710790514471.
[70] R.K. Jain, T.P. Padera, Antilymphangiogenic Therapy, J. Natl. Cancer Inst. 94 (2002) 785–787.
[71] M.G. Achen, G.B. Mann, S.A. Stacker, Targeting lymphangiogenesis to prevent tumour metastasis, Br. J. Cancer. 94 (2006) 1355–1360. doi:10.1038/sj.bjc.6603120.
[72] E. Lee, E.J. Fertig, K. Jin, S. Sukumar, N.B. Pandey, A.S. Popel, Breast cancer cells condition lymphatic endothelial cells within pre-metastatic niches to promote metastasis, Nat. Commun. 5 (2014) 1–16. doi:10.1038/ncomms5715.
[73] E. Lee, N.B. Pandey, A.S. Popel, Lymphatic endothelial cells support tumor growth in breast cancer, Sci. Rep. 4 (2014) 1–11. doi:10.1038/srep05853.
[74] A.R. Harris, M.J. Perez, J.M. Munson, Docetaxel facilitates lymphatic-tumor crosstalk to promote lymphangiogenesis and cancer progression, BMC Cancer. 18 (2018) 1–16. doi:10.1186/s12885-018-4619-8.
[75] K. Jin, N.B. Pandey, A.S. Popel, Simultaneous blockade of IL-6 and CCL5 signaling for synergistic inhibition of triple-negative breast cancer growth and metastasis, Breast Cancer Res. 20 (2018) 1–10. doi:10.1186/s13058-018-0981-3.
[76] C.H. Nguyen, D. Senfter, J. Basilio, S. Holzner, S. Stadler, S. Krieger, N. Huttary, D. Milovanovic, K. Viola, I. Simonitsch-Klupp, W. Jäger, R. de Martin, G. Krupitza, NF-κB contributes to MMP1 expression in breast cancer spheroids causing paracrine PAR1 activation and disintegrations in the lymph endothelial barrier in vitro, Oncotarget. 6 (2015) 39262–39275. doi:10.18632/oncotarget.5741.
[77] S.D. Sackett, D.M. Tremmel, F. Ma, A.K. Feeney, R.M. Maguire, M.E. Brown, Y. Zhou, X. Li, C. O'Brien, L. Li, W.J. Burlingham, J.S. Odorico, Extracellular matrix scaffold and hydrogel derived from decellularized and delipidized human pancreas, Sci. Rep. 8 (2018) 1–16. doi:10.1038/s41598-018-28857-1.
[78] K.O. Osuala, M. Sameni, S. Shah, N. Aggarwal, M.L. Simonait, O.E. Franco, Y. Hong, S.W. Hayward, F. Behbod, R.R. Mattingly, B.F. Sloane, Il-6 signaling between ductal carcinoma in situ cells and carcinoma-associated fibroblasts mediates tumor cell growth and migration, BMC Cancer. 15 (2015) 584. doi:10.1186/s12885-015-1576-3.
[79] A. Orimo, P.B. Gupta, D.C. Sgroi, F. Arenzana-Seisdedos, T. Delaunay, R. Naeem, V.J. Carey, A.L. Richardson, R.A. Weinberg, Stromal fibroblasts present in invasive human breast carcinomas promote tumor growth and angiogenesis through elevated SDF-1/CXCL12 secretion, Cell. 121 (2005) 335–348. doi:10.1016/j.cell.2005.02.034.
[80] X. Qin, M. Yan, J. Zhang, X. Wang, Z. Shen, Z. Lv, Z. Li, W. Wei, W. Chen, TGFβ3-mediated induction of Periostin facilitates head and neck cancer growth and is associated

with metastasis, Sci. Rep. 6 (2016) 1–15. doi:10.1038/srep20587.
[81] X. Qin, M. Yan, X. Wang, Q. Xu, X. Wang, X. Zhu, J. Shi, Z. Li, J. Zhang, W. Chen, Cancer-associated Fibroblast-derived IL-6 promotes head and neck cancer progression via the osteopontin-NF-kappa B signaling pathway, Theranostics. 8 (2018) 921–940. doi:10.7150/thno.22182.
[82] S.M. Kakkad, M. Solaiyappan, P. Argani, S. Sukumar, L.K. Jacobs, D. Leibfritz, Z. Bhujwalla, K. Glunde, Collagen I fiber density increases in lymph node positive breast cancers : pilot study breast cancers : pilot study, J. Biomed. Opt. (2012). doi:10.1117/1.JBO.17.11.116017.
[83] F. Bruyere, A. Noel, Lymphangiogenesis: in vitro and in vivo models, FASEB J. 24 (2010) 8–21. doi:10.1096/fj.09-132852.
[84] F. Bruyère, L. Melen-Lamalle, S. Blacher, G. Roland, M. Thiry, L. Moons, F. Frankenne, P. Carmeliet, K. Alitalo, C. Libert, J.P. Sleeman, J.M. Foidart, A. Noël, Modeling lymphangiogenesis in a three-dimensional culture system, Nat. Methods. 5 (2008) 431–437. doi:10.1038/nmeth.1205.
[85] T. Karpanen, M. Egeblad, M.J. Karkkainen, H. Kubo, S. Ylä-Herttuala, K. Alitalo, Vascular endothelial growth factor C promotes tumor lymphangiogenesis and intralymphatic tumor growth, Cancer Res. 61 (2001) 1786–1790. doi:10.1016/j.bbi.2012.07.009.
[86] J. Matsui, Y. Funahashi, T. Uenaka, T. Watanabe, A. Tsuruoka, M. Asada, Multi-kinase inhibitor E7080 suppresses lymph node and lung metastases of human mammary breast tumor MDA-MB-231 via inhibition of vascular endothelial growth factor-receptor (VEGF-R) 2 and VEGF-R3 kinase, Clin. Cancer Res. 14 (2008) 5459–5465. doi:10.1158/1078-0432.CCR-07-5270.
[87] M. Giussani, G. Merlino, V. Cappelletti, E. Tagliabue, M.G. Daidone, Tumor-extracellular matrix interactions: Identification of tools associated with breast cancer progression, Semin. Cancer Biol. 35 (2015) 3–10. doi:10.1016/j.semcancer.2015.09.012.
[88] K. Duval, H. Grover, L.H. Han, Y. Mou, A.F. Pegoraro, J. Fredberg, Z. Chen, Modeling physiological events in 2D vs. 3D cell culture, Physiology. 32 (2017) 266–277. doi:10.1152/physiol.00036.2016.
[89] R. Edmondson, J.J. Broglie, A.F. Adcock, L. Yang, Three-dimensional cell culture systems and their applications in drug discovery and cell-based biosensors, Assay Drug Dev. Technol. 12 (2014) 207–218. doi:10.1089/adt.2014.573.
[90] G.Y. Lee, P.A. Kenny, E.H. Lee, M.J. Bissell, The expression of Sox17 identifies and regulates hemogenic endothelium Raedun, 377 (2009) 364–377. doi:10.1038/nmeth1015.Three-dimensional.
[91] P.A. Kenny, G.Y. Lee, C.A. Myers, R.M. Neve, J.R. Semeiks, P.T. Spellman, K. Lorenz, E.H. Lee, M.H. Barcellos-Hoff, O.W. Petersen, J.W. Gray, M.J. Bissell, The morphologies of breast cancer cell lines in three-dimensional assays correlate with their profiles of gene expression, Mol. Oncol. 1 (2007) 84–96. doi:10.1016/j.molonc.2007.02.004.
[92] C.C. Liang, A.Y. Park, J.L. Guan, In vitro scratch assay: A convenient and inexpensive method for analysis of cell migration in vitro, Nat. Protoc. 2 (2007) 329–333. doi:10.1038/nprot.2007.30.
[93] and K.M.Y. Andrew D. Doyle, Ryan J. Petrie, Matthew L. Kutys, Dimensions in Cell Migration, Curr Opin Cell Biol. 25 (2013) 642–649. doi:10.1016/j.ceb.2013.06.004.

[94] L.L. Bischel, K.E. Sung, J.A. Jiménez-Torres, B. Mader, P.J. Keely, D.J. Beebe, The importance of being a lumen, FASEB J. 28 (2014) 4583–4590. doi:10.1096/fj.13-243733.
[95] K.E. Sung, X. Su, E. Berthier, C. Pehlke, A. Friedl, D.J. Beebe, Understanding the Impact of 2D and 3D Fibroblast Cultures on In Vitro Breast Cancer Models, PLoS One. 8 (2013) 1–13. doi:10.1371/journal.pone.0076373.
[96] D. Huh, G.A. Hamilton, D.E. Ingber, From Three-Dimensional Cell Culture to Organs-on-Chips, Trends Cell Biol. 21 (2011) 745–754. doi:10.1016/j.tcb.2011.09.005.From.
[97] J.A. Jiménez-Torres, M. Virumbrales-Muñoz, K.E. Sung, M.H. Lee, E.J. Abel, D.J. Beebe, Patient-specific organotypic blood vessels as an in vitro model for anti-angiogenic drug response testing in renal cell carcinoma, EBioMedicine. 42 (2019) 408–419. doi:10.1016/j.ebiom.2019.03.026.
[98] M. Swartz, The physiology of the lymphatic system, Adv. Drug Deliv. Rev. 50 (2001) 3–20. doi:10.1016/S0169-409X(01)00150-8.
[99] R. Küppers, Mechanisms of B-cell lymphoma pathogenesis, Nat. Rev. Cancer. 5 (2005) 251.
[100] T.P. Padera, E.F.J. Meijer, L.L. Munn, The Lymphatic System in Disease Processes and Cancer Progression, Annu. Rev. Biomed. Eng. 18 (2016) 125–158. doi:10.1146/annurev-bioeng-112315-031200.
[101] A. Kaipainen, J. Korhonen, T. Mustonen, V.W. van Hinsbergh, G.H. Fang, D. Dumont, M. Breitman, K. Alitalo, Expression of the fms-like tyrosine kinase 4 gene becomes restricted to lymphatic endothelium during development., Proc. Natl. Acad. Sci. 92 (1995) 3566–3570. doi:10.1073/pnas.92.8.3566.
[102] S. Banerji, J. Ni, S.-X. Wang, S. Clasper, J. Su, R. Tammi, M. Jones, D.G. Jackson, LYVE-1, a New Homologue of the CD44 Glycoprotein, Is a Lymph-specific Receptor for Hyaluronan, J. Cell Biol. 144 (1999) 789–801. doi:10.1083/jcb.144.4.789.
[103] F. Bruyère, A. Noël, Lymphangiogenesis: in vitro and in vivo models, FASEB J. 24 (2010) 8–21. doi:10.1096/fj.09-132852.
[104] D. Huh, Y.S. Torisawa, G.A. Hamilton, H.J. Kim, D.E. Ingber, Microengineered physiological biomimicry: Organs-on-Chips, Lab Chip. 12 (2012) 2156–2164. doi:10.1039/c2lc40089h.
[105] S.N. Bhatia, D.E. Ingber, Microfluidic organs-on-chips., Nat. Biotechnol. 32 (2014) 760–72. doi:10.1038/nbt.2989.
[106] B. Zhang, A. Korolj, B.F.L. Lai, M. Radisic, Advances in organ-on-a-chip engineering, Nat. Rev. Mater. 3 (2018) 257–278. doi:10.1038/s41578-018-0034-7.
[107] K.M. Chrobak, D.R. Potter, J. Tien, Formation of perfused, functional microvascular tubes in vitro, Microvasc. Res. 71 (2006) 185–196. doi:10.1016/j.mvr.2006.02.005.
[108] S. Raghavan, C.M. Nelson, J.D. Baranski, E. Lim, C.S. Chen, Geometrically Controlled Endothelial Tubulogenesis in Micropatterned Gels, Tissue Eng. Part A. 16 (2010) 2255–2263. doi:10.1089/ten.tea.2009.0584.
[109] Y. Zheng, J. Chen, M. Craven, N.W. Choi, S. Totorica, A. Diaz-Santana, P. Kermani, B. Hempstead, C. Fischbach-Teschl, J.A. Lopez, A.D. Stroock, In vitro microvessels for the study of angiogenesis and thrombosis, Proc. Natl. Acad. Sci. 109 (2012) 9342–9347. doi:10.1073/pnas.1201240109.
[110] L.L. Bischel, S.-H. Lee, D.J. Beebe, A Practical Method for Patterning Lumens through ECM Hydrogels via Viscous Finger Patterning, J. Lab. Autom. 17 (2012) 96–103. doi:10.1177/2211068211426694.

[111] L.L. Bischel, E.W.K. Young, B.R. Mader, D.J. Beebe, Tubeless microfluidic angiogenesis assay with three-dimensional endothelial-lined microvessels, Biomaterials. 34 (2013) 1471–1477. doi:10.1016/j.biomaterials.2012.11.005.
[112] J.A. Jiménez-Torres, S.L. Peery, K.E. Sung, D.J. Beebe, LumeNEXT: A Practical Method to Pattern Luminal Structures in ECM Gels, Adv. Healthc. Mater. 5 (2016) 198–204. doi:10.1002/adhm.201500608.
[113] P.N. Ingram, L.E. Hind, J.A. Jiminez-Torres, A. Huttenlocher, D.J. Beebe, An Accessible Organotypic Microvessel Model Using iPSC-Derived Endothelium, Adv. Healthc. Mater. 7 (2018) 1–10. doi:10.1002/adhm.201700497.
[114] S. Kim, H. Lee, M. Chung, N.L. Jeon, Engineering of functional, perfusable 3D microvascular networks on a chip, Lab Chip. 13 (2013) 1489. doi:10.1039/c3lc41320a.
[115] J.S. Jeon, S. Bersini, J.A. Whisler, M.B. Chen, G. Dubini, J.L. Charest, M. Moretti, R.D. Kamm, Generation of 3D functional microvascular networks with human mesenchymal stem cells in microfluidic systems, Integr. Biol. 6 (2014) 555–563. doi:10.1039/C3IB40267C.
[116] M. Sato, N. Sasaki, M. Ato, S. Hirakawa, K. Sato, K. Sato, Microcirculation-on-a-Chip: A Microfluidic Platform for Assaying Blood- and Lymphatic-Vessel Permeability, PLoS One. 10 (2015) e0137301. doi:10.1371/journal.pone.0137301.
[117] S. Kim, M. Chung, N.L. Jeon, Three-dimensional biomimetic model to reconstitute sprouting lymphangiogenesis in vitro, Biomaterials. 78 (2016) 115–128. doi:10.1016/j.biomaterials.2015.11.019.
[118] G.M. Price, K.M. Chrobak, J. Tien, Effect of cyclic AMP on barrier function of human lymphatic microvascular tubes, Microvasc. Res. 76 (2008) 46–51. doi:10.1016/j.mvr.2008.02.003.
[119] K.H.K. Wong, J.G. Truslow, A.H. Khankhel, K.L.S. Chan, J. Tien, Artificial lymphatic drainage systems for vascularized microfluidic scaffolds, J. Biomed. Mater. Res. Part A. 101A (2013) 2181–2190. doi:10.1002/jbm.a.34524.
[120] M.H. Ulvmar, T. Mäkinen, Heterogeneity in the lymphatic vascular system and its origin, Cardiovasc. Res. 111 (2016) 310–321. doi:10.1093/cvr/cvw175.
[121] S. Mohanakumar, J. Majgaard, N. Telinius, N. Katballe, E. Pahle, V. Hjortdal, D. Boedtkjer, Spontaneous and α-adrenoceptor-induced contractility in human collecting lymphatic vessels require chloride, Am. J. Physiol. Circ. Physiol. 315 (2018) H389–H401. doi:10.1152/ajpheart.00551.2017.
[122] J. Schindelin, I. Arganda-Carreras, E. Frise, V. Kaynig, M. Longair, T. Pietzsch, S. Preibisch, C. Rueden, S. Saalfeld, B. Schmid, J.-Y. Tinevez, D.J. White, V. Hartenstein, K. Eliceiri, P. Tomancak, A. Cardona, Fiji: an open-source platform for biological-image analysis, Nat. Methods. 9 (2012) 676.
[123] V.H. Huxley, F.E. Curry, R.H. Adamson, Quantitative fluorescence microscopy on single capillaries: alpha-lactalbumin transport., Am. J. Physiol. 252 (1987) H188-97. doi:10.1152/ajpheart.1987.252.1.H188.
[124] F.J. Byfield, R.K. Reen, T.P. Shentu, I. Levitan, K.J. Gooch, Endothelial actin and cell stiffness is modulated by substrate stiffness in 2D and 3D, J. Biomech. 42 (2009) 1114–1119. doi:10.1016/j.jbiomech.2009.02.012.
[125] Y. Xiong, C.C. Brinkman, K.S. Famulski, E.F. Mongodin, C.J. Lord, K.L. Hippen, B.R. Blazar, J.S. Bromberg, A robust in vitro model for trans-lymphatic endothelial migration, Sci. Rep. 7 (2017) 1–14. doi:10.1038/s41598-017-01575-w.

[126] V.A. Nguyen, C. Fürhapter, P. Obexer, H. Stössel, N. Romani, N. Sepp, Endothelial cells from cord blood CD133+CD34+ progenitors share phenotypic, functional and gene expression profile similarities with lymphatics, J. Cell. Mol. Med. 13 (2009) 522–534. doi:10.1111/j.1582-4934.2008.00340.x.
[127] L.S. Cooley, M.M. Handsley, Z. Zhou, M.A. Lafleur, C.J. Pennington, E.W. Thompson, E. Poschl, D.R. Edwards, Reversible transdifferentiation of blood vascular endothelial cells to a lymphatic-like phenotype in vitro, J. Cell Sci. 123 (2010) 3808–3816. doi:10.1242/jcs.064279.
[128] G.M. Walker, D.J. Beebe, A passive pumping method for microfluidic devices, Lab Chip. V (2002) 131–134. doi:10.1039/b204381e.
[129] D.T. Sweet, J.M. Jiménez, J. Chang, P.R. Hess, P. Mericko-Ishizuka, J. Fu, L. Xia, P.F. Davies, M.L. Kahn, Lymph flow regulates collecting lymphatic vessel maturation in vivo, J. Clin. Invest. 125 (2015) 2995–3007. doi:10.1172/JCI79386.
[130] U. Michel, O. Schneider, C. Kirchhof, S. Meisel, A. Smirnov, J. Wiltfang, P. Rieckmann, Production of follistatin in porcine endothelial cells: differential regulation by bacterial compounds and the synthetic glucocorticoid RU 28362., Endocrinology. 137 (1996) 4925–4934. doi:10.1210/endo.137.11.8895365.
[131] D.H. Kozian, M. Ziche, H.G. Augustin, The activin-binding protein follistatin regulates autocrine endothelial cell activity and induces angiogenesis., Lab. Invest. 76 (1997) 267–76.
[132] V. Kirkin, W. Thiele, P. Baumann, R. Mazitschek, K. Rohde, G. Fellbrich, H. Weich, J. Waltenberger, A. Giannis, J.P. Sleeman, MAZ51, an indolinone that inhibits endothelial cell and tumor cell growth in vitro, suppresses tumor growth in vivo., Int. J. Cancer. 112 (2004) 986–93. doi:10.1002/ijc.20509.
[133] P. Cirri, P. Chiarugi, Cancer-associated-fibroblasts and tumour cells: a diabolic liaison driving cancer progression, Cancer Metastasis Rev. 31 (2012) 195–208. doi:10.1007/s10555-011-9340-x.
[134] P. Baluk, J. Fuxe, H. Hashizume, T. Romano, E. Lashnits, S. Butz, D. Vestweber, M. Corada, C. Molendini, E. Dejana, D.M. McDonald, Functionally specialized junctions between endothelial cells of lymphatic vessels, J. Exp. Med. 204 (2007) 2349–2362. doi:10.1084/jem.20062596.
[135] K.N. Margaris, R. a Black, Modelling the lymphatic system : challenges and opportunities, J R Soc Interface. 9 (2012) 601–612. doi:10.1098/rsif.2011.0751.
[136] C.C. O'Morchoe, P.J. O'Morchoe, Differences in lymphatic and blood capillary permeability: ultrastructural-functional correlations., Lymphology. 20 (1987) 205–9.
[137] J.P. Scallan, V.H. Huxley, In vivo determination of collecting lymphatic vessel permeability to albumin: A role for lymphatics in exchange, J. Physiol. 588 (2010) 243–254. doi:10.1113/jphysiol.2009.179622.
[138] K. Niessen, G. Zhang, J.B. Ridgway, H. Chen, M. Yan, ALK1 signaling regulates early postnatal lymphatic vessel development, Blood. 115 (2010) 1654–1661. doi:10.1182/blood-2009-07-235655.
[139] K. Kajiya, S. Hirakawa, B. Ma, I. Drinnenberg, M. Detmar, Hepatocyte growth factor promotes lymphatic vessel formation and function, EMBO J. 24 (2005) 2885–2895. doi:10.1038/sj.emboj.7600763.
[140] R. Cao, M. a Bjorndahl, M.I. Gallego, S. Chen, P. Religa, a J. Hansen, Y. Cao, Hepatocyte growth factor is a novel lymphangiogenic factor with an indirect mechamism

of action, Blood. . (2006) 3531–3537. doi:10.1182/blood-2005-06-2538.Supported.
[141] L. Jussila, K. Alitalo, Vascular growth factors and lymphangiogenesis., Physiol. Rev. 82 (2002) 673–700. doi:10.1152/physrev.00005.2002.
[142] E. Kriehuber, S. Breiteneder-Geleff, M. Groeger, A. Soleiman, S.F. Schoppmann, G. Stingl, D. Kerjaschki, D. Maurer, Isolation and Characterization of Dermal Lymphatic and Blood Endothelial Cells Reveal Stable and Functionally Specialized Cell Lineages, J. Exp. Med. 194 (2001) 797 LP – 808.
[143] Y. Cao, P. Linden, J. Farnebo, R. Cao, A. Eriksson, V. Kumar, J.-H. Qi, L. Claesson-Welsh, K. Alitalo, Vascular endothelial growth factor C induces angiogenesis in vivo, Proc. Natl. Acad. Sci. 95 (1998) 14389 LP – 14394.
[144] S. Nakao, S. Zandi, Y. Hata, S. Kawahara, R. Arita, A. Schering, D. Sun, M.I. Melhorn, Y. Ito, N. Lara-Castillo, T. Ishibashi, A. Hafezi-Moghadam, Blood vessel endothelial VEGFR-2 delays lymphangiogenesis: an endogenous trapping mechanism links lymph- and angiogenesis, Blood. 117 (2011) 1081 LP – 1090.
[145] T. Natori, M. Sata, M. Washida, Y. Hirata, R. Nagai, M. Makuuchi, G-CSF stimulates angiogenesis and promotes tumor growth: potential contribution of bone marrow-derived endothelial progenitor cells., Biochem. Biophys. Res. Commun. 297 (2002) 1058–61.
[146] A.W. Roberts, G-CSF: A key regulator of neutrophil production, but that's not all!, Growth Factors. 23 (2005) 33–41. doi:10.1080/08977190500055836.
[147] M.E. Hammond, G.R. Lapointe, P.H. Feucht, S. Hilt, C.A. Gallegos, C.A. Gordon, M.A. Giedlin, G. Mullenbach, P. Tekamp-Olson, IL-8 induces neutrophil chemotaxis predominantly via type I IL-8 receptors., J. Immunol. 155 (1995) 1428–33.
[148] D.J. Phillips, D.M. De Kretser, Follistatin: A multifunctional regulatory protein, Front. Neuroendocrinol. 19 (1998) 287–322. doi:10.1006/frne.1998.0169.
[149] M. Heinz, H.L. Niederleithner, E. Puujalka, A. Soler-Cardona, M. Grusch, H. Pehamberger, R. Loewe, P. Petzelbauer, Activin A Is Anti-Lymphangiogenic in a Melanoma Mouse Model, J. Invest. Dermatol. 135 (2015) 212–221. doi:10.1038/jid.2014.328.
[150] K.L. Jones, A. Mansell, S. Patella, B.J. Scott, M.P. Hedger, D.M. de Kretser, D.J. Phillips, Activin A is a critical component of the inflammatory response, and its binding protein, follistatin, reduces mortality in endotoxemia, Proc. Natl. Acad. Sci. 104 (2007) 16239–16244. doi:10.1073/pnas.0705971104.
[151] J.S. Hansen, S. Rutti, C. Arous, J.O. Clemmesen, N.H. Secher, A. Drescher, C. Gonelle-Gispert, P.A. Halban, B.K. Pedersen, C. Weigert, K. Bouzakri, P. Plomgaard, Circulating Follistatin Is Liver-Derived and Regulated by the Glucagon-to-Insulin Ratio., J. Clin. Endocrinol. Metab. 101 (2016) 550–60. doi:10.1210/jc.2015-3668.
[152] and D.C.Z. Walter E Cromer, Scott D. Zawieja, Binu Tharakan, F.A.H.A., Ed W. Childs, M. Karen Newell, The effects of inflammatory cytokines on lymphatic endothelial barrier function, Angiogenesis. 17 (2014) 395–406. doi:10.1007/s10456-013-9393-2.
[153] M.B. Aldrich, E.M. Sevick-muraca, Cytokine Cytokines are systemic effectors of lymphatic function in acute inflammation q, Cytokine. 64 (2013) 362–369. doi:10.1016/j.cyto.2013.05.015.
[154] J.W. Breslin, S.Y. Yuan, M.H. Wu, VEGF-C alters barrier function of cultured lymphatic endothelial cells through a VEGFR-3-dependent mechanism., Lymphat. Res. Biol. 5 (2007) 105–13. doi:10.1089/lrb.2007.1004.
[155] J. Wilting, J. Becker, K. Buttler, H.A. Weich, Lymphatics and inflammation., Curr. Med.

Chem. 16 (2009) 4581–92.
[156] R. Huggenberger, S.S. Siddiqui, D. Brander, S. Ullmann, K. Zimmermann, M. Antsiferova, S. Werner, K. Alitalo, M. Detmar, An important role of lymphatic vessel activation in limiting acute inflammation., Blood. 117 (2011) 4667–78. doi:10.1182/blood-2010-10-316356.
[157] P.-A. Lachance, A. Hazen, E.M. Sevick-Muraca, Lymphatic Vascular Response to Acute Inflammation, PLoS One. 8 (2013) e76078.
[158] K.W. Tan, S.Z. Chong, F.H.S. Wong, M. Evrard, S.M.-L. Tan, J. Keeble, D.M. Kemeny, L.G. Ng, J.-P. Abastado, V. Angeli, Neutrophils contribute to inflammatory lymphangiogenesis by increasing VEGF-A bioavailability and secreting VEGF-D, Blood. 122 (2013) 3666 LP – 3677.
[159] J.D. McAllaster, M.S. Cohen, Role of the lymphatics in cancer metastasis and chemotherapy applications, Adv. Drug Deliv. Rev. 63 (2011) 867–875. doi:10.1016/j.addr.2011.05.014.
[160] A. Alitalo, M. Detmar, Interaction of tumor cells and lymphatic vessels in cancer progression, Oncogene. 31 (2012) 4499–4508. doi:10.1038/onc.2011.602.
[161] J. Stachura, M. Wachowska, W.W. Kilarski, E. Güç, J. Golab, A. Muchowicz, The dual role of tumor lymphatic vessels in dissemination of metastases and immune response development, Oncoimmunology. 5 (2016). doi:10.1080/2162402X.2016.1182278.
[162] K.A. Mouchemore, R.L. Anderson, J.A. Hamilton, Neutrophils, G-CSF and their contribution to breast cancer metastasis., FEBS J. 285 (2018) 665–679. doi:10.1111/febs.14206.
[163] C. Zabkiewicz, J. Resaul, R. Hargest, W.G. Jiang, L. Ye, Increased expression of follistatin in breast cancer reduces invasiveness and clinically correlates with better survival, Cancer Genomics and Proteomics. 14 (2017) 241–251. doi:10.21873/cgp.20035.
[164] B. Strilic, L. Yang, J. Albarrán-Juárez, L. Wachsmuth, K. Han, U.C. Müller, M. Pasparakis, S. Offermanns, Tumour-cell-induced endothelial cell necroptosis via death receptor 6 promotes metastasis., Nature. 536 (2016) 215–8. doi:10.1038/nature19076.
[165] P.G. Balasubramanian, R. Chiquet-ehrismann, R.P. Tucker, J.C. Adams, The Evolution of Extracellular Matrix, 21 (2010) 4300–4305. doi:10.1091/mbc.E10.
[166] A. Teti, Regulation of cellular functions by extracellular matrix., J. Am. Soc. Nephrol. 2 (1992) S83-7. http://www.ncbi.nlm.nih.gov/pubmed/1318112.
[167] T.R. Cox, J.T. Erler, Remodeling and homeostasis of the extracellular matrix: implications for fibrotic diseases and cancer., Dis. Model. Mech. 4 (2011) 165–178. doi:10.1242/dmm.004077.
[168] P. Lu, V.M. Weaver, Z. Werb, The extracellular matrix : A dynamic niche in cancer progression, 196 (2012) 395–406. doi:10.1083/jcb.201102147.
[169] M.W. Conklin, P.J. Keely, Why the stroma matters in breast cancer: Insights into breast cancer patient outcomes through the examination of stromal biomarkers, Cell Adhes. Migr. 6 (2012) 249–260. doi:10.4161/cam.20567.
[170] M. Fang, J. Yuan, C. Peng, Y. Li, Collagen as a double-edged sword in tumor progression, (2014) 2871–2882. doi:10.1007/s13277-013-1511-7.
[171] G. -G Zhu, A. Kauppila, L. Risteli, M. Mäkinen, F. Stenbäck, J. Risteli, Immunohistochemical study of type I collagen and type I pN-collagen in benign and malignant ovarian neoplasms, Cancer. 75 (1995) 1010–1017. doi:10.1002/1097-0142(19950215)75:4<1010::AID-CNCR2820750417>3.0.CO;2-O.

[172] C.R. Drifka, J. Tod, A.G. Loeffler, Y. Liu, G.J. Thomas, K.W. Eliceiri, W.J. Kao, Periductal stromal collagen topology of pancreatic ductal adenocarcinoma differs from that of normal and chronic pancreatitis, Mod. Pathol. 28 (2015) 1470–1480. doi:10.1038/modpathol.2015.97.
[173] I.J. Huijbers, M. Iravani, S. Popov, D. Robertson, S. Al-Sarraj, C. Jones, C.M. Isacke, A role for fibrillar collagen deposition and the collagen internalization receptor endo180 in glioma invasion, PLoS One. 5 (2010) 1–12. doi:10.1371/journal.pone.0009808.
[174] R. a W. Christine L Chaffer, A perspective on cancer cell metastasis, Nat. Med. 19 (2013) 179–92. doi:10.1126/science.1203543.
[175] C.M. Ghajar, X. Chen, J.W. Harris, V. Suresh, C.C.W. Hughes, L. Jeon, A.J. Putnam, S.C. George, The Effect of Matrix Density on the Regulation of 3-D Capillary Morphogenesis, 94 (2008) 1930–1941. doi:10.1529/biophysj.107.120774.
[176] E. Kniazeva, A.J. Putnam, Endothelial cell traction and ECM density influence both capillary morphogenesis and maintenance in 3-D, (2009) 179–187. doi:10.1152/ajpcell.00018.2009.
[177] L.T. Edgar, C.J. Underwood, J.E. Guilkey, J.B. Hoying, J.A. Weiss, Extracellular Matrix Density Regulates the Rate of Neovessel Growth and Branching in Sprouting Angiogenesis, 9 (2014) 1–10. doi:10.1371/journal.pone.0085178.
[178] A.M.I.R.S. Hamloo, N.E.M. Ohammadaliha, S.A.C.H. Eilshorn, A.M.Y.L.B. Auer, A Comparative Study of Collagen Matrix Density Effect on Endothelial Sprout Formation Using Experimental and Computational Approaches, 44 (2016) 929–941. doi:10.1007/s10439-015-1416-2.
[179] Simona Podgrabinska, D.G.J. and M.S. Pascal Braun, Paula Velasco, Bryan Kloos, Michael S. Pepper, Molecular characterization of lymphatic endothelial cells, 99 (2002). doi:doi/10.1073/pnas.242401399.
[180] D.M. M, P. Baluk, Significance of blood vessel leakiness in cancer, Cancer Res. 62 (2002) 5381–5385.
[181] C.T. Mierke, Role of the Endothelium during Tumor Cell Metastasis: Is the Endothelium a Barrier or a Promoter for Cell Invasion and Metastasis?, J. Biophys. 2008 (2009) 1–13. doi:10.1155/2008/183516.
[182] E.J.L. and J.H. Myron Moskowitz, Peter Russell, James Fidler, Darryl Sutorius, BREAST CANCER SCREENING, Cancer. 36 (1975) 2245–2250.
[183] S. Ran, L. Volk, K. Hall, M.J. Flister, Lymphangiogenesis and lymphatic metastasis in breast cancer, Pathophysiology. 17 (2010) 229–251. doi:10.1016/j.pathophys.2009.11.003.
[184] M.M. Gong, K.M. Lugo-Cintron, B.R. White, S.C. Kerr, P.M. Harari, D.J. Beebe, Human organotypic lymphatic vessel model elucidates microenvironment-dependent signaling and barrier function, Biomaterials. (2019) 119225. doi:10.1016/j.biomaterials.2019.119225.
[185] and B.D. Jiménez-Torres J, Peery S, Sung K, LumeNEXT: A Practical Method to Pattern Luminal Structures in ECM Gels José, 165 (2016) 255–269. doi:10.1016/j.trsl.2014.08.005.The.
[186] S.-H.L.B.J.D. Bischel, Lauren L; Lee, Hydrogels via Viscous Finger Patterning, J. Lab Autom. 17 (2012) 96–103. doi:10.1177/2211068211426694.A.
[187] J.M. Ayuso, A. Gillette, K. Lugo-Cintrón, S. Acevedo-Acevedo, I. Gomez, M. Morgan, T. Heaster, K.B. Wisinski, S.P. Palecek, M.C. Skala, D.J. Beebe, Organotypic microfluidic

breast cancer model reveals starvation-induced spatial-temporal metabolic adaptations, EBioMedicine. 37 (2018) 144–157. doi:10.1016/j.ebiom.2018.10.046.
[188] M.M. Gong, K.M. Lugo-Cintron, B.R. White, S.C. Kerr, P.M. Harari, D.J. Beebe, Human organotypic lymphatic vessel model elucidates microenvironment-dependent signaling and barrier function, Biomaterials. 214 (2019) 119225. doi:10.1016/j.biomaterials.2019.119225.
[189] J.T. Wigle, G. Oliver, An essential role for Prox1 in the induction of the LEC phenotype, EMBO J. 21 (2002) 1505–1513.
[190] V.M. Sanjay Kumar, Weaver, Mechanics, malignancy, and metastasis: The force journey of a tumor cell, Cancer Metastasis Rev. 28 (2009) 113–127. doi:10.1007/s10555-008-9173-4.Mechanics.
[191] S.I. Fraley, P.-H. Wu, L. He, Y. Feng, R. Krisnamurthy, G.D. Longmore, D. Wirtz, Three-dimensional matrix fiber alignment modulates cell migration and MT1-MMP utility by spatially and temporally directing protrusions., Sci. Rep. 5 (2015) 14580. doi:10.1038/srep14580.
[192] J.S. Bredfeldt, Y. Liu, C.A. Pehlke, M.W. Conklin, J.M. Szulczewski, D.R. Inman, P.J. Keely, R.D. Nowak, T.R. Mackie, K.W. Eliceiri, Computational segmentation of collagen fibers from second-harmonic generation images of breast cancer, J. Biomed. Opt. 19 (2014) 016007. doi:10.1117/1.jbo.19.1.016007.
[193] Z. Xie, C.C. Ghosh, R. Patel, S. Iwaki, D. Gaskins, C. Nelson, N. Jones, P.R. Greipp, S.M. Parikh, K.M. Druey, Vascular endothelial hyperpermeability induces the clinical symptoms of Clarkson disease (the systemic capillary leak syndrome), Blood. 119 (2012) 4321–4332. doi:10.1182/blood-2011-08-375816.
[194] M. Virumbrales-Muñoz, J.M. Ayuso, M. Olave, R. Monge, D. De Miguel, L. Martínez-Lostao, S. Le Gac, M. Doblare, I. Ochoa, L.J. Fernandez, Multiwell capillarity-based microfluidic device for the study of 3D tumour tissue-2D endothelium interactions and drug screening in co-culture models, Sci. Rep. 7 (2017) 1–15. doi:10.1038/s41598-017-12049-4.
[195] D.J. Lavalley, C.A. Reinhart-king, Matrix stiffening in the formation of blood vessels, 8517 (2014). doi:10.3402/arb.v1.25247.
[196] Y.T. Yeh, S.S. Hur, J. Chang, K.C. Wang, J.J. Chiu, Y.S. Li, S. Chien, Matrix Stiffness Regulates Endothelial Cell Proliferation through Septin 9, PLoS One. 7 (2012) 1–13. doi:10.1371/journal.pone.0046889.
[197] and K.W.E. Caroline A. Schneider, Wayne S. Rasband, NIH Image to ImageJ: 25 years of Image Analysis, Nat Methods. 9 (2012) 671–675. doi:10.1007/978-1-84882-087-6_9.
[198] R. Krishnan, D.D. Klumpers, C.Y. Park, K. Rajendran, X. Trepat, J. van Bezu, V.W.M. van Hinsbergh, C. V. Carman, J.D. Brain, J.J. Fredberg, J.P. Butler, G.P. van Nieuw Amerongen, Substrate stiffening promotes endothelial monolayer disruption through enhanced physical forces, Am. J. Physiol. Physiol. 300 (2011) C146–C154. doi:10.1152/ajpcell.00195.2010.
[199] and C.A.R.-K. John Huynh, Nozomi Nishimura, Kuldeepsinh Rana, John M. Peloquin, Joseph P. Califano, Christine R. Montague, Michael R. King, Chris B. Schaffer, Age-Related Intimal Stiffening Enhances Endothelial Permeability and Leukocyte Transmigration, Sci Transl Med. (2011). doi:10.1038/mp.2011.182.doi.
[200] K.G. Neiva, K.A. Warner, M.S. Campos, Z. Zhang, J. Moren, T.E. Danciu, J.E. Nör, Endothelial cell-derived interleukin-6 regulates tumor growth, BMC Cancer. 14 (2014) 1–

11. doi:10.1186/1471-2407-14-99.
[201] G. Gopinathan, C. Milagre, O.M.T. Pearce, L.E. Reynolds, K. Hodivala-Dilke, D.A. Leinster, H. Zhong, R.E. Hollingsworth, R. Thompson, J.R. Whiteford, F. Balkwill, Interleukin-6 stimulates defective angiogenesis, Cancer Res. 75 (2015) 3098–3107. doi:10.1158/0008-5472.CAN-15-1227.
[202] A.H. Sprague, R.A. Khalil, Inflammatory cytokines in vascular dysfunction and vascular disease, Biochem. Pharmacol. 78 (2009) 539–552. doi:10.1016/j.bcp.2009.04.029.
[203] T.R. Desai, N.J. Leeper, K.L. Hynes, B.L. Gewertz, Interleukin-6 causes endothelial barrier dysfunction via the protein kinase C pathway, J. Surg. Res. 104 (2002) 118–123. doi:10.1006/jsre.2002.6415.
[204] H. Alsaffar, N. Martino, J.P. Garrett, A.P. Adam, Interleukin-6 promotes a sustained loss of endothelial barrier function via Janus kinase-mediated STAT3 phosphorylation and de novo protein synthesis, Am. J. Physiol. Physiol. (2018). doi:10.1152/ajpcell.00235.2017.
[205] E. Weber, F. Sozio, E. Gabbrielli, A. Rossi, Lymphatic vessels in health and disease, Transl. Vasc. Med. Pathog. Diagnosis, Treat. 5 (2013) 137–150. doi:10.1007/978-0-85729-920-8_9.
[206] M.J. Paszek, N. Zahir, K.R. Johnson, J.N. Lakins, G.I. Rozenberg, A. Gefen, C.A. Reinhart-King, S.S. Margulies, M. Dembo, D. Boettiger, D.A. Hammer, V.M. Weaver, Tensional homeostasis and the malignant phenotype, Cancer Cell. 8 (2005) 241–254. doi:10.1016/j.ccr.2005.08.010.
[207] B.R. Seo, P. Bhardwaj, S. Choi, J. Gonzalez, R.C.A. Eguiluz, K. Wang, S. Mohanan, P.G. Morris, B. Du, X.K. Zhou, L.T. Vahdat, A. Verma, O. Elemento, C.A. Hudis, R.M. Williams, D. Gourdon, A.J. Dannenberg, C. Fischbach, Obesity-dependent changes in interstitial ECM mechanics promote breast tumorigenesis, 7 (2015) 1–12.
[208] J.E. Deanfield, J.P. Halcox, T.J. Rabelink, Contemporary Reviews in Cardiovascular Medicine Endothelial Function and Dysfunction Testing and Clinical Relevance Endothelium in Normal Vascular Homeostasis, (2007) 1285–1295. doi:10.1161/CIRCULATIONAHA.106.652859.
[209] J.O. Den Buijs, M. Musters, T. Verrips, J.A. Post, B. Braam, N. Van Riel, Mathematical modeling of vascular endothelial layer maintenance: The role of endothelial cell division, progenitor cell homing, and telomere shortening, Am. J. Physiol. - Hear. Circ. Physiol. 287 (2004) 2651–2658. doi:10.1152/ajpheart.00332.2004.
[210] T. Asahara, T. Murohara, A. Sullivan, M. Silver, R. Van Der Zee, T. Li, B. Witzenbichler, G. Schatteman, J.M. Isner, Isolation of putative progenitor endothelial cells for angiogenesis, Science (80-.). 275 (1997) 964–967. doi:10.1126/science.275.5302.964.
[211] J. Zhao, C.G. Mitrofan, S.L. Appleby, N.W. Morrell, A.M.L. Lever, Disrupted Endothelial Cell Layer and Exposed Extracellular Matrix Proteins Promote Capture of Late Outgrowth Endothelial Progenitor Cells, Stem Cells Int. 2016 (2016). doi:10.1155/2016/1406304.
[212] A. Woywodt, Circulating endothelial cells: life, death, detachment and repair of the endothelial cell layer, Nephrol. Dial. Transplant. 17 (2002) 1728–1730. doi:10.1093/ndt/17.10.1728.
[213] S.B. Campos, S.L. Ashworth, S. Wean, M. Hosford, R.M. Sandoval, M.A. Hallett, S.J. Atkinson, B.A. Molitoris, Cytokine-induced F-actin reorganization in endothelial cells involves RhoA activation, Am. J. Physiol. Physiol. 296 (2009) F487–F495. doi:10.1152/ajprenal.00112.2008.
[214] G.V. Chaitanya, S.E. Franks, W. Cromer, S.R. Wells, M. Bienkowska, M.H. Jennings, A.

Ruddell, T. Ando, Y. Wang, Y. Gu, M. Sapp, J.M. Mathis, P.A. Jordan, A. Minagar, J.S. Alexander, Differential Cytokine Responses in Human and Mouse Lymphatic Endothelial Cells to Cytokines in Vitro , Lymphat. Res. Biol. 8 (2010) 155–164. doi:10.1089/lrb.2010.0004.

[215] D.C. Zawieja, C.Á. Barrier, The effects of inflammatory cytokines on lymphatic endothelial barrier function, (2014) 395–406. doi:10.1007/s10456-013-9393-2.

[216] C. Dethlefsen, G. Højfeldt, P. Hojman, The role of intratumoral and systemic IL-6 in breast cancer, Breast Cancer Res. Treat. 138 (2013) 657–664. doi:10.1007/s10549-013-2488-z.

[217] M. Gallo, D. Frezzetti, C. Roma, N. Chicchinelli, A. Barbieri, C. Arra, G. Scognamiglio, G. Botti, A. De Luca, N. Normanno, RANTES and IL-6 cooperate in inducing a more aggressive phenotype in breast cancer cells, Oncotarget. 9 (2018) 17543–17553. doi:10.18632/oncotarget.24784.

[218] H.S. Kim, M. Jung, S.K. Choi, J. Woo, Y.J. Piao, E.H. Hwang, H. Kim, S.J. Kim, W.K. Moon, IL-6-mediated cross-talk between human preadipocytes and ductal carcinoma in situ in breast cancer progression, (2018) 1–13.

[219] L. Hou, S. Xie, G. Li, B. Xiong, Y. Gao, X. Zhao, J. Hu, S. Deng, J. Jiang, IL-6 Triggers the Migration and Invasion of Oestrogen Receptor-Negative Breast Cancer Cells via Regulation of Hippo Pathways, Basic Clin. Pharmacol. Toxicol. 123 (2018) 549–557. doi:10.1111/bcpt.13042.

[220] J.Y.S. Tsang, Y.B. Ni, S.K. Chan, M.M. Shao, Y.K. Kwok, K.W. Chan, P.H. Tan, G.M. Tse, CX3CL1 expression is associated with poor outcome in breast cancer patients., Breast Cancer Res. Treat. 140 (2013) 495–504. doi:10.1007/s10549-013-2653-4.

[221] Y. Liang, L. Yi, P. Liu, L. Jiang, H. Wang, A. Hu, C. Sun, J. Dong, CX3CL1 involves in breast cancer metastasizing to the spine via the Src/FAK signaling pathway, J. Cancer. 9 (2018) 3603–3612. doi:10.7150/jca.26497.

[222] F. Guo, Y. Wang, J. Liu, S.C. Mok, F. Xue, W. Zhang, CXCL12/CXCR4: A symbiotic bridge linking cancer cells and their stromal neighbors in oncogenic communication networks, Oncogene. 35 (2016) 816–826. doi:10.1038/onc.2015.139.

[223] D.K. Ahirwar, M.W. Nasser, M.M. Ouseph, M. Elbaz, M.C. Cuitiño, R.D. Kladney, S. Varikuti, K. Kaul, A.R. Satoskar, B. Ramaswamy, X. Zhang, M.C. Ostrowski, G. Leone, R.K. Ganju, Fibroblast-derived CXCL12 promotes breast cancer metastasis by facilitating tumor cell intravasation, Oncogene. 37 (2018) 4428–4442. doi:10.1038/s41388-018-0263-7.

[224] V. Mirisola, A. Zuccarino, B.E. Bachmeier, M.P. Sormani, J. Falter, A. Nerlich, U. Pfeffer, CXCL12/SDF1 expression by breast cancers is an independent prognostic marker of disease-free and overall survival, Eur. J. Cancer. 45 (2009) 2579–2587. doi:10.1016/j.ejca.2009.06.026.

[225] J. Chen, Y. Lai, P. Chu, S. Chan, L. Wang, W. Hung, Cancer-Derived VEGF-C Increases Chemokine Production in Lymphatic Endothelial Cells to Promote CXCR2-Dependent Cancer Invasion and MDSC Recruitment, Cancers (Basel). (2019). doi:doi:10.3390/cancers11081120.

[226] R.W. Tilghman, C.R. Cowan, J.D. Mih, Y. Koryakina, D. Gioeli, J.K. Slack-Davis, B.R. Blackman, D.J. Tschumperlin, J.T. Parsons, Matrix rigidity regulates cancer cell growth and cellular phenotype, PLoS One. 5 (2010) 1–13. doi:10.1371/journal.pone.0012905.

[227] J.D. Cramer, B. Burtness, Q.T. Le, R.L. Ferris, The changing therapeutic landscape of

head and neck cancer, Nat. Rev. Clin. Oncol. (2019). doi:10.1038/s41571-019-0227-z.
[228] T. Sugiura, Y. Inoue, R. Matsuki, K. Ishii, VEGF-C and VEGF-D expression is correlated with lymphatic vessel density and lymph node metastasis in oral squamous cell carcinoma : Implications for use as a prognostic marker, (2009) 673–680. doi:10.3892/ijo.
[229] G. Warburton, N.G. Nikitakis, P. Roberson, N.J. Marinos, T. Wu, J.J. Sauk, R.A. Ord, S.M. Wahl, Histopathological and Lymphangiogenic Parameters in Relation to Lymph Node Metastasis in Early Stage Oral Squamous Cell Carcinoma, J. Oral Maxillofac. Surg. 65 (2007) 475–484. doi:10.1016/j.joms.2005.12.074.
[230] S.A. Stacker, C. Caesar, M.E. Baldwin, G.E. Thornton, R.A. Williams, R. Prevo, D.G. Jackson, S.I. Nishikawa, H. Kubo, M.G. Achen, VEGF-D promotes the metastatic spread of tumor cells via the lymphatics, Nat. Med. 7 (2001) 186–191. doi:10.1038/84635.
[231] T.K. and K. Alitalo, Molecular Biology and Pathology of Lymphangiogenesis, Annu. Rev. OfPathology Mech. Dis. (2008) 367–397. doi:10.1146/annurev.pathmechdis.3.121806.151515.
[232] M. Jeltsch, A. Kaipainen, V. Joukov, X. Meng, M. Lakso, H. Rauvala, M. Swartz, D. Fukumura, R.K. Jain, K. Alitalo, Hyperplasia of lymphatic vessels in VEGF-C transgenic mice, Science (80-.). 276 (1997) 1423–1425. doi:10.1126/science.276.5317.1423.
[233] W. Zheng, A. Aspelund, K. Alitalo, W. Zheng, A. Aspelund, K. Alitalo, Lymphangiogenic factors, mechanisms, and applications, 124 (2014) 878–887. doi:10.1172/JCI71603.878.
[234] K. Vaahtomeri, S. Karaman, T. Mäkinen, K. Alitalo, Lymphangiogenesis guidance by paracrine and pericellular factors, (2017) 1615–1634. doi:10.1101/gad.303776.117.GENES.
[235] K.C. Boardman, M.A. Swartz, Interstitial flow as a guide for lymphangiogenesis, Circ. Res. 92 (2003) 801–808. doi:10.1161/01.RES.0000065621.69843.49.
[236] P. Yu, K. Wilhelm, A. Dubrac, J.K. Tung, T.C. Alves, J.S. Fang, Y. Xie, J. Zhu, Z. Chen, F. De Smet, J. Zhang, FGF-dependent metabolic control of vascular development, 545 (2017) 224–228. doi:10.1038/nature22322. Europe.
[237] B.W. Wong, X. Wang, A. Zecchin, B. Thienpont, I. Cornelissen, J. Kalucka, M. García-Caballero, R. Missiaen, H. Huang, U. Brüning, S. Blacher, S. Vinckier, J. Goveia, M. Knobloch, H. Zhao, C. Dierkes, C. Shi, R. Hägerling, V. Moral-Dardé, S. Wyns, M. Lippens, S. Jessberger, S.M. Fendt, A. Luttun, A. Noel, F. Kiefer, B. Ghesquière, L. Moons, L. Schoonjans, M. Dewerchin, G. Eelen, D. Lambrechts, P. Carmeliet, The role of fatty acid β-oxidation in lymphangiogenesis, Nature. 542 (2017) 49–54. doi:10.1038/nature21028.
[238] P. Gao, C. Li, Z. Chang, X. Wang, M. Xuan, Carcinoma associated fibroblasts derived from oral squamous cell carcinoma promote lymphangiogenesis via c-Met/PI3K/AKt in vitro, Oncol. Lett. 15 (2018) 331–337. doi:10.3892/ol.2017.7301.
[239] R. Wei, M. Lv, F. Li, T. Cheng, Z. Zhang, G. Jiang, Y. Zhou, R. Gao, X. Wei, J. Lou, X. Wu, D. Luo, X. Ma, J. Jiang, D. Ma, L. Xi, Human CAFs promote lymphangiogenesis in ovarian cancer via the Hh-VEGF-C signaling axis, Oncotarget. 8 (2017) 67315–67328. doi:10.18632/oncotarget.18621.
[240] B. Yu, K. Wu, X. Wang, J. Zhang, L. Wang, Y. Jiang, X. Zhu, W. Chen, M. Yan, Periostin secreted by cancer-associated fibroblasts promotes cancer stemness in head and neck cancer by activating protein tyrosine kinase 7, Cell Death Dis. 9 (2018). doi:10.1038/s41419-018-1116-6.

[241] J. Zhou, X.H. Wang, Y.X. Zhao, C. Chen, X.Y. Xu, Q. Sun, H.Y. Wu, M. Chen, J.F. Sang, L. Su, X.Q. Tang, X.B. Shi, Y. Zhang, Q. Yu, Y.Z. Yao, W.J. Zhang, Cancer-associated fibroblasts correlate with tumor-associated macrophages infiltration and lymphatic metastasis in triple negative breast cancer patients, J. Cancer. 9 (2018) 4635–4641. doi:10.7150/jca.28583.

[242] H. Kashima, K. Noma, T. Ohara, T. Kato, Y. Katsura, S. Komoto, H. Sato, R. Katsube, T. Ninomiya, H. Tazawa, Y. Shirakawa, T. Fujiwara, Cancer-associated fibroblasts (CAFs) promote the lymph node metastasis of esophageal squamous cell carcinoma, Int. J. Cancer. 144 (2019) 828–840. doi:10.1002/ijc.31953.

[243] S.E. Wheeler, H. Shi, F. Lin, S. Dasari, J. Bednash, S. Thorne, S. Watkins, R. Joshi, Tumor associated fibroblasts enhance head and neck squamous cell carcinoma proliferation, invasion, and metastasis in preclinical models, 36 (2014) 385–392. doi:10.1002/hed.23312.Tumor.

[244] M.E.P.P. John Henry Owen, Martin P. Graham, Steven B. Chinn, Owen F. Darr, Douglas B. Chepeha, Gregory T. Wolf, Carol R. Bradford, Thomas E. Carey, A Novel Method of Cell Line Establishment Utilizing Fluorescence-Activated Cell Sorting Resulting in Six New Head and Neck Squamous Cell Carcinoma Lines, Head Neck. (2016) E459–E467. doi:10.1002/hed.24019.

[245] S.A. Stacker, M.G. Achen, L. Jussila, M.E. Baldwin, K. Alitalo, Metastasis: Lymphangiogenesis and cancer metastasis, Nat. Rev. Cancer. 2 (2002) 573–583. doi:10.1038/nrc863.

[246] S. Shigematsu, K. Yamauchi, K. Nakajima, S. Iijima, T. Aizawa, K. Hashizume, IGF-1 regulates migration and angiogenesis of human endothelial cells, Endocr. J. 46 (1999) 59–62. doi:10.1507/endocrj.46.suppl_s59.

[247] H. Hayashi, H. Sano, S. Seo, T. Kume, The Foxc2 transcription factor regulates angiogenesis via induction of integrin β3 expression, J. Biol. Chem. 283 (2008) 23791–23800. doi:10.1074/jbc.M800190200.

[248] J.H. Qi, Q. Ebrahem, N. Moore, G. Murphy, L. Claesson-Welsh, M. Bond, A. Baker, B. Anand-Apte, A novel function for tissue inhibitor of metalloproteinases-3 (TIMP3): Inhibition of angiogenesis by blockage of VEGF binding to VEGF receptor-2, Nat. Med. 9 (2003) 407–415. doi:10.1038/nm846.

[249] and W.P.F. Jianbo Wu, Tammy L. Strawn, Mao Luo, Liqun Wang, Rong Li, Meiping Ren, Jiyi Xia, Zhuo Zhang, Weizhong Ma, Tingting Luo, Daniel A. Lawrence, Plasminogen Activator Inhibitor-1 Inhibits Angiogenic Signaling by Uncoupling VEGF Receptor-2-αV β3 Integrin Cross-talk, Arter. Thromb Vasc Biol. 35 (2015) 111–120. doi:10.1161/ATVBAHA.114.304554.

[250] J. Lawler, Thrombospondin-1 as an endogenous inhibitor of angiogenesis and tumor growth, J. Cell. Mol. Med. 6 (2002) 1–12. doi:10.1111/j.1582-4934.2002.tb00307.x.

[251] G. Bergers, R. Brekken, G. McMahon, T.H. Vu, T. Itoh, K. Tamaki, K. Tanzawa, P. Thorpe, S. Itohara, Z. Werb, D. Hanahan, Matrix metalloproteinase-9 triggers the angiogenic switch during carcinogenesis, Nat. Cell Biol. 2 (2000) 737–744. doi:10.1038/35036374.

[252] P. CARMELIET, D. COLLEN, Molecular Basis of Angiogenesis: Role of VEGF and VE-Cadherin, Ann. N. Y. Acad. Sci. 902 (2006) 249–264. doi:10.1111/j.1749-6632.2000.tb06320.x.

[253] P. Carmeliet, M.G. Lampugnani, L. Moons, F. Breviario, V. Compernolle, F. Bono, G.

Balconi, R. Spagnuolo, B. Oosthuyse, M. Dewerchin, A. Zanetti, A. Angellilo, V. Mattot, D. Nuyens, E. Lutgens, F. Clotman, M.C. De Ruiter, A.G. De Groot, R. Poelmann, F. Lupu, J.M. Herbert, D. Collen, E. Dejana, Targeted deficiency or cytosolic truncation of the VE-cadherin gene in mice impairs VEGF-mediated endothelial survival and angiogenesis, Cell. 98 (1999) 147–157. doi:10.1016/S0092-8674(00)81010-7.

[254] Y. Takuwa, Roles of sphingosine-1-phosphate signaling in angiogenesis, World J. Biol. Chem. 1 (2010) 298. doi:10.4331/wjbc.v1.i10.298.

[255] L.O. Myat, S. Thangada, M.T. Wu, C.H. Liu, T.L. Macdonald, K.R. Lynch, C.Y. Lin, T. Hla, Immunosuppressive and anti-angiogenic sphingosine 1-phosphate receptor-1 agonists induce ubiquitinylation and proteasomal degradation of the receptor, J. Biol. Chem. 282 (2007) 9082–9089. doi:10.1074/jbc.M610318200.

[256] T. Osaki, J.C. Serrano, R.D. Kamm, Cooperative Effects of Vascular Angiogenesis and Lymphangiogenesis, Regen. Eng. Transl. Med. (2018) 1–13. doi:http://dx.doi.org/10.1007/s40883-018-0054-2.

[257] N.C.I. NIH, Female Breast Cancer - Cancer Stat Facts, (2019).

[258] Special Section: Breast Carcinoma In Situ, n.d.

[259] D. Medina, The mammary gland: A unique organ for the study of development and tumorigenesis, J. Mammary Gland Biol. Neoplasia. 1 (1996) 5–19. doi:10.1007/BF02096299.

[260] S. Nawaz, The Normal Breast and Benign Diseases of the Breast, Early Diagnosis Treat. Cancer Ser. Breast Cancer. (2011) 1–10. doi:10.1016/B978-1-4160-4932-6.50006-8.

[261] C.R. Eheman, K.M. Shaw, A.B. Ryerson, J.W. Miller, U.A. Ajani, M.C. White, The Changing Incidence of In situ and Invasive Ductal and Lobular Breast Carcinomas: United States, 1999-2004, Cancer Epidemiol. Biomarkers Prev. 18 (2009) 1763–1769. doi:10.1158/1055-9965.EPI-08-1082.

[262] W.D. Dupont, D.L. Page, Risk Factors for Breast Cancer in Women with Proliferative Breast Disease, N. Engl. J. Med. 312 (1985) 146–151. doi:10.1056/NEJM198501173120303.

[263] K. Polyak, Breast cancer: origins and evolution., J. Clin. Invest. 117 (2007) 3155–63. doi:10.1172/JCI33295.

[264] P.T. Simpson, J.S. Reis-Filho, T. Gale, S.R. Lakhani, Molecular evolution of breast cancer, J. Pathol. 205 (2005) 248–254. doi:10.1002/path.1691.

[265] W. Boecker, H. Buerger, K. Schmitz, I.A. Ellis, P.J. van Diest, H.-P. Sinn, J. Geradts, R. Diallo, C. Poremba, H. Herbst, Ductal epithelial proliferations of the breast: a biological continuum? Comparative genomic hybridization and high-molecular-weight cytokeratin expression patterns, J. Pathol. 195 (2001) 415–421. doi:10.1002/path.982.

[266] G. Delaney, O. Ung, M. Bilous, S. Cahill, M. Greenberg, J. Boyages, DUCTAL CARCINOMA IN SITU PART I: DEFINITION AND DIAGNOSIS, ANZ J. Surg. 67 (1997) 81–93. doi:10.1111/j.1445-2197.1997.tb01909.x.

[267] S.K. Gupta, A.G. Douglas-Jones, B. Jasani, J.M. Morgan, M. Pignatelli, R.E. Mansel, E-Cadherin (E-cad) expression in duct carcinoma in situ (DCIS) of the breast, Virchows Arch. 430 (1997) 23–28. doi:10.1007/BF01008012.

[268] S. Curran, G.I. Murray, Matrix metalloproteinases: molecular aspects of their roles in tumour invasion and metastasis., Eur. J. Cancer. 36 (2000) 1621–30. doi:10.1016/S0959-8049(00)00156-8.

[269] S. Valastyan, R.A. Weinberg, Tumor metastasis: Molecular insights and evolving

paradigms, Cell. 147 (2011) 275–292. doi:10.1016/j.cell.2011.09.024.
[270] C. Khanna, K. Hunter, Modeling metastasis in vivo, Carcinogenesis. 26 (2004) 513–523. doi:10.1093/carcin/bgh261.
[271] L. Gómez-Cuadrado, N. Tracey, R. Ma, B. Qian, V.G. Brunton, Mouse models of metastasis: progress and prospects., Dis. Model. Mech. 10 (2017) 1061–1074. doi:10.1242/dmm.030403.
[272] C.G. Marsden, M.J. Wright, L. Carrier, K. Moroz, R. Pochampally, B.G. Rowan, "A novel in vivo model for the study of human breast cancer metastasis using primary breast tumor-initiating cells from patient biopsies", BMC Cancer. 12 (2012) 10. doi:10.1186/1471-2407-12-10.
[273] M. Kapałczyńska, T. Kolenda, W. Przybyła, M. Zajączkowska, A. Teresiak, V. Filas, M. Ibbs, R. Bliźniak, Ł. Łuczewski, K. Lamperska, 2D and 3D cell cultures – a comparison of different types of cancer cell cultures, Arch. Med. Sci. 14 (2016) 910–919. doi:10.5114/aoms.2016.63743.
[274] M.M. Shenouda, A. Gillgrass, T. Nham, R. Hogg, A.J. Lee, M. V. Chew, M. Shafaei, C. Aarts, D.A. Lee, J. Hassell, A. Bane, S. Dhesy-Thind, A.A. Ashkar, Ex vivo expanded natural killer cells from breast cancer patients and healthy donors are highly cytotoxic against breast cancer cell lines and patient-derived tumours, Breast Cancer Res. 19 (2017) 76. doi:10.1186/s13058-017-0867-9.
[275] Y. Choi, E. Hyun, J. Seo, C. Blundell, H.C. Kim, E. Lee, S.H. Lee, A. Moon, W.K. Moon, D. Huh, A microengineered pathophysiological model of early-stage breast cancer., Lab Chip. 15 (2015) 3350–7. doi:10.1039/c5lc00514k.
[276] M.A. Swartz, An in vitro model of the tumor–lymphatic microenvironment with simultaneous transendothelial and luminal flows reveals mechanisms of flow enhanced invasion, Integr. Biol. 7 (2015) 525–533. doi:10.1039/c5ib00085h.
[277] J.W. Song, S.P. Cavnar, A.C. Walker, K.E. Luker, M. Gupta, Y.-C. Tung, G.D. Luker, S. Takayama, Microfluidic Endothelium for Studying the Intravascular Adhesion of Metastatic Breast Cancer Cells, PLoS One. 4 (2009) e5756. doi:10.1371/journal.pone.0005756.
[278] I.K. Zervantonakis, S.K. Hughes-Alford, J.L. Charest, J.S. Condeelis, F.B. Gertler, R.D. Kamm, Three-dimensional microfluidic model for tumor cell intravasation and endothelial barrier function, Proc. Natl. Acad. Sci. U. S. A. 109 (2012) 13515–13520. doi:10.1073/pnas.1210182109.
[279] J.S. Jeon, I.K. Zervantonakis, S. Chung, R.D. Kamm, J.L. Charest, In Vitro Model of Tumor Cell Extravasation, PLoS One. 8 (2013) e56910. doi:10.1371/journal.pone.0056910.
[280] J.S. Jeon, S. Bersini, M. Gilardi, G. Dubini, J.L. Charest, M. Moretti, R.D. Kamm, Human 3D vascularized organotypic microfluidic assays to study breast cancer cell extravasation., Proc. Natl. Acad. Sci. U. S. A. 112 (2015) 214–9. doi:10.1073/pnas.1417115112.
[281] Y. Tang, F. Soroush, J.B. Sheffield, B. Wang, B. Prabhakarpandian, M.F. Kiani, A Biomimetic Microfluidic Tumor Microenvironment Platform Mimicking the EPR Effect for Rapid Screening of Drug Delivery Systems, Sci. Rep. 7 (2017) 9359. doi:10.1038/s41598-017-09815-9.
[282] C.F. Buchanan, S.S. Verbridge, P.P. Vlachos, M.N. Rylander, Flow shear stress regulates endothelial barrier function and expression of angiogenic factors in a 3D microfluidic tumor vascular model, Cell Adh. Migr. 8 (2014) 517–524.

doi:10.4161/19336918.2014.970001.
[283] H.R. Kwag, J. V. Serbo, P. Korangath, S. Sukumar, L.H. Romer, D.H. Gracias, A Self-Folding Hydrogel *In Vitro* Model for Ductal Carcinoma, Tissue Eng. Part C Methods. 22 (2016) 398–407. doi:10.1089/ten.tec.2015.0442.
[284] L.L. Bischel, D.J. Beebe, K.E. Sung, Microfluidic model of ductal carcinoma in situ with 3D, organotypic structure., BMC Cancer. 15 (2015) 12. doi:10.1186/s12885-015-1007-5.
[285] M.M.G. Grafton, L. Wang, P.-A. Vidi, J. Leary, S.A. Lelièvre, O.W. Petersen, M.J. Bissell, D.W. Hutmacher, H. Yu, N.E. Davidson, S. Sukumar, Breast on-a-chip: mimicry of the channeling system of the breast for development of theranostics, Integr. Biol. 3 (2011) 451. doi:10.1039/c0ib00132e.
[286] P.-A. Vidi, T. Maleki, M. Ochoa, L. Wang, S.M. Clark, J.F. Leary, S.A. Lelièvre, Disease-on-a-chip: mimicry of tumor growth in mammary ducts, Lab Chip. 14 (2014) 172–177. doi:10.1039/C3LC50819F.
[287] M.M. Morgan, M.K. Livingston, J.W. Warrick, E.M. Stanek, E.T. Alarid, D.J. Beebe, B.P. Johnson, Mammary fibroblasts reduce apoptosis and speed estrogen-induced hyperplasia in an organotypic MCF7-derived duct model, Sci. Rep. 8 (2018) 7139. doi:10.1038/s41598-018-25461-1.
[288] M.M. Morgan, L.M. Arendt, E.T. Alarid, D.J. Beebe, B.P. Johnson, Mammary adipose stromal cells derived from obese women reduce sensitivity to the aromatase inhibitor anastrazole in an organotypic breast model, FASEB J. (2019) fj.201802347RRR. doi:10.1096/fj.201802347RRR.
[289] N. Harbeck, M. Gnant, Breast cancer, Lancet. 389 (2017) 1134–1150. doi:10.1016/S0140-6736(16)31891-8.
[290] O.J. Scully, B.-H. Bay, G. Yip, Y. Yu, Breast cancer metastasis., Cancer Genomics Proteomics. 9 (2012) 311–20. doi:9/5/311 [pii].
[291] and J.W. Yan Mao, Evan T. Keller, David H. Garfield, Kunwei Shen, Stroma Cells in Tumor Microenvironment and Breast Cancer, Cancer Metastasis Rev. 32 (2013) 303–315. doi:10.1007/s10555-012-9415-3.Stroma.
[292] L. Hui, Y. Chen, Tumor microenvironment: Sanctuary of the devil, Cancer Lett. 368 (2015) 7–13. doi:10.1016/j.canlet.2015.07.039.
[293] H.-Y. Xie, Z.-M. Shao, D.-Q. Li, Tumor microenvironment: driving forces and potential therapeutic targets for breast cancer metastasis., Chin. J. Cancer. 36 (2017) 36. doi:10.1186/s40880-017-0202-y.
[294] M. Wang, J. Zhao, L. Zhang, F. Wei, Y. Lian, Y. Wu, Z. Gong, S. Zhang, J. Zhou, K. Cao, X. Li, W. Xiong, G. Li, Z. Zeng, C. Guo, Role of tumor microenvironment in tumorigenesis, J. Cancer. 8 (2017) 761–773. doi:10.7150/jca.17648.
[295] T. Oskarsson, Extracellular matrix components in breast cancer progression and metastasis., Breast. 22 Suppl 2 (2013) S66-72. doi:10.1016/j.breast.2013.07.012.
[296] T. Alkasalias, L. Moyano-Galceran, M. Arsenian-Henriksson, K. Lehti, Fibroblasts in the tumor microenvironment: Shield or spear?, Int. J. Mol. Sci. 19 (2018) 1–21. doi:10.3390/ijms19051532.
[297] K. Räsänen, A. Vaheri, Activation of fibroblasts in cancer stroma, Exp. Cell Res. 316 (2010) 2713–2722. doi:10.1016/j.yexcr.2010.04.032.
[298] P. Gascard, T.D. Tlsty, Carcinoma-associated fibroblasts: Orchestrating the composition of malignancy, Genes Dev. 30 (2016) 1002–1019. doi:10.1101/gad.279737.116.
[299] T. Liu, L. Zhou, D. Li, T. Andl, Y. Zhang, Cancer-associated fibroblasts build and secure

the tumor microenvironment, Front. Cell Dev. Biol. 7 (2019) 1–14. doi:10.3389/fcell.2019.00060.
[300] H. Luo, G. Tu, Z. Liu, M. Liu, Cancer-associated fibroblasts: A multifaceted driver of breast cancer progression, Cancer Lett. 361 (2015) 155–163. doi:10.1016/j.canlet.2015.02.018.
[301] A. Ray, Z.M. Slama, R.K. Morford, S.A. Madden, P.P. Provenzano, Enhanced Directional Migration of Cancer Stem Cells in 3D Aligned Collagen Matrices, Biophys. J. 112 (2017) 1023–1036. doi:10.1016/j.bpj.2017.01.007.
[302] E. Ioachim, A. Charchanti, E. Briasoulis, V. Karavasilis, H. Tsanou, D.L. Arvanitis, N.J. Agnantis, N. Pavlidis, Immunohistochemical expression of extracellular matrix components tenascin, fibronectin, collagen type IV and laminin in breast cancer: Their prognostic value and role in tumour invasion and progression, Eur. J. Cancer. 38 (2002) 2362–2370. doi:10.1016/S0959-8049(02)00210-1.
[303] D. You, S.P. Jung, Y. Jeong, S.Y. Bae, J.E. Lee, S. Kim, Fibronectin expression is upregulated by PI-3K/Akt activation in tamoxifen-resistant breast cancer cells, BMB Rep. 50 (2017) 615–620. doi:10.5483/BMBRep.2017.50.12.096.
[304] and R.D.K. William J. Polacheck, Ioannis K. Zervantonakis, Tumor cell migration in complex microenvironments, Cell Mol Life Sci. 70 (2013) 1335–1356. doi:10.1007/s00018-012-1115-1.
[305] and L.Q. Yuanqing Zhang, Weijia Zhang, Mesenchymal-Mode Migration Assay and Antimetastatic Drug Screening via High Throughput Microfluidics Channel Networks, Angew Chem Int Ed Engl. 53 (2014) 2344–2348. doi:10.1002/anie.201309885.
[306] G. Cheng, K. Zygourakis, Cell migration, 2007. doi:10.1016/B978-0-12-378630-2.00420-5.
[307] E. Chinchar, K.L. Makey, J. Gibson, F. Chen, S.A. Cole, G.C. Megason, S. Vijayakumar, L. Miele, J.W. Gu, Sunitinib significantly suppresses the proliferation, migration, apoptosis resistance, tumor angiogenesis and growth of triple-negative breast cancers but increases breast cancer stem cells, Vasc. Cell. 6 (2014) 1–12. doi:10.1186/2045-824X-6-12.
[308] P. Chaudhuri, M. Ebrahimi Warkiani, T. Jing, K. Kenry, C.T. Lim, Microfluidics for Research and Applications in Oncology, Analyst. (2015). doi:10.1039/C5AN00382B.
[309] M. Shang, H. Soon, Lab on a Chip microenvironment for anti-cancer drug, (2019) 369–386. doi:10.1039/c8lc00970h.
[310] G. Velve-Casquillas, M. Le Berre, M. Piel, P.T. Tran, Microfluidic tools for cell biological research, Nano Today. 5 (2010) 28–47. doi:10.1016/j.nantod.2009.12.001.
[311] A.L. Paguirigan, D.J. Beebe, Microfluidics meet cell biology: Bridging the gap by validation and application of microscale techniques for cell biological assays, BioEssays. 30 (2008) 811–821. doi:10.1002/bies.20804.
[312] J. Ahn, Y. Sei, N. Jeon, Y. Kim, Tumor Microenvironment on a Chip: The Progress and Future Perspective, Bioengineering. 4 (2017) 64. doi:10.3390/bioengineering4030064.
[313] K.E. Sung, D.J. Beebe, Microfluidic 3D models of cancer, Adv. Drug Deliv. Rev. 79 (2014) 68–78. doi:10.1016/j.addr.2014.07.002.
[314] L. Businaro, A. De Ninno, G. Schiavoni, V. Lucarini, G. Ciasca, A. Gerardino, F. Belardelli, L. Gabriele, F. Mattei, Cross talk between cancer and immune cells: Exploring complex dynamics in a microfluidic environment, Lab Chip. 13 (2013) 229–239. doi:10.1039/c2lc40887b.

[315] K.E. Sung, N. Yang, C. Pehlke, P.J. Keely, K.W. Eliceiri, D.J. Beebe, Transition to invasion in breast cancer : a microfluidic in vitro model enables examination of spatial and temporal effects, Integr. Biol. (2011) 439–450. doi:10.1039/c0ib00063a.
[316] D.D. Truong, A. Kratz, J.G. Park, E.S. Barrientos, H. Saini, T. Nguyen, B. Pockaj, G. Mouneimne, J. LaBaer, M. Nikkhah, A human organotypic microfluidic tumor model permits investigation of the interplay between patient-derived fibroblasts and breast cancer cells, Cancer Res. 79 (2019) 3139–3151. doi:10.1158/0008-5472.CAN-18-2293.
[317] M. Anguiano, C. Castilla, M. Maška, C. Ederra, R. Peláez, X. Morales, G. Muñoz-Arrieta, M. Mujika, M. Kozubek, A. Muñoz-Barrutia, A. Rouzaut, S. Arana, J.M. Garcia-Aznar, C. Ortiz-de-Solorzano, Characterization of three-dimensional cancer cell migration in mixed collagen-Matrigel scaffolds using microfluidics and image analysis, PLoS One. 12 (2017). doi:10.1371/journal.pone.0171417.
[318] S.I. Montanez-Sauri, K.E. Sung, E. Berthier, D.J. Beebe, Enabling screening in 3D microenvironments: probing matrix and stromal effects on the morphology and proliferation of T47D breast carcinoma cells., Integr. Biol. 5 (2013) 631–40. doi:10.1039/c3ib20225a.
[319] H.S. Lee, E.Y. Seo, N.E. Kang, W.K. Kim, [6]-Gingerol inhibits metastasis of MDA-MB-231 human breast cancer cells, J. Nutr. Biochem. 19 (2008) 313–319. doi:10.1016/j.jnutbio.2007.05.008.
[320] D. Hanahan, R.A. Weinberg, Review Hallmarks of Cancer : The Next Generation, Cell. 144 (2011) 646–674. doi:10.1016/j.cell.2011.02.013.
[321] H.A.B. Multhaupt, B. Leitinger, D. Gullberg, J.R. Couchman, Extracellular matrix component signaling in cancer, Adv. Drug Deliv. Rev. 97 (2016) 28–40. doi:10.1016/j.addr.2015.10.013.
[322] J. Insua-Rodríguez, T. Oskarsson, The extracellular matrix in breast cancer, Adv. Drug Deliv. Rev. (2015). doi:10.1016/j.addr.2015.12.017.
[323] E.S. Radisky, D.C. Radisky, Stromal induction of breast cancer: Inflammation and invasion, Rev. Endocr. Metab. Disord. 8 (2007) 279–287. doi:10.1007/s11154-007-9037-1.
[324] E.S. Radisky, D.C. Radisky, Matrix metalloproteinase-induced epithelial-mesenchymal transition in breast cancer, J. Mammary Gland Biol. Neoplasia. 15 (2010) 201–212. doi:10.1007/s10911-010-9177-x.
[325] K. Kessenbrock, V. Plaks, Z. Werb, Matrix Metalloproteinases: Regulators of the tumor, Cell. 141 (2010) 52–67. doi:10.1016/j.cell.2010.03.015.
[326] C.H. Stuelten, Breast cancer cells induce stromal fibroblasts to express MMP-9 via secretion of TNF- and TGF- , J. Cell Sci. 118 (2005) 2143–2153. doi:10.1242/jcs.02334.
[327] E.S. Radisky, M. Raeeszadeh-Sarmazdeh, D.C. Radisky, Therapeutic Potential of Matrix Metalloproteinase Inhibition in Breast Cancer, J. Cell. Biochem. 118 (2017) 3531–3548. doi:10.1002/jcb.26185.
[328] and Z.W. Kai Kessenbrock, Gerrit J. P. Dijkgraaf, Devon A. Lawson, Laurie E. Littlepage, Payam Shahi, Ursula Pieper, A Novel Role for Matrix Metalloproteinases In Regulating Mammary Stem Cell Function via the Wnt Signaling Pathway Kai, 13 (2013) 300–313. doi:10.1016/j.stem.2013.06.005.
[329] S. Saad, L.J. Bendall, D.J. Gottlieb, K.F. Bradstock, C.M. Overall, Cancer cell-associated fibronectin induces release of matrix metalloproteinase-2 from normal fibroblasts, Cancer Res. 62 (2002) 283–289.

[330] S.P. Carey, K.E. Martin, C.A. Reinhart-King, Three-dimensional collagen matrix induces a mechanosensitive invasive epithelial phenotype, Sci. Rep. 7 (2017) 1–14. doi:10.1038/srep42088.
[331] L.M. Coussens, B. Fingleton, L.M. Matrisian, Matrix metalloproteinase inhibitors and cancer: Trials and tribulations, Science (80-.). 295 (2002) 2387–2392. doi:10.1126/science.1067100.
[332] J.A. Sparano, P. Bernardo, P. Stephenson, W.J. Gradishar, J.N. Ingle, S. Zucker, N.E. Davidson, Randomized phase III trial of marimastat versus placebo in patients with metastatic breast cancer who have responding or stable disease after first-line chemotherapy: Eastern Cooperative Oncology Group Trial E2196, J. Clin. Oncol. 22 (2004) 4631–4638. doi:10.1200/JCO.2004.08.054.
[333] K.D. Miller, W. Gradishar, L. Schuchter, J.A. Sparano, M. Cobleigh, N. Robert, H. Rasmussen, G.W. Sledge, A randomized phase II pilot trial of adjuvant marimastat in patients with early-stage breast cancer, Ann. Oncol. 13 (2002) 1220–1224. doi:10.1093/annonc/mdf199.
[334] K.D. Miller, T.J. Saphner, D.M. Waterhouse, T.T. Chen, A. Rush-Taylor, J.A. Sparano, A.C. Wolff, M.A. Cobleigh, S. Galbraith, G.W. Sledge, A Randomized Phase II Feasibility Trial of BMS-275291 in Patients with Early Stage Breast Cancer, Clin. Cancer Res. 10 (2004) 1971–1975. doi:10.1158/1078-0432.CCR-03-0968.
[335] A.H. Webb, B.T. Gao, Z.K. Goldsmith, A.S. Irvine, N. Saleh, R.P. Lee, J.B. Lendermon, R. Bheemreddy, Q. Zhang, R.C. Brennan, D. Johnson, J.J. Steinle, M.W. Wilson, V.M. Morales-Tirado, Inhibition of MMP-2 and MMP-9 decreases cellular migration, and angiogenesis in in vitro models of retinoblastoma, BMC Cancer. 17 (2017) 1–11. doi:10.1186/s12885-017-3418-y.
[336] D.X. Nguyen, P.D. Bos, J. Massagué, Metastasis: from dissemination to organ-specific colonization., Nat. Rev. Cancer. 9 (2009) 274–284. doi:10.1038/nrc2622.
[337] D.M. Pegtel, S.J. Gould, Exosomes, (2019).
[338] B.H. Sung, T. Ketova, D. Hoshino, A. Zijlstra, A.M. Weaver, Directional cell movement through tissues is controlled by exosome secretion, Nat. Commun. 6 (2015) 1–14. doi:10.1038/ncomms8164.
[339] D. Millimaggi, M. Mari, S. D'Ascenzo, E. Carosa, E.A. Jannini, S. Zucker, G. Carta, A. Pavan, V. Dolo, Tumor vesicle-associated CD147 modulates the angiogenic capability of endothelial cells, Neoplasia. 9 (2007) 349–357. doi:10.1593/neo.07133.
[340] J. Webber, R. Steadman, M.D. Mason, Z. Tabi, A. Clayton, Cancer exosomes trigger fibroblast to myofibroblast differentiation, Cancer Res. 70 (2010) 9621–9630. doi:10.1158/0008-5472.CAN-10-1722.
[341] J.A. Cho, H. Park, E.H. Lim, K.W. Lee, Exosomes from breast cancer cells can convert adipose tissue-derived mesenchymal stem cells into myofibroblast-like cells, Int. J. Oncol. 40 (2012) 130–138. doi:10.3892/ijo.2011.1193.
[342] Y.J. Piao, H.S. Kim, E.H. Hwang, J. Woo, M. Zhang, W.K. Moon, Y.J. Piao, H.S. Kim, E.H. Hwang, J. Woo, M. Zhang, W.K. Moon, Y.J. Piao, H.S. Kim, E.H. Hwang, J. Woo, M.Z. and W.K. Moon, Breast cancer cell-derived exosomes and macrophage polarization are associated with lymph node metastasis, Oncotarget. 9 (2018) 7398–7410. doi:10.18632/oncotarget.23238.
[343] M.C. Lowry, W.M. Gallagher, L. O'Driscoll, The role of exosomes in breast cancer, Clin. Chem. 61 (2015) 1457–1465. doi:10.1373/clinchem.2015.240028.

[344] A. Hoshino, B. Costa-Silva, T.L. Shen, G. Rodrigues, A. Hashimoto, M. Tesic Mark, H. Molina, S. Kohsaka, A. Di Giannatale, S. Ceder, S. Singh, C. Williams, N. Soplop, K. Uryu, L. Pharmer, T. King, L. Bojmar, A.E. Davies, Y. Ararso, T. Zhang, H. Zhang, J. Hernandez, J.M. Weiss, V.D. Dumont-Cole, K. Kramer, L.H. Wexler, A. Narendran, G.K. Schwartz, J.H. Healey, P. Sandstrom, K. Jørgen Labori, E.H. Kure, P.M. Grandgenett, M.A. Hollingsworth, M. De Sousa, S. Kaur, M. Jain, K. Mallya, S.K. Batra, W.R. Jarnagin, M.S. Brady, O. Fodstad, V. Muller, K. Pantel, A.J. Minn, M.J. Bissell, B.A. Garcia, Y. Kang, V.K. Rajasekhar, C.M. Ghajar, I. Matei, H. Peinado, J. Bromberg, D. Lyden, Tumour exosome integrins determine organotropic metastasis, Nature. 527 (2015) 329–335. doi:10.1038/nature15756.

[345] Y. Liu, Y. Gu, Y. Han, Q. Zhang, Z. Jiang, X. Zhang, B. Huang, X. Xu, J. Zheng, X. Cao, Tumor Exosomal RNAs Promote Lung Pre-metastatic Niche Formation by Activating Alveolar Epithelial TLR3 to Recruit Neutrophils, Cancer Cell. 30 (2016) 243–256. doi:10.1016/j.ccell.2016.06.021.

[346] B.H. Sung, A.M. Weaver, Exosome secretion promotes chemotaxis of cancer cells, Cell Adhes. Migr. 11 (2017) 187–195. doi:10.1080/19336918.2016.1273307.